Multiscale modeling of heterogeneous materials : application to Shape Memory Alloys

Rui Xu

UNIVERSITÉ DE LORRAINE

École doctorale C2MP

Multiscale modeling of heterogeneous materials : application to Shape Memory Alloys

THÈSE

présentée et soutenue publiquement le 13 juillet 2020

pour l'obtention du

Doctorat de l'Université de Lorraine

(Spécialité Mécanique des Matériaux)

par

Rui XU

Composition du jury

Rapporteurs :	Prof. Abel Cherouat	Université de Technologie de Troyes, France
	Prof. Shabnam Arbab Chirani	Ecole Nationale d'Ingénieurs de Brest, France
Examinateurs :	Dr. Marianne Beringhier	Ecole Nationale Supérieure de Mécanique et d'Aérotechnique, France
	Dr. Gaetano Giunta	Luxembourg Institute of Science and Technology, Luxembourg
	Dr. Céline Bouby	Université de Lorraine, France
	Prof. Heng Hu	Wuhan University, China
	Prof. Tarak Ben Zineb	Université de Lorraine, France
	Prof. Hamid Zahrouni	Université de Lorraine, France
Invités :	Dr. Salim Belouettar	Luxembourg Institute of Science and Technology, Luxembourg
	Prof. Michel Potier-Ferry	Université de Lorraine, France

Laboratoire d'Étude des Microstructures et de Mécanique des Matériaux
LEM3 UMR CNRS 7239 - Université de Lorraine
7 rue Félix Savart - 57073 Metz Cedex 03 - France

Mis en page avec la classe thesul.

Acknowledgment

This thesis has been written during my position as a joint-supervised doctoral candidate at University of Lorraine and Wuhan University.

I would like to express my deeply-felt gratitude to my PhD advisors, Prof. Hamid Zahrouni, Prof. Tarak Ben Zineb and Prof. Heng Hu, for their expertise, invaluable advice and continuous support throughout my studies. Their solid theoretical foundation and tireless academic enthusiasm deeply affect me, and I am honored to acknowledge their mentoring along the way. I deeply look forward to continue our collaboration in both research and life.

An appreciation goes to all my colleagues and friends from University of Lorraine, Wuhan University and Luxembourg Institute of Science and Technology, especially Prof. Michel Potier-Ferry, Dr. Salim Belouettar, Dr. Celine Bouby, Dr. Gaetano Giunta, Dr. Qun Huang and Dr. Jie Yang.

I sincerely thank my family ! Thanks for your constant support and encouragement that backs me to complete my PhD !

Contents

General introduction

Heterogeneous materials, such as composites and cellular materials, are widely used in advanced engineering fields, such as aerospace, medical instrument. Composites have high strength, rich functions and good durability in complicated working conditions. For example, carbon fiber reinforced composites present high strength/weight ratio and high modulus, and have been used in wind turbine blades and cars ; cellular materials present high strength-to-weight ratio and high energy absorption performance. For instance, honeycomb, folded cellular materials and foam are usually used as the core of sandwich structures for dissipating the kinetic energy, damping or reducing the weight of the structure.

Shape Memory Alloys (SMAs) are smart materials which can recover from large inelastic strains by unloading or heating, with an obvious hysteresis effect. Benefiting from this capability, SMAs are used in wide range of applications, such as aircraft, spacecraft, robotics and biomedical. Composites consisting of SMAs and other components may extend the range of the SMAs' applications for more complex situation as well as leads to structure lightening. Besides, developing SMA into architected cellular materials can increases the ratios stiffness/weight and damping/weight and amplify the aforementioned reversible deformation. In recent years, smart applications made by SMA heterogeneous materials have been found in engineering fields, such as SMA wire reinforced concrete which can heal cracks by itself, and soft actuator with SMA and silicon rubber, which can achieve crawling and grasping. Thanks to the highly developed additive manufacturing techniques, such as 3D and 4D printing, users can design a composite or architected material with a certain behavior by tuning its microscopic parameters. Better understanding and controlling these properties will contribute on the development of innovative applications. In that way it is important to develop an adapted and efficient numerical design tool for aforementioned SMA heterogeneous materials considering their multiscale thermomechanical behaviors, based on finite element method and accurate thermomechanical constitutive model for SMAs.

It is usually difficult to model and simulate SMA composites or architected materials due to the following obstacles : (1) the macroscopic response interacts with its microscopic material properties and behaviors in real time. Multiscale homogenization methods which couple the macroscopic and microscopic scales are required to ensure accurate solutions ; (2) the thermomechanical mechanisms of SMAs are particularly complex and strongly non-linear. An appropriate SMA constitutive model must be adopted to accurately simulate its complex thermomechanical behavior ; (3) in the case of diverse microscopic material properties and complex geometrical shapes, an generic and user-friendly modeling tool must be developed to meet the needs of different designs ; (4) since above heterogeneous materials are usually designed in thin-walled shapes, buckling phenomena which often lead to the failure of structures should also be considered. Its modes are multiple and wavelengths can be small, thus advanced non-linear solvers must be used to accurately and efficiently simulate such strong geometrical non-linear phenomena ; (5) based on the classical concurrent multiscale computing framework, tremendous microscopic

calculations must be performed in each macroscopic iterative step to update the information on each integration point. Thus, the computational efficiency needs to be further improved. Facing above challenges, the main aim of this thesis is to develop advanced and efficient multiscale modeling and simulation techniques for SMA composites and architected materials. A comprehensive using of existing methods, such as computational homogenization methods, model reduction techniques and advanced nonlinear solver, and developments for new computational schemes, such as data-driven computing, can be found in this thesis.

A brief review of SMA heterogeneous materials, homogenization methods, fiber instability phenomenon and data-driven methods is presented in chapter 1. In chapter 2, the first three aforementioned problems are addressed by developing a 3D generic numerical tool for SMA heterogeneous materials. A multiscale finite element method (FE^2) is proposed for modeling the pseudo-elasticity (PE) and the shape memory effects (SMEs). In this method, heterogeneous materials are separated into a macroscopic and a microscopic level, where the constitutive behavior of each integration point on macroscopic level is represented by the effective behavior of a corresponding Representative Volume Element (RVE). This effective behavior is computed by finite element method under the RVE meshed by volume element. The real-time information transition between the two levels is realized on a commercial platform ABAQUS via its user defined material subroutine (UMAT). A thermomechanical model, proposed by Chemisky et al. [1], is adopted to describe the total constitutive behavior of SMA. This model considers three path-dependent strain mechanisms related to phase transformation, martensite reorientation and twin accommodation by the derivation of Gibbs free energy. Considering an SMA fiber reinforced composite, several thermomechanical tests from the literature subjected to tension-compression and bending loads are studied to validate our multiscale model, which shows good accuracy and reliability. Further, this model is used for design and simulation of architected SMAs thanks to its generic computing platform ABAQUS. Firstly, a parametric analysis at the cellular level with a series of RVEs is carried out to predict relations between the void fraction, the total stiffness, the hysteresis effect and the mass of SMAs. Secondly, the structural responses of the architected SMAs are studied by the FE^2 method, which uses the effective constitutive behavior of the RVE to represent the behavior of the macroscopic structure. Through a three point bending test, it is observed that the structure inherits the strong nonlinear responses—both the hysteresis effect and the PE—of the architected SMAs at the cellular level. Furthermore, the influence of the void fraction at the RVE level to the materials' structural responses can be more specifically and directly described, instead of using an RVE to predict the behavior at the microscopic level. Thus, this work could be referred for optimizing the stiffness, the hysteresis effect and the mass of architected SMA structures and extended for possible advanced applications.

Despite the multiscale modeling of SMA cellular material and structures, buckling instability phenomenon is a typical complicated problem in the investigated thin structures. However, the adopted concurrent multiscale method requires a RVE at each integration point of the macroscopic finite element model. The element size of RVEs depends on the wavelength of the microscopic buckled fiber, resulting in a large amount of computations. Besides, the relationship between the microscopic fiber buckling modes and macroscopic instability is also to be further studied. Thus, in chapter 3 a computationally efficient multiscale model is proposed to accurately simulate and analyze the instability phenomenon of long fiber reinforced composites. The FE^2 method based on the homogenization theory is adopted to realize the real-time interaction between the microscopic and the macroscopic levels. To increase the computational efficiency in the microscopic level and control the nonlinear calculations, the Fourier-related analysis is carried out on the RVEs using the Technique of Slowly Variable Fourier Coefficients (TSVFC). In this method, all fast varying unknowns are replaced by slowly varying unknowns. The established nonlinear

multiscale system is solved by the Asymptotic Numerical Method (ANM), which is more reliable and less time consuming than other classical iterative methods. This model is used to study the structural instability and the fiber micro-buckling of long fiber reinforced composites. The effects of fiber wavelength on the buckling and post-buckling of macro structure are discussed.

Although an efficient nonlinear solver and a reduced RVE model is developed to improve the overall computational efficiency of the multiscale modeling approach, the computational cost still requires to be reduced in this concurrent multiscale framework. Because the information over each macroscopic integration point is supposed to be updated at each iteration during the online macroscopic computation, which requires tremendous repetitive computations over associated RVE. Inspired by data-driven computing, in chapter 4 novel approaches which decouple scales are proposed to reduce the online computational cost for composite structures, namely data-driven multiscale finite element method (data-driven FE^2) and Structural-Genome-Driven (SGD) computing. In the data-driven FE^2 method, the correlated scales in the classical FE^2 method are here split to be computed sequentially and separately : the microscopic problems are calculated in advance to construct an offline material genome database, which is later used in the macroscopic data-driven analysis. In this new framework, the difficulties in formulating and solving complicated multiscale system are avoided by dealing with single scale problems. Moreover, the online computation of microscopic problems in the classical FE^2 method is replaced by searching data points over the offline database in the data-driven FE^2 method. Thus, the online computing efficiency of structural analysis is significantly improved. After that, SGD computing is proposed for thin-walled composite structures, where the Structural-Genome database is collected through the FE^2 method. Compared to Material-Genome-Driven (MGD) analysis, proposed by Kirchdoerfer and Ortiz, 2016, the new SGD method benefits from not only the model reduction, but also the ability to easily deal with complex microscopic geometry and material properties. Several numerical tests are considered to demonstrate the efficiency and robustness of the proposed method.

Generally, this thesis develops efficient multiscale modeling and simulation schemes for SMA composites and architected cellular materials. The thermomechanical behaviors of those materials are in-depth studied, providing a solid theoretical and technical support for their design and application. Also, those highly efficient multiscale methods can be used for other composite materials and structures.

Table des figures

1

State of art

Contents

In this chapter, a brief state of art is presented including the following three aspects : (1) SMA heterogeneous materials and their modeling ; (2) instability phenomenon in long fiber reinforced composites ; (3) multiscale homogenization methods.

1.1 SMA heterogeneous materials and their modeling

SMA heterogeneous materials subject to thermomechanical fields have very complicated behavior. Because it depends on not only the macroscopic load, but also the microscopic material properties, geometrical parameters and phase transformations of SMAs. Thus, SMA heterogeneous materials present typical multi-physical and multi-scale behavior. To understand their macroscopic-microscopic interaction and predict the thermomechanical behavior, appropriate multiscale and user-friendly numerical tool is required. To this end, this section will introduce the multiscale and multi-physical modeling and simulation techniques for SMA heterogeneous materials from the following three aspects : (1) SMAs and their constitutive modeling ; (2) SMA composites and their multiscale modeling ; (3) architected cellular SMAs and their multiscale modeling.

1.1.1 SMAs and their constitutive modeling

SMAs are smart materials used in wide range of applications, such as aircraft, spacecraft, robotics and biomedical, benefiting from the capability of sustaining large inelastic strains. This latter can be recovered by unloading or heating, with an obvious hysteresis effect. Two main features, namely pseudo-elasticity (PE) and the shape memory effect (SME), of SMAs are illustrated in Fig. 1.1, where Fig. 1.1a shows the PE and hysteresis effect subject to partial loading, and Fig. 1.1b gives the SME in a "cooling-loading-unloading-heating" cycle. One typical appli-

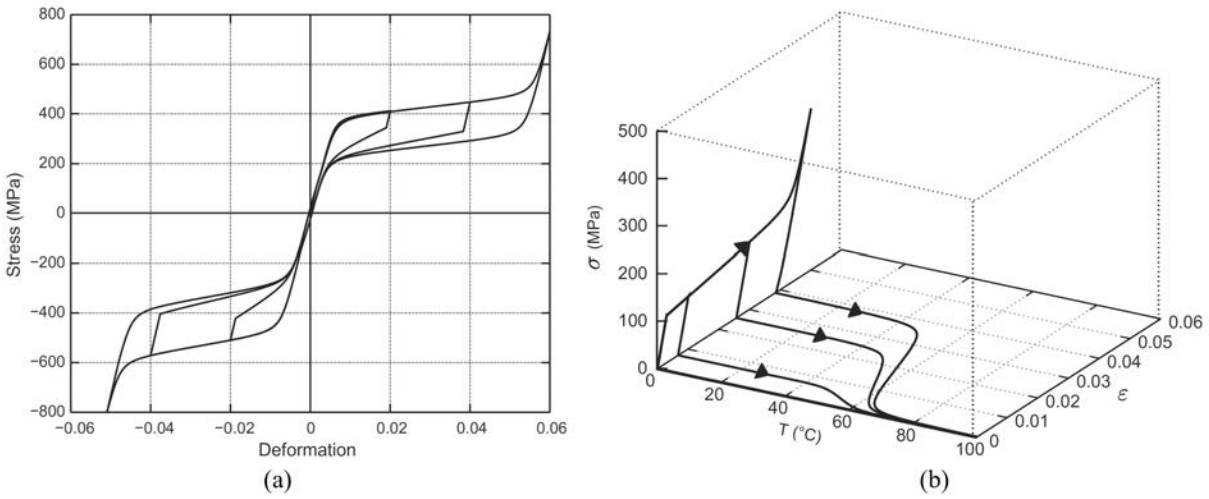

FIGURE 1.1 – (a) the PE considering partial loading and tension-compression asymmetry and (b) the SME simulated by model Chemisky et al. [1].

cation of SMA can be found in Fig. 1.2a. The SMA beam components embedded inside chevrons can change the shape of the chevrons automatically in different temperature conditions, which is varying along with the current altitude of the plane ; Fig. 1.2b presents an artificial wing made by SMA, which can change its shape when the temperature is varying. An overview on SMAs' possible applications could be found in the work of Lagoudas [2] and Jani et al. [3].

FIGURE 1.2 – (a) Boeing variable geometry chevron, flight testing (Hartl and Lagoudas [4]) ; (b) An artificial wing made by SMA (Sofla et al. [5]).

These specific thermomechanical effects are highly related to the microscopic phase transformations. SMAs present two different phases, which differ from each other in their crystal structures and the yielded mechanical properties. One is the austenite in high temperature state and the other is the martensite in low temperature. The crystal structure of austenite is generally cubic, while those of martensite are generally tetragonal, monoclinic or orthorhombic (Lagoudas [2]). The so-called martensitic transformation between two phases occurs when lattices of atoms are distorted by shear stress (Lagoudas [2]). The martensitic crystal structures can differ from each other in different orientation directions, which are called variants. There are two types of martensite by assembly martensitic variants in different forms. One is the twinned martensite formed by a set of martensitic variants, which self-accommodate each other such that the average macroscopic shape change is negligible. The other is the detwinned martensite formed by a specific dominant variant such that the average macroscopic shape change is visible. The reversible phase transformation from austenite (parent phase) to martensite (product phase) and vice versa forms the basis for the specific behavior of SMAs. The phase transformation between austenite and martensite is reversible along with varying of an applied thermomechanical load, which contributes to the unique behavior of SMAs. For example, when the material is cooled, the crystal structure changes from austenite to twinned martensite and vice versa the crystal structure changes back to austenite when the material is heated. Fig. 1.3 illustrates several typical phase transformations upon different thermomechanical loadings, yielding changes in the crystal structure.

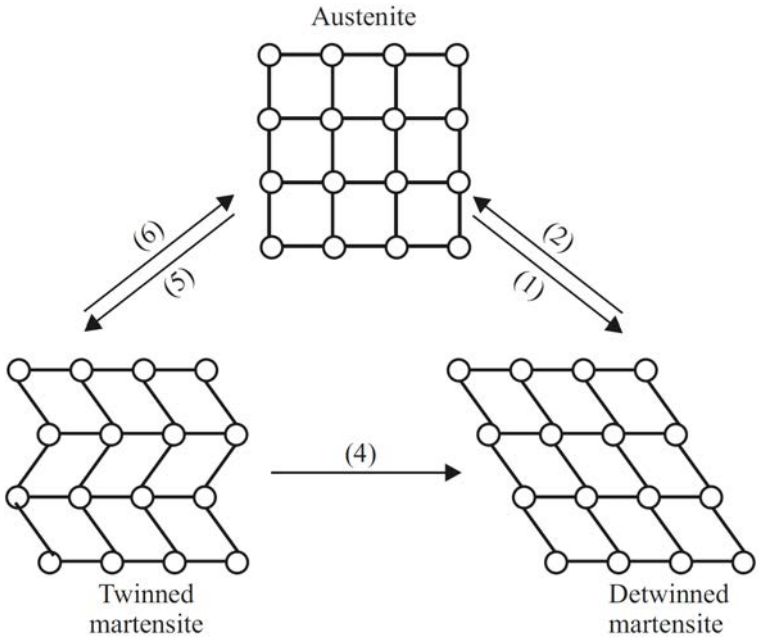

FIGURE 1.3 – Changes in the crystal structure : (1) loading/cooling ; (2) unloading/heating ; (4) loading ; (5) cooling ; (6) heating. (Sun and Huang [6]).

Over the past 40 years, researchers have proposed various models to simulate the thermomechanical behavior of SMAs. These models can be broadly classified as microscopic thermodynamic models (Uehara et al. [7], Saitoh and Liu [8]), micro-macroscopic models (Wang et al. [9], Niclaeys et al. [10]), and macroscopic phenomenological models (see the review paper of Cisse et al. [11]). Microscopic thermodynamic models intend to describe microstructureal features of SMAs at the lattice or grain-crystal levels. Some of them are developed relying on

the Ginzburge-Landau theory or molecular dynamics. Micro-macroscopic models describe the material behavior at the micro or meso scales by micromechanics and then derive macroscopic constitutive equations using appropriate scale transition techniques. Macroscopic phenomenological models are based on phenomenological analysis, simplified micro-macro thermodynamics or direct experimental data fitting, approximating the effective behavior of SMAs. Among above models, macroscopic phenomenological models are widely used in engineering problems, for their simple assumptions and compatibility with finite element computation. Boyd and Lagoudas [12] proposed a phenomenological SMA model using a free energy function and a dissipation potential based on the ideas of Patoor et al. [13], Raniecki and Lexcellent [14], Sun and Hwang [15, 16]. This model is able to describe PE and SME due to martensitic transformation and reorientation of polycrystalline SMA materials. This model was later developed by Lagoudas et al. [17] and implemented in combination with finite element method, in which a return mapping technique was adopted to derive its incremental formulation. After experimentally validation, this model was applied for the thermomechanical simulation of an active composite with SMA fibers embedded in matrix. Leclercq and Lexcellent [18] developed a general macroscopic model which separated the volume fraction of martensite into oriented and self-accommodated parts in order to describe the reorientation of martensite variants. By assuming five yield functions related to different thermomechanical process, this model defined the criteria for phase transformation and derived corresponding kinetic equations considering consistency equations. Three specific types of SMAs were chosen to calibrate the parameters of the model and the experimental data showed good agreement with the results simulated by the numerical model. Souza et al. [19] presented a 3D phenomenological model to describe the mechanical behavior of polycrystalline SMAs with stress-induced phase transformations. In this model, an admissibility condition is assumed for thermodynamic forces and a locking constraint is considered for phase transition. To describe the stress-induced phase transformations, a transformation strain tensor is introduced to describe its corresponding overall kinematic behavior. The numerical results of this model are in a good agreement with the experimental results carried out by Sittner et al. [20]. Based on the model of Souza, Auricchio and Petrini [21] proposed a robust algorithm that can simulate the SME and PE behavior subjected to non-proportional loading by a finite element method. A model based on a thermodynamic description of the phase transformation and martensite reorientation was implemented by Peultier et al. [22, 23] in the ABAQUS finite element software. Two internal variables, namely the overall martensite volume fraction and the averaged transformation strain, were considered to account the phase transformations. Derived from Gibbs free energy potential, the control equations for a set of internal variables were formulated and implemented in finite element scheme. This model presented good results which were simulated by uniaxial tensile loadings and a three-point bending test. Note that in this model, the tension and compression asymmetry and non-proportional loading cases were not considered yet. This model was latterly improved by Chemisky et al. [1] with a 3D model dedicated to NiTi alloy. Chemisky et al. [1] considered the strain mechanism related to the twins accommodation by adding a new internal variable. The description of internal loops for partial loading was also improved by redefining the critical threshold according to experimental results. In addition, the tension-compression asymmetry effect during transformation was taken account, see Fig. 1.1. Zaki and Moumni [24] developed a phenomenological model for NiTi SMAs within the framework of generalized standard materials with internal constraints (Halphen and Son [25]). The numerical predictions show good agreement with the experimental data for both pseudoelasticity and orientation of self-accommodated martensite. Saintsulpice et al. [26] carried out a series of cyclic tests to develop a 3D macroscopic model for the super-elasticity of SMAs able to describe the evolution of permanent inelastic strain during cycles.

Based on the above-mentioned classic constitutive models, researchers have continuously developed a series of new models in recent years. Extended from Khalil et al. [27], Sallami et al. [28] developed a constitutive model for Fe-based SMA, in which the phase transformation, plastic sliding and large strain were considered. Two internal variables, namely volume fraction of martensite and the plastic strain, were adopted, with the assumption that the local deformation gradient split into elastic and inelastic parts in the so-called total Lagrangina formulation. Wang et al. [29] proposed a constitutive model to describe the phase transformation and martensite reorientation mechanisms of SMAs in a finite strain formulation. The deformation gradient was split into different parts accounting for elastic, thermal and inelastic strains, where the inelastic part was further assumed to be composited by phase transformation and martensite reorientation. The control equations were formulated in a time-discrete form and implemented in the finite element framework via the UMAT on ABAQUS. Results showed that this model had good in simulating the response of SMA wires considering large strains and rotations cases. Xiao [30] proposed a constitutive model based on classical elastoplastic J_2-flow to simulate the PE hysteresis of SMAs. The varying of the yield surface and its center are related to formulate the nonlinear hardening rule for this model. Ojha and Sehitoglu [31] proposed a model regarding the Bogers-Burgers double shear mechanism to simulate the bcc-fcc transformation in FeMnAlNi SMA. This model derived the fcc martensite formation stress by formulating the energy expression, in which the transformation shear potential and the elastic interaction between dislocations were both considered. Mahnken et al. [32] developed a constitutive model to describe the phase transformations and asymmetric plasticity mechanisms in the cutting processes of steels. To address the asymmetric plasticity behavior which was highly dependent on the strain rate and temperature, the so-called Johnson-Cook model and a transformation induced plasticity model were utilized to formulate this model. The numerical results obtained by finite element analysis demonstrated strain softening mechanisms related to temperature and strain rate in a cutting process of steels. Gu et al. [33] later implemented the model of Zaki and Moumni [24] using an explicit closed-form expression of the material jacobian to simulate the multiaxial non-proportional loading response of SMAs. Hazar et al. [34] combined the model of Zaki and Moumni [24] with a nonlocal stationary method to analyze phase transformation around the tip of a stable growing edge crack in a semi-infinite Nitinol plate. Note the overview of constitutive models in this thesis is not exhaustive. More details can be found in Lagoudas [2], Cisse et al. [11].

In summary, the micromechanical mechanism of SMA is quite complicated, involving various phenomenons such as phase transition, plastic slip, and twinning adaptation. It is necessary to select an accurate thermodynamic constitutive model according to specific problems. However, the SMA based heterogeneous materials concerned in this paper involve more complex multiscale behavior, which requires a reliable SMA constitutive model. Among the aforementioned constitutive models, the NiTi alloy constitutive model developed by Chemisky et al. [1] is compatible with the finite element method, and can effectively investigate the general thermodynamic mechanisms such as phase transition, martensite reorientation, and twin accommodation. Therefore, this paper will use this model as an example to carry out multiscale modeling and simulation on SMA based heterogeneous materials.

1.1.2 SMA composites and their multiscale modeling

Composites are widely used in advanced engineering fields such as aerospace, medical instruments, due to their high strength, rich functions and good durability in complicated working conditions (Węcławski et al. [35], Vesely et al. [36], Liu et al. [37], Jochum et al. [38]). For example, carbon fiber reinforced composites present high strength/weight ratio and high modu-

lus, and have been used in wind turbine blades and cars (Murdani et al. [39], Fasana et al. [40]). Along with the development of manufacturing techniques, more and more complicated composites can be manufactured nowadays and present great potential in the future. For example, using 4D printing (Ge et al. [41], Momeni et al. [42], Tibbits and Skylar [43], Ding et al. [44]), Ge et al. [41] designed an active composite origami which can deform automatically when the temperature is changed. This structure is composed by elastic matrix and shape memory polymer fiber.

As aforementioned, SMA are widely used in the design for functional applications. However, the high cost of SMAs limits their promotion to a certain degree. Composites consisting of SMAs and other cheaper components could be an alternative choice for designing SMAs applications. Moreover, the combination of different material characteristics may extend the range of the SMAs' applications for more complex situation as well as leads to structure lightening (Lester et al. [45]), see for example the hybrid SMA woven composite depicted in Fig. 1.4, which presents good impact resistance (Meo et al. [46]). Concretes reinforced by shape memory alloys

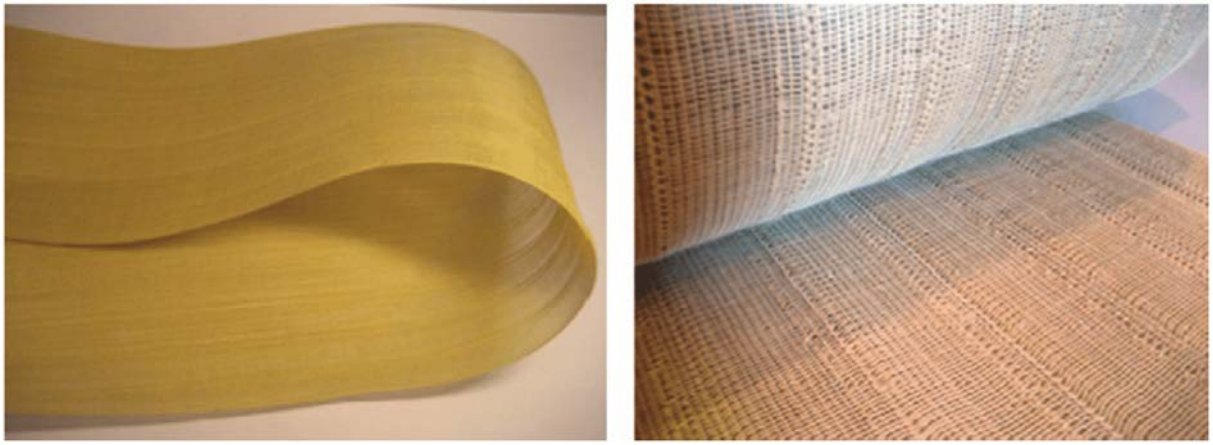

FIGURE 1.4 – Hybrid PPS/SMA/Kevlar fabric (Meo et al. [46])

present good seismic performance and crack self-healing capacity, which provide a wide application prospect in civil engineering (Halahla et al. [47]). Feng et al. [48] designed a multifunctional composite formed by elastomer embedded with SMA wires. Their composites show good in-plane and out-plane deformation capability and varying stiffness characteristics in different environment temperatures. Li et al. [49] designed a simple soft actuator with SMA and silicon rubber, based on a periodic deformation mechanism. This soft actuator can achieve crawling and grasping by electrical heating methods.

SMA composites subject to thermomechanical load have very complicated behavior. Because it depends on not only the macroscopic load, but also the microscopic material properties, geometrical parameters and phase transformations of SMAs. Thus, SMA composites present typical multi-physical and multi-scale behavior. Valuable works using multiscale homogenization methods to study the thermomechanical behavior of SMA composites have been presented over the past few decades. The models using self-consistent method (Lagoudas et al. [50], Siredey et al. [51], Patoor et al. [52], Helm and Haupt [53], Marfia [54]), unit cell methods (Damanpack et al. [55], Kawai et al. [56]), asymptotic methods (Chatzigeorgiou et al. [57], Dehaghani et al. [58]) and FE^2 methods (Kohlhaas and Klinkel [59], Chatzigeorgiou et al. [60]) can be mentioned as a review. Chatzigeorgiou et al. [57] proposed a model which can simulate the fully coupled thermomechanical response of a multilayered composites by using the asymptotic expansion homogenization technique. Kohlhaas and Klinkel [59] proposed a FE^2 scheme to simulate the free,

two-way and the constrained SME of randomly oriented and distributed SMA fiber reinforced composites. The pseudo-plasticity at low temperature range and the pseudo-elasticity at high temperature range were also studied. This model considers a 1D element for the SMA fiber and 3D element for the matrix. The 1D formulation allows for easy meshing in the framework of the finite element method. The present model puts emphasis on the proper simulation of the phase transition from martensite to austenite within the SMA—no matter which loading conditions are applied. This allows for the ability to prestress a surrounding matrix and amend brittle material. The SMA fiber material model is embedded into two meshing approaches which are compared. The approaches proof each other by yielding same results. It is shown that the rebar concept has crucial advantages over the conform meshing concept. Dehaghani et al. [58] presented a 3D finite element based hierarchical multiscale analysis framework to solve the macro and micro scale problems simultaneously. The proposed approach is applied to a number of problems involving SMA fiber reinforced composites and porous SMAs to assess its accuracy and effectiveness. The PE response of SMA constituents in micro scale is modeled based on the work by Boyd and Lagoudas [12], Qidwai and Lagoudas [61]. Macro problems are solved under various stress loading/unloading conditions including tension, flexure, and torsion. Detailed illustrations are presented regarding the distribution and concentration of different field variables such as the martensitic volume fraction and the stress state in the micro scale along the austenite to martensite transformation and the reverse path. Due to lack of plane symmetry, 2D general plane strain models cannot accurately predict the microscopic behavior of porous materials. Hence, the effect of shape of 3D ellipsoid pores on the mechanical response of the porous SMA is investigated through a detailed parametric study.

1.1.3 Architected cellular SMAs and their multiscale modeling

Cellular materials are widely used for their high strength-to-weight ratio and high energy absorption performance (Ashby and Gibson [62], Ashby et al. [63]). For instance, honeycomb, folded cellular materials and foam are usually used as the core of the sandwich structures for dissipating the kinetic energy, damping or reducing the weight of the structure (Ashby et al. [63], Sarvestani et al. [64], García-Moreno [65], Hangai et al. [66], Strano et al. [67]). However, honeycomb and folded cellular materials have high manufacturing costs and moisture problem, as well as buckling problems (Rashed et al. [68]). The mechanical behaviors of foams are too difficult to be accurately measured for their stochastic cells, which always results in the excessive use of materials to satisfy the safety factor. To overcome these shortcomings, partially-ordered foams allowing limited structural control of the pore and spatial distribution of pore levels, such as metal syntactic foams (Taherishargh et al. [69, 70, 71], Broxtermann et al. [72], Linul et al. [73], Luong et al. [74]) are studied. Furthermore, architected cellular materials with an ordered structure were designed and studied during these years (Rashed et al. [68], Pingle et al. [75], Schaedler et al. [76], Schaedler and Carter [77], Lehmhus et al. [78]), such as the ultralight metallic microlattice, see Fig. 1.5a. Thanks to the highly developed additive manufacturing techniques, such as 3D printing (Ngo et al. [79], Mostafaei et al. [80]) and selective laser melting (Rashed et al. [68], Mehrpouya et al. [81]), the manufacturing of architected cellular materials is no longer impossible, see Fig. 1.5b. Users can design a cellular material with a certain behavior by tuning its cellular parameters, such as the geometry, components, local mechanical properties, etc.

Architected cellular materials' functionality could be extended by combining the features of various materials, such as SMAs. It is well known that SMAs, such as NiTi, can endure large deformation and recover their initial shape after unloading (see for example the reviews of

(a) (b)

FIGURE 1.5 – (a) a ultralight metallic microlattice (Schaedler et al. [82]) ; (b) a graded lattice core manufactured using the selective laser melting process (Mines [83]).

Lagoudas [2], Patoor et al. [84], Lagoudas et al. [85], Tobushi et al. [86], Cisse et al. [87]). This PE brings high performance to SMA in energy absorption. When the given load reaches a critical level in a superelastic test, SMA will apparently soften due to its inner phase transformation. This behavior enables SMA to absorb the external energy as much as possible and prevents material from crushing or buckling. Such a kind of response is very similar to the ideal response of the cellular material designed by Schaedler et al. [76]. Meanwhile, the hysteresis effects observed in SMA behavior can dissipate a large amount of energy. All mentioned features of SMAs meet the requirements of an architected structure for energy absorption applications very well. In addition, taking advantage of the lightweight and SME, architected SMAs may be designed for advanced applications in aerospace, civil engineering, etc.

To investigate the behavior of architected cellular SMAs, rare, but valuable works have been proposed (Machado et al. [88], Ravari et al. [89], Ashrafi et al. [90]). Machado et al. [88] proposed an experimental and modeling study on the cellular NiTi tube based materials. In order to design and optimize the architected SMA tube materials, the authors studied the effective behavior of the thin-walled NiTi cellular materials by carrying out a study based on experiment and numerical simulation. The influences of SMAs' material properties and cellular architecture on the effective behavior were investigated. To reduce the high cost of fabrication, Ravari et al. [89] focused mainly on numerical modeling for designing and optimizing SMA cellular lattice structures. The effects of the geometry and cellular imperfections on the effective behavior of the material were investigated by unit cell and multi-cell methods. This work was later developed by Ashrafi et al. [90], who proposed an efficient unit cell model with modified boundary conditions for SMA cellular lattice structures. The SME was also simulated by this model, which had good agreement with the experiment. Cissé et al. [91] proposed an effective constitutive model for architected cellular iron-based shape memory alloys considering the pressure dependency and transformation-plasticity interaction. Zhu et al. [92] realized the accurate 3D reconstitution of porous SMAs and studied their superelastic behavior considering different geometrical parameters.

The above works mainly focused on the effective cellular response in order to represent or predict the behavior of architected SMA structures. Considering the scale separation between the microscopic cellular scale and macroscopic structural scale, however, it is difficult to predict the structural response of a unit cell without certain assumed boundary conditions, because the stress-strain states of the macroscopic structure are usually not uniform and the deformations at the microscopic level could be totally different. Thus, in order to directly simulate the structural

responses of architected SMA, more appropriate numerical methods should be used. During the past few decades, multiscale modeling approaches have been developed and widely used (Kanouté et al. [93], Geers et al. [94], El Hachemi et al. [95], Kinvi-Dossou et al. [96]). As one of the most effective multiscale methods, the FE^2 method (Feyel [97]) to describe the response of high nonlinear structures using generalized continua shows good performance in various applications, such as fiber buckling (Nezamabadi et al. [98]), composite shells (Cong et al. [99]), rate-dependent response (Tikarrouchine et al. [100]) and SMA based fiber/matrix composites (Kohlhaas and Klinkel [59], Chatzigeorgiou et al. [60]). In this approach, both the structural level and the RVE level are simulated by the finite element method (FEM). Two levels are fully coupled and computed simultaneously, where the unknown constitutive behaviors on the structure level are represented by the effective behaviors of homogenized RVEs, and the strain states of the RVEs are given by the associated integration points. In order to make multiscale procedures more generic and easy to use for industries, works to extend them on commercial computing platform, such as finite element software ABAQUS, have been proposed (see Yuan and Fish [101] and Tchalla et al. [102]). A brief review on multiscale homogenization methods is given in Section 1.3. Generic and user-friendly numerical modeling tool is of importance to significantly reduce the modeling cost in the design for architected SMA, as well as SMA composites. Thus, this thesis is about to implement the FE^2 framework on ABAQUS with the SMA constitutive model, and develop a generic multi-physical and multiscale tool for the simulation of SMA heteregeneous materials.

The aforementioned structures with microscopic fiber and thin-walled cells are prone to buckling phenomenon which usually leads to structural failure. This mechanism is very complex due to its strong nonlinearity and multiple modes. Thus, efficient multiscale modeling on buckling phenomenon is also concerned in this thesis. As a typical multiscale instability problem, the buckling of long fiber composites under compressive stress is quite complicated, and is taken into account as an example. The modeling for the instability problem of long fiber reinforced composite is briefly introduced in the next section.

1.2 Instability phenomenon of long fiber reinforced composites

Composite materials containing slender fiber inclusions widely exist in nature (Węcławski et al. [35], Su et al. [103]) and are also widely used in aviation, aerospace, biology, medicine and other engineering fields (Vesely et al. [36], Liu et al. [37], Jochum et al. [38]). The macroscopic instability of these long fiber composites under compressive stress has been paid high attention by academia. Its importance is mainly reflected in the following two aspects : (1) in reinforced composites, the critical load of the microscopic fiber buckling is often lower than the strength limit of the material (Farooq and Myler [104]), and the macroscopic kinking induced by the fiber buckling almost determines the lower limit of the structural strength (Poulios and Niordson [105]), see Fig. 1.6 a kink band in a composite plate. For example, the strength of the carbon fiber laminate is sometimes only 60% of the tensile strength (Budiansky and Fleck [106]) ; (2) in functional composites, the micro-buckling of the fiber is closely related to the macroscopic function, sometimes even to the health in life sciences. For example, Alzheimer's disease and Parkinson's disease are both related to the instability of amyloid fibrils during growth (Chiti and Dobson [107]).

The macroscopic instability of long fiber composites under compressive stress is quite complicated because it not only depends on the macroscopic geometry and load form but also depends on the volume ratio of the fiber/matrix, the matrix's shear modulus and fiber instability wavelength on the microscopic scale. Thus, the instability of long fiber composite structures is a

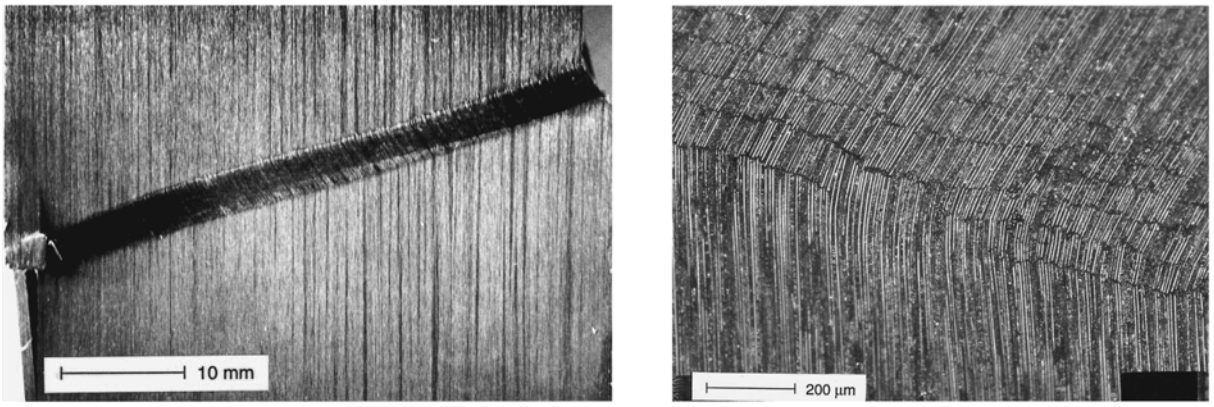

FIGURE 1.6 – A kink band in a composite plate (a) macroscopic graph and (b) microscopic graph (Vogler and Kyriakides [108]).

typical multiscale mechanical behavior. Whether to predict its process or to reveal its mechanism, multiscale modeling and simulation is the most suitable numerical scheme, but facing two significant challenges : (1) the macroscopic response and microscopic fiber buckling are closely related to each other. Therefore, it is necessary to accurately model the behavior on both the two scales and to exchange the stress and the strain information between the two scales in real-time, which results in a vast number of Degrees Of Freedoms (DOFs) and many computations. Thus, it is difficult to balance the computational efficiency and the calculation accuracy ; (2) the nonlinear calculations are complicated to be controlled due to the interaction between the fiber buckling on the microscopic level and the instability of the macroscopic structure.

1.2.1 Microscopic numerical models

The numerical simulation for the instability of long fiber composites under compressive stress can be traced back to the 1990s. In 1992, Guynn et al. [109] constructed a two-dimensional numerical model for studying the micro-buckling of fibers and calculated the nonlinear instability of the "matrix-fiber-matrix" unit cell by applying periodic boundary conditions. The effects of parameters, such as shear strength and instability wavelength, on fiber micro-buckling were studied. The method was later extended by Gutkin et al. [110] to study the kink-band formation in shear mode. Kyriakides et al. [111] demonstrated the effects of the entire kinking process by simulating the deformation of the multilayer fibers and substrates. Then, Vogler et al. [112] extended this work to three-dimensional structures and found that the kink features of the three-dimensional model and the two-dimensional model are the same. Guimard et al. [113], Feld et al. [114] introduced a statistical theory in the analytical models of Budiansky and Fleck [106] and constructed a numerical model that describes the peak distribution of intensity. In recent years, Romanowicz [115], Wind et al. [116] systematically summarized and compared the work of predecessors, and also proposed their respective two-dimensional microscopic models to explore the effect of boundary conditions, dislocation angles and their distribution to kink-band.

In the above works, both the infinite-width model using periodic boundary conditions (Guynn et al. [109], Gutkin et al. [110]) and the finite-width model with free boundary (Kyriakides et al. [111], Vogler et al. [112], Wind et al. [116]) use a simple microscopic method with a microscopic structure consisting of one fiber or several fibers embedded in a matrix, in which the effect

from the macroscopic scale is still neglected. In addition, the microscopic numerical model is not proper for structures with large size or complex geometry, because both the fiber and the matrix need to be discretized, which requires a large number of DOFs and calculation costs. Therefore, the microscopic numerical model is not suitable to study the multiscale instability of long fiber composite structures.

1.2.2 Multiscale homogenization models and their nonlinear solver

As mentioned above, the instability of long fiber composite structures is a typical multiscale mechanical behavior, so numerical homogenization techniques (Feyel [97], Kouznetsova et al. [117], Koutsawa [118], Koutsawa et al. [119]) should be the best numerical scheme to study the instability. At the end of the 20th century, Fleck and Shu [120], Jensen and Christoffersen [121] proposed efficient macro-microscopic numerical models based on the homogenization theory, but the former is based on phenomenological analysis of some specific experimental observations, while the latter ignores the fiber bending stiffness. Drapier et al. [122] successfully expressed the displacement and strain variables as the superposition of macroscopic and microscopic mechanical fields to realize the analysis in two scales, but their model is limited to analyzing the local structure with few wavenumbers. Poulios and Niordson [105], under the inspiration of Fleck and Shu [120], deduced a new kinematic internal variable vector in the large deformation frame to construct a homogenization model which can explicitly introduce the hyperelastic fiber and the super elasto-plastic matrix. This model can predict the macroscopic instability process of long fiber composite structures accurately, but the effect of the fiber's micro-buckling on the macroscopic instability is neglected in the kinematic hypothesis. Therefore, in subsequent studies, Poulios and Niordson [123] used macroscopic structural defects to induce microscopic fiber instability. Nezamabadi et al. [98] analyzed the relationship between macroscopic and microscopic instability using the FE^2 method (Feyel [97], Kouznetsova et al. [117], Nezamabadi et al. [124]) based on the computational homogenization theory. The FE^2 method realizes the bi-directional real-time transmission of macroscopic and microscopic information by "the macroscopic level transmits the strain to the microscopic RVE, and the RVE transmits the stress to the macroscopic level". However, this method requires a RVE at each integration point of the macroscopic finite element model, of which the element size depends on the wavelength of the microscopic buckled fiber, resulting in a large amount of computations. Besides, the relationship between the microscopic fiber buckling modes and macroscopic instability is also to be further studied. Thus, the numerical homogenization model still needs to be improved to accurately and efficiently simulate the double-scale instability of long fiber reinforced composites.

In recent years, instability problems have been studied by model order reducing techniques, such as Proper Orthogonal Decomposition (POD) (Yvonnet et al. [125], van Tuijl et al. [126]), Empirical Interpolation Method (Hernández et al. [127]), Fourier-related envelope model (Damil and Potier-Ferry [128, 129], Huang et al. [130]). The results in Refs. Huang et al. [131, 132], Damil et al. [133] show that the Fourier-related envelope model is efficient in solving fiber instability problem because its element size is independent of the fiber wavelength. Also, it can capture the instability mode by the given wavelength and even simulate the coupling of the global buckling and local wrinkling instability, see Liu et al. [134], Mhada et al. [135], Attipou et al. [136], Huang et al. [137]. Therefore, it is adopted in this work to simulate the fiber buckling.

Compared with the traditional Newton-Raphson method, the ANM (Nezamabadi et al. [98], Cochelin [138], Boutyour et al. [139], Zahrouni et al. [140], Cadou et al. [141], Abichou et al. [142], Assidi et al. [143], Tri et al. [144], Yang et al. [145], Choe et al. [146]) is more efficient and more stable when applied to strong nonlinear and multi-bifurcation problems. In this method,

the unknowns are expanded by high order power series to convert the nonlinear equations into a series of linear equations. Details on the use of the ANM for the resolution of non linear problems are given in chapter 5. The ANM shows high computational efficiency because the tangent matrix is consistent in a nonlinear increment step and its length is self-adaptive. Liu et al. [134] and Huang et al. [147] have shown that the ANM's application in the Fourier envelope model can significantly improve computational efficiency when considering the instability of both the sandwich structure and the thin film structure. In addition, Vannucci et al. [148] defined a bifurcation indicator by searching the singularity points along the load-displacement curve in the ANM. This indicator has been successfully used for the winkling evolution of thin film/substrate system (Xu et al. [149]) and sandwich structures (Choe et al. [146]). Thus, the ANM is used to improve the controllability of the nonlinear path.

1.3 Multiscale homogenization methods

As mentioned before, multiscale homogenization methods are the best solutions for the modeling of SMA heterogeneous materials. For a comprehensive understanding, a brief introduction for these methods is given in this section.

1.3.1 Sequential multiscale homogenization methods

To study heterogeneous materials, appropriate multiscale methods have been proposed (see Kanouté et al. [93], Geers et al. [94] for a review) in order to deduce the effective behavior based on the local behavior of each phase and the morphology of the RVE. These models, based on homogenization theory, can be separated into two main categories according to the information transfer order between two scales : sequential multiscale procedures and hierarchical/integrated multiscale procedures. For the sequential multiscale procedures, the problems on different scales are solved sequentially and independently (see Nemat-Nasser and Hori [150] for a review). Specifically, an overall behavior which gives an effective response of the microscopic model during a specific loading history is computed firstly on the microscopic level, and then is used as the constitutive behavior of macroscopic structure. Some mean-field homogenization methods, such as the self-consistent method and Mori-Tanaka method under simple assumptions (Perdahcıoğlu and Geijselaers [151], Wu et al. [152]), have the advantage of very low time cost.

Instead of computing the fields for all the material points in a RVE, mean-field homogenization methods only seek to compute the averaged variables in different phase sub-domains. Assuming that the averaged variables among each phase sub-domain still follows its continuum material behavior, the microscopic problem is described by formulating the averaged stress-strain relation of each phase sub-domain and the interaction effect between different sub-domains :

$$\begin{cases} \langle \boldsymbol{\sigma} \rangle_{\omega_r} = \mathbb{C}_r : \langle \boldsymbol{\varepsilon} \rangle_{\omega_r} \\ \langle \boldsymbol{\sigma} \rangle_{\omega_r} = \mathbb{A}_{rk} : \langle \boldsymbol{\sigma} \rangle_{\omega_k} \\ \langle \boldsymbol{\varepsilon} \rangle_{\omega_r} = \mathbb{B}_{rk} : \langle \boldsymbol{\varepsilon} \rangle_{\omega_k} \end{cases} \tag{1.1}$$

where $\langle \cdot \rangle_{\omega_r}$ stands for the averaged value over sub-domain ω_r, $\boldsymbol{\sigma}$ and $\boldsymbol{\varepsilon}$ the stress and strain, $\mathbb{A}_{rk}$ and $\mathbb{B}_{rk}$ the fourth-order stress and the strain interaction tensors between sub-domain ω_r and ω_k, respectively. Once the interaction tensors are known, the microscopic problem can be solved analytically. The averaged response of the RVE can be further computed to represent the macroscopic behavior of composites. Mean-field homogenization methods, such as the previously

mentioned self-consistent method and Mori-Tanaka method, differ from each other by the definition of these interaction tensors. Perdahcıoğlu and Geijselaers [151] proposed mean-field homogenization framework for two phase materials considering distinct elastoplastic properties. Among classical mean-field homogenization schemes, the proposed new methods were both computationally efficiency and presented good accuracy compared with experimental results. However, these analytical methods are unable to give microscopic fields precisely and present difficulties to take into account complex geometrical characteristics, such as shape, spatial orientation, size, volume fraction, and phase distribution. Sequential model using numerical homogenization method was also developed to induce the overall behavior of microscopic model, such as the class of so-called unit cell methods (Li et al. [153], Green et al. [154]). However, for non-linear cases, the sequential methods neglect the influence of the macroscopic factors, such as boundary conditions and loading cases, to the microscopic level.

1.3.2 Integrated multiscale homogenization methods

The integrated multiscale procedures, which are also referred as multiscale computational procedures, realize the information transaction between macroscopic and microscopic levels by numerical methods to solve problems in the two levels simultaneously. Although their computational cost is very high compared to the sequential methods, it is practicable enough for simulating realistic composite materials (Feyel and Chaboche [155]). During the past twenty years, multiscale computational techniques, such as the FE^2 method (Feyel [97], Kouznetsova et al. [117], Feyel and Chaboche [155], Miehe et al. [156], Feyel [157]), asymptotic methods (Boso et al. [158], Fish et al. [159]), have been widely used in various mechanical problems, for instance fiber buckling (Nezamabadi et al. [98]), damping (Attipou et al. [160]), heterogeneous shells (Cong et al. [99]) and SMA superelastic fiber/epoxy matrix composites (Kohlhaas and Klinkel [59]).

Feyel and Chaboche [155] proposed the first-order FE^2 method to study the multiscale behavior of long fiber reinforced composite. The results showed that this method can simulate the realistic composite structures with detailed microscopic information. Fig. 1.7 showed the schematic diagram of the FE^2 method. The information between the macroscopic and microscopic finite element models is correlated based on the homogenization theory, where the macroscopic deformation gradient $\bar{\boldsymbol{F}}$ is transferred to the microscopic level and macroscopic tangent and stress $\bar{\boldsymbol{P}}$ averaged over the RVE are transferred to macroscopic level. Kouznetsova et al. [117] proposed second-order computational homogenization procedure for multiscale modeling regarding macroscopic localization and size effects. This scheme is extended based on the first-order FE^2 framework by deriving the higher-order macroscopic constitutive tangents through static perturbations among microscopic overall response. Fig. 1.8 shows the schematic diagram of the second-order FE^2 approach. Both the macroscopic deformation gradient $\bar{\boldsymbol{F}}$ and its gradient $\nabla_0\bar{\boldsymbol{F}}$ are transferred to the microscopic scale, while the tangents, averaged stress $\bar{\boldsymbol{P}}$ and the higher-order stress tensor $\bar{\boldsymbol{Q}}$ conjuncted to $\nabla_0\bar{\boldsymbol{F}}$ are transferred to macroscopic scale. Nezamabadi et al. [98] proposed an efficient nonlinear multiscale scheme based on the FE^2 method to study the instability phenomenon of fiber reinforced composites. Cong et al. [99] proposed the multiscale approach for shell structures based on computational homogenization framework. This approach can simulate the large displacements and large rotations of a heterogeneous shell structure. In order to make multiscale procedures more generic and easy to use for industries, works to extend them on commercial computing platform, such as finite element software ABAQUS, have been proposed (see Yuan and Fish [101] and Tchalla et al. [102]). Tchalla et al. [102] presented a two-scale homogenization approach implemented on ABAQUS using UMAT subroutines. This model is completely compatible with finite element framework and benefits from the generic com-

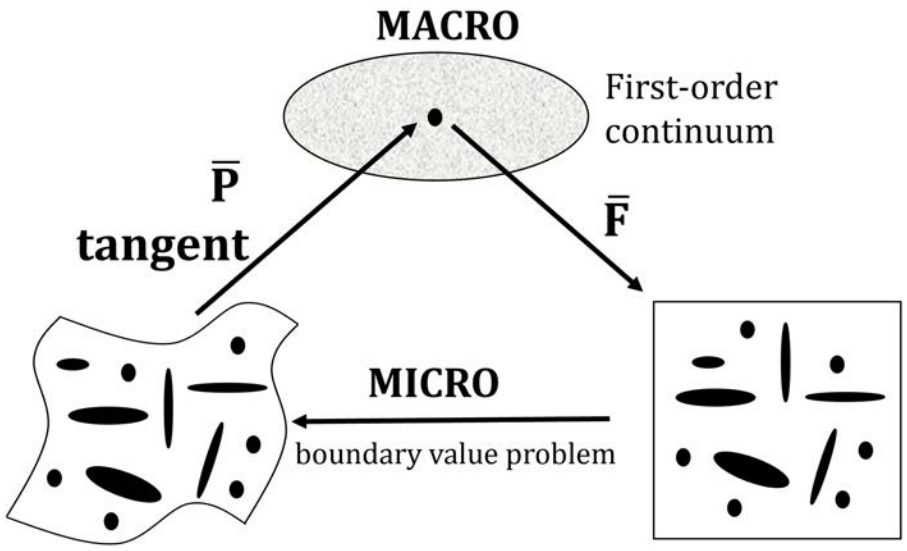

FIGURE 1.7 – Schematic diagram of the first-order FE^2 model.

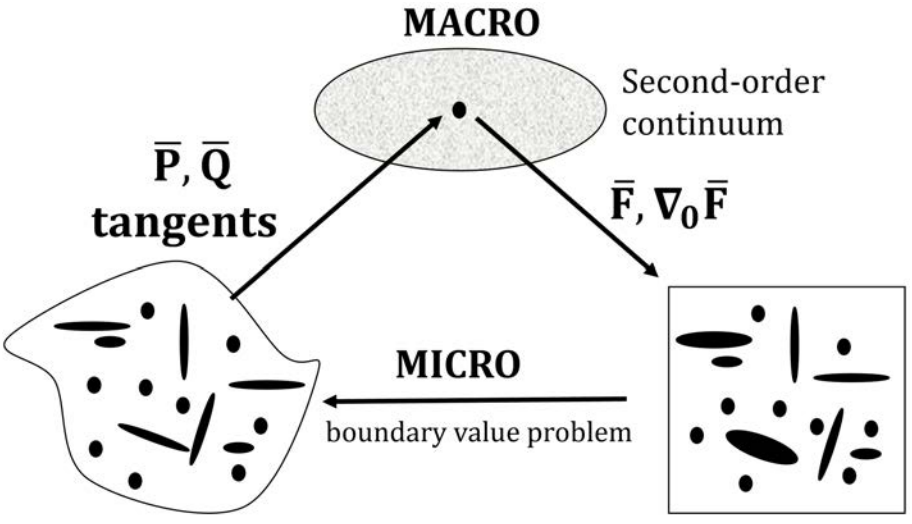

FIGURE 1.8 – Schematic diagram of the second-order FE^2 model.

putational platform ABAQUS. Based on the first-order homogenization theory, this multiscale approach can simulate the linear and non-linear response of various composite structures.

1.3.3 Data-driven multiscale homogenization methods

Multiscale simulation methods for heterogeneous materials have been intensively developed during the past decades. Based on homogenization theory, a series of analytical methods, such as the mean-field methods (Perdahcıoğlu and Geijselaers [151], Wu et al. [152]), were proposed to study the effective behavior of microscopic heterogeneities. Later, numerical approaches, such as the FE^2 method (Feyel [97], Kouznetsova et al. [117], Nezamabadi et al. [124], Miehe et al. [156], Hughes et al. [161], Kodjo et al. [162]), asymptotic homogenization method (Dehaghani et al. [58], Boso et al. [158], Fish et al. [159]), mechanics of structure genome (Liu and Yu [163], Liu et al. [164], Rouf et al. [165]), coarse-graining technique (Budarapu et al. [166]) and multiscale modeling softwares (Tchalla et al. [102], Talebi et al. [167]), were developed to conduct structural analyses by the finite element method. During the past years, the accuracy of homogenization methods made great progresses. However, the computation cost still remains one of the main issues. To guarantee high accuracy within an online simulation for complex heterogeneous material, the pieces of information from different scales needs to be all correlated together. For example, in the framework of the classical FE^2 method, the information over each macroscopic integration point is supposed to be updated at each iteration, which requires tremendous repetitive computations over associated RVE (van Tuijl et al. [126]).

Many works were devoted to address this issue by improving the computation efficiency. The empirical interpolation method (van Tuijl et al. [126], Hernández et al. [127]), the empirical cubature method (Hernandez et al. [168]), POD (Yvonnet et al. [125], Yvonnet and He [169]), Fourier's series method (Huang et al. [130], Attipou et al. [136], Huang et al. [137], Moulinec and Suquet [170], Göküzüm et al. [171], Rambausek et al. [172]), structural elements (Klarmann et al. [173], Hui et al. [174]), specific FE^2 computing strategy (Praster et al. [175]) and high performance nonlinear solver (Nezamabadi et al. [98]) contributed to solve this issue during the past 10 years. However, these methods are usually used in the classical multiscale computing framework, in which the problems at different scales have to be solved concurrently. The correlation of scales benefits multiscale computation with high accuracy, but yields a complex multiscale nonlinear system in comparison with single scale problems. On the one hand, the accuracy in different scales will affect each other directly in an online computing process (see chapter 2). On the other hand, convergence issues in a scale will retard and even compromise the solution of the whole problem. Some examples with strong microscopic nonlinear problem, such as fiber buckling (see chapter 3), require very small incremental steps and fine meshes. Thus, structural analysis has to withstand the burden of high computational costs or sacrifice accuracy eventually. To overcome this issue, one of the most promising spirits is the decoupling of the macroscopic and microscopic problems, which can be recalled in most recent works (Le et al. [176], Lu et al. [177], Nguyen-Thanh et al. [178], Yang et al. [179]).

Le et al. [176], Lu et al. [177], Yvonnet et al. [180], Clément et al. [181] first proposed the use of constitutive data to fit the explicit equivalent strain energy density function of heterogeneous materials, and then obtained the offline equivalent constitutive relationship. Compared with the concurrent computing homogenization method, this method does not require real-time exchange of information between macro and micro scales. Once the explicit equivalent strain energy density function $\bar{w}(\bar{\boldsymbol{\varepsilon}})$ is constructed in the offline phase, the equivalent stress $\bar{\boldsymbol{\sigma}}$ and the equivalent elastic constitutive $\bar{\mathbb{L}}$ can be derived without any new meso-scale finite element calculations. It greatly improves the online calculation efficiency of heterogeneous materials. It is worth pointing out

that the above method is limited to non-dissipative materials, while the classical method of concurrent computational homogenization is not limited by this. In addition, the key of this calculation framework is how to approximate the equivalent strain energy density function $\bar{w}(\bar{\boldsymbol{\varepsilon}})$ efficiently and accurately. The equivalent strain energy density function $\bar{w}(\bar{\boldsymbol{\varepsilon}})$ constructed by the above approximate method is highly dependent on the density of the data and the selection of the interpolation function. The number of sample points increases exponentially with the increase of the problem dimension, and the computational efficiency in high-dimensional problems is not high. Based on the previous work, Le et al. [176] used a neural network algorithm to obtain the equivalent strain energy density function $\bar{w}(\bar{\boldsymbol{\varepsilon}})$, and then derived the explicit stress $\bar{\boldsymbol{\sigma}}$ and equivalent constitutive expression $\bar{\mathbb{L}}$. Compared with the regular grid-based interpolation technique (Yvonnet et al. [180]), this method has the following two advantages : (1) the amount of sample data required is small and can be random in the interpolation space ; (2) on the premise of ensuring a certain accuracy, the required samplle data does not increase exponentially with the increase of the variable dimension, which greatly reduces the offline calculation cost required for high-dimensional problems.

Also based on the idea of scale separation, Yang et al. [179] trained the implicit equivalent constitutive relationship of heterogeneous materials through neural network algorithms, greatly reducing the training cost required to construct the constitutive model of the material. Firstly, the displacement in the RVE is decomposed into a set of principle elongations $(\lambda_1, \lambda_2, \lambda_3)$:

$$\boldsymbol{u} = (\lambda_1 - 1)X\boldsymbol{e}_1 + (\lambda_2 - 1)Y\boldsymbol{e}_2 + (\lambda_3 - 1)Z\boldsymbol{e}_3. \tag{1.2}$$

where $\boldsymbol{e}_1, \boldsymbol{e}_2, \boldsymbol{e}_3$ stand for a set of orthonormal basis, and X, Y, Z the lengths of a cubic RVE. Secondly, perform loading experiments under different paths on the RVE, and construct a database consisting of the square of the principle elongations $a_i = \lambda_i^2$ and the second Piola-Kirchhoff principle stress components S_i, where $i = 1, 2, 3$. Subsequently, a neural network algorithm is used to establish the implicit relationship between equivalent stress and equivalent strain. This method greatly reduces the training cost required to construct a material constitutive model, and can be used in a multi-scale homogenization framework.

In order to improve the efficiency of multi-scale simulation of heterogeneous materials, Liu et al. [182, 183], Tang et al. [184], Kafka et al. [185], Shakoor et al. [186], Han et al. [187] proposed a data-driven clustering analysis method. This method significantly reduces the number of degrees of freedom on the mesoscale by performing dimensionality reduction clustering analysis on complex RVE, thereby significantly improving its solution efficiency. It first performs a linear elastic loading test on the high-fidelity RVE, calculates the strain concentration tensor $\mathbb{G}(x)$ of each material point, and then divide each material point into several low-resolution material clustering according to the similarity of $\mathbb{G}(x)$. Among them, the strain concentration tensor $\mathbb{G}(x)$ reflects the relationship between the macroscopic strain and the microscopic strain field :

$$\boldsymbol{\varepsilon}^{micro} = \mathbb{G}(x) : \boldsymbol{\varepsilon}^{macro}, \tag{1.3}$$

In this way, the high-density mesh model can be reduced to a RVE composed of several clusters. As shown in Fig. 1.9, a 100×100 mesh high-fidelity RVE is converted into a reduced RVE composed of only 8 material clusters.

Based on the work of Le et al. [176], Liu et al. [182], Bessa et al. [188] constructed a data-driven computing framework for heterogeneous materials and structures to assist in the design and development of new materials. As shown in Fig. 1.10, this framework integrates three parts of content : (1) design experiments to collect independent variable data describing the micro-morphology of materials, the properties of each phase, and external input parameters ; (2) efficiently perform analysis for each designed sample to collect targeted response data of materials

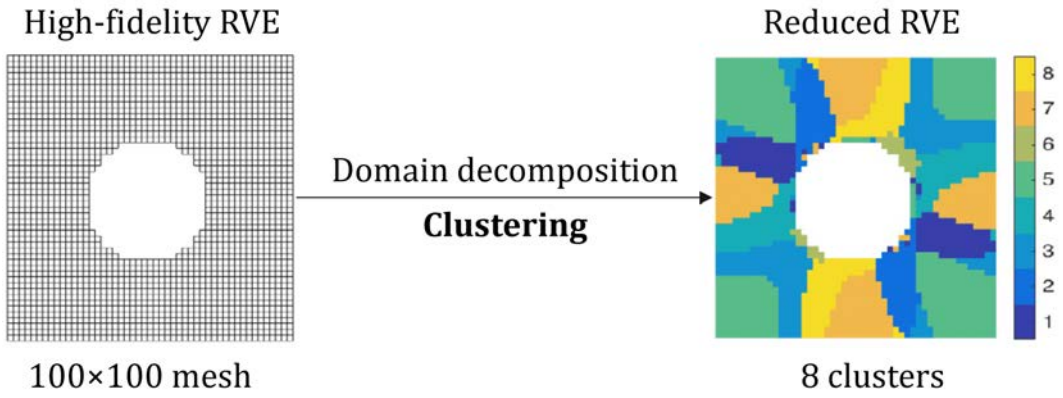

FIGURE 1.9 – The clustering analysis for model reduction in the RVE level (Liu et al. [182]).

and structures ; (3) mining independent variable data and targeted response data to guide new experimental design and modeling. In addition, self-consistent cluster analysis can be used to improve the computational efficiency of designed samples to meet this framework's demand for high-throughput databases.

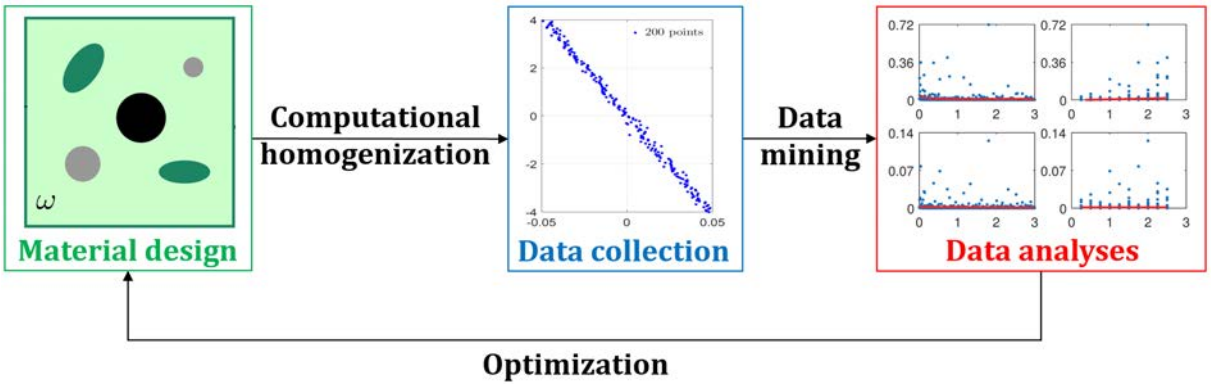

FIGURE 1.10 – Schematic of global framework for data-driven material design/modeling (Bessa et al. [188]).

1.3.4 Material-genome-driven multiscale homogenization method

Standard simulations in the fields of material science and computational mechanics involve two types of equations. The first one is the conservation laws, an axiomatic character in physics relating to the balance of energy, momentum, mass, etc., whereas the second one is the constitutive laws of material extracted from experimental or numerical data. The latter one defines a continuous functional relationship between general stress and strain, which makes it possible to conduct the mechanical computing by numerical methods, for instance the finite element method. However there exist two main obstacles in the process of calibrating the material constitutive equations. On the one hand, it is difficult to characterize materials within high-dimensional phase spaces and with complex behavior. On the other hand, fitting the constitutive model from experimental data generally introduces priori error and uncertainty to the simulations.

To circumvent the difficulties in the conventional approaches, an effective MGD scheme is proposed by Kirchdoerfer and Ortiz [189], in which the experimental data is incorporated di-

rectly for computing the boundary-value problems, whereas the constitutive model is completely abandoned. As depicted in Fig. 1.11, the material data point closest to the conservation laws is searched as the final solution, which will be introduced more detailedly in Section 4.1. At this point, data-driven computing opens up a new route for simulations of mechanical engineering in the brand-new era of data, see Fig. 1.12. Up till now, the data-driven computing has been rapidly extended to solve elasticity with noisy material data sets (Kirchdoerfer and Ortiz [190]), geometrical nonlinearity (Nguyen and Keip [191]), computational plasticity (Chinesta et al. [192]) and dynamics (Kirchdoerfer and Ortiz [193]). It is worth noting that many efforts have been devoted to calibrating constitutive modeling or corrections of existing models by using new material data (Oishi and Yagawa [194], Ibáñez et al. [195, 196], Latorre and Montáns [197]). It would be too lengthy to elaborate all these works here that is beyond the interest of the present thesis. The key point that differs the MDG computing in Kirchdoerfer and Ortiz [189] from these works associated with information science lies in the directly embedding the material data into mechanical simulations. Besides, breaking the chain of computing real-time effective constitutive law in online structural analysis, data-driven mechanics brings new possibilities for the multiscale simulation of heterogeneous materials.

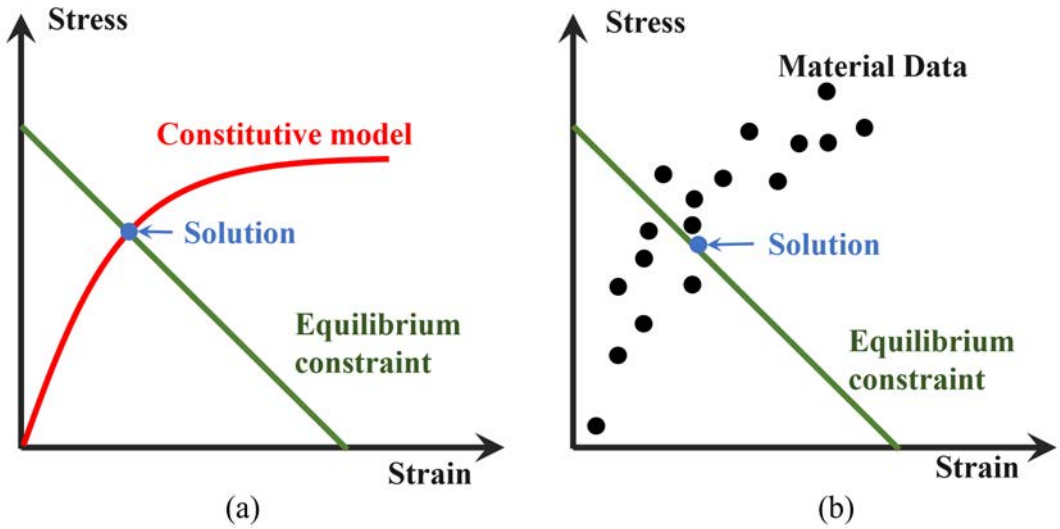

FIGURE 1.11 – (a) classical computational mechanics ; (b) data-driven computational mechanics (Kirchdoerfer and Ortiz [189]).

Inspired by data-driven computing scheme and the spirit of scale decoupling, we aim to propose a novel FE^2 to overcome the difficulties in classical multiscale computation. In the proposed method, the shift from scale concurrency to separation is realized by splitting the multiscale system into several single scale problems. Specifically, numerous offline microscopic calculations are firstly performed within RVEs using computational homogenization. Then, information is collected in a material genome database to feed the online data-driven computation for the macroscopic problem. Since no real-time constitutive law is required any more, the information transfer between macroscopic and microscopic scales is not necessary either. Microscopic information in database can be called at any time and at a minimal cost by the macroscopic analysis. In this manner, the online computing of a multiscale system becomes much easier and faster. To be noticed, the computational cost in offline stage could still be expensive, which remains to be improved in our further work.

The main difference between the above-mentioned works of Le et al. [176], Lu et al. [177],

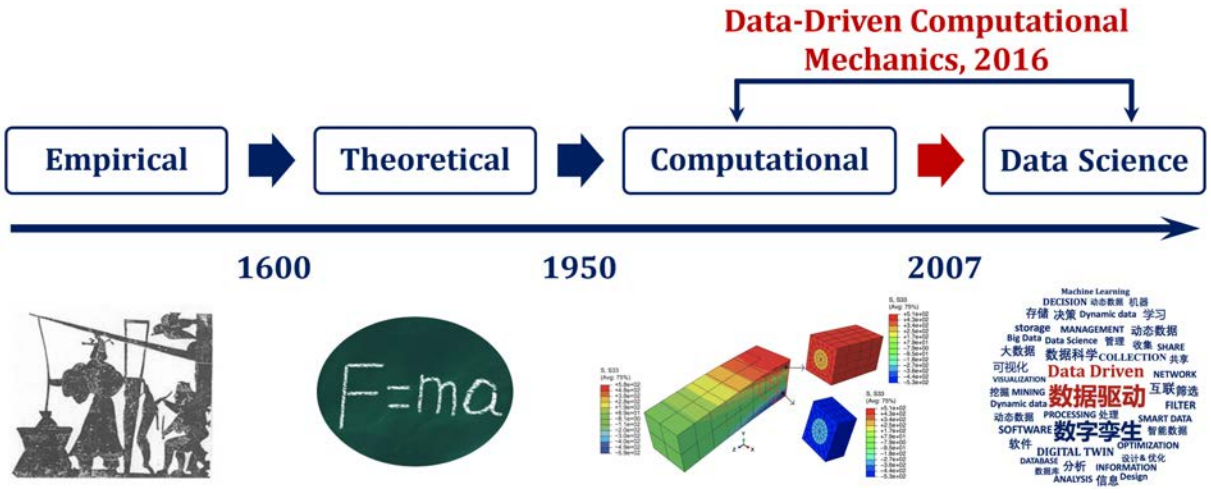

FIGURE 1.12 – Data-driven computational mechanics links the third and the fourth paradigms of science (Kirchdoerfer and Ortiz [189], Hey et al. [198]).

Nguyen-Thanh et al. [178] and the current thesis is the way the macroscopic boundary value problem is solved. These papers use a neural network to construct the strain energy density for the homogenized material, which plays a role of macroscopic constitutive law. Such strain energy density is a good characterization of the heterogeneous materials or composites under consideration. The current thesis employs the distance-minimizing method which uses the material data directly instead of macroscopic constitutive law, and benefits from the advantages of data-driven computing paradigm (Kirchdoerfer and Ortiz [189]). In addition, the proposed data-driven computing scheme is totally compatible with finite element methods, which means that already existing single scale models can contribute to the novel multiscale framework at the concerned scale. Multiscale computing for heterogeneous materials can make a big progress by this new computing scheme.

1.3.5 Structural-genome-driven multiscale homogenization method

Recently, data-driven computing schemes (Kirchdoerfer and Ortiz [189]) opened up a new route for computational mechanics. Up to now, data-driven computing has been rapidly employed to solve elasticity with noisy material data sets (Kirchdoerfer and Ortiz [190]), geometrical nonlinearity (Nguyen and Keip [191]), dynamics (Kirchdoerfer and Ortiz [193]), composite structures (Yang et al. [199]) and inelasticity (Eggersmann et al. [200]). In this computing framework, the constitutive relation is not presented by functions, but saved in so-called material or structural genome databases obtained through by actual or numerical experiments before. Therefore, "material modeling empiricism, error and uncertainty are eliminated entirely and no loss of experimental information is incurred" (Kirchdoerfer and Ortiz [189]).

Along with more and more interests, barriers to the prevailing data-driven framework emerge, such as the curse of dimensionality for both that of macro-structures and material database (Bessa et al. [188], Neggers et al. [201]). For instance, an example of three-dimensional linear elasticity considered in Kirchdoerfer and Ortiz [189] involves 6428 eight-node hexahedral elements and 8 Gauss quadrature points for each element (totally 51424 Gauss points). The sample size of the largest material data set is 192^3 in case with plane-stress assumption, in which the phase space of the material data set is limited in three dimensions. Note that the basic idea of MGD

computing is to find iteratively the best local state that satisfies compatibility constraints and conservation laws from the database for each Gauss point. That means each iteration in the considered case during the process of MGD computing requires about 45 billion basic matching processes. Besides, the computational cost increases exponentially with the increase of phase space of the material data set and the scale of problem in hand.

To alleviate the dimensionality problem arisen in the framework of data-driven computing, the idea of the present work is to associate the data-driven computing with model reduction, which is referred to as SGD computing. In this manner, the mechanical simulation is then driven by generalized stress and strain, referred to as structural-genome here, instead of material-genome. Liu and Yu [163], Liu et al. [164], Rouf et al. [165], Liu and Yu [202] employ structure genome to conduct numerical analysis for composites. The key point that differs the present work from their works lies in the directly embedding structure genome in data-driven computing. Using reduced models and the corresponding structural-genome is willing to decrease not only the number of integration points, but also the dimensions of phase space of required database. During the past decades, model reduction is a constantly immutable topic in the field of computational mechanics. Numerous reduced models can be found in the literature, for instance, the beam (Yang et al. [145], He et al. [203], De Pietro et al. [204], Hui et al. [205]), plate (Huang et al. [131], Reddy [206], Yu et al. [207]) and shell models (Reddy [208]), the Fourier-related reduced models (Huang et al. [130, 132], Liu et al. [134]) and the FE^2 method (Feyel [97]). The use of these existing reduced models in the framework of data-driven computing could significantly release the computational costs.

In order to explain the principle of SGD computing scheme, a 1D Euler-Bernoulli beam model with complex microscopic geometries and variable material properties is taken as an example. It is well known that the internal work of Euler-Bernoulli beam is determined by bending moment and normal force. Thus, the structural-genome consists of two groups of database : the normal force and related normal strain, and the bending moment and related curvature. Both of them can be collected by practical or numerical experiments via tension and bending experiments. In this work, the structural-genome database is constructed by the FE^2 method (Feyel [97], Kouznetsova et al. [117], Nezamabadi et al. [124]). This method can correctly simulate the structural responses of composites whilst consider the irregular microscopic heterogeneities simultaneously. Since the structural genome database is constructed before online structural computations, SGD computing will significantly save the computational cost in comparison with direct multi-scale simulation via the FE^2 method. In summary, the proposed SGD scheme permits to efficiently conduct the numerical analysis of thin-walled composite structures especially with complex microscopic geometry and material properties, which is quite difficult to explicitly obtain the constitutive equations. It is worth noting that SGD computing scheme could be further extended to structural analysis of thin-walled composites by employing the existing plate and shell models. In authors' opinion, this new method may open a door for the structural analysis of thin-walled composites during the current data age.

1.4 Conclusion

This chapter reviews the multiscale modeling for SMA heterogeneous materials involving SMA composites and architected materials and buckling phenomenon which is common in above materials. Then, multiscale homogenization methods are introduced in order to find efficient solutions for the modeling of SMA heterogeneous materials.

In summary, the modeling for SMA heterogeneous materials presents three difficulties : (1) the

macroscopic response interacts with its microscopic material properties and behaviors (such as instability) in real time. Coupling between the macroscopic and microscopic scales is required to ensure accurate solutions ; (2) The thermodynamic mechanisms of SMA are particularly complex and strongly non-linear. An appropriate SMA constitutive model must be adopted to accurately simulate its complex thermodynamic behavior ; (3) In the case of diverse microscopic material properties and complex geometrical shapes, an efficient and stable modeling and solving system must be developed to meet the needs of different designs. To solve these problems, this thesis adopts the FE^2 method to realize the coupling between macroscopic and microscopic scales, then introduces a SMA constitutive model which is compatible with finite element method. By implementing the FE^2 framework and SMA model in commercial finite element software ABAQUS, a generic numerical tool is constructed for SMA heterogeneous materials. This work will be detailed in chapter 2.

Buckling instability phenomenon is a typical problem when the SMA heterogeneous materials are designed in thin-walled shape. Advanced non-linear solvers must be used to accurately and efficiently simulate such strong geometrical non-linear phenomena. Taking the instability problem of long fiber reinforced composite as an example, this thesis adopts ANM to efficiently follow the nonlinear path. Moreover, Fourier-related envelope model is introduced in the microscopic level to capture the fiber buckling modes and reduce the DOFs of microscopic model. This work will be detailed in chapter 3.

In the concurrent multiscale computing framework established in chapters 2 and 3, tremendous microscopic calculations must be performed in each macroscopic iterative step to update the information on each integration point. The computational cost is expensive especially considering strong nonlinear behaviors, such as shape memory effect and buckling. Inspired by data-driven computing, in chapter 4 novel approaches which decouple scales are proposed to reduce the online computational cost for composite structures, namely data-driven multiscale finite element method (data-driven FE^2) and Structural-Genome-Driven (SGD) computing.

2

Formulations and applications of multiscale modeling for SMA heterogeneous materials

Contents

In this chapter, a 3D generic FE^2 procedure is proposed for modeling the pseudo-elasticity and the shape memory effects of SMA based composites. In this method, composites are separated into a macroscopic and a microscopic level, where the constitutive behavior of each integration point on macroscopic level is represented by the effective behavior of a corresponding RVE. This effective behavior is computed by finite element method under the RVE meshed by volume element. The real-time information transition between the two levels is realized on a commercial platform ABAQUS via UMAT. A thermodynamic model, proposed by Chemisky et al. [1], is adopted to describe the total constitutive behavior of the SMA. This model considers three path-dependent strain mechanisms related to phase transformation, martensite reorientation and twin accommodation by the derivation of Gibbs free energy. Considering an SMA fiber reinforced composite, several thermodynamic tests from the literature subjected to tension-compression and bending loads are studied to validate our multiscale model, which shows good accuracy and reliability.

Further, this model is used for design and simulation of architected SMAs thanks to its generic computing platform ABAQUS. Firstly, a parametric analysis at the cellular level with a series of RVEs is carried out to predict the relations between the void fraction, the total stiffness, the hysteresis effect and the mass of the SMAs. Secondly, the structural responses of the architected

SMAs are studied by the FE^2, which uses the effective constitutive behavior of the RVE to represent the behavior of the macroscopic structure. Through a three point bending test, it is observed that the structure inherits the strong nonlinear responses—both the hysteresis effect and the PE—of the architected SMAs at the cellular level. Furthermore, the influence of the void fraction at the RVE level to the materials' structural responses can be more specifically and directly described, instead of using an RVE to predict at the microscopic level. Thus, this work could be referred to for optimizing the stiffness, the hysteresis effect and the mass of architected SMA structures and extended for possible advanced applications.

The detailed implementation of the multiscale scheme and the SMA constitutive behavior are illustrated in Section 2.1. In Section 2.2, isothermal loading and unloading cycles for PE and thermomechanical loading cycles for SME are discussed in detail considering an SMA fiber/epoxy matrix composite. Further, the proposed multiscale approach is applied on the multiscale modeling for architected SMA materials in Section 2.3.

2.1 Scale transition technique and local thermomechanical SMA model

2.1.1 FE^2 scale transition technique

The composite material is described by infinite repeating a RVE, which has periodic boundary conditions and multiphase materials. In that case, the heterogeneous composite is divided into a continuous macroscopic scale and a multiphase microscopic scale (Kouznetsova et al. [117], Feyel and Chaboche [155], Miehe et al. [156]). For instance, the scale separation of SMA/epoxy composite is illustrated in Fig. 2.1. Two models are implemented on ABAQUS which represent the macroscopic structure with a domain Ω and the microscopic structure with a domain ω respectively, see Fig. 2.1. Then, the multiscale problem is solved by using the effective behavior of the microscopic structure to represent the behavior of the corresponding continuous point in the macroscopic structure.

Macroscopic scale

Let us consider a domain $\Omega \in R^D$ with an external boundary $\partial\Omega$, describing the macroscopic structure in its current configuration, where R is a vector space and D is the dimension of the space. Large displacements are considered and the so-called update Lagrangian formulation is adopted. Notation $\bar{(\cdot)}$ representing the macroscopic values are introduced in order to distinguish the values of two scales. The equilibrium equation neglecting the body force is formulated as :

$$\boldsymbol{\nabla} \cdot \bar{\boldsymbol{\sigma}}(\bar{\boldsymbol{x}}) = 0 \ in \ \Omega, \tag{2.1}$$

where $\bar{\boldsymbol{\sigma}}(\bar{\boldsymbol{x}})$ stands for the Cauchy stress tensor at the point $\bar{\boldsymbol{x}}$ in the current configuration. Since most of constitutive material models in ABAQUS are path dependent and usually defined in rate form, the strain rate $\bar{\boldsymbol{D}}$ conjugated to Cauchy stress is adopted by given as :

$$\bar{\boldsymbol{D}} = \frac{1}{2}(\boldsymbol{\nabla}\bar{\boldsymbol{v}} + (\boldsymbol{\nabla}\bar{\boldsymbol{v}})^t), \tag{2.2}$$

where $\bar{\boldsymbol{v}}$ is the velocity field.

After taking into account boundary conditions, the virtual work for the macroscopic problem is given by :

$$\int_{\Omega} \bar{\boldsymbol{\sigma}} : \boldsymbol{\delta}\bar{\boldsymbol{D}} d\Omega = \bar{\lambda} \int_{\partial\Omega_\sigma} \bar{\boldsymbol{f}} \cdot \boldsymbol{\delta}\bar{\boldsymbol{v}} d\Gamma, \tag{2.3}$$

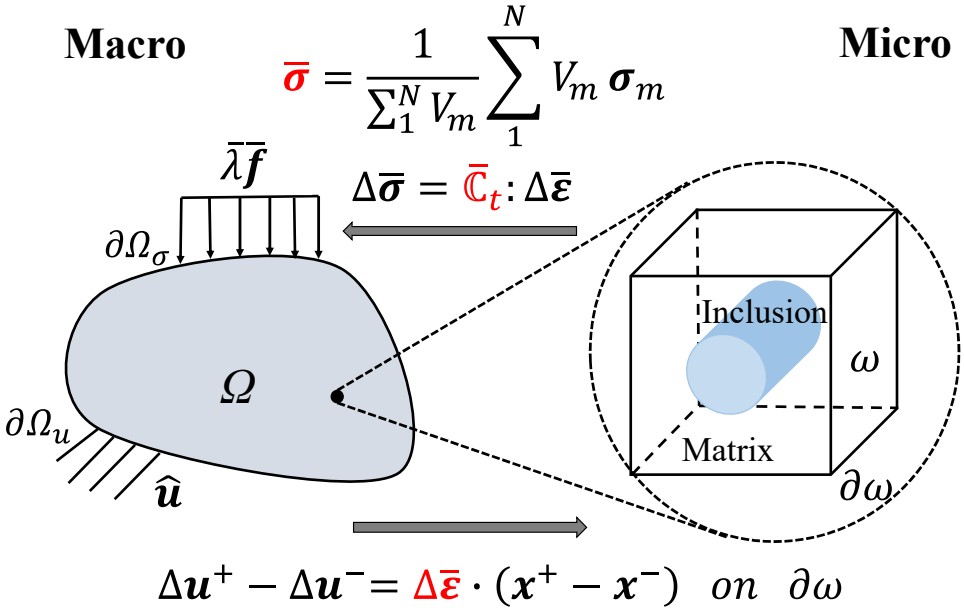

FIGURE 2.1 – Basic concept of finite element square method.

where parameter $\bar{\lambda}$ is the intensity of the prescribed external force $\bar{\boldsymbol{f}}$ applied on boundary $\partial\Omega_\sigma$ (Neumann boundaries), prescribed displacement $\hat{\boldsymbol{u}}$ is given on boundary $\partial\Omega_u$ (Dirichlet boundaries).

As the constitutive relationship between $\bar{\boldsymbol{\sigma}}$ and $\bar{\boldsymbol{D}}$ is unknown, the macroscopic model cannot be solved independently. The macroscopic stress tensor $\bar{\boldsymbol{\sigma}}$ and the tangent constitutive tensor $\bar{\mathbb{C}}_t$ are calculated in microscopic level, as shown in Fig. 2.1, by solving a nonlinear microscopic structure using a numerical homogenization method via UMAT. The formulation of the microscopic problem is developed in the next section.

Microscopic scale

Assuming the boundaries of the repeating microscopic structures can match together perfectly without any overlap, it requires that the RVE must have parallel pair boundaries. As shown in Fig. 2.1, the microscopic structure with given geometry and the mechanical parameters are represented by a periodic RVE with a domain ω and an external boundary $\partial\omega$ in its initial configuration. Based on the principles of separation of scales, the characteristic length of the RVE and that of macroscopic structure should satisfy :

$$||\omega|| \ll ||\Omega|| \tag{2.4}$$

where $||\omega||$ is the characteristic length of the RVE and $||\Omega||$ is the characteristic length of the macroscopic model. The equilibrium equation is given in absence of body forces by :

$$\boldsymbol{\nabla} \cdot \boldsymbol{\sigma}(\boldsymbol{x}) = 0 \ in \ \omega, \tag{2.5}$$

where $\boldsymbol{\sigma}$ stands for the stress tensor at microscopic material point $\boldsymbol{x}$ in the current configuration. As the material parameters are known in the microscopic level, the material behavior, which can be explicitly written, is given as :

$$\Delta\boldsymbol{\sigma} = \mathbb{C}_t^{(r)} : \Delta\boldsymbol{\varepsilon}, \tag{2.6}$$

where $\mathbb{C}_t^{(r)}$ refers to the tangent operator associated with phase $^{(r)}$, Δ is the incremental notation and $\boldsymbol{\varepsilon}$ denotes the strain measure of the microscopic level. As for the SMAs, the implicit constitutive behavior is introduced via a UMAT model which will be discussed in the next section. For the sake of simplicity, the stress-strain relation in SMAs is also expressed as Eq. (2.6) here. It is worth noting that any other constitutive relation can be introduced into the RVE via a UMAT model.

To formulate the virtual work of the microscopic model, appropriate boundary conditions are required to describe the deformation of the microscopic model. In the FE^2 procedure, the macroscopic strain on a macroscopic material point is transferred into the associated RVE as the boundary conditions. In order to keep the RVE repeating periodically during deforming, the periodic boundary conditions are introduced as follows :

$$\Delta \boldsymbol{u}^+ - \Delta \boldsymbol{u}^- = \Delta \bar{\boldsymbol{\varepsilon}} \cdot (\boldsymbol{x}^+ - \boldsymbol{x}^-) \quad on \quad \partial\omega, \tag{2.7}$$

where $\boldsymbol{u}$ is the microscopic displacement vector and $\bar{\boldsymbol{\varepsilon}}$ is the macroscopic strain tensor which is defined as the integral of the strain rate in an increment using a central difference algorithm. The exponents $+$ and $-$ represent the nodes on opposite boundaries of the RVE.

Notice that we do not specify the dimension of RVE, because in the concept of homogenization theory, the dimension of microscopic structure and that of the macroscopic structure have to satisfy the scale separation principle, see Eq. (2.4). Here, the RVE cube is given with an initial size $1 \times 1 \times 1$ in Cartesian coordinate system.

In mechanical meaning, periodic boundary conditions satisfy the so-called *averaging theorem*, which requests that the average of the work decomposes into the product of work-averages (Hill [209]) :

$$\frac{1}{|\omega|}\int_\omega \boldsymbol{\sigma} : \boldsymbol{\varepsilon} d\omega - \frac{1}{|\omega|}\int_\omega \boldsymbol{\sigma} d\omega : \frac{1}{|\omega|}\int_\omega \boldsymbol{\varepsilon} d\omega = 0. \tag{2.8}$$

where $|\omega|$ is the volume of RVE. In that case, the stress and strain between the macroscopic level and microscopic level are related by :

$$\bar{\boldsymbol{\sigma}} = \frac{1}{|\omega|}\int_\omega \boldsymbol{\sigma} d\omega = \frac{1}{\sum_1^N V_m}\sum_1^N V_m \boldsymbol{\sigma}_m \tag{2.9}$$

$$\bar{\boldsymbol{\varepsilon}} = \frac{1}{|\omega|}\int_\omega \boldsymbol{\varepsilon} d\omega = \frac{1}{\sum_1^N V_m}\sum_1^N V_m \boldsymbol{\varepsilon}_m \tag{2.10}$$

where macroscopic strain $\bar{\boldsymbol{\varepsilon}}$ is the applied strain on the boundary of the RVE, $\boldsymbol{\sigma}_m$, $\boldsymbol{\varepsilon}_m$ and V_m are respectively the stress, strain tensors and the volume of m^{th} element in RVE, N is the total element number of RVE. The averaged stress $\bar{\boldsymbol{\sigma}}$ computed via Eq. (2.9) will be transferred to macroscopic model as the macroscopic stress. There are other types of boundary conditions which also satisfy the homogenization theory, such as the linear boundary conditions which requires homogeneous strains on the boundary of the microscopic structure, as follows :

$$\Delta \boldsymbol{u} = \Delta \bar{\boldsymbol{\varepsilon}} \cdot \boldsymbol{x} \quad on \quad \partial\omega. \tag{2.11}$$

Comparing with the linear boundary conditions, the periodic boundary condition produces more compliant (less kinematically constrained) solution. As our work is based on ABAQUS, a generic computing platform, periodic boundary conditions are introduced automatically by using a homemade python script with the function of Multi-point constraints (MPCs). Specifically,

it is just needed to first specify the opposite nodes on boundaries and save them as sets, then create corresponding Equation constraints for the sets. Considering the multilevel procedure in a general nonlinear case with boundary condition Eq. (2.7), the microscopic problem is defined as the following incremental form :

$$\begin{cases} \int_{\omega} \Delta\boldsymbol{\sigma} : \boldsymbol{\delta\varepsilon} d\omega = 0, \\ \Delta\boldsymbol{\sigma} = \mathbb{C}_t^{(r)} : \Delta\boldsymbol{\varepsilon}, \\ \Delta\boldsymbol{u}^+ - \Delta\boldsymbol{u}^- = \Delta\bar{\boldsymbol{\varepsilon}} \cdot (\boldsymbol{x}^+ - \boldsymbol{x}^-) \quad on \quad \partial\omega. \end{cases} \tag{2.12}$$

In the general nonlinear computation framework of ABAQUS, the Newton-Raphson method is adopted in the macroscopic model. Thus, a tangent constitutive tensor $\bar{\mathbb{C}}_t$ at each integration point is required for predicting the initial tangent response of the macroscopic structure at the beginning of current macroscopic increment.

Considering engineering components are used in user subroutine UMAT on ABAQUS, the nonlinear averaged stress-strain relation is of the form :

$$\Delta\bar{\boldsymbol{\sigma}} = \bar{\mathbb{C}}_t : \Delta\bar{\boldsymbol{\varepsilon}}. \tag{2.13}$$

where

$$\Delta\bar{\boldsymbol{\sigma}}^t = [\Delta\bar{\sigma}_{11}, \Delta\bar{\sigma}_{22}, \Delta\bar{\sigma}_{33}, \Delta\bar{\sigma}_{12}, \Delta\bar{\sigma}_{13}, \Delta\bar{\sigma}_{23}],$$
$$\Delta\bar{\boldsymbol{\varepsilon}}^t = [\Delta\bar{\varepsilon}_{11}, \Delta\bar{\varepsilon}_{22}, \Delta\bar{\varepsilon}_{33}, \Delta\bar{\gamma}_{12}, \Delta\bar{\gamma}_{13}, \Delta\bar{\gamma}_{23}].$$

Thus, six independent linear perturbation calculations over each RVE are required (considering the symmetry $\bar{\varepsilon}_{ij} = \bar{\varepsilon}_{ji}$) to compute the components of the tangent constitutive tensor. For the sake of simplicity, a set of independent unit strain $\bar{\boldsymbol{\varepsilon}}_i^{unit}$ (i varies from 1 to 6), in which the i^{th} component is equal to 1 and other components are equal to 0, is adopted in the perturbation calculations.

Once the effective tangent operator $\bar{\mathbb{C}}_t$ is obtained, an iterative process between the microscopic and macroscopic scales is carried out to eliminate the residual of macroscopic model until it converges. The iterative process between the microscopic and macroscopic scales is mainly summarized as two parts, as shown in Fig. 2.2.

Part 1 : Initialization

As the constitutive behavior of the macroscopic model is unknown, it is needed to compute an effective constitutive behavior $\bar{\mathbb{C}}_t$ for each integration points by an initialization procedure. Thus, a computational homogenization procedure is carried out on the microscopic model with a unit strain $\bar{\boldsymbol{\varepsilon}}^{unit}$. Firstly, PBCs are implemented by a Python script. Then, a *Static Linear Perturbation Step* is executed in order to get the tangent response of the microscopic structure. Finally, the effective constitutive behavior $\bar{\mathbb{C}}_t$ can be computed according to Eqs. (2.8) and (2.13).

Part 2 : Analysis and convergence check

With the effective constitutive behavior $\bar{\mathbb{C}}_t$, the macroscopic strain increment $\Delta\bar{\boldsymbol{\varepsilon}}$ at each integration point can be computed. The strain increment $\Delta\bar{\boldsymbol{\varepsilon}}$ should be transfered to the microscopic model to update the macroscopic stress, which will be used for checking the macroscopic convergence. If the macroscopic convergence is not satisfied, a macroscopic strain increment $\Delta\bar{\boldsymbol{\varepsilon}}'$ will be computed and transfered to the microscopic model for updating the macroscopic stress again. This iteration between the two scales ends when the macroscopic convergence is satisfied. Some technical details about the implementation of this multiscale approach on ABAQUS are available in the contribution of Tchalla et al. [102].

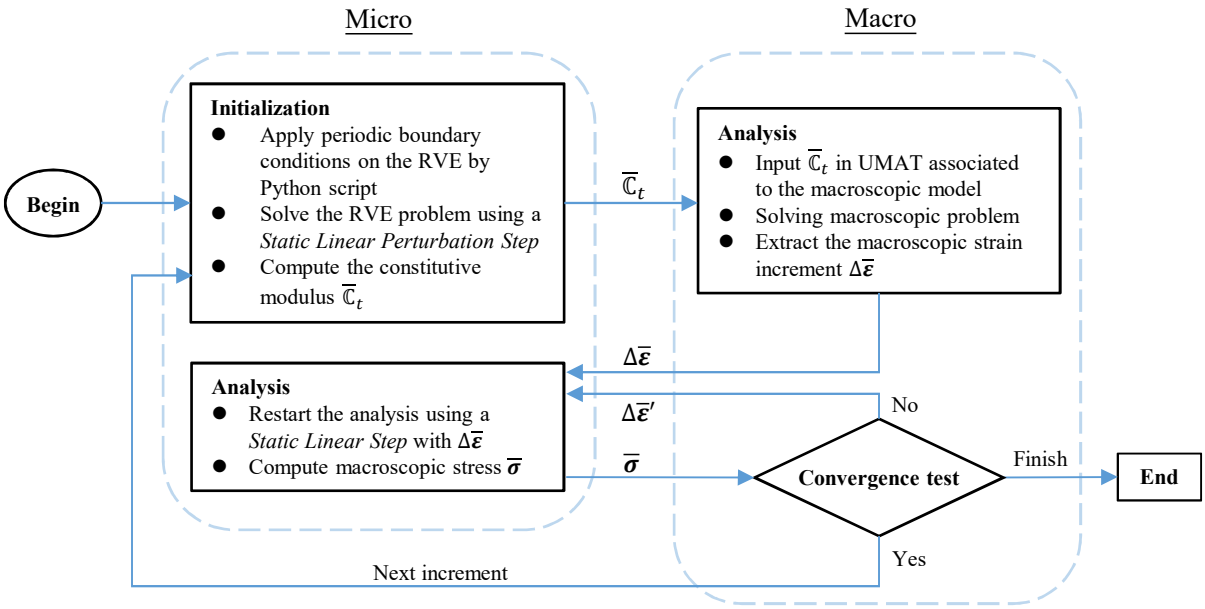

FIGURE 2.2 – The nonlinear interactive procedure between the microscopic and macroscopic models.

This scale transition approach is applied to predict the thermomechanical response of an SMA fiber/epoxy matrix composite. The matrix behavior is assumed elastic, whereas the thermomechanical behavior of the SMA is described by Chemisky et al. [1]. The next section details the foundation of this model.

2.1.2 Thermomechanical formulation of SMA constitutive behavior

The adopted 3D SMA constitutive model, proposed by Chemisky et al. [1], is implemented in ABAQUS via UMAT. This model can describe the mechanisms of the phase transformation, the martensite reorientation and the twin accommodation.

Assuming that the behavior of a microscopic RVE containing martensite and austenite can represent the total thermomechanical behavior of SMAs. The total strain without considering the plastic or viscoplastic strain could be decomposed with the following formulation :

$$\boldsymbol{\varepsilon} = \boldsymbol{\varepsilon}^e + \boldsymbol{\varepsilon}^{th} + \boldsymbol{\varepsilon}^{tr} + \boldsymbol{\varepsilon}^{tw}, \tag{2.14}$$

where $\boldsymbol{\varepsilon}^e$ represents the elastic strain, $\boldsymbol{\varepsilon}^{th}$ stands for the thermal expansion strain, $\boldsymbol{\varepsilon}^{tr}$ denotes the inelastic strain related to martensitic transformation and $\boldsymbol{\varepsilon}^{tw}$ stands for the inelastic strain related to the twin accommodation mechanism between martensite variants.

Both the martensite and austenite are assumed to be isotropic with the same thermo-elastic constants. Thus, the elastic strain $\boldsymbol{\varepsilon}^e$ and the thermal expansion strain $\boldsymbol{\varepsilon}^{th}$ can be formulated as :

$$\boldsymbol{\varepsilon}^e = \mathbb{S} : \boldsymbol{\sigma}, \tag{2.15}$$

$$\boldsymbol{\varepsilon}^{th} = \boldsymbol{\alpha}(T - T_{ref}), \tag{2.16}$$

where the isotropic fourth order tensor $\mathbb{S}$, called the compliance tensor, and the isotropic tensor $\boldsymbol{\alpha}$ describing the thermal expansion are introduced. The reference temperature T_{ref} is the temperature with zero thermal expansion strain.

The total transformation strain $\boldsymbol{\varepsilon}^{tr}$ is defined as the average of the local transformation strain field over the microscopic RVE :

$$\boldsymbol{\varepsilon}^{tr} = f_{ma}\tilde{\boldsymbol{\varepsilon}}^{tr}, \tag{2.17}$$

where the martensitic volume fraction f_{ma} describes the strain mechanism of the martensitic transformation, the mean transformation strain $\tilde{\boldsymbol{\varepsilon}}^{tr}$ over the martensite volume describes the strain mechanism related to the martensite reorientation.

The inelastic strain $\boldsymbol{\varepsilon}^{tw}$ related to the twin accommodation is written :

$$\boldsymbol{\varepsilon}^{tw} = f^{FA}\tilde{\boldsymbol{\varepsilon}}^{tw}, \tag{2.18}$$

where f^{FA} represents the volume fraction associated with self-accommodated martensite. The mean twin accommodation strain $\tilde{\boldsymbol{\varepsilon}}^{tw}$ over the martensitic volume describes the strain mechanism related to the inelastic twin accommodation. It is worth noting that the self-accommodated martensitic behavior in this model is considered dependent on the activated martensite variants, thus f^{FA} is defined as a function of f_{ma}. With the three presented internal variables f_{ma}, $\tilde{\boldsymbol{\varepsilon}}^{tr}$, $\tilde{\boldsymbol{\varepsilon}}^{tw}$, Gibbs free energy potential is defined :

$$\begin{aligned} G =& U^A - TS^A + B_{en}(T-T_0)f_{ma} - \frac{1}{2}\boldsymbol{\sigma} : \mathbb{S} : \boldsymbol{\sigma} - \boldsymbol{\sigma} : \boldsymbol{\alpha}\Delta T \\ & - \boldsymbol{\sigma} : \tilde{\boldsymbol{\varepsilon}}^{tr} f_{ma} - \boldsymbol{\sigma} : \tilde{\boldsymbol{\varepsilon}}^{tw} f^{FA} + \frac{1}{2} f_{ma} H_{tr} \tilde{\boldsymbol{\varepsilon}}^{tr} : \tilde{\boldsymbol{\varepsilon}}^{tr} + \frac{1}{2} H_f f_{ma}^2 \\ & + \frac{1}{2} f^{FA} H_{tw} \tilde{\boldsymbol{\varepsilon}}^{tw} : \tilde{\boldsymbol{\varepsilon}}^{tw} + C_v \left[(T-T_0) - T \log \frac{T}{T_0} \right]. \end{aligned} \tag{2.19}$$

Considering $T_0 = \frac{\Delta U}{\Delta S_{en}}$ the equilibrium temperature of transformation, a linear variation of entropy around T_0 is defined as $B_{en} = -\Delta S_{en}$. U^A and U^M are the austenitic and the martensitic internal energy, S^A_{en} and S^M_{en} are the austenitic and the martensitic entropy. Several symbols, such as $\Delta U = U^M - U^A$, $\Delta S_{en} = S^M_{en} - S^A_{en}$ and $\Delta T = T - T_{ref}$, are also introduced. The terms H_{tr}, H_f and H_{tw} are, respectively, a set of material parameters characterizing interactions between grains of the microscopic RVE, between variants inside grains and between twins and C_v is the transformation latent heat coefficient.

The Clausius-Duhem inequality written in terms of the Gibbs free energy G is introduced to establish the state equations of the thermodynamic system :

$$-\dot{G} - \boldsymbol{\varepsilon} : \dot{\boldsymbol{\sigma}} - S_{en}\dot{T} - \overrightarrow{q} \cdot \frac{\overrightarrow{grad}\, T}{T} \geq 0. \tag{2.20}$$

Substituting of Eq. (2.19) into Eq. (2.20) leads to the following explicit expression of the Clausius-Duhem inequality :

$$-\left(\frac{\partial G}{\partial \boldsymbol{\sigma}} + \boldsymbol{\varepsilon}\right) : \dot{\boldsymbol{\sigma}} - \left(\frac{\partial G}{\partial T} + S_{en}\right)\dot{T} - \frac{\partial G}{\partial f_{ma}}\dot{f}_{ma} - \frac{\partial G}{\partial \tilde{\boldsymbol{\varepsilon}}^{tr}} : \dot{\tilde{\boldsymbol{\varepsilon}}}^{tr} - \frac{\partial G}{\partial \tilde{\boldsymbol{\varepsilon}}^{tw}} : \dot{\tilde{\boldsymbol{\varepsilon}}}^{tw} - \overrightarrow{q} \cdot \frac{\overrightarrow{grad}\, T}{T} \geq 0. \tag{2.21}$$

where the terms related to $\dot{f}^{FA}_{ma}$ in Gibbs free energy are replaced by their expression as a function of $\dot{f}_{ma}$. The thermo-elastic balance is assumed to be instantaneously satisfied, which results the following equations :

$$\begin{cases} -\left(\dfrac{\partial G}{\partial \boldsymbol{\sigma}} + \boldsymbol{\varepsilon}\right) = 0, \\ -\left(\dfrac{\partial G}{\partial T} + S_{en}\right) = 0. \end{cases} \tag{2.22}$$

Substituting of Eq. (2.19) into Eq. (2.22) leads to the following explicit expression of the thermo-elastic balance conditions :

$$\begin{cases} \mathbb{S} : \boldsymbol{\sigma} + \boldsymbol{\alpha}\Delta T + f_{ma}\tilde{\boldsymbol{\varepsilon}}^{tr} + f^{FA}\tilde{\boldsymbol{\varepsilon}}^{tw} - \boldsymbol{\varepsilon} = 0, \\ S_{en}^{A} - B_{en}f_{ma} + \boldsymbol{\sigma} : \boldsymbol{\alpha} - C_v\left(\log\dfrac{T}{T_0}\right) - S_{en} = 0. \end{cases} \tag{2.23}$$

The Clausius-Duhem inequality is then reduced to the dissipation expression :

$$\phi = -\frac{\partial G}{\partial f_{ma}}\dot{f}_{ma} - \frac{\partial G}{\partial \tilde{\boldsymbol{\varepsilon}}^{tr}} : \dot{\tilde{\boldsymbol{\varepsilon}}}^{tr} - \frac{\partial G}{\partial \tilde{\boldsymbol{\varepsilon}}^{tw}} : \dot{\tilde{\boldsymbol{\varepsilon}}}^{tw} - \overrightarrow{q} \cdot \frac{\overrightarrow{grad}\, T}{T} \geq 0. \tag{2.24}$$

The dissipation ϕ can be divided into two contributions :

1. An intrinsic dissipation linked to the evolution of internal variables :

$$\phi_1 = -\frac{\partial G}{\partial f_{ma}}\dot{f}_{ma} - \frac{\partial G}{\partial \tilde{\boldsymbol{\varepsilon}}^{tr}} : \dot{\tilde{\boldsymbol{\varepsilon}}}^{tr} - \frac{\partial G}{\partial \tilde{\boldsymbol{\varepsilon}}^{tw}} : \dot{\tilde{\boldsymbol{\varepsilon}}}^{tw}. \tag{2.25}$$

2. A thermal dissipation :

$$\phi_2 = -\overrightarrow{q} \cdot \frac{\overrightarrow{grad}\, T}{T}. \tag{2.26}$$

The intrinsic dissipation can be divided into a transformation, an orientation and a twin accommodation dissipation, assuming these dissipation mechanisms can be described as, see Chemisky et al. [1], Peultier et al. [23], for a detailed presentation :

$$\begin{cases} \phi_{1f_{ma}} = -\dfrac{\partial G}{\partial f}\dot{f}_{ma} = F_{f_{ma}}^{crit}\dot{f}_{ma}, \\ \phi_{1\tilde{\varepsilon}^{tr}} = \left|-\dfrac{\partial G}{\partial \tilde{\boldsymbol{\varepsilon}}^{tr}}\right|_{\sigma} \dot{\tilde{\boldsymbol{\varepsilon}}}^{tr} = f_{ma}F_{\tilde{\varepsilon}^{tr}}^{crit}\dot{\tilde{\boldsymbol{\varepsilon}}}^{tr}, \\ \phi_{1\tilde{\varepsilon}^{tw}} = -\dfrac{\partial G}{\partial \tilde{\boldsymbol{\varepsilon}}^{tw}} : \dot{\tilde{\boldsymbol{\varepsilon}}}^{tw} = 0. \end{cases} \tag{2.27}$$

where $F_{f_{ma}}^{crit}$ is a predefined critical transformation threshold, which is dependent on the thermo-mechanical conditions :

$$\begin{cases} F_{f_{ma}}^{crit} = F_{f_{ma}}^{max} + (B_f - B_{en})(T - T_0) \quad if \ \dot{f}_{ma} > 0, \\ F_{f_{ma}}^{crit} = -F_{f_{ma}}^{max} + (B_r - B_{en})(T - T_0) \quad if \ \dot{f}_{ma} < 0, \end{cases} \tag{2.28}$$

where $F_{f_{ma}}^{max}$, B_f, B_r are material parameters. Operator $|\cdot|_{\sigma}$ corresponds to Mises equivalent stress as $|\boldsymbol{\varsigma}|_{\sigma} = \sqrt{\frac{3}{2}\boldsymbol{\varsigma} : \boldsymbol{\varsigma}}$, $F_{\tilde{\varepsilon}^{tr}}^{crit}$ is the critical orientation threshold as a given constant value, assuming an isotropic criterion for the orientation surface. The dissipation coming from the twin accommodation is neglected as it is very low compared to the ones associated to transformation and reorientation.

It is also needed to take into account the physical limitation of the internal variables in the model :

$$\begin{cases} 0 \leqslant f_{ma} \leqslant 1, \\ \tilde{\varepsilon}_{eq}^{tr} \leqslant \varepsilon_{max}^{tr}, \end{cases} \tag{2.29}$$

where $\tilde{\varepsilon}^{tr}_{eq} = \sqrt{\frac{2}{3}\tilde{\boldsymbol{\varepsilon}}^{tr} : \tilde{\boldsymbol{\varepsilon}}^{tr}}$ and ε^{tr}_{max} is the maximum value of the transformation strain magnitude which is considered history dependent. Lagrange multipliers λ_a, λ_b and λ_c based on the Karush-Kuhn-Tuker conditions are introduced into Eq. (2.19) : $\lambda_a = 0$ if $f_{ma} \geqslant 0$, $\lambda_a > 0$ otherwise ; $\lambda_b = 0$ if $f_{ma} \leqslant 1$, $\lambda_b > 0$ otherwise ; $\lambda_c = 0$ if $\tilde{\varepsilon}^{tr}_{eq} \leqslant \varepsilon^{tr}_{max}$, $\lambda_c > 0$ otherwise. The driving forces expressed with the Lagrangian form of Gibbs free energy are defined :

1. *Transformation driving force related to f_{ma} :*

$$F_{f_{ma}} = -\frac{\partial G}{\partial f_{ma}} - \lambda_a - \lambda_b = \boldsymbol{\sigma} : \tilde{\boldsymbol{\varepsilon}}^{tr} + \zeta^{FA}\boldsymbol{\sigma} : \tilde{\boldsymbol{\varepsilon}}^{tw} - B_{en}(T - T_0) - \frac{1}{2} f_{ma} H_{tr} \tilde{\boldsymbol{\varepsilon}}^{tr} : \tilde{\boldsymbol{\varepsilon}}^{tr} - H_f f_{ma} - \frac{1}{2}\zeta^{FA} H_{tw} \tilde{\boldsymbol{\varepsilon}}^{tw} : \tilde{\boldsymbol{\varepsilon}}^{tw} - \lambda_a - \lambda_b. \tag{2.30}$$

   where the definition of $\dot{f}^{FA} = \zeta^{FA}\dot{f}_{ma}$ is introduced here.

2. *Orientation force related to $\tilde{\boldsymbol{\varepsilon}}^{tr}$:*

$$F_{\tilde{\varepsilon}^{tr}} = -\frac{1}{f_{ma}}\frac{\partial G}{\partial \tilde{\boldsymbol{\varepsilon}}^{tr}} - \lambda_c \tilde{\boldsymbol{\varepsilon}}^{tr} = \boldsymbol{\sigma}' - H_{tr}\tilde{\boldsymbol{\varepsilon}}^{tr} - \lambda_c \tilde{\boldsymbol{\varepsilon}}^{tr}. \tag{2.31}$$

   where $\boldsymbol{\sigma}'$ denotes the deviatoric part of the stress tensor $\boldsymbol{\sigma}$.

3. *Twin accommodation related to $\tilde{\boldsymbol{\varepsilon}}^{tw}$:*

$$F_{\tilde{\varepsilon}^{tw}} = -\frac{1}{f^{FA}}\frac{\partial G}{\partial \tilde{\boldsymbol{\varepsilon}}^{tw}} = \boldsymbol{\sigma}' - H_{tw}\tilde{\boldsymbol{\varepsilon}}^{tw}. \tag{2.32}$$

The driving forces above have to satisfy the predefined dissipation principles Eq. (2.27) as :

$$\begin{cases} F_{f_{ma}} = F^{crit}_{f_{ma}}, \\ |F_{\tilde{\varepsilon}^{tr}}|_\sigma = F^{crit}_{\tilde{\varepsilon}^{tr}}, \\ F_{\tilde{\varepsilon}^{tw}} = 0. \end{cases} \tag{2.33}$$

Thus, the evolution for phase transformation is controlled by the predefined critical thresholds and the driving forces. For the detailed formulation of the phase transformation and the definition for the critical thresholds, please refer to the paper by Chemisky et al. [1]. Besides the evolution of the martensitic phase transformation corresponding to the loading history, the model also takes into account the tension-compression asymmetry and effect of the internal loops related to a change of the thermodynamic transformation force when non-complete transformation occurs.

Eqs. (2.23) and (2.33), depending on the activation condition for the different mechanisms, lead to a system of equation to solve for stress, and all the considered internal variables :

$$\begin{aligned} R_{f_{ma}} &= F_{f_{ma}} - F^{crit}_{f_{ma}}, \\ R_{\tilde{\varepsilon}^{tr}} &= |F_{\tilde{\varepsilon}^{tr}}|_\sigma - F^{crit}_{\tilde{\varepsilon}^{tr}}, \\ \boldsymbol{R}_s &= \mathbb{S} : \boldsymbol{\sigma} + \boldsymbol{\alpha}\Delta T + f_{ma}\tilde{\boldsymbol{\varepsilon}}^{tr} + f^{FA}\tilde{\boldsymbol{\varepsilon}}^{tw} - \boldsymbol{\varepsilon}. \end{aligned} \tag{2.34}$$

where $R_{f_{ma}}, R_{\tilde{\varepsilon}^{tr}}, \boldsymbol{R}_s$ stand for the residuals of the system. For a given increment of strain and temperature, these residuals are eliminated using the return mapping algorithm, where an initial thermoelastic prediction followed by a series of transformation/orientation/accommodation of twins corrections (involving a change of f_{ma}, $\tilde{\boldsymbol{\varepsilon}}^{tr}$, $\tilde{\boldsymbol{\varepsilon}}^{tw}$). This constitutive relation is implemented on ABAQUS via UMAT. The tangent operator for each increment is :

$$\mathbb{C}_t = \frac{\partial \boldsymbol{\sigma}}{\partial \boldsymbol{R}_s} \tag{2.35}$$

This model was validated with experimental results (Duval et al. [210]). To illustrate the prediction capability of the present model, it is used to simulate the NiTi SMA material response under proportional and complex thermomechanical cyclic loadings. The model predictions are then compared to experimental measurements which were obtained by Sittner et al. [211] for respectively tension and tension–torsion loadings. In Fig. 2.3a, the model response is compared to the experience in the case of an initially austenitic material submitted to tension loading/unloading cycle. It shows that the model well describes the whole superelastic behavior (start and finish of transformation, hysteresis size, internal loop size). However it doesn't detect the transformation localization pick and the plateau induced by transformation propagation. The same remarks can be made for the shape memory effect behavior presented in Fig. 2.3b. It corresponds to the response of an initially martensitic NiTi SMA, submitted to tension loading/unloading.

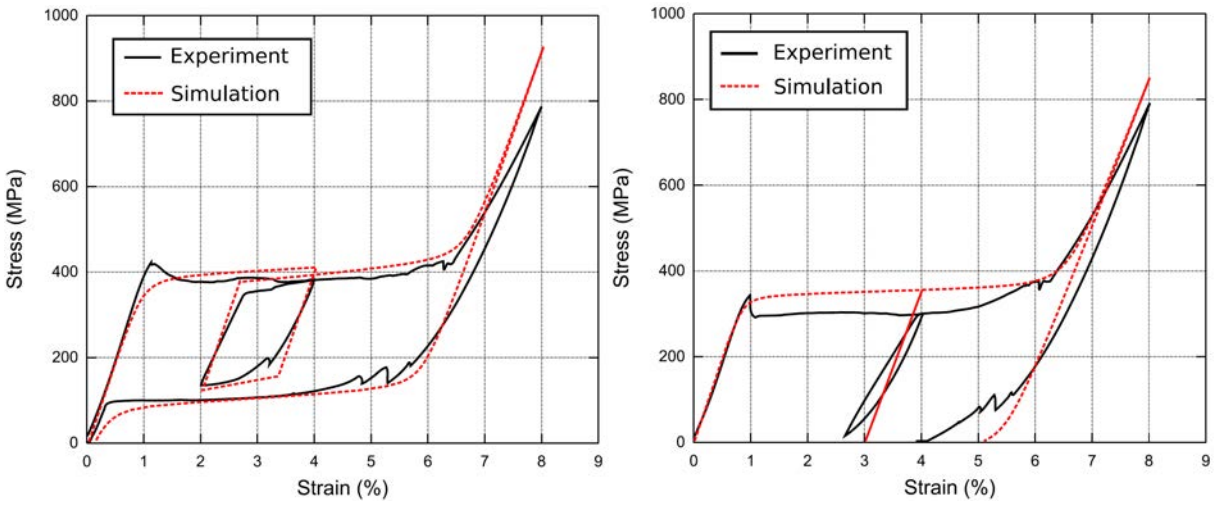

(a) (b)

FIGURE 2.3 – (a) superelastic behavior under tension loading/unloading ; (b) shape memory effect behavior under tension loading/unloading (Duval et al. [210]).

This SMAs constitutive model is used to describe the response of the SMA fiber, while an elastic behavior is chosen for the epoxy matrix. At this point, the nonlinear computational homogenization procedure is implemented for simulating a SMA fiber/epoxy matrix composite. In the next section, applications of proposed approach are simulated and discussed.

2.2 SMA fiber reinforced composite

In this section, two parts of examples for isothermal and thermomechanical loading are tested respectively to validate the reliability of the proposed multiscale thermodynamic model. For the first part, two isothermal loading examples are presented to show the pseudo-elasticity of the SMA/epoxy composite. For the first example, a composite cube under isothermal tension-compression displacement load and simply supported boundary are simulated respectively by the multiscale model and a fully meshed model. The results of the multiscale model are compared with that of the fully meshed model to validate the developed procedure. For the second example, a bending composite beam is studied to be compared with the results in Dehaghani et al. [58]. For the second part, two thermomechanical loading examples with a tension cube and a bending

beam respectively are carried out to study the shape memory effect.

2.2.1 Pseudo-elasticity

Tensile-compressive composite cube

A 3D cube composed of SMA fibers and polymer matrix, with fiber volume fraction of 28%, face X=0, face Y=0 and face Z=0 simply supported, is shown in Fig. 2.4. A displacement, which gradually increases until reach a given maximum value and then be inactivated, is applied on face Z=10 mm. For the microscopic level, the inclusion and the matrix are assumed to be fully bonded. The detailed material properties of the elastic matrix and the SMA inclusion are given in Tables 2.1 and 2.2.

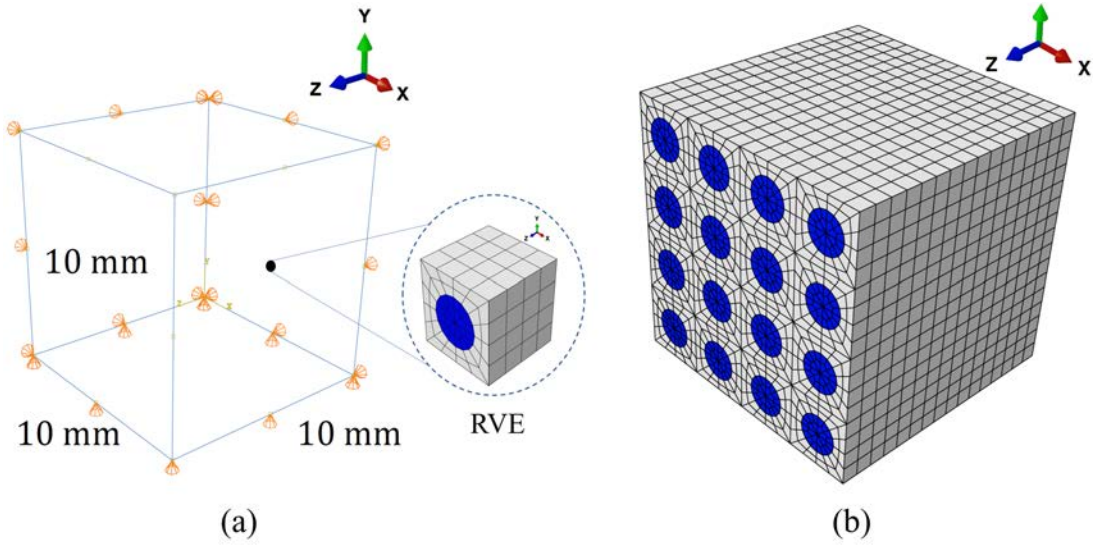

FIGURE 2.4 – Geometry, mesh and boundary conditions for the composite cube : (a) FE^2 model ; (b) Fully meshed model.

TABLE 2.1 – Material parameters for SMA fibers.

E (MPa)	70000	B_r (MPa °C^{-1})	6	H_f (MPa)	4
ν	0.33	B_f (MPa °C^{-1})	5	H_{tr} (MPa)	1000
ε^T_{trac}	0.05	M_s (°C)	−50	H_{tw} (MPa)	40000
ε^{TFA}_{trac}	0.04	A_f (°C)	−20	H_s (MPa)	50
ε^T_{comp}	0.04	F_ε (MPa)	100		

TABLE 2.2 – Material parameters for matrix.

E_m (MPa)	20000
ν_m	0.3

Two loading-unloading cycles (tension and compression) are performed by the multiscale model and the fully meshed model, respectively. Fig. 2.4 give the mesh for the cube respectively for the two models. For the multiscale model, the macroscopic structure is meshed with 1 element along both X, Y and Z directions based on C3D8 linear elements with 8 Gauss integration points per element. RVE with totally 224 C3D8 linear elements, shown in Fig. 2.4a, is introduced to calculate the behavior of each macroscopic integration point. The fully meshed model with 14336 C3D8 linear elements, shown in Fig. 2.4b, consists of 4 RVEs arranged in each directions respectively. The loading-unloading progresses for both two models are performed on ABAQUS with *General Static Procedure* under isothermal condition.

Fig. 2.5 illustrates the stress-strain diagrams averaged on the whole volume of multiscale model and fully meshed model under tension-compression cycles with maximum strain up to 0.06. The loading curves obtained by two models show a good agreement especially before fully transformation is completed, and even during fully martensite state, their responses are quite close to each other. Moreover, the loading path highlights the tension-compression asymmetry. When fully forward transformation is completed, the strain reaches 0.06 in tension case while the strain in compression case is 0.04. The transformation slopes and the hysteresis loops are also apparently affected by the asymmetry. Fig. 2.5 also depicts the partial loading effect of the composite when non-complete forward transformation occurs (applied displacement load up to 0.4 mm and 0.2 mm) and two models coincide with each other closely. As the fiber volume fraction is 28% and the matrix is stiffer than fibers during SMAs' phase transformation, the hysteresis effect is quite weaker than that of the pure SMAs.

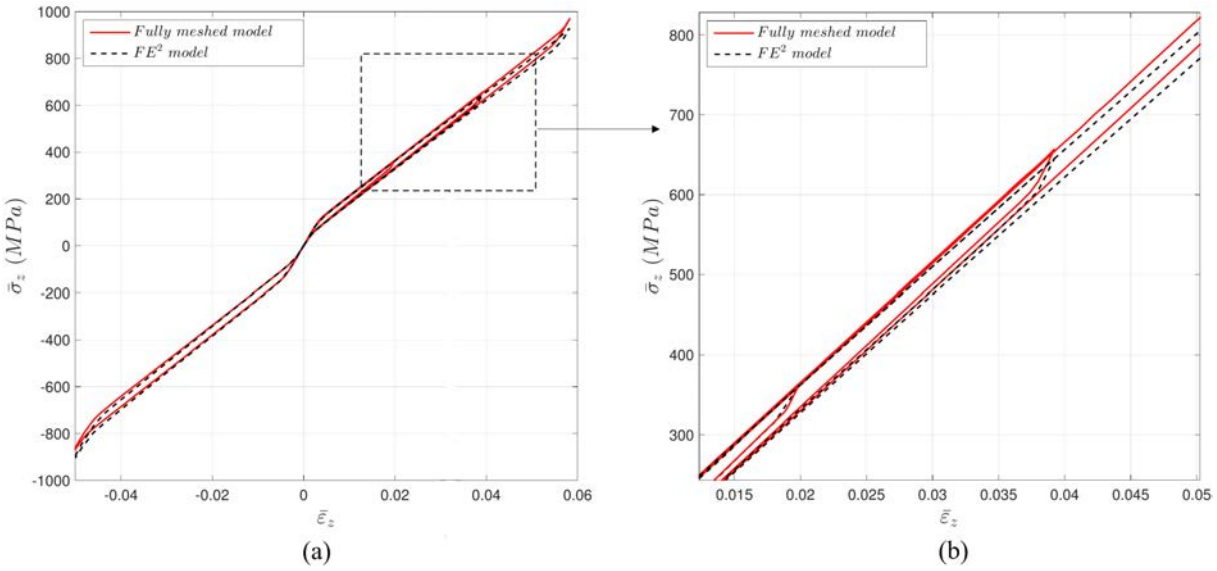

FIGURE 2.5 – The averaged stress-strain diagram of the composite cube subjected to partial tensile-compressive loading : (a) global ; (b) local.

RVEs with different geometric periodic boundaries but same volume fiber fraction are studied as given in Fig. 2.6. The response of a cube subjected to isothermal tensile loading is illustrated in Fig. 2.7, considering these three different types of RVE respectively. The global tensile response of the cube is consistent due to the periodic repeating feature of the RVEs.

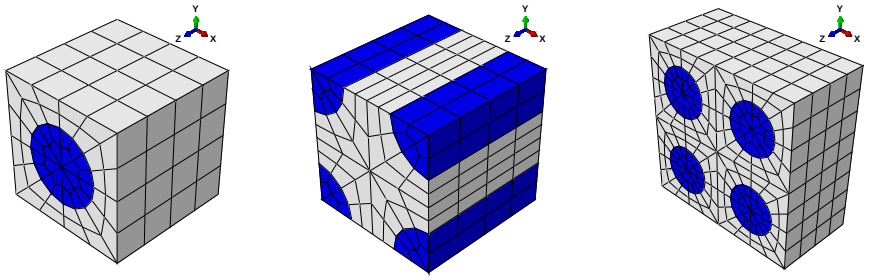

(a) Type A (b) Type B (c) Type C

FIGURE 2.6 – Three types of fine meshed RVE.

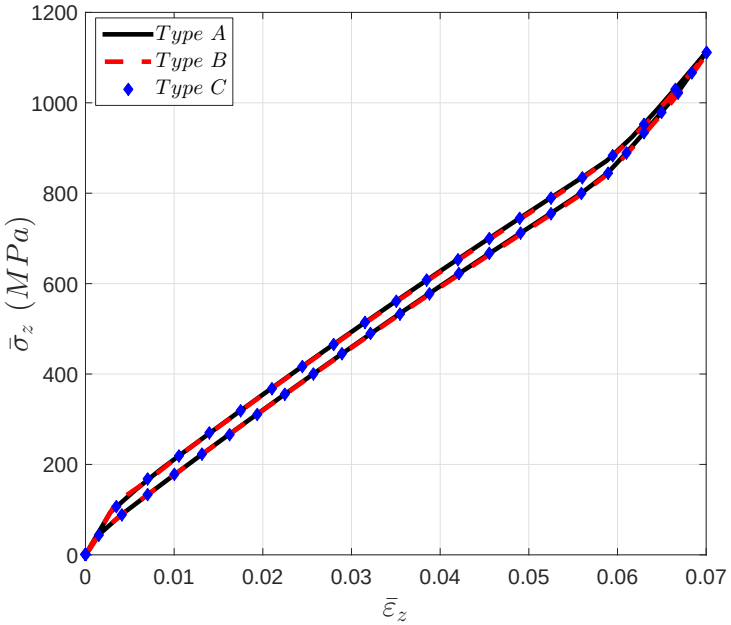

FIGURE 2.7 – The averaged stress-strain diagram of composite cube when considering three different types of RVE.

Bending composite beam

A 3D bending composite beam is considered with face Z=0 fully clamped and face Z=100 mm subjected to a transversely surface load $\sigma = 33.33$ MPa (see Fig. 2.8). In order to validate this model, mechanical properties, as given in Table 2.3, are taken according to the bending example in Dehaghani et al. [58], where the fiber volume fraction is 26.7% and the tension-compression asymmetry is not considered. Notice that the SMA behavior adopted in our work differs slightly from that of Dehaghani et al. [58], as illustrated in Fig. 2.9, where the martensite Young's modulus in our model is assumed equal to that of the austenite. The macroscopic model is meshed by 32 C3D8I incompatible mode elements (2 elements along X, Y direction and 8 elements along Z direction, see Fig. 2.11) with 8 integration points per element, taking advantage of the high performance of C3D8I element in bending problems. The microscopic model remains the same, see Fig. 2.4a.

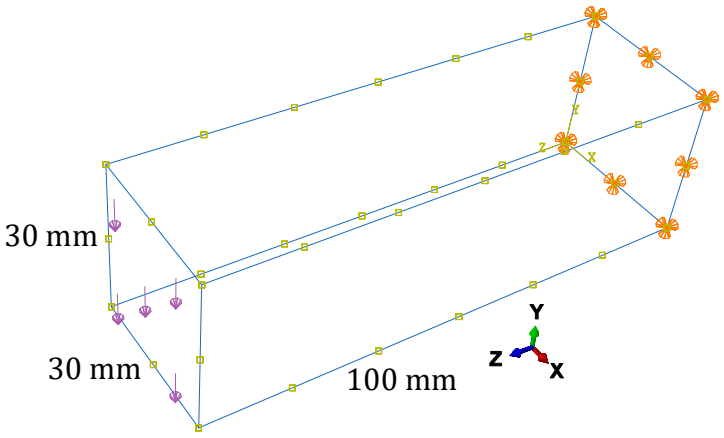

FIGURE 2.8 – Geometric parameters and boundary conditions for a bending composite beam.

TABLE 2.3 – Material parameters for SMA fibers similar to Dehaghani et al. [58] .

E (MPa)	70000	B_r (MPa °C^{-1})	10	H_f (MPa)	7.8
ν	0.33	B_f (MPa °C^{-1})	10	H_{tr} (MPa)	1000
ε^T_{trac}	0.054	M_s (°C)	16.85	H_{tw} (MPa)	40000
ε^{TFA}_{trac}	0.04	A_f (°C)	35.85	H_s (MPa)	45
ε^T_{comp}	0.054	F_ε (MPa)	100		

Fig. 2.10 gives the applied load versus the transverse displacement of the central node of face Z=100 mm, simulated by the adopted FE^2 and the reference models, which show a good agreement. The distribution of stress for a RVE above neutral axis and a RVE below neutral axis are also presented in comparison with the results of Dehaghani et al. [58]. The position of the associated two Gauss points is given in Fig. 2.11. Notice that taking into account the tension-compression asymmetry should be more realistic for bending problem.

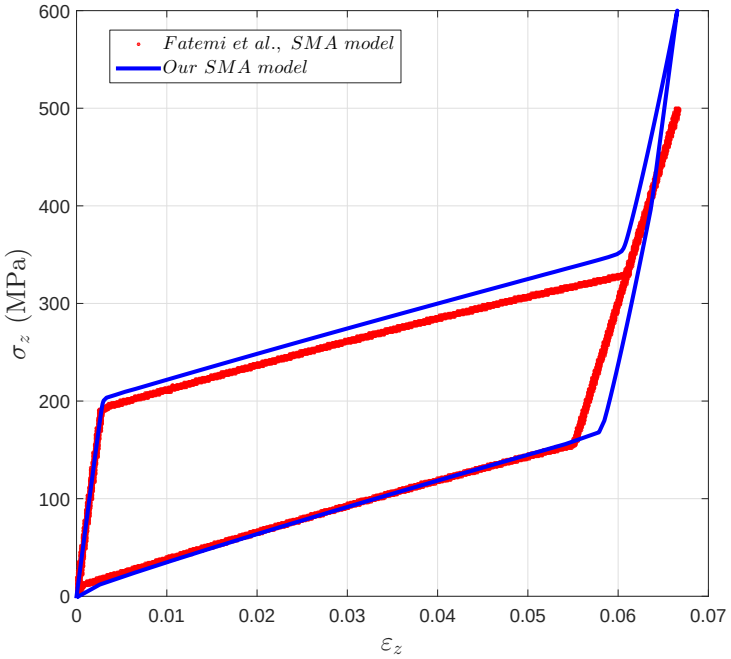

FIGURE 2.9 – The stress-strain diagram of our adopted and reference Dehaghani et al. [58] SMA model subjected to tensile loading.

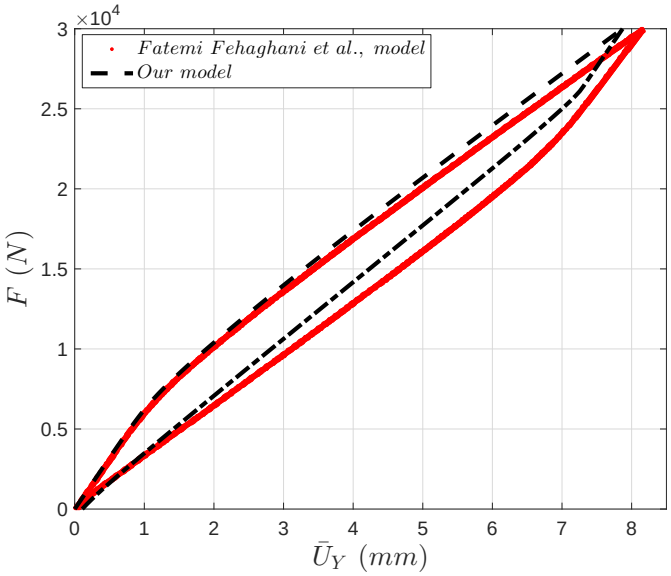

FIGURE 2.10 – Comparison of force versus averaged transverse displacement diagrams over face Z=100 mm, simulated by the adopted FE^2 model and the reference Dehaghani et al. [58] model respectively.

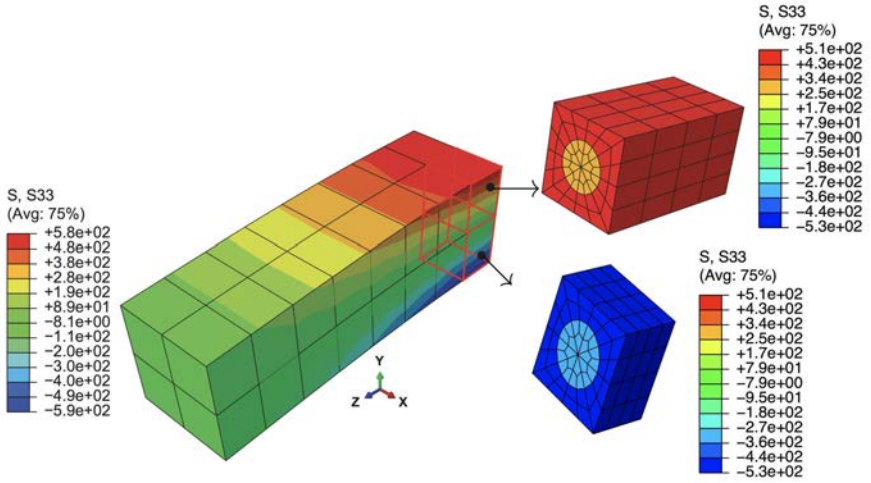

FIGURE 2.11 – The distribution of stress in Z direction for macroscopic structure and microscopic structure, where the magnification scale factor for microscopic structure is 15.

2.2.2 Shape memory effect

Tensile composite cube

The 3D composite cube subjected to a thermomechanical loading is now studied. The boundary constraints, meshes and material parameters are exactly the same as those in last subsection, while the loading-unloading progress is replaced by four steps : 1) Cool the cube until a temperature below M_f ; 2) Give a displacement load on face Z=10 mm ; 3) Inactivate the displacement load ; 4) Heat the cube until a temperature above A_f. For this example, the material parameters are the same as in Tables 2.1 and 2.2 except M_s=20 ℃ and A_f=60 ℃. Fig. 2.12 gives the SME behavior of a pure SMA cube subjected to a cooling from 100 ℃ to 0 ℃ at zero stress, an isothermal tensile loading-unloading and a heating to its initial temperature in turn. Fig. 2.13 gives the orientation and reverse orientation of SMA subjected to several tensile-compression loadings after cooling to 0 ℃.

The averaged stress, strain and temperature paths simulated by the FE^2 model are given in Fig. 2.14. Partial loadings with maximum strain level up to 0.01, 0.03 and 0.05 are considered respectively. Fig. 2.15 gives the martensitic volume fraction of the fiber in RVE. The cooling step begins at point A and ends at B, with SMA fibers transform from austenite phase into self-accommodated martensite. Then mechanical loading begins at point B and BC is the elastic response of self-accommodated martensite. The martensite orientation of SMA fibers happens in stage CD. DE is the elastic part of the twinned-detwinned mixed martensite. A reverse orientation begins at point E and then stops until the macroscopic external load vanishes at point F with a residual strain. At last, heating step from point F to I is carried out and the residual strain vanishes along with martensite transforms into austenite during stage GH. The response of the composite is between the elastic matrix and the SMAs fibers. The proposed FE^2 model is validated by the fully meshed model as shown in Fig. 2.16, where two curves have a good agreement.

The reverse orientation of the unloading stage DF is very interesting during the loading cycles. Fig. 2.17 gives the stresses distribution in one RVE. When the macroscopic mechanical load is totally inactivated, the compressive stress in fiber and the tensile stress in matrix achieve a balance in Z direction. The compressive stress leads to the reverse orientation of the martensite,

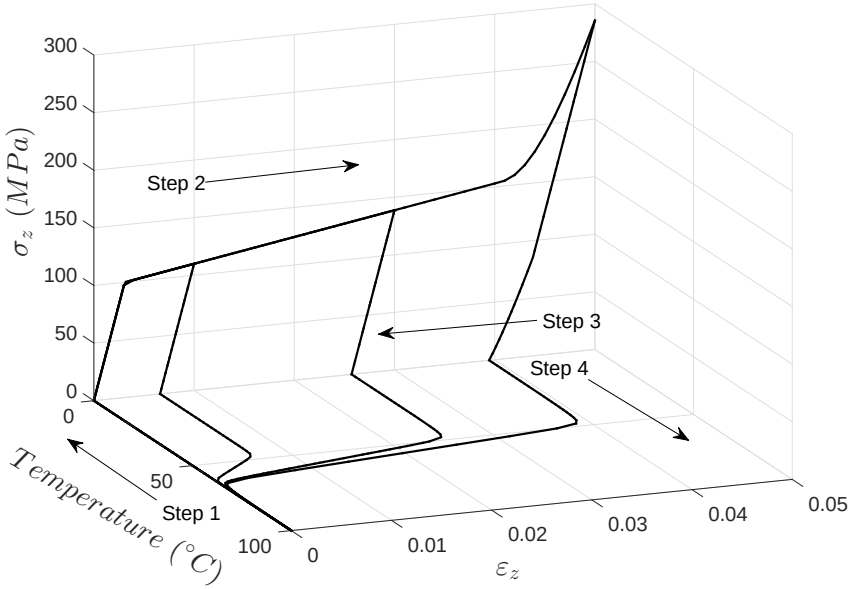

FIGURE 2.12 – The SME of pure SMA cube subjected to several strain levels.

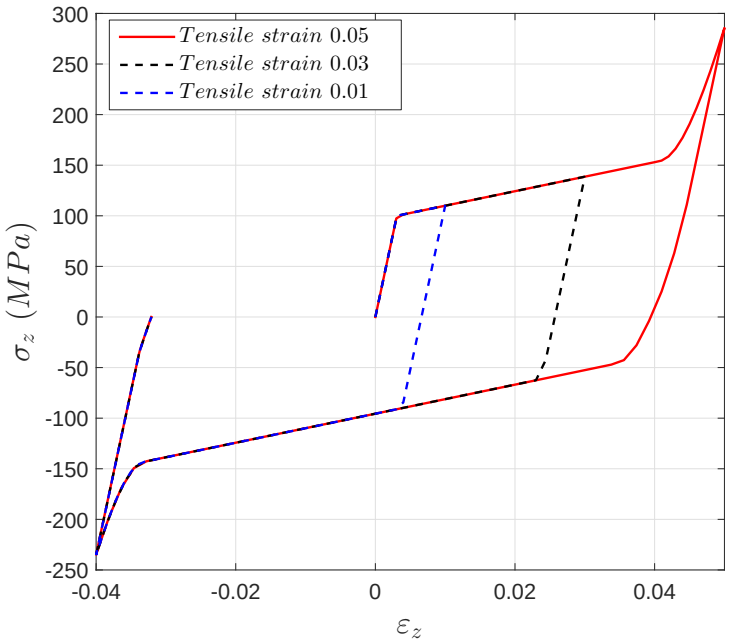

FIGURE 2.13 – Orientation of SMA subjected to several tensile-compression loadings at 0 °C.

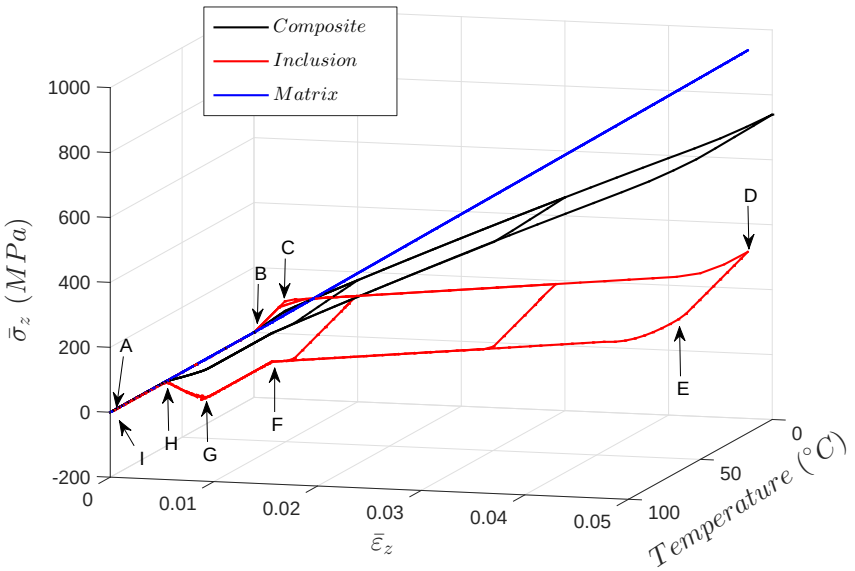

FIGURE 2.14 – Averaged stress, strain and temperature diagrams of face Z=10 mm of composite cube subjected to several thermomechanical strain levels.

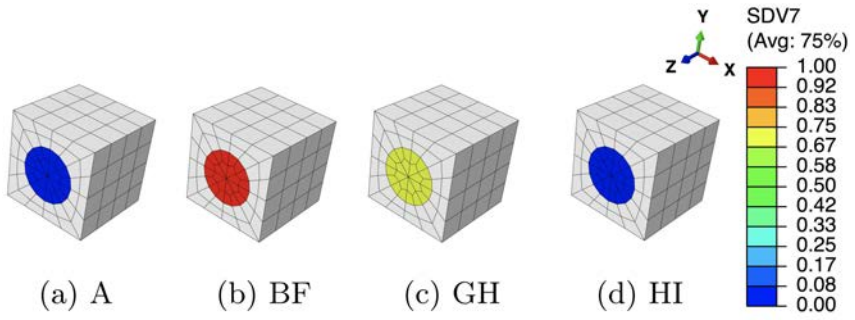

FIGURE 2.15 – Distribution of martensitic volume fraction in fiber.

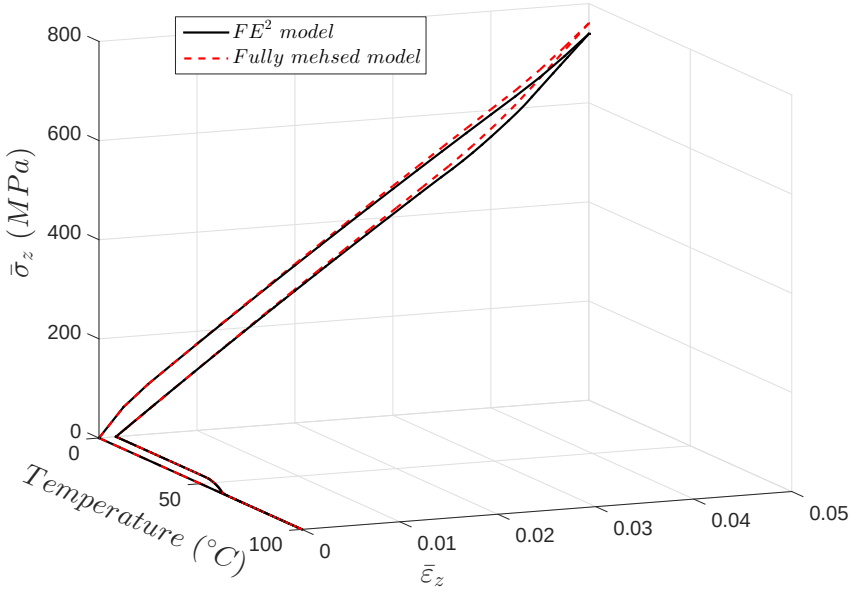

FIGURE 2.16 – Averaged stress, strain and temperature diagrams of face Z=10 mm of composite modeled by the FE^2 model and fully meshed model respectively.

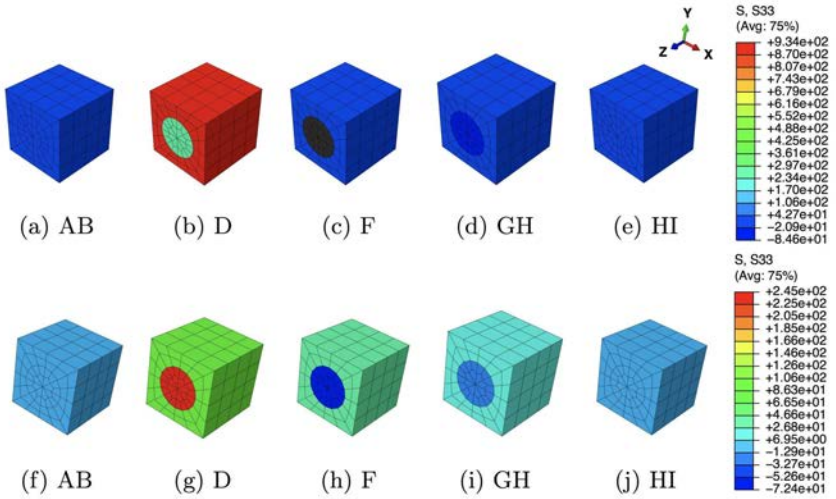

FIGURE 2.17 – Stresses in Z direction distributed in the RVE of composite cube, where figure (a) to (e) are for the composite with stiffer matrix and figure (f) to (j) are for the softer one.

which finally eliminates a part of the residual strain, similar to the response shown in Fig. 2.13. Another test with softer matrix is carried out to show how the internal stress affects the thermo-mechanical behavior of the fiber and composite. As given in Fig. 2.18, red curve shows a softer averaged response, which keeps composite undergoing a lower stress level than the black one. Fig. 2.17 gives a clear comparison of the stress distribution in Z direction of two tests' RVEs. Higher internal stresses in stiff matrix lead to a bigger amount of reverse orientation and less residual strain.

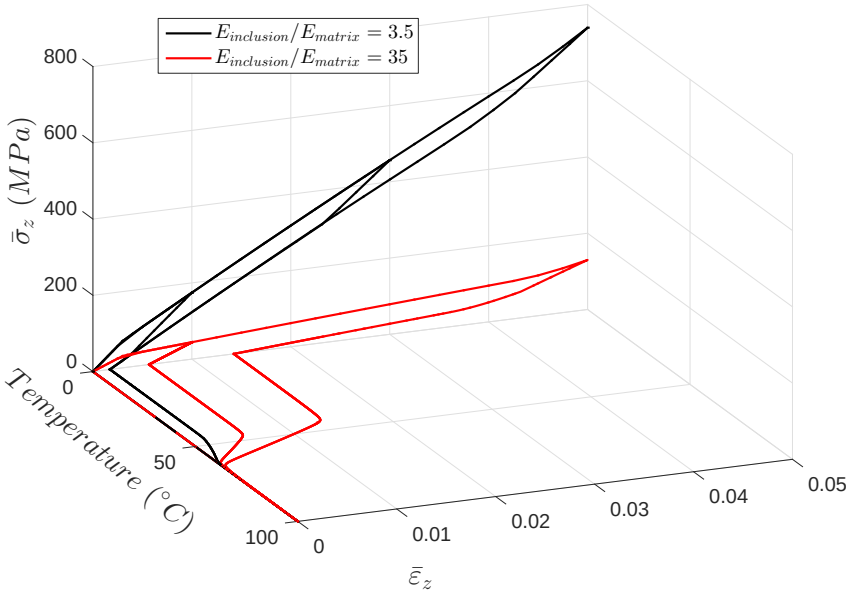

FIGURE 2.18 – The SME of composite with different matrix stiffness.

Bending composite beam

The same cantilever beam (see Fig. 2.8) subjected to thermomechanical cycles is considered to show the response of a bending beam with SME. The mechanical parameters are the same as that of the SME cube. Cooling from 70 ℃ to 10 ℃ is carried out in the first step, then a shearing surface stress up to 10 MPa in -Y direction is applied on face Z=100 mm in the second step. After unloading and heating, the cantilever beam recovered its initial shape. Fig. 2.19 gives the varying transversal displacement of the central node on face Z=100 mm during the whole loading history. Stage AB is the cooling step where the beam has no deformation. BC is the elastic response of the cantilever beam where the fiber remains in self-accommodated martensite. The slope of presented curve changes in stage CD mainly due to the martensite orientation. A residual strain at point E stops the beam to recover its initial shape after unloading. At last, the beam recovers its initial shape along with the reverse transformation removes the residual strain during stage FG.

2.2.3 Comments on the computational resources

Some comments on the computational resources in the presented numerical tests may be useful for possible practical applications of the SMA based composites. The PE bending test in Section 2.2.2 is performed on a PC with Intel(R) Xeon(R) CPU (2.30GHz, 36 cores) and 64 GB of RAM. There are 256 integration points and 200 increments on the macroscopic model. The total computing time is about 131 hours with 1 processor or 18 hours with 16 processors.

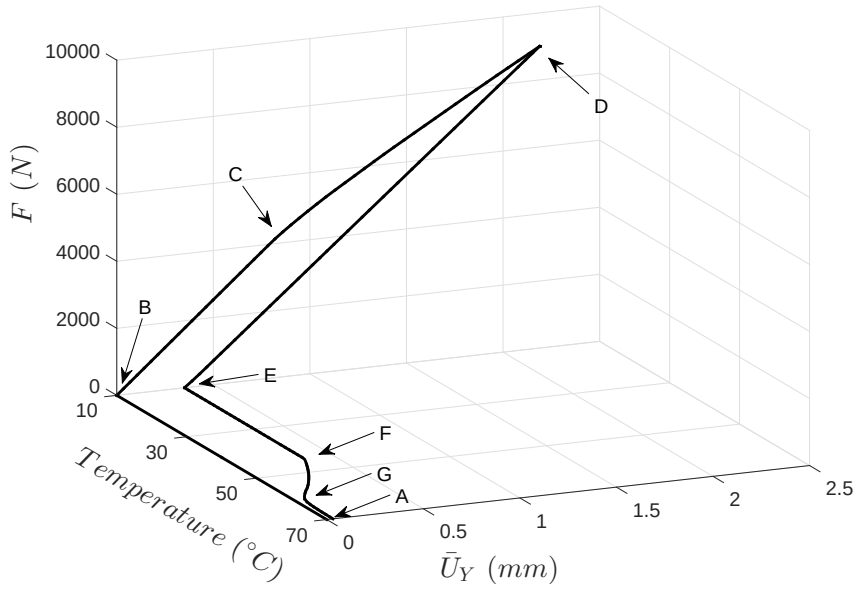

FIGURE 2.19 – The SME of a cantilever beam subjected to thermomechanical cycles.

The proposed model is time-consuming for the moment, due to the real-time interaction between scales. However, the computational resources could be optimized in the FE^2 approach. According to van Tuijl et al. [126], the total computational resources $\#_{LA}^{flop}$ of the FE^2 approach can be estimated by $\#_{LA}^{flop} \propto O\left(n_M^g\right) \times O\left(n_M^{it}\right) \times O\left(n_m^{it}\right) \times O\left(n_m^d log(n_m^d)\right)$, where n_M^g denotes the number of macroscopic integration points, n_M^{it} and n_m^{it} denote the amount of iteration required in macroscopic and microscopic level respectively, n_m^d denotes the DOFs on the microscopic model. According to this formula, the computational efficiency can be improved by many ways. For example, the order reducing modeling (van Tuijl et al. [126], Huang et al. [131, 132], Hernandez et al. [168]) is useful in reducing the computing time of finite element model on both macroscopic and microscopic level. The parallel computation strategy on the macroscopic level is also powerful in this case because RVEs are individual to each other. For a practical application, different numerical models may be required for different parts of the structure in order to optimize the computational resources. In that case, the FE^2 model could be combined with other reduced models by bridging techniques (Hu et al. [212], Yu et al. [213]), which are capable to couple various FE models. Moreover, the authors are optimistic with the proposed multiscale model because of the rapid updating of processor performance during the past decades.

2.3 Architected cellular SMA

With the proposed multiscale modeling tool, an architected cellular SMA is studied in this section. Firstly, RVEs with different geometrical parameters are discussed, then the structural response is investigated further by our tool.

2.3.1 Cellular response

Convergence analysis for the RVE mesh

An architected SMA RVE is introduced to describe the microscopic structure ; see Fig. 2.20. It is formed by excavating cylindrical holes through the center of each face of a cube SMA. The size

of the cube is given by 1 mm × 1 mm × 1 mm, while the radius of the cylindrical holes is given as 0.38 mm. According to computational homogenization theory, periodic boundary conditions are introduced into the RVE by the multi-point constraints (MPCs) on ABAQUS :

$$\Delta \boldsymbol{u}^{+} - \Delta \boldsymbol{u}^{-} = \Delta \bar{\boldsymbol{\varepsilon}} \cdot (\boldsymbol{x}^{+} - \boldsymbol{x}^{-}) \quad on \quad \partial\omega, \tag{2.36}$$

where $\boldsymbol{u}$ is the displacement vector, $\boldsymbol{x}$ is the coordinates of nodes and $\bar{\boldsymbol{\varepsilon}}$ is the strain load applied on the RVE. The notations $+$ and $-$ denote the nodes on opposite boundaries; the notation Δ represents the incremental case. Thus, a set of reference points (RPs) for three different directions is introduced in MPCs and the meshes on the opposite boundaries must be the same in order to create periodic boundaries; see Fig. 2.20. Both the continuum 3D solid element with full integration (labeled C3D8 on ABAQUS) and continuum 3D solid element with reduced integration (labeled C3D8R on ABAQUS) for the mesh in Fig. 2.20a are studied in order to optimize the computation efficiency on the RVE. Following the constitutive model introduced in the last subsection, the material parameters of a conventional NiTi alloy are given in Table 2.4, which are identified with the experimental data of Rashed et al. [68].

TABLE 2.4 – Material parameters for SMA.

E (MPa)	39,500	B_r (MPa °C^{-1})	7	H_f (MPa)	2
ν	0.3	B_f (MPa °C^{-1})	7	H_{tr} (MPa)	1635
ε^{T}_{trac}	0.056	M_s (°C)	-80	H_{tw} (MPa)	25,000
ε^{TFA}_{trac}	0.053	A_f (°C)	-2	H_s (MPa)	68.5
ε^{T}_{comp}	0.044	F_ε (MPa)	220		

To check the effective response of the RVE, a tensile strain up to 10% in the Y direction is applied on the RVE at a constant temperature of 30 °C.

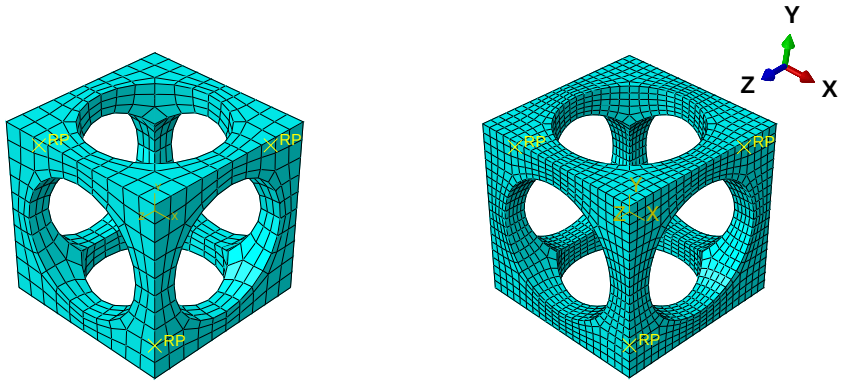

(a) 720 elements (b) 4120 elements

FIGURE 2.20 – Architected RVE with fine meshes and reference points (RPs).

To describe the effective behavior of RVE, the averaged values, such as stress $\bar{\boldsymbol{\sigma}}$, strain $\bar{\boldsymbol{\varepsilon}}$ and martensitic volume fraction $\bar{f}_t$, are introduced. The averaged values are computed by volume averaging over the whole 1 mm^3 cube from Element 1 to N, where N denotes the total element number. Note the averaged strain is equal to the prescribed strain due to the periodic boundary conditions, Eq. (2.7). Fig. 2.21a shows the stress-strain relations simulated with different meshes and element types. The hysteresis effect is observed during the loading/unloading cycle. This nonlinear response is caused by the inner forward phase transformation of SMA. The averaged

martensitic volume fraction $\bar{f}_t$ increases along with the loads until reaching a maximum value; see Fig. 2.21b. When the unloading begins, $\bar{f}_t$ decreases immediately until recovering to zero. From the comparison of the curves, it is observed that the mesh with 720 elements is fine enough to model this architected SMA RVE. Furthermore, the RVEs simulated by the C3D8R and C3D8 elements have exactly the same responses; see Fig. 2.21.

Generally speaking, the mesh with 720 C3D8R elements has relatively enough accuracy and lower computational cost than other meshes. Thus, meshes like density and C3D8R elements are used for the RVE in the following work.

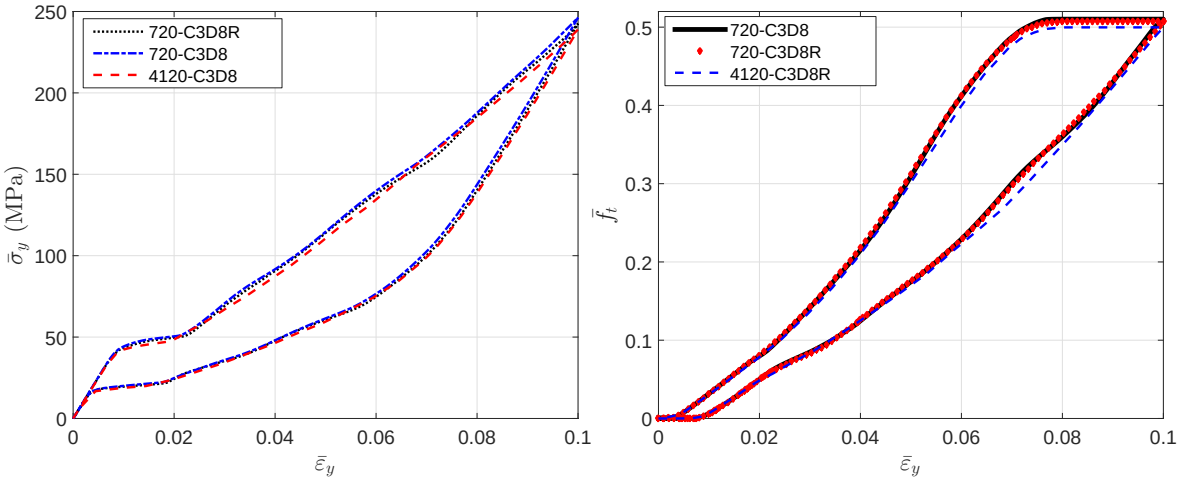

(a) Stress versus strain (b) Martensitic volume fraction versus strain

FIGURE 2.21 – The evolution of the averaged stress and the averaged martensitic volume fraction simulated by RVEs with different meshes.

Cells with different geometries

In this subsection, five types of RVEs with different void volume factions ξ are studied, as illustrated in Fig. 2.22. The size of the cube is given by 1 mm × 1 mm × 1 mm, while the radius of the cylindrical hole varying along with ξ is given in Table 2.5. The material parameters of SMA remain the same as those in the last subsection.

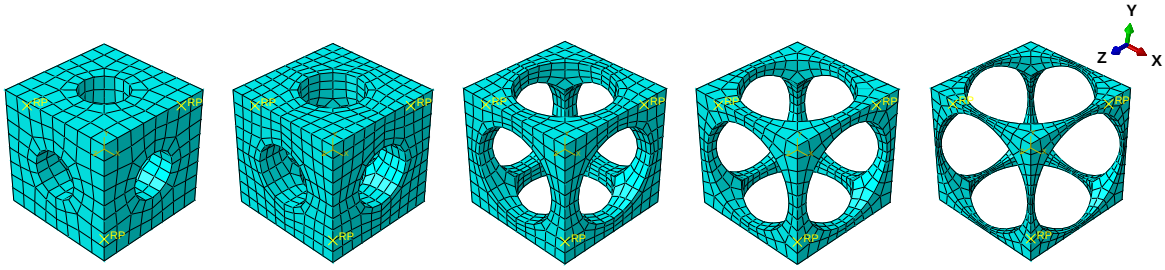

(a) $\xi = 29.1\%$ (b) $\xi = 40.7\%$ (c) $\xi = 72.5\%$ (d) $\xi = 82.2\%$ (e) $\xi = 90.7\%$

FIGURE 2.22 – Meshes for architected SMA RVEs with different void volume fractions ξ.

A tensile strain up to 10% and a compressive strain up to −10% in the Y direction are respectively applied on the RVEs to simulate effective responses for different RVEs. Fig. 2.23 gives

TABLE 2.5 – Geometrical parameters for RVEs.

Radius (mm)	0.2	0.24	0.38	0.42	0.47
Void volume fraction ξ	29.1%	40.7%	72.5%	82.2%	90.7%

the curves of averaged stress versus the averaged stain along the loading direction, simulated by the above RVEs respectively. The absolute value of stress in different RVEs at a certain strain level increases along with the decreasing of the void volume fraction, as depicted in Fig. 2.23. In more detail, Fig. 2.24 gives the relation of maximum stress and material volume fraction (1-ξ) when the absolute value of strain is up to 10%. The trend of the curve shows that the higher the material volume fraction is, the faster the stress increases. This trend could be explained by exploring the stress distribution on the RVE at the maximum strain level 10%, as shown in Figs. 2.25 and 2.26. The high stresses are mainly distributed over the middle of the pillars along the loading direction. Lower material volume fraction results in a stronger stress concentration effect. Thus, the stiffness of the RVE decreases more rapidly than the material volume fraction. This test could be a reference for designers to balance the stiffness and the mass of the architected structure.

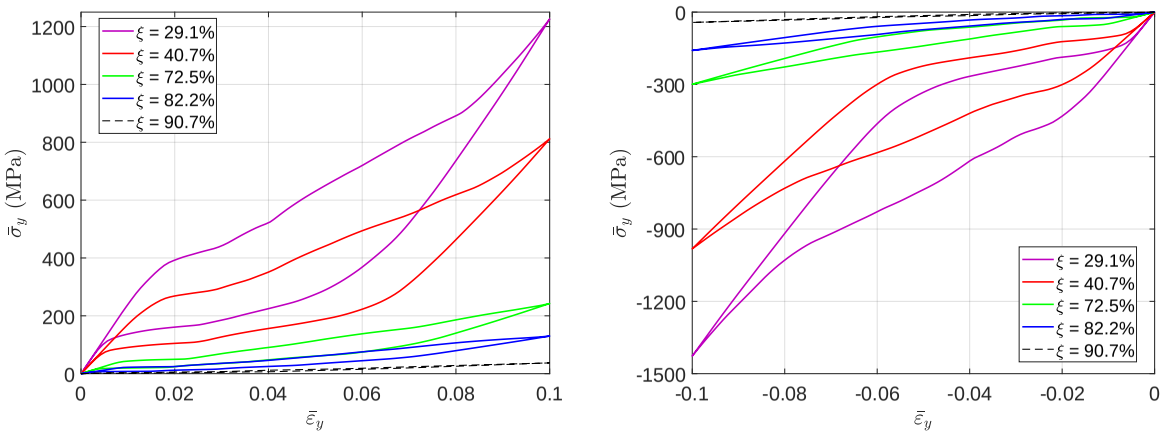

(a) Tensile loading (b) Compressive loading

FIGURE 2.23 – The evolution of the averaged stress-strain curves simulated by RVEs with different void fractions.

Fig. 2.27 gives the martensitic volume fraction averaged over SMA versus the strain averaged over the cube. The martensitic volume fraction $\bar{f}_t$ increases along with the increasing of the strain level, but stops before it reaches one. More specifically, each RVE has a certain maximum $\bar{f}_t$ value in this loading case. The maximum martensitic volume fraction versus the material volume fraction at the maximum absolute strain level of 10% is depicted in Fig. 2.28. It shows that the lower the material volume fraction is, the more rapidly the martensitic volume fraction decreases. This also means the usage rate of SMA is at a very low level when the material volume fraction is low, and it could result in a waste of SMA. For example, the hysteresis effect of the SMA architected structure is not proportional to the SMA mass, but to the product of the SMA mass and the SMA usage rate. Thus, the hysteresis effect could be very weak when the SMA usage rate is very low. Like the stiffness discussed before, this phenomenon could also be

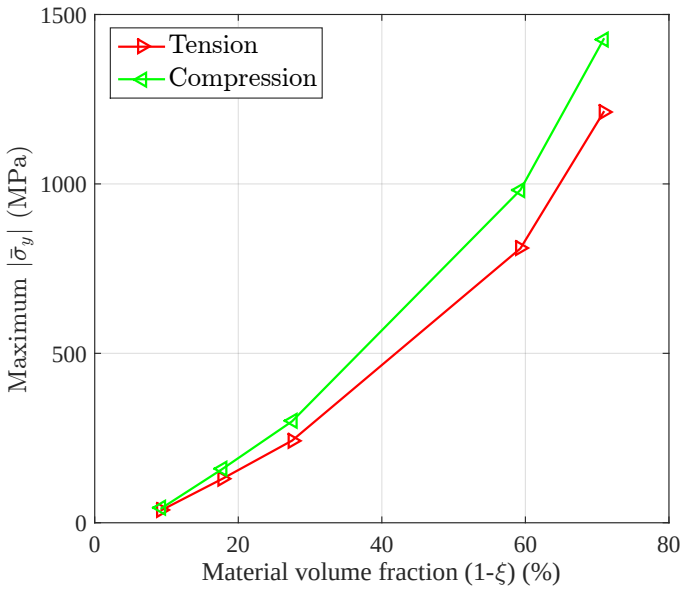

FIGURE 2.24 – The relation between the stiffness and the material volume fraction (1-ξ) of the RVE when the absolute value of strain is up to 10%.

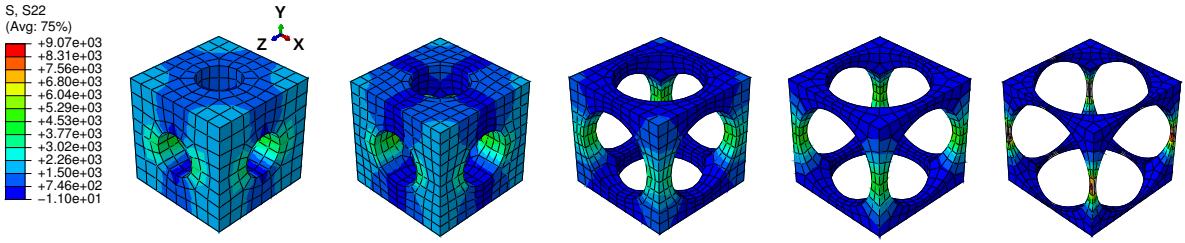

(a) $\xi = 29.1\%$ (b) $\xi = 40.7\%$ (c) $\xi = 72.5\%$ (d) $\xi = 82.2\%$ (e) $\xi = 90.7\%$

FIGURE 2.25 – Distribution of stress in Y direction (S22) on the RVEs with different void volume fractions ξ in tension loading at strain level 10%.

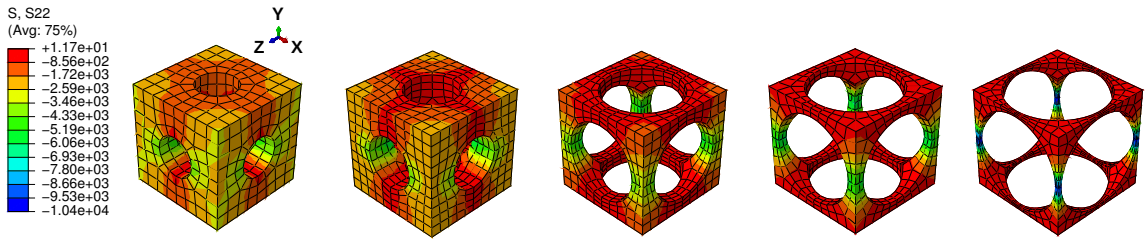

(a) $\xi = 29.1\%$ (b) $\xi = 40.7\%$ (c) $\xi = 72.5\%$ (d) $\xi = 82.2\%$ (e) $\xi = 90.7\%$

FIGURE 2.26 – Distribution of stress in Y direction (S22) on the RVEs with different void volume fractions ξ in compression loading at strain level -10%.

explained by the stress concentration where only the high stress area transforms into martensite ; see Figs. 2.29 and 2.30. This also means SMA cannot completely transform from austenite into martensite. Thus, as long as the unloading begins, the reverse transformation starts immediately, resulting in the reduction of $\bar{f}_t$.

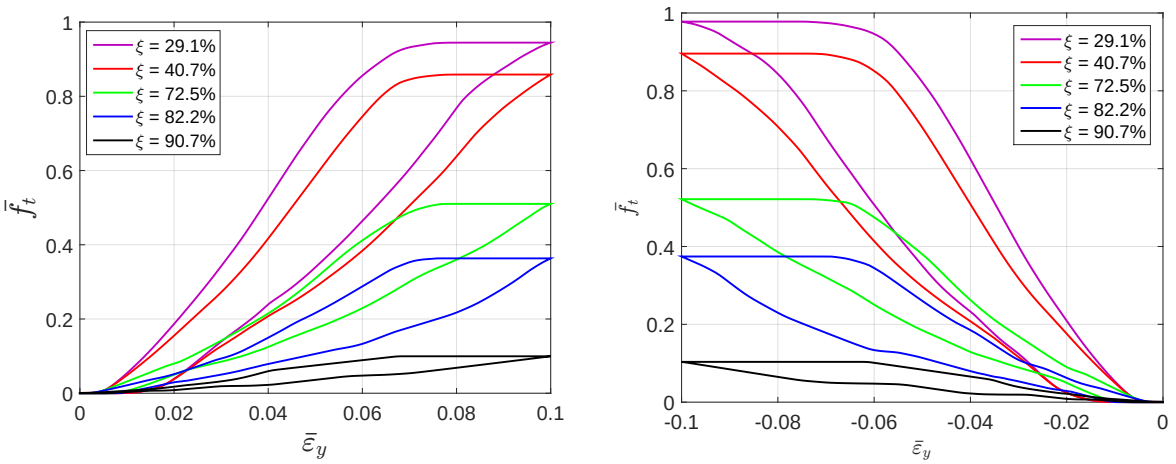

(a) Tensile loading (b) Compressive loading

FIGURE 2.27 – The evolution of the martensitic volume fraction versus the averaged strain curves simulated by RVEs with different void volume fractions.

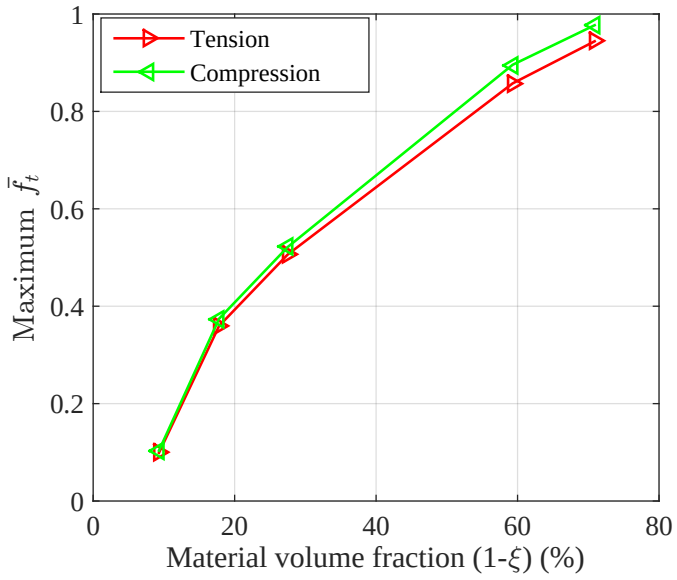

FIGURE 2.28 – The relation between maximum martensitic volume fraction versus the material volume fraction when the absolute value of strain is up to 10%.

To design a light weight architected SMA structure, it is required to minimize the material volume fraction in order to decrease the weight and cost of the structure. However, the necessary stiffness of the structure should be firstly satisfied. It should be noticed that the waste of SMA

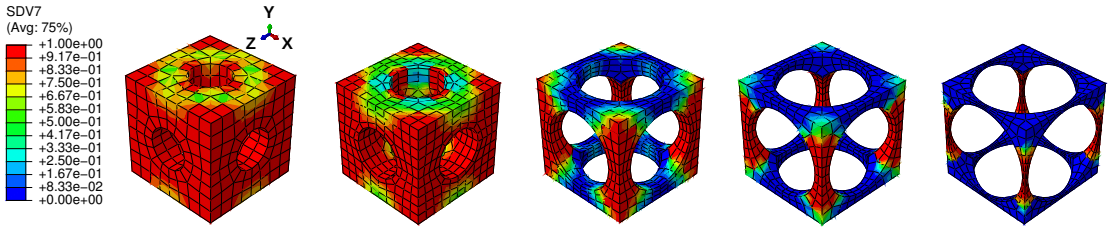

(a) $\xi = 29.1\%$ (b) $\xi = 40.7\%$ (c) $\xi = 72.5\%$ (d) $\xi = 82.2\%$ (e) $\xi = 90.7\%$

FIGURE 2.29 – Distribution of martensitic volume fraction $\bar{f}_t$ (named SDV7 in colorbar) on the RVEs with different void volume fractions ξ in tension loading at strain level 10%.

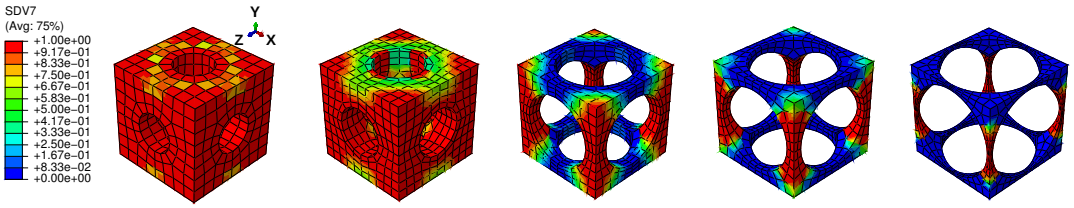

(a) $\xi = 29.1\%$ (b) $\xi = 40.7\%$ (c) $\xi = 72.5\%$ (d) $\xi = 82.2\%$ (e) $\xi = 90.7\%$

FIGURE 2.30 – Distribution of martensitic volume fraction $\bar{f}_t$ (named SDV7 in colorbar) on the RVEs with different void volume fractions ξ in compression loading at strain level -10%.

should also be avoided as much as possible due to SMA's high price. Therefore, the results given in Figs. 2.24 and 2.28 can be a reference for the designers to balance the stiffness, mass and SMA usage according to their specific requirements.

Following the tests at the RVE level, the structural response of the architected SMAs is studied in the next section.

2.3.2 Structural response

In this section, the structural responses of the architected SMAs are focused on. The constitutive behavior of the macroscopic structure is represented by the computational homogenized RVEs in the last subsection.

Beam with three kinds of cells subject to three-point bending

A 3D beam subjected to three-point bending load is shown in Fig. 2.31. This beam is composed of architected SMA. The width, length and height of the beam are 5 mm, 20 mm and 5 mm, respectively. Edge Y = 5 mm, Z = 10 mm is fixed in the Y and Z directions. A displacement load up to 0.5 mm in the Y direction is applied on the edges Y = Z = 0 mm and Z = 20 mm, Y = 0 mm. Node X = 0 mm, Y = 5 mm, Z = 10 mm is fixed in the X direction in order to eliminate the rigid body displacement in the X direction. Considering the symmetry of the structure and the boundaries, only the left half of the structure is simulated in order to reduce the computation cost. To do this, an additional displacement constraint in the Z direction is given on face Z = 10 mm. Since the deformation in the X direction is not obvious in the three-point bending test, one element is used in this direction. Each edge in the Y direction is meshed by two elements and in the Z direction by four elements; see Fig. 2.32. The continuum 3D solid element with

incompatible modes (labeled C3D8I in ABAQUS) is adopted for the modeling of the macroscopic beam since it is enhanced by incompatible modes to improve its bending behavior. The RVEs studied in the last section are used herein with void volume fractions ξ of 40.7%, 72.5% and 82.2%, respectively.

As the macroscopic constitutive behavior on each integration point is not clear, it has to be represented by the effective behavior of the associated RVE at each macroscopic increment. A brief flow diagram, showing how this multiscale problem is solved, is illustrated in Fig. 2.33. Specifically, the effective behavior of the RVE is computed by seeking the relations between the averaged stresses and averaged strains over the RVE via a series of loading tests. Once the effective behavior is obtained, the macroscopic problem is to be solved. Considering the nonlinear response of the RVE during loading, the macroscopic convergence has to be checked in each macroscopic iteration of the Newton–Raphson framework. In an iteration, the strain states of RVEs are updated with the macroscopic strains, and in return, the macroscopic stresses are renewed by updating the averaged stress of the RVE at the new strain states.

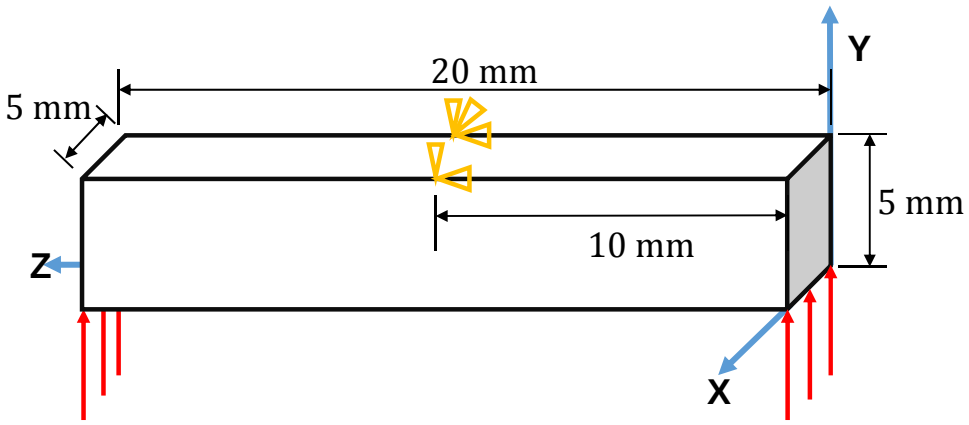

FIGURE 2.31 – Geometry and boundary conditions for the three-point bending beam.

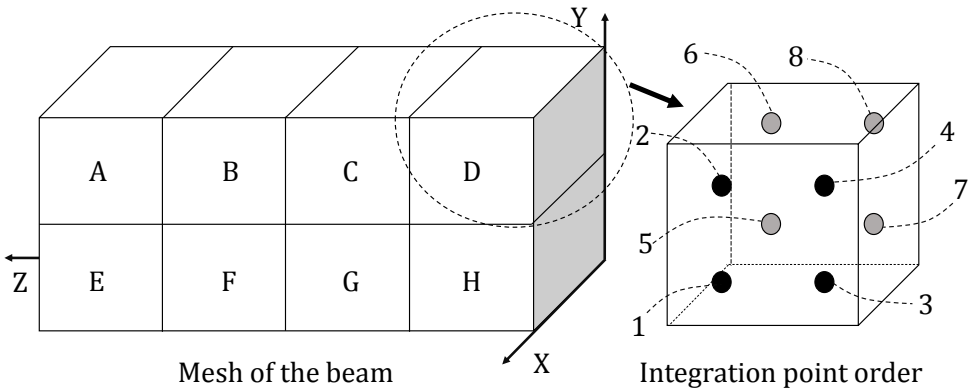

FIGURE 2.32 – The meshes for the left half beam and the integration points in each C3D8I element.

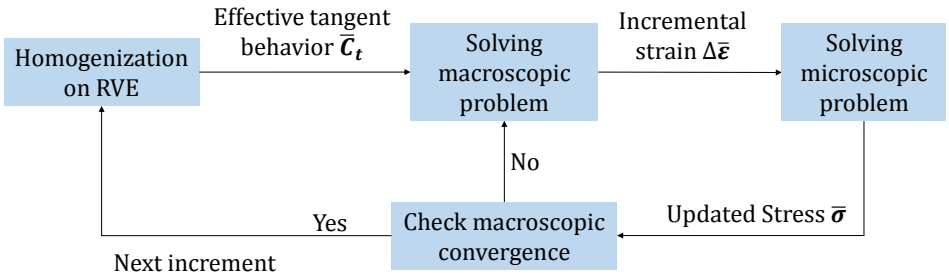

FIGURE 2.33 – The nonlinear interaction between two scales in the Newton–Raphson framework.

Stress distributions at the macroscopic and microscopic levels

Let us consider the case with volume fraction $\xi = 40.7\%$. The stress distribution of the bending beam with the prescribed displacement in the Y direction reaching 0.5 mm is illustrated in Fig. 2.34. The deformations of both the macroscopic and microscopic structures are magnified by three times. The high compressive stresses in the Z direction are observed in the elements above the middle plane Y = 2.5 mm, while in contrast, the compressive stresses are observed in the elements below the middle plane. In the meantime, for different macroscopic points, the RVEs have different stress states in correspondence with their associated macroscopic strain states. To specify the microscopic structure more clearly, we introduce RVE_{kl} to denote an RVE corresponding to the integration point l of the macroscopic element k. The RVEs above the middle plane, such as RVE_{A4} and RVE_{D4}, are mainly subjected to compression, while the RVEs below the middle plane, such as RVE_{E3} and RVE_{H3}, are mainly subjected to tension. The stresses in the RVEs far from face Z = 10 mm, such as RVE_{A4} and RVE_{E3}, are at a relatively low level compared to those RVEs near face Z = 10 mm, such as RVE_{D4} and RVE_{H3}.

Evolution of the loading

Fig. 2.35 shows the nonlinear response of the macroscopic structure with three different void fractions. The linear response is observed at the very beginning, and the microscopic structures deform without any phase transformation. As the loading increases, the forward phase transformation begins over the high stress area of the beam. For example, Fig. 2.36 gives the stress strain relations of integration points in element D and element H with $\xi = 40.7\%$, which also represent the effective behavior of the associated RVEs. Note that Integration Points 5 to 8 in each element are not illustrated considering the symmetry of the structure in the middle plane X = 2.5 mm. It is observed that the hysteresis effects in RVE_{D3} and RVE_{H3} are relatively much more obvious than those in RVE_{D4} and RVE_{H4}, because RVE_{D3} and RVE_{H3} are located in the high stress area. The martensite transformation states of the RVEs with the prescribed displacement in the Y direction reaching 0.5 mm, shown in Fig. 2.37, also give a reasonable confirmation from the RVE level. This figure depicts the RVEs corresponding to these integration points closest to the face Z = 10 mm. Only the RVEs far from the middle plane Y = 2.5 mm have an obvious phase transformation. Simultaneously, the phase transformation at the RVE level is accompanied by the softening of macroscopic stiffness. This softening goes gradually, because the thermomechanical phase transformations at the microscopic level are not synchronous, considering that the stress states of the macroscopic structure are not uniform over the whole beam and that the microscopic structure is architected. Once the unloading begins, the behaviors of the structure and RVEs immediately turn into the linear case. Later, the reverse transformation follows, and finally, all the phases transform back into austenite.

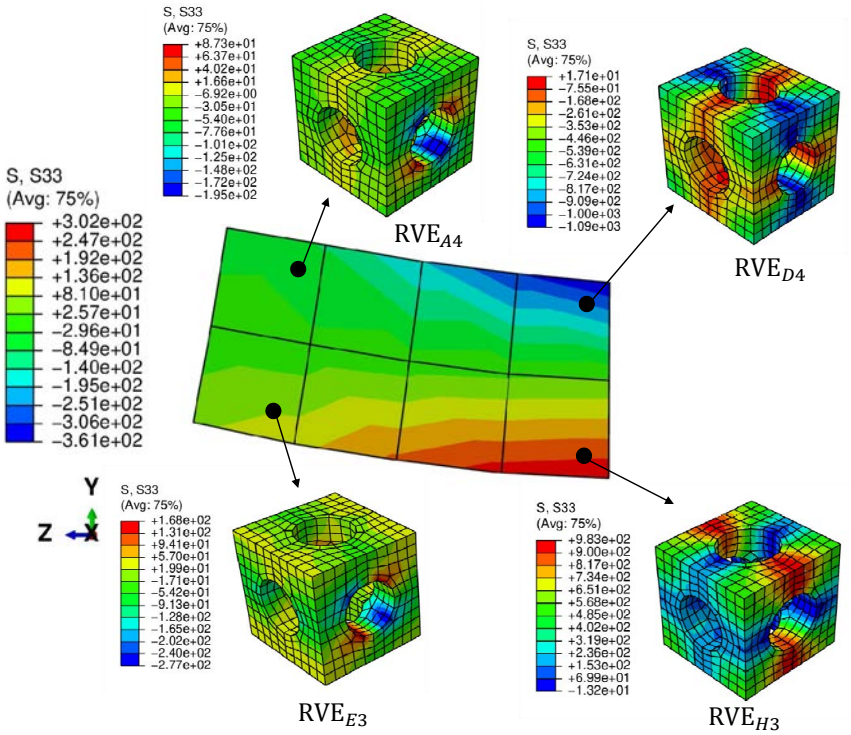

FIGURE 2.34 – The distribution of stress in Z direction (S33) for the macroscopic structure and microscopic structure with $\xi = 40.7\%$, where the deformations of both levels are magnified by three times.

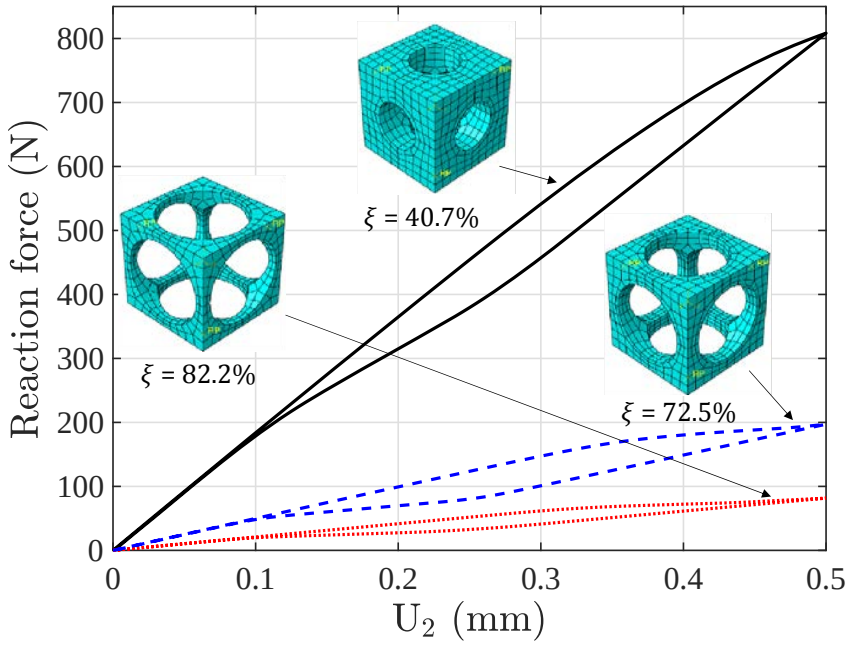

FIGURE 2.35 – Force-displacement curve of the boundary Z = 20 mm, Y = 0 mm on the bending beam.

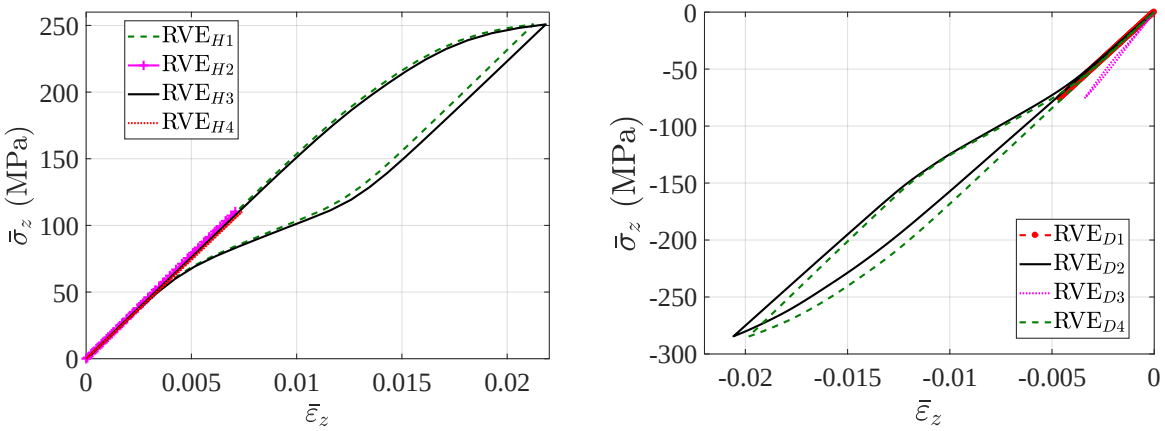

(a) Element H (b) Element D

FIGURE 2.36 – The stress-strain relations on the macroscopic integration points with $\xi = 40.7\%$.

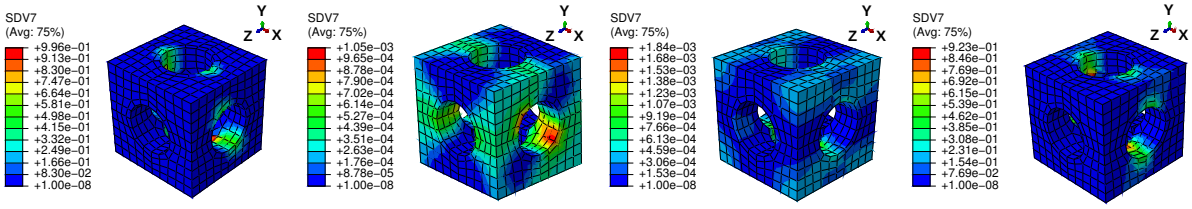

(a) RVE$_{D4}$ (b) RVE$_{D3}$ (c) RVE$_{H4}$ (d) RVE$_{H3}$

FIGURE 2.37 – Distribution of martensitic volume fraction $\bar{f}_t$ (named SDV7 in colorbar) on the RVEs with the prescribed displacement in the Y direction reaching 0.5 mm and $\xi = 40.7\%$.

Structural response with different microscopic structures

The differences between structural responses with three void fractions are observed in Fig. 2.35. With a higher void fraction, the macroscopic structure shows lower stiffness and a weaker hysteresis effect, because the macroscopic behavior is represented by the mean behavior of the microscopic structures. The stress-strain relations of Integration Points *H3* and *D4*, which are also the averaged stress-strain relations of RVE_{H3} and RVE_{D4}, are depicted in Fig. 2.38 to investigate the microscopic response of the structure. Fig. 2.39 gives the stress distributions in the Z direction for associated RVEs at maximum loads corresponding to the displacement of the beam ends $U_2 = 0.5$ mm. It is observed that the averaged stiffness and the hysteresis effect of the RVE with a higher void fraction are lower than those of the RVE with a lower void fraction, which is consistent with the response at the macroscopic level. As we have discussed in Section 2.3.1, the high void fraction results in less SMA, which can provide low stiffness for the structure. For this architected structure, the stresses are concentrated over the pillars along the main loading direction when the void fraction is high. This also results in the martensite phase being mainly concentrated over the pillars.

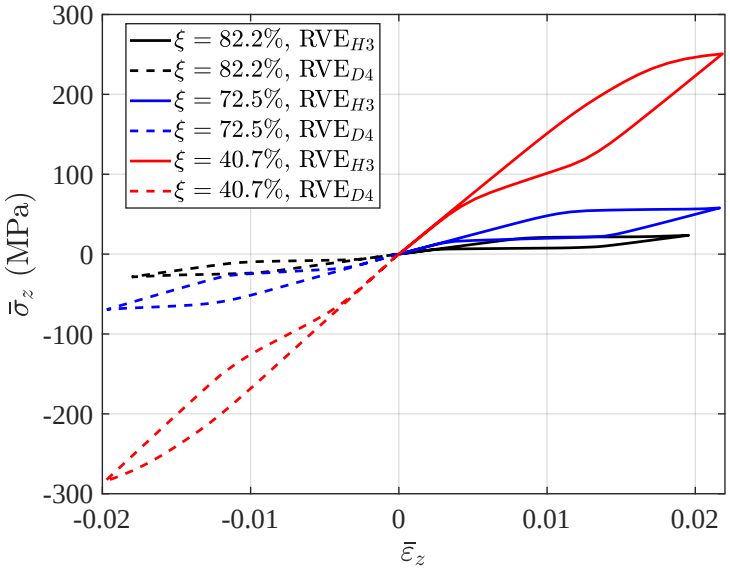

FIGURE 2.38 – The comparison of the stress-strain relations on the macroscopic Integration Points *H3* and *D4* simulated by three kinds of RVEs respectively.

Comments on the computational efficiency

The proposed numerical tool contributes to the design of innovative SMA applications, which can optimize the quantity of material with the required functionalities (actuation, recovery force, damping, energy absorption, etc.), lighten the structure and consider alternative manufacturing processes such as additive manufacturing. The latter can consider more complex geometries of the unit cell, which has a direct influence on the overall behavior of the structure. Note that this numerical multiscale procedure is very time consuming. To reduce the CPU time, the authors propose to associate this method with model reduction techniques. Among these techniques, we can introduce POD technique to build up a small number of basis functions where the solution can be computed (Yvonnet et al. [125]). When this technique is used in an optimization procedure

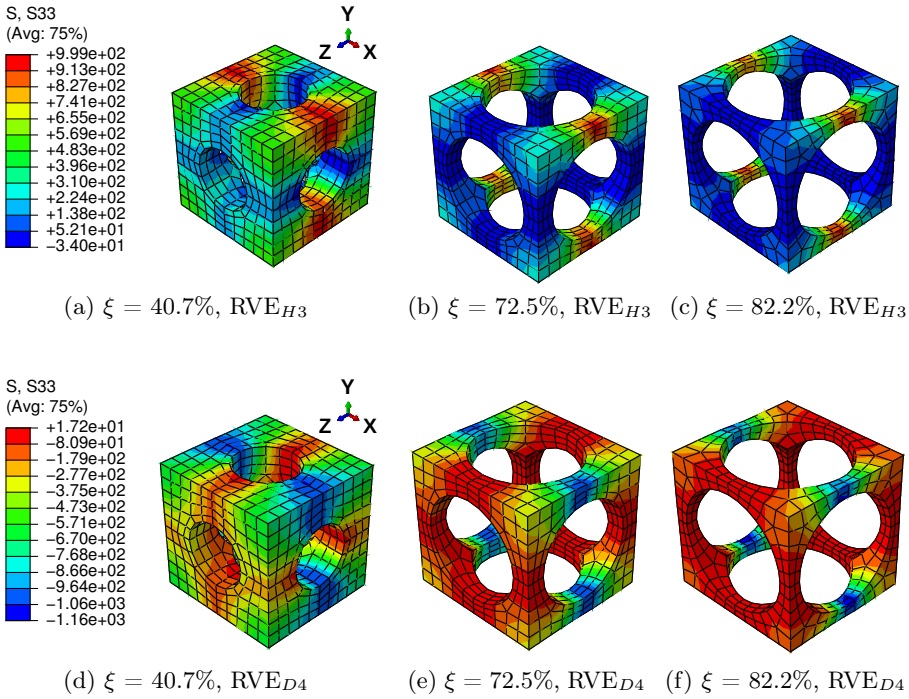

(a) $\xi = 40.7\%$, RVE_{H3} (b) $\xi = 72.5\%$, RVE_{H3} (c) $\xi = 82.2\%$, RVE_{H3}

(d) $\xi = 40.7\%$, RVE_{D4} (e) $\xi = 72.5\%$, RVE_{D4} (f) $\xi = 82.2\%$, RVE_{D4}

FIGURE 2.39 – Distribution of stress in Z direction (S33) on RVE_{H3} and RVE_{D4} of different beams corresponding to the displacement of the beam ends $U_2 = 0.5$ mm.

requiring several repetitive calculations, it can significantly reduce the computation time. We can also consider the proper generalized decomposition (PGD) technique (Ammar et al. [214], Kpogan et al. [215]), which can reduce the dimensionality of the problem to be solved and which is well adapted for unsteady problems, as well as parametric studies. Another technique that has proven its efficiency in solving non-linear problems and that was developed by our group is the ANM (Asymptotic Numerical Method). This technique is based on the development of variables in the form of Taylor series truncated at large order, which allows one to reduce the computation time significantly by reducing the number of computation steps. This technique can be considered as a high order predictor algorithm without the need for any iteration phase. It is particularly suited for strong nonlinearities and for FE^2-structure problems involving instability phenomena (Nezamabadi et al. [124], Assidi et al. [143], Aggoune et al. [216]). In addition, bridging techniques (Hu et al. [212], Yu et al. [213]) can also be considered to combine the advantages of different reduced finite element models. These tools will be associated with the present algorithm to reduce the computation time and to deal with complex structural geometry and complex response curves.

2.4 Conclusion

In this chapter, a 3D generic multiscale finite element procedure is proposed and used to model the PE and SME of SMAs based composite and architected SMAs. For the SMA fiber/epoxy matrix composite, the constitutive model developed by Chemisky et al. [1] is used for modeling the SMA fiber embedded on elastic matrix. The FE^2 method is adopted for building the multiscale analysis of fiber reinforced composite. Then, the responses of the composite structure subjected to tensile and bending load cycles are simulated and discussed. Specifically, simulation for the PE

response of the composite is carried out in this work and validated by comparison with results from literature. Hysteresis effects are observed during the loading-unloading progress, where a part of the external energy is dissipated during the phase transformation in the fibers. Besides, the SME of the composite subjected to thermal and mechanical loading is also presented. The behavior of the SMA fiber could be highly related to internal stress. When the stiffness of the matrix is at a relative high level, the SME could be weak because the internal stress may remove some of the residual strain in SMA fiber during unloading stage. This proposed model could be applied for predicting the response of fiber reinforced composite taking advantage of SMAs' PE and SME. Furthermore, it can also be used for designing other SMA composite structures thanks to the versatility and reliability of its computing platform ABAQUS.

Despite the SMA fiber reinforced composite, the PE of an architected SMA structure is also studied with the multiscale finite element model. Firstly, RVEs with architected SMA are built to simulate the cellular responses of the structure. Both tension and compression loading cycles are applied on the RVEs with different void fractions. The PE responses and the hysteresis effects are observed in the RVEs. The effect of changing the void fraction on the stiffness, the maximum martensitic volume fraction and hysteresis effect are discussed in detail. Moreover, a multiscale approach is carried out to model the structural response, as well as the cellular response. The relations between the structural and cellular responses are studied in a three-point bending test. It is observed that the macroscopic response is related to the phase transformation in the RVE, which changes the effective constitutive behavior of the structure. The stress-strain state of the RVE directly depends on the stress strain state of the associated macroscopic point. Thus, the multiscale model is necessary and successful for simulating the nonlinear behavior of the architected SMA structure. Furthermore, structural responses with different void fractions are studied, which gives a good reference of the void fractions' influences on structural stiffness and hysteresis.

In above works, FE^2 microscopic structures are constructed, such as SMA fiber/epoxy matrix and architected SMA. These structures are prone to instability problems, which are quite complicated and have not been considered in the proposed multiscale model. Besides, the computational efficiency of the proposed multiscale model still requires to be improved as discussed in Section 2.2.2. Thus, it is necessary to formulate efficient approach taking into account instability phenomenon. Work using reduction method to study microscopic fiber instability is presented in the next chapter.

3

Multiscale modeling for the instability of long fiber reinforced composites

Contents

This chapter aims to develop a computationally efficient multiscale model to accurately simulate and analyze the instability phenomena of long fiber reinforced composites. FE^2 method based on the homogenization theory is adopted to realize the real-time interaction between the microscopic and the macroscopic levels. To increase the computational efficiency in the microscopic level and control the nonlinear calculations, the Fourier-related analysis is carried out on the RVEs using the Technique of Slowly Variable Fourier Coefficients (TSVFC), where all fast varying unknowns are replaced by slowly varying unknowns. The established nonlinear multiscale system is solved by the ANM, which is more reliable and less time consuming than other classical iterative methods. This model is used to study the structural instability and the fiber micro-buckling of long fiber reinforced composites. The effects of fiber wavelength on the buckling and post-buckling of macro structure are discussed.

The formulation of the proposed multiscale model is given in Section 3.1. This model is firstly validated by a fully meshed model and then used for simulating the failure of the fiber reinforced composite beam in Section 3.2. The long fiber reinforced composite subjected to compressive load is also simulated with different fiber buckling wavelengths.

3.1 Modeling

3.1.1 Macroscopic scale

Let consider a domain $\Omega \in R^D$ with an external boundary $\partial\Omega$, where D is the dimension of the domain. Domain Ω represents the reference configuration of the macroscopic structure. A periodic multiphase microscopic structure is assumed to describe the heterogeneity of the material, see Fig. 3.1. Large strains are considered and a total Lagrangian formulation is adopted. In order to distinguish the unknowns of the two scales, all the macroscopic values are represented by notation $\bar{(\cdot)}$.

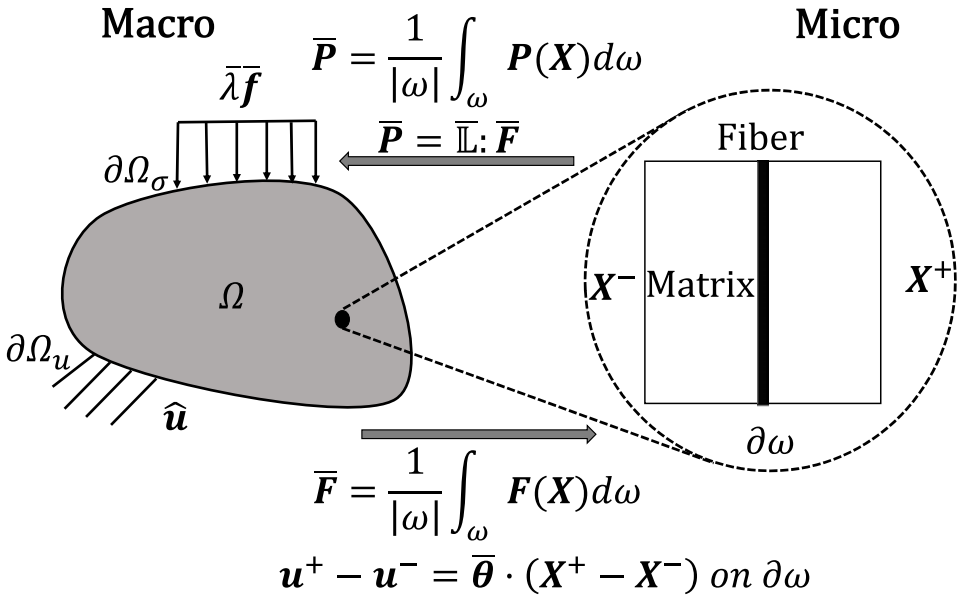

FIGURE 3.1 – Basic concept of multilevel finite element method.

The equilibrium equation neglecting body forces is formulated as :

$$\boldsymbol{\nabla} \cdot \bar{\boldsymbol{P}}(\bar{\boldsymbol{X}}) = 0 \ in \ \Omega, \tag{3.1}$$

where $\bar{\boldsymbol{P}}(\bar{\boldsymbol{X}})$ is the first Piola-Kirchhoff stress tensor at the point $\bar{\boldsymbol{X}}$ in the initial configuration. The virtual work of the macroscopic scale is given by :

$$\int_{\Omega} \bar{\boldsymbol{P}} : \boldsymbol{\nabla}_{\bar{\boldsymbol{X}}} \boldsymbol{\delta}\bar{\boldsymbol{u}} d\Omega = \int_{\Omega} \bar{\boldsymbol{P}} : \boldsymbol{\delta}\bar{\boldsymbol{F}} d\Omega = \bar{\lambda} \int_{\partial\Omega_\sigma} \bar{\boldsymbol{f}} \cdot \boldsymbol{\delta}\bar{\boldsymbol{u}} d\Gamma, \tag{3.2}$$

where $\bar{\boldsymbol{u}} = \bar{\boldsymbol{x}} - \bar{\boldsymbol{X}}$ represents the macroscopic displacement field, and $\bar{\boldsymbol{x}}$ is the coordinates of the points in the current configuration. Prescribed load $\boldsymbol{f}$ is the external force applied on boundary $\partial\Omega_\sigma$ and parameter $\bar{\lambda}$ is the intensity of the prescribed load, with prescribed displacement $\hat{\boldsymbol{u}}$ being given on boundary $\partial\Omega_u$. Macroscopic deformation gradient tensor $\bar{\boldsymbol{F}} = \boldsymbol{\nabla}_{\bar{\boldsymbol{X}}} \bar{\boldsymbol{u}} + \boldsymbol{I}$ is associated with the work-conjugate stress $\bar{\boldsymbol{P}}$, where $\boldsymbol{I}$ is the second-order identify tensor. As the constitutive relationship between $\bar{\boldsymbol{P}}$ and $\bar{\boldsymbol{F}}$ is unknown, $\bar{\boldsymbol{P}}$ is to be transferred from the microscopic scale by solving nonlinear equations at microscopic level using finite element method. Subsequently, the microscopic problem is formulated in the next subsection.

3.1.2 Microscopic scale

Microscopic problem

Assuming the microscopic structure as a periodic RVE with domain ω in R^D and external boundary $\partial\omega$ in its initial configuration. Based on the principles of scale separation, characteristic length of the RVE $||\omega||$ and that of the macroscopic structure $||\Omega||$ should satisfy :

$$||\omega|| \ll ||\Omega|| \tag{3.3}$$

The equilibrium equation is given in absence of body forces as :

$$\boldsymbol{\nabla} \cdot \boldsymbol{P}(\boldsymbol{X}) = 0 \ in \ \omega, \tag{3.4}$$

where $\boldsymbol{P}$ is the first Piola-Kirchhoff stress at microscopic point $\boldsymbol{X}$ in the initial configuration. The strains at each macroscopic integration point are applied on the boundaries of the corresponding RVE with periodic and linear deformation conditions :

$$\boldsymbol{u} = \bar{\boldsymbol{\theta}} \cdot \boldsymbol{X} \quad on \quad \partial\omega, \tag{3.5}$$

$$\boldsymbol{u}^+ - \boldsymbol{u}^- = \bar{\boldsymbol{\theta}} \cdot (\boldsymbol{X}^+ - \boldsymbol{X}^-) \quad on \quad \partial\omega, \tag{3.6}$$

where $\boldsymbol{u}$ is the microscopic displacement and $\bar{\boldsymbol{\theta}} = \boldsymbol{\nabla}_{\bar{\boldsymbol{X}}} \bar{\boldsymbol{u}}$ is the macroscopic displacement gradient. The exponents $+$ and $-$ represent the nodes on the opposite boundaries of a RVE. These two boundary conditions, Eqs. (3.5) and (3.6), satisfy the so-called *averaging theorem*, see Hill [209], which demands that the average of the work decomposes into the product of work-averages (Miehe et al. [156]) :

$$\frac{1}{|\omega|} \int_\omega \boldsymbol{P} : \boldsymbol{F} d\omega - \bar{\boldsymbol{P}} : \bar{\boldsymbol{F}} = 0. \tag{3.7}$$

Following Eqs. (3.5) and (3.6), the deformation gradients between the two levels have relation as :

$$\bar{\boldsymbol{F}} = \frac{1}{|\omega|} \int_\omega \boldsymbol{F}(\boldsymbol{X}) d\omega, \tag{3.8}$$

The constitutive law of each phase in the RVE is given as :

$$\boldsymbol{S}(\boldsymbol{X}) = \mathbb{C}^{(r)} : \boldsymbol{\gamma}(\boldsymbol{X}), \tag{3.9}$$

where $\boldsymbol{S}$ denotes the second Piola-Kirchhoff stress, $\mathbb{C}$ refers to the fourth-order elastic tensor associated with phase (r), and $\boldsymbol{\gamma}$ is Green-Lagrange strain tensor which is expressed as :

$$\boldsymbol{\gamma} = \frac{1}{2}(\boldsymbol{F}^T \cdot \boldsymbol{F} - \boldsymbol{I}). \tag{3.10}$$

It is worth noting that any other constitutive law can be introduced into the RVE.

The relation between $\boldsymbol{S}$ and $\boldsymbol{P}$ is expressed by :

$$\boldsymbol{P} = \boldsymbol{F} \cdot \boldsymbol{S}. \tag{3.11}$$

The formulation of microscopic virtual work is written as :

$$\begin{cases} \displaystyle\int_\omega \boldsymbol{P} : \boldsymbol{\nabla}_{\boldsymbol{X}} \boldsymbol{\delta u} d\omega = \int_\omega \boldsymbol{S} : \boldsymbol{\delta\gamma} d\omega = 0, \\ \boldsymbol{u} = \bar{\boldsymbol{\theta}} \cdot \boldsymbol{X} \quad or \quad \boldsymbol{u}^+ - \boldsymbol{u}^- = \bar{\boldsymbol{\theta}} \cdot (\boldsymbol{X}^+ - \boldsymbol{X}^-) \quad on \quad \partial\omega. \end{cases} \tag{3.12}$$

For a $2D$ case the macroscopic displacement gradient $\bar{\boldsymbol{\theta}}$ is composed of four independent components $\{\bar{\boldsymbol{\theta}}^{11}\ \bar{\boldsymbol{\theta}}^{12}\ \bar{\boldsymbol{\theta}}^{21}\ \bar{\boldsymbol{\theta}}^{22}\}$, which result in the decomposition of Eqs. (3.5) and (3.6) :

$$\boldsymbol{u}^{(ij)} = \bar{\boldsymbol{\theta}}^{(ij)} \cdot \boldsymbol{X}^{(ij)} \quad on \quad \partial\omega, \tag{3.13}$$

$$\boldsymbol{u}^{(ij)+} - \boldsymbol{u}^{(ij)-} = \bar{\boldsymbol{\theta}}^{(ij)} \cdot (\boldsymbol{X}^{(ij)+} - \boldsymbol{X}^{(ij)-}) \quad on \quad \partial\omega, \tag{3.14}$$

where exponents i and j $(i, j = 1, 2)$ denote a set of opposite edges normal to direction i under deformation $\bar{\boldsymbol{\theta}}^{(ij)}$ in direction j.

With the macroscopic strains loaded on the microscopic boundaries, we solve the microscopic problem, then calculate macroscopic stress $\bar{\boldsymbol{P}}$ by :

$$\bar{\boldsymbol{P}} = \frac{1}{|\omega|} \int_{\omega} \boldsymbol{P}(\boldsymbol{X}) d\omega, \tag{3.15}$$

where $|\omega|$ is the volume of the RVE. Subsequently, $\bar{\boldsymbol{P}}$ is transferred into the macroscopic scale to solve the macroscopic problem. Based on above multiscale framework, an efficient microscopic model is introduced in the next subsection.

Fourier-related 2D RVE model

For periodic responses which vary rapidly in one direction, the unknown fields can be expanded in the form of Fourier series whose coefficients vary slowly (Damil and Potier-Ferry [128, 129], Liu et al. [134], Huang et al. [137]) :

$$\boldsymbol{u}(x, y) = \sum_{j=-\infty}^{+\infty} \boldsymbol{u}_j(x, y) e^{\mathrm{i}j(qx+\varphi(x,y))}, \tag{3.16}$$

where (x, y) is the Cartesian coordinates adopted in the $2D$ microscopic structure, i is the imaginary unit, and $\boldsymbol{u}(x, y)$ is the unknown field that is assumed to only vary rapidly in the x direction. To describe the periodic field, the wavenumber in the x direction is defined as $q = \frac{\pi}{l} q_0$, with l being the length of the structure in the x direction and q_0 being a given number of half-waves ($q_0 \in \mathbb{N}$, $q_0 \geq 2$). Fourier coefficient $\boldsymbol{u}_j(x, y)$ denotes the envelope for the j^{th} order harmonic, which varies slowly over period $[x, x + \frac{2\pi}{q}]$.

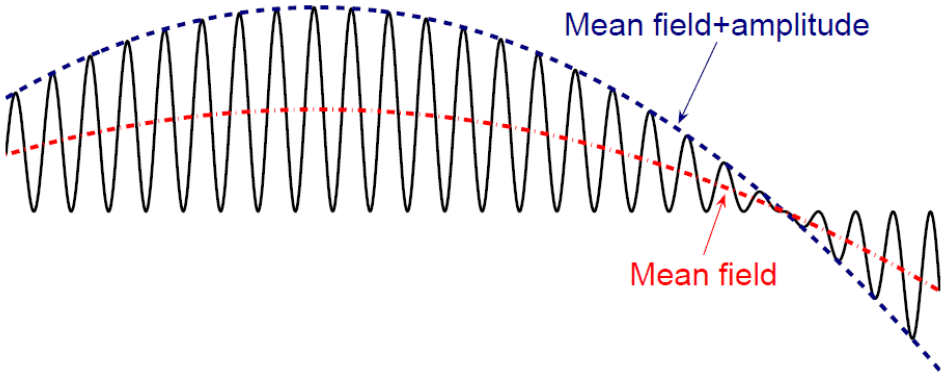

FIGURE 3.2 – The mean field and the amplitude of periodic spacial oscillations.

Assuming the fiber has only one wavelength when it is buckled, we consider three envelops $\boldsymbol{u}_0$, $\boldsymbol{u}_1$ and $\boldsymbol{u}_{-1}$ to formulate the $2D$ RVE model. As pictured in Fig. 3.2, the envelopes of 0^{th}

order harmonic $\boldsymbol{u}_0$ and complex-valued $\boldsymbol{u}_{\pm 1}$ represent the mean value and the amplitude of spatial oscillations respectively. The model with only three envelopes can correctly describe the buckling instabilities in sandwich structures, see Liu et al. [134]. In this chapter, $\boldsymbol{u}_{-1}$ is conjugated with $\boldsymbol{u}_1(\boldsymbol{u}_{-1} = \boldsymbol{u}_1)$. The phase angle $\varphi(x, y)$ describes the phase of spatial oscillations (Mhada et al. [135], Huang et al. [147]). The right side of Eq. (3.16) can be explicitly expressed as :

$$\boldsymbol{u}_j e^{\mathrm{i}j(qx+\varphi(x,y))} = \boldsymbol{u}_j[\cos(j\varphi) + \mathrm{i}\sin(j\varphi)]e^{\mathrm{i}jqx}. \tag{3.17}$$

Because j varies in $[-1, 0, 1]$ in our $2D$ model, we introduce two variables :

$$\boldsymbol{u}_R = \boldsymbol{u}_1 \cos(\varphi), \tag{3.18}$$

$$\boldsymbol{u}_I = \boldsymbol{u}_1 \sin(\varphi). \tag{3.19}$$

Insertion of Eqs. (3.17) to (3.19) in Eq. (3.16) yields :

$$\boldsymbol{u} = \boldsymbol{u}_0 + (\boldsymbol{u}_R + \mathrm{i}\boldsymbol{u}_I)e^{\mathrm{i}qx} + (\boldsymbol{u}_R - \mathrm{i}\boldsymbol{u}_I)e^{-\mathrm{i}qx}. \tag{3.20}$$

Here we define $\boldsymbol{u}_R$ as the real-value part and $\boldsymbol{u}_I$ as the complex-value part of oscillations. Thus, all the unknowns of the displacement field, as in Mhada et al. [135], Huang et al. [147], are represented by $\{\boldsymbol{u}_0\ \boldsymbol{u}_R\ \boldsymbol{u}_I\}$. In this way, the change of the phase angle $\varphi(x, y)$ can be taken into account, which could treat boundary conditions more accurately compared with these assuming the phase as constant (Huang et al. [147]).

Internal virtual work of the microscopic model

For the convenience of introducing the Fourier coefficients into the microscopic model, the tensor form of all the unknowns are replaced by a vector form in the implementation of the internal virtual work. Specifically, the components of tensors are rearranged as follows :

$$\begin{cases} \vec{\boldsymbol{\theta}} = \{\boldsymbol{\theta}^{11}\ \ \boldsymbol{\theta}^{12}\ \ \boldsymbol{\theta}^{21}\ \ \boldsymbol{\theta}^{22}\}^T, \\ \vec{\boldsymbol{\gamma}} = \{\boldsymbol{\gamma}^{11}\ \ \boldsymbol{\gamma}^{22}\ \ 2\boldsymbol{\gamma}^{12}\}^T, \\ \vec{\boldsymbol{S}} = \{\boldsymbol{S}^{11}\ \ \boldsymbol{S}^{22}\ \ \boldsymbol{S}^{12}\}^T. \end{cases}$$

Deriving from Eqs. (3.9) and (3.12), the governing equations of the microscopic structure is expressed as :

$$\begin{cases} \displaystyle\int_w \vec{\boldsymbol{S}}^T \cdot \boldsymbol{\delta}\vec{\boldsymbol{\gamma}} d\omega = 0, \\ \vec{\boldsymbol{\gamma}} = [\boldsymbol{H} + \frac{1}{2}\boldsymbol{A}(\vec{\boldsymbol{\theta}})] \cdot \vec{\boldsymbol{\theta}}, \\ \vec{\boldsymbol{S}} = \mathbb{D}^{(r)} \cdot \vec{\boldsymbol{\gamma}}, \\ \boldsymbol{u}^+ - \boldsymbol{u}^- = \bar{\boldsymbol{\theta}} \cdot (\boldsymbol{X}^+ - \boldsymbol{X}^-) \ \ on \ \ \partial\omega, \\ or \ \ \boldsymbol{u} = \bar{\boldsymbol{\theta}} \cdot \boldsymbol{X} \ \ on \ \ \partial\omega, \end{cases} \tag{3.21}$$

where

$$\boldsymbol{H} = \begin{bmatrix} 1 & 0 & 0 & 0 \\ 0 & 0 & 0 & 1 \\ 0 & 1 & 1 & 0 \end{bmatrix}, \mathbb{D}^{(r)} = \frac{E^{(r)}}{1-\nu^{(r)2}} \begin{bmatrix} 1 & \nu^{(r)} & 0 \\ \nu^{(r)} & 1 & 0 \\ 0 & 0 & \frac{1-\nu^{(r)}}{2} \end{bmatrix},$$

$$\boldsymbol{A}(\vec{\boldsymbol{\theta}}) = \begin{bmatrix} \boldsymbol{\theta}^{11} & 0 & \boldsymbol{\theta}^{21} & 0 \\ 0 & \boldsymbol{\theta}^{12} & 0 & \boldsymbol{\theta}^{22} \\ \boldsymbol{\theta}^{12} & \boldsymbol{\theta}^{11} & \boldsymbol{\theta}^{22} & \boldsymbol{\theta}^{21} \end{bmatrix},$$

where a plane stress constitutive law is considered, $E^{(r)}$ and $\nu^{(r)}$ being the Young's modulus and the Poisson's ratio, respectively. Green-Lagrange strain $\vec{\boldsymbol{\gamma}}$ is related to displacement gradient $\vec{\boldsymbol{\theta}}$ with a nonlinear geometrical relationship, $\boldsymbol{A}(\cdot)$ being a linear operator.

Like displacement $\boldsymbol{u}$, all unknowns $\boldsymbol{\Psi}$ can be expressed as :

$$\boldsymbol{\Psi} = \boldsymbol{\Psi}_0 + (\boldsymbol{\Psi}_R + \mathrm{i}\boldsymbol{\Psi}_I)e^{\mathrm{i}qx} + (\boldsymbol{\Psi}_R - \mathrm{i}\boldsymbol{\Psi}_I)e^{-\mathrm{i}qx}, \tag{3.22}$$

where $\boldsymbol{\Psi}$ is saved in the generalized forms :

$$\begin{aligned}
\boldsymbol{u} &= \{\boldsymbol{u}_0\ \boldsymbol{u}_R\ \boldsymbol{u}_I\}^T,\ \vec{\boldsymbol{\theta}} = \{\vec{\boldsymbol{\theta}}_0\ \vec{\boldsymbol{\theta}}_R\ \vec{\boldsymbol{\theta}}_I\}^T,\\
\vec{\boldsymbol{\gamma}} &= \{\vec{\boldsymbol{\gamma}}_0\ \vec{\boldsymbol{\gamma}}_R\ \vec{\boldsymbol{\gamma}}_I\}^T,\ \vec{\boldsymbol{S}} = \{\vec{\boldsymbol{S}}_0\ \vec{\boldsymbol{S}}_R\ \vec{\boldsymbol{S}}_I\}^T.
\end{aligned}$$

Submitting Eq. (3.22) into Eq. (3.21), the virtual work is expanded as :

$$\begin{aligned}
\int_\omega \boldsymbol{\delta}\vec{\boldsymbol{\gamma}}^{\boldsymbol{T}} \cdot \vec{\boldsymbol{S}} d\omega &= \int_\omega \boldsymbol{\delta}\vec{\boldsymbol{\gamma}}_0^{\boldsymbol{T}} \cdot \vec{\boldsymbol{S}}_0 + 2\boldsymbol{\delta}\vec{\boldsymbol{\gamma}}_R^{\boldsymbol{T}} \cdot \vec{\boldsymbol{S}}_R + 2\boldsymbol{\delta}\vec{\boldsymbol{\gamma}}_I^{\boldsymbol{T}} \cdot \vec{\boldsymbol{S}}_I d\omega,\\
&= \int_\omega \boldsymbol{\delta}\vec{\boldsymbol{\Gamma}}_0^{\boldsymbol{T}} \cdot \vec{\boldsymbol{S}}_0 + \boldsymbol{\delta}\vec{\boldsymbol{\Gamma}}_R^{\boldsymbol{T}} \cdot \vec{\boldsymbol{S}}_R + \boldsymbol{\delta}\vec{\boldsymbol{\Gamma}}_I^{\boldsymbol{T}} \cdot \vec{\boldsymbol{S}}_I d\omega,
\end{aligned} \tag{3.23}$$

where $\vec{\boldsymbol{\Gamma}}$ is defined as a generalized strain :

$$\vec{\boldsymbol{\Gamma}} = \{\vec{\boldsymbol{\gamma}}_0\ 2\vec{\boldsymbol{\gamma}}_R\ 2\vec{\boldsymbol{\gamma}}_I\}^T.$$

As $\boldsymbol{A}(\cdot)$ is a linear operator, we write $\boldsymbol{A}(\vec{\boldsymbol{\theta}})$ in the form of Eq. (3.22) :

$$\boldsymbol{A}(\vec{\boldsymbol{\theta}}) = \boldsymbol{A}(\vec{\boldsymbol{\theta}}_0) + [\boldsymbol{A}(\vec{\boldsymbol{\theta}}_R) + \mathrm{i}\boldsymbol{A}(\vec{\boldsymbol{\theta}}_I)]e^{\mathrm{i}qx} + [\boldsymbol{A}(\vec{\boldsymbol{\theta}}_R) - \mathrm{i}\boldsymbol{A}(\vec{\boldsymbol{\theta}}_I)]e^{-\mathrm{i}qx}. \tag{3.24}$$

Insertion of Eq. (3.24) in Eq. (3.21) deduces strain $\vec{\boldsymbol{\Gamma}}$ in detail :

$$\begin{cases}
\vec{\boldsymbol{\Gamma}}_0 = \boldsymbol{H} \cdot \vec{\boldsymbol{\theta}}_0 + \dfrac{1}{2}\boldsymbol{A}(\vec{\boldsymbol{\theta}}_0) \cdot \vec{\boldsymbol{\theta}}_0 + \boldsymbol{A}(\vec{\boldsymbol{\theta}}_R) \cdot \vec{\boldsymbol{\theta}}_R + \boldsymbol{A}(\vec{\boldsymbol{\theta}}_I) \cdot \vec{\boldsymbol{\theta}}_I,\\
\vec{\boldsymbol{\Gamma}}_R = 2\boldsymbol{H} \cdot \vec{\boldsymbol{\theta}}_R + \boldsymbol{A}(\vec{\boldsymbol{\theta}}_R) \cdot \vec{\boldsymbol{\theta}}_0 + \boldsymbol{A}(\vec{\boldsymbol{\theta}}_0) \cdot \vec{\boldsymbol{\theta}}_R,\\
\vec{\boldsymbol{\Gamma}}_I = 2\boldsymbol{H} \cdot \vec{\boldsymbol{\theta}}_I + \boldsymbol{A}(\vec{\boldsymbol{\theta}}_I) \cdot \vec{\boldsymbol{\theta}}_0 + \boldsymbol{A}(\vec{\boldsymbol{\theta}}_0) \cdot \vec{\boldsymbol{\theta}}_I.
\end{cases}$$

The generalized constitutive law can be deduced as follows :

$$\begin{cases}
\vec{\boldsymbol{S}} = \mathbb{D}_{gen} \cdot \vec{\boldsymbol{\Gamma}},\\
\vec{\boldsymbol{\Gamma}} = [\boldsymbol{H}_{gen} + \dfrac{1}{2}\boldsymbol{A}_{gen}(\vec{\boldsymbol{\theta}})] \cdot \vec{\boldsymbol{\theta}},
\end{cases} \tag{3.25}$$

where

$$\mathbb{D}_{gen} = \begin{pmatrix} \mathbb{D} & 0 & 0 \\ 0 & \mathbb{D}/2 & 0 \\ 0 & 0 & \mathbb{D}/2 \end{pmatrix}, \boldsymbol{H}_{gen} = \begin{pmatrix} \boldsymbol{H} & 0 & 0 \\ 0 & 2\boldsymbol{H} & 0 \\ 0 & 0 & 2\boldsymbol{H} \end{pmatrix}$$

$$\boldsymbol{A}_{gen} = \begin{pmatrix} \boldsymbol{A}(\vec{\boldsymbol{\theta}}_0) & 2\boldsymbol{A}(\vec{\boldsymbol{\theta}}_R) & 2\boldsymbol{A}(\vec{\boldsymbol{\theta}}_I) \\ 2\boldsymbol{A}(\vec{\boldsymbol{\theta}}_R) & 2\boldsymbol{A}(\vec{\boldsymbol{\theta}}_0) & 0 \\ 2\boldsymbol{A}(\vec{\boldsymbol{\theta}}_I) & 0 & 2\boldsymbol{A}(\vec{\boldsymbol{\theta}}_0) \end{pmatrix}.$$

It is easy to obtain displacements $\{\boldsymbol{u}_0\ \boldsymbol{u}_R\ \boldsymbol{u}_I\}$ over the whole RVE by interpolating the values at nodes. Then, the real displacement field can be calculated by inserting the Euler's formula to Eq. (3.20) :

$$\boldsymbol{u} = \boldsymbol{u}_0 + 2\boldsymbol{u}_R \cos(qx) - 2\boldsymbol{u}_I \sin(qx). \tag{3.26}$$

The first Piola-Kirchhoff stress tensor $\boldsymbol{P}$ can also be calculated by :

$$\boldsymbol{P} = \boldsymbol{P}_0 + 2\boldsymbol{P}_R \cos(qx) - 2\boldsymbol{P}_I \sin(qx). \tag{3.27}$$

where

$$\begin{cases} \boldsymbol{P}_0 = \boldsymbol{F}_0 \cdot \boldsymbol{S}_0 + 2\boldsymbol{F}_R \cdot \boldsymbol{S}_R + 2\boldsymbol{F}_I \cdot \boldsymbol{S}_I, \\ \boldsymbol{P}_R = \boldsymbol{F}_0 \cdot \boldsymbol{S}_R + \boldsymbol{F}_R \cdot \boldsymbol{S}_0, \\ \boldsymbol{P}_I = \boldsymbol{F}_0 \cdot \boldsymbol{S}_I + \boldsymbol{F}_I \cdot \boldsymbol{S}_0. \end{cases}$$

3.1.3 Formulation of the ANM

Many papers (Zahrouni et al. [140], Abichou et al. [142], Tri et al. [144], Choe et al. [146], Huang et al. [147]) show that the ANM has high efficiency in strong nonlinear problems compared with classical interactive procedures, such as Newton-Raphson method. Details on the use of the ANM for the resolution of non linear problems are given in chapter 5. By expanding unknowns $\boldsymbol{\Psi}$ and load parameter $\bar{\lambda}$ into power series with respect to a path parameter a, a nonlinear system can be transferred into a series of linear problems :

$$\left\{ \begin{array}{c} \boldsymbol{\Psi}(a) \\ \bar{\lambda}(a) \end{array} \right\} = \left\{ \begin{array}{c} \boldsymbol{\Psi}_0 \\ \bar{\lambda}_0 \end{array} \right\} + \sum_{p=1}^{N} a^p \left\{ \begin{array}{c} \boldsymbol{\Psi}_p \\ \bar{\lambda}_p \end{array} \right\}, \ p \in [1, N] \tag{3.28}$$

where $(\cdot)(a)$ refers to the quantities defined continuously with respect to path parameter a, $(\cdot)_0$ denotes an initial solution such that $(\cdot)_0 = (\cdot)(0)$, N is the truncation order of power series, and $(\cdot)_p$ indicates a term to be determined at order p. According to the principle of the validity range of power series in Cochelin [138], the maximal value of the path parameter a is defined automatically :

$$a_{max} = \left(\epsilon \frac{\| \boldsymbol{\Psi}_1 \|}{\| \boldsymbol{\Psi}_N \|} \right)^{\frac{1}{N-1}}, \tag{3.29}$$

where ϵ is a given accuracy parameter and $\| \cdot \|$ refers to the norm of variables. More details of the ANM can be consulted in Nezamabadi et al. [124], Cochelin [138], Cadou et al. [141]. Within the ANM framework, the virtual work of the macroscopic level is expanded as :

$$\int_{\Omega} \bar{\boldsymbol{F}}_p : \bar{\mathbb{L}} : \boldsymbol{\delta}\bar{\boldsymbol{F}} d\Omega = \bar{\lambda}_p \int_{\Omega_\sigma} \bar{\boldsymbol{f}} \cdot \boldsymbol{\delta}\bar{\boldsymbol{u}} d\Gamma - \int_{\Omega} \bar{\boldsymbol{P}}_p^{nl} : \boldsymbol{\delta}\bar{\boldsymbol{F}} d\Omega. \tag{3.30}$$

where the macroscopic constitutive law $\bar{\mathbb{L}}$ and the nonlinear force $\bar{\boldsymbol{P}}_p^{nl}$ are computed by averaging on the microscopic structure. The microscopic problem is expanded as follows :

$$\begin{cases} \mathcal{L}(\boldsymbol{u}_p, \boldsymbol{\delta u}) = \mathcal{F}_p^{nl}(\boldsymbol{\delta u}), \\ \boldsymbol{u}_p = \bar{\boldsymbol{F}}_p \cdot \boldsymbol{X} \quad or \quad \boldsymbol{u}_p^+ - \boldsymbol{u}_p^- = \bar{\boldsymbol{F}}_p \cdot (\boldsymbol{X}^+ - \boldsymbol{X}^-) \quad on \quad \partial\omega. \end{cases} \tag{3.31}$$

where the linear boundary conditions are applied on the corners of boundary $\partial\omega$ and the periodic conditions are applied on the remaining nodes. One can refer to Nezamabadi et al. [124] for the detailed formulation of operator $\mathcal{L}$, nonlinear forces $\mathcal{F}_p^{nl}$, $\bar{\boldsymbol{P}}_p^{nl}$ and macroscopic constitutive law $\bar{\mathbb{L}}$.

3.2 Numerical results

The proposed multiscale Fourier-series based model is firstly validated by comparison with a fully meshed model on ABAQUS. Then, this approach is used to examine different failure modes of long fiber reinforced composites.

TABLE 3.1 – Material parameters for matrix and fiber.

E_m (MPa)	E_f (MPa)	ν_m	ν_f
100	100000	0.3	0.3

3.2.1 Validation for the multiscale model

A fiber reinforced composite plate subjected to compressive loads is examined, see Fig. 3.3a. A displacement $\bar{\lambda}\hat{\boldsymbol{u}}$ is applied on the top edge of the plate along the fiber's length direction. The left and the right edges are fixed in the horizontal direction, while the bottom edge is fixed in the vertical direction.

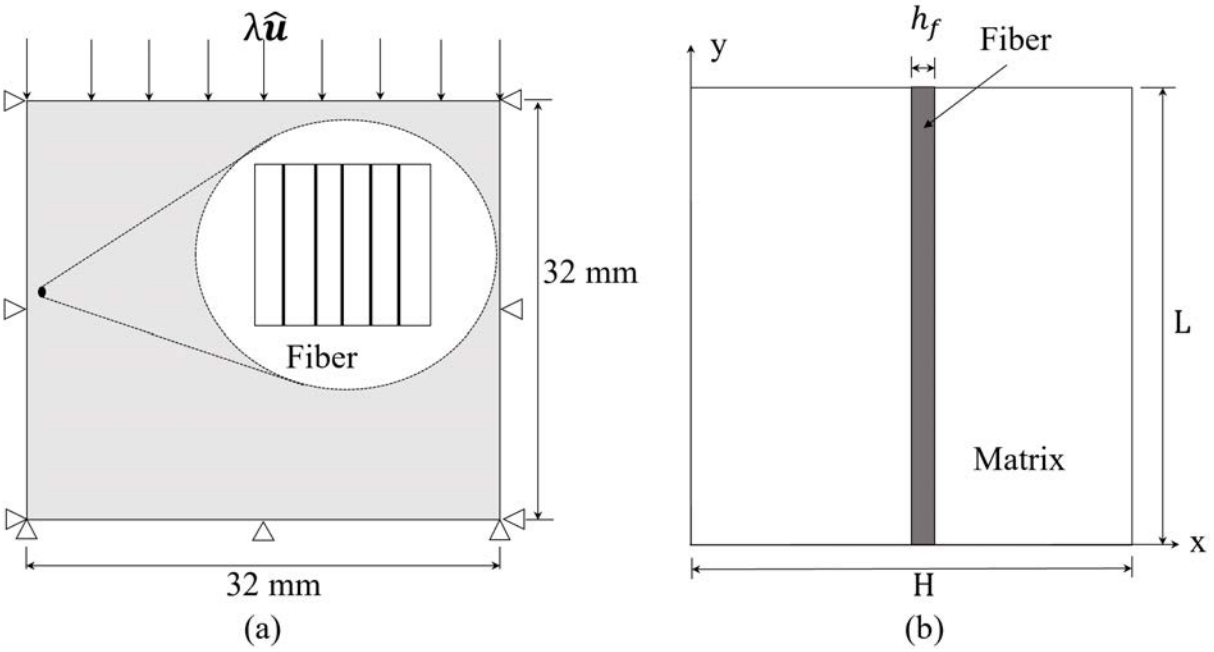

FIGURE 3.3 – (a) the fiber reinforced composite plate subjected to compressive displacement load ; (b) Elementary cell of fiber reinforced material, H = L = 1 mm, h_f/L = 1/20.

In order to specify the details of the microscopic structure, an elementary cell is introduced to construct different kinds of RVEs, see Fig. 3.3b. This cell is assumed as a sandwich structure composed of a stiff fiber perfectly bonded with a soft matrix. By the linear pattern of the elementary cell, different types of RVEs with the same fiber volume fraction can be defined as RVE_{mn}, where m, n are the quantities of elementary cells in the horizontal and the vertical directions, respectively. In this example, the volume fraction of the fiber is 1/20. Both the fiber and the matrix are assumed isotropic and linear elastic. Their detailed material properties are given in Table 3.1.

The microscopic fiber buckling is simulated in comparison with the multiscale model and a fully meshed ABAQUS model respectively. For the multiscale model, the displacement fields along the fiber's length direction y are expanded by Fourier series since they vary very fast in this direction. To set a specific wavelength of the microscopic fiber, the microscopic structure is represented by RVE_{14} with half-wave number $q_0 = 2$. A small transversal perturbation force $f = 1$

N is applied on the middle of the fiber in order to trigger the fiber buckling. Further, to specify an asymmetric buckling mode (the shear buckling mode, see Rosen [217], Parnes and Chiskis [218]), the phase angle $\varphi(x, y)$ is set by locking real-value part of the microscopic displacement in the x direction $\boldsymbol{u}_{x,R}$ and the complex-value part of the microscopic displacement in the y direction $\boldsymbol{u}_{y,I}$. The RVE is meshed with 2 elements along the vertical direction and 3 elements along the horizontal direction based on 8-node quadrilateral elements and Gauss-Legendre quadrature with 9 integration points per element. The macroscopic structure is meshed with 10 elements along its length and width respectively, based on the same quadrilateral elements as the RVE. This multiscale model is solved by the ANM with the accuracy parameter $\epsilon = 10^{-6}$ and the truncation order of power series $N = 15$.

The fully meshed ABAQUS model with 32 RVE_{14} along the horizontal and 8 RVE_{14} along the vertical direction is developed by the linear pattern function on ABAQUS. Note for a practice fiber composite structure, the dimension of the fully meshed macroscopic structure should be much greater than that of the RVE. However, limited to the computational resources, herein a fully meshed model is constructed within the same dimension as that of the RVE. Nevertheless, this model is sufficient to be a reference for validation. Its RVE is meshed with 12 elements along its width and 40 elements along its length based on 4-node bilinear plane stress quadrilateral reduced integration elements. A total number of $32 \times 8 \times 12 \times 40$ elements are used in this fully meshed model. Before the compression test, a buckling analysis (Eigenvalue analysis) has to be carried out in order to obtain the specific mode with the same wavelength as that of the multiscale model. This analysis is solved with Static General Step on ABAQUS by Newton-Raphson method.

Fig. 3.4 gives the buckling mode of the fibers in the fully meshed model. As we can see, although the displacements of fibers near boundaries are somehow more constrained than those of the middle area of the plate, all the fibers present same wavelength and buckling mode. Namely, the stresses in all the fibers have the same distribution when the microscopic fiber buckling is triggered. Thus, the boundary effect could be neglected if we focus on the buckling problem at this moment.

Fig. 3.5 gives the compressive stress, along the fiber's length direction, distribution over the middle area of the plate when fiber buckling occurs. Fig. 3.5a and Fig. 3.5b are simulated by the fully meshed model and the multiscale model respectively, which shows good agreement. The bifurcation curves of the fibers' maximal transversal displacement over the middle area of the plate are given in Fig. 3.6. These two models still show good agreement when fibers are buckled. The differences of their initial imperfections induce the gap between these two curves. The smaller imperfection results in the sharper bifurcation curve. The imperfection given in the ABAQUS model to trigger the post-buckling has been minimized. However, the proposed model can use a smaller imperfection than that of the model in ABAQUS. This means our model is less sensitive to the initial imperfection than the ABAQUS model. The averaged critical compressive stress over the RVE is 40 MPa, which could be validated by the fiber buckling stress 40.5 MPa obtained according to Rosen's analytical model (Rosen [217]). Both the proposed model and Rosen's model assume that the matrix is still elastic when fibers are buckled. Rosen's model has been validated by some experimental results considering boron fiber-metal matrix composites (Schuerch [219]).

This model has not only a good accuracy but also the ability to capture the fibers' instability modes. In the next subsection, the influence of different micro instability modes to the composite plate will be examined with our proposed multiscale model.

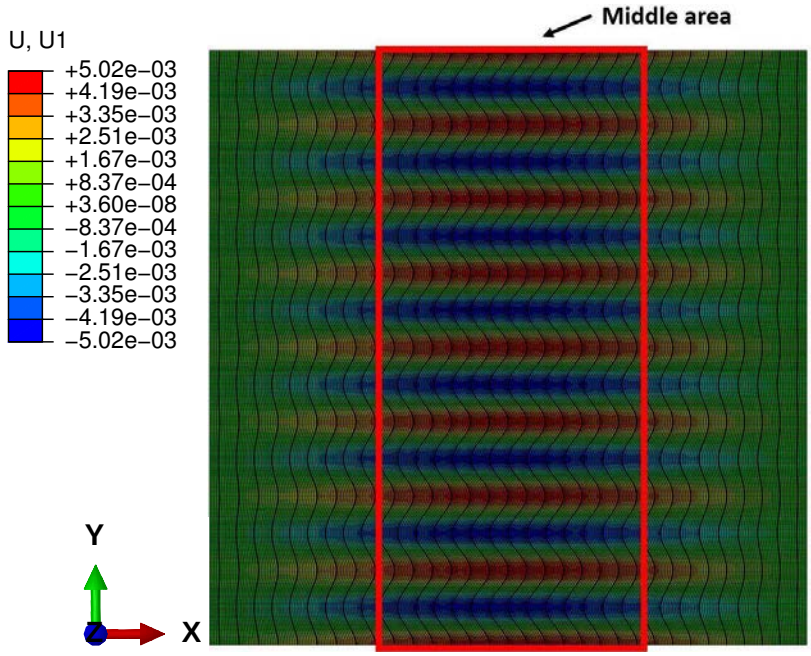

FIGURE 3.4 – The transversal displacement (mm) distribution of the fully meshed model, deformation scale=100.

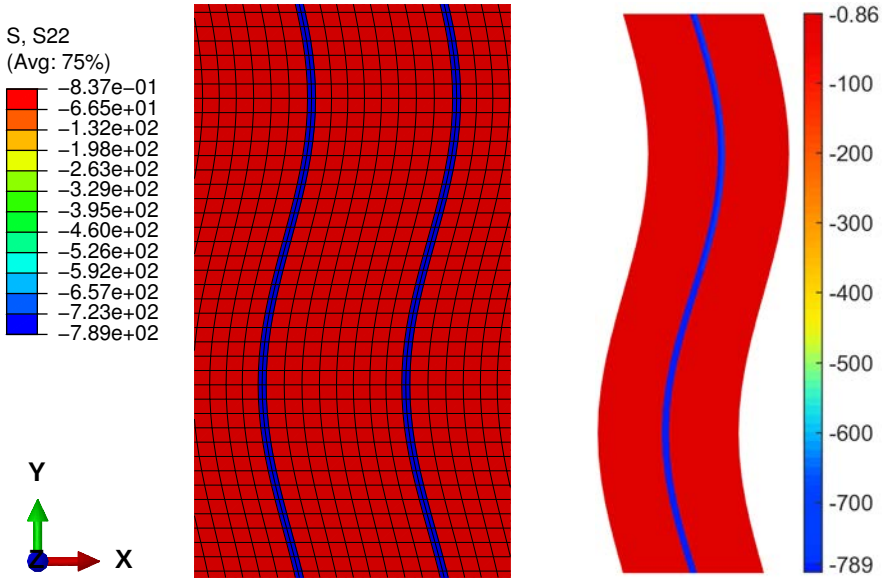

(a) A zoom on fully meshed model

(b) A RVE of multiscale model

FIGURE 3.5 – The compressive second Piola-Kirchhoff stress (MPa), along the fiber's length direction, distribution in the middle area of the composite simulated by the fully meshed model and the multiscale model respectively.

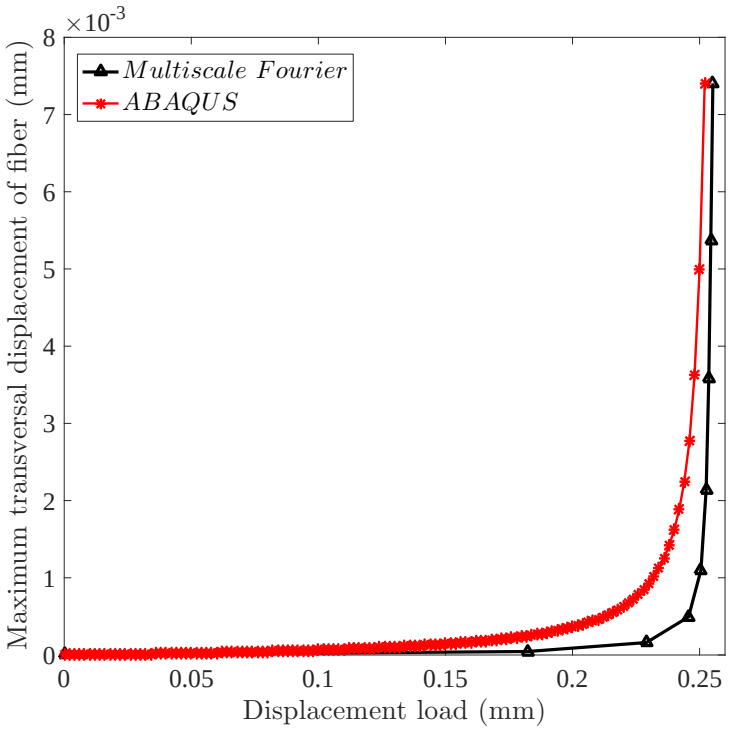

FIGURE 3.6 – The maximum transversal displacement of the fibers versus the applied load, simulated by fully meshed model and the multiscale model respectively.

3.2.2 Microscopic instability modes

To identify the instability modes of the fiber, different fiber wavelengths are given by two different ways : 1) give different half-wave number q_0 while keeping the RVE size unchanged ; 2) give a certain half-wave number q_0 while increasing the vertical length of the RVE. All other parameters remain the same as those in the last section.

Figs. 3.7 and 3.8 give the bifurcation curves of the fibers over the middle area of the plate with different instability modes respectively. It is observed that the maximal transversal displacement of fiber increases as the RVE length n increases and the half-wave number q_0 decreases, however, the critical fiber buckling stress remains unchanged. This critical compressive stress is consistent with the minimal critical stress proposed by Rosen's model (Rosen [217], Damil et al. [220]) and the numerical results obtained by Nezamabadi et al. [98, 124], where the compressive failure of the composite is mainly related to the shear strength of the composite. It is worth noting that the minimal critical stress, proposed in Rosen [217], Damil et al. [220], is obtained by the analytical model with the simplified assumption that the critical stress is dependent on the fiber's wavelengths. However, our fine-meshed numerical model shows that the critical stress of the composite is not related to the wavelength of the fiber and the fiber buckling always occurs at the minimal buckling stress.

Besides above modes, the tension buckling mode (Rosen [217]) with symmetric buckled fibers is also examined. The 1^{th} order displacements in x direction of edges $x = 0$ mm and $x = 1$ mm are fixed in RVEs as the additive symmetric conditions. In this case, the matrix is assumed to undergo tension or compression in the direction vertical to fibers. The fiber shall be more constrained in its vertical direction by the matrix than in the shear case. Fig. 3.9 shows the stress distribution in the RVE over the middle area of the plate with symmetric buckling conditions. The fiber's

compressive stress in the fiber's length direction increases slightly from 789 MPa (shear buckling mode) to 800 MPa. This means the tension buckling mode requires higher stress level because the fiber is more constrained by the matrix than that of the asymmetric mode. According to Fig. 3.9, no fiber buckling but a global shearing of the whole RVE is observed when the failure of the plate happens. It means that the RVE is more likely to have a global shearing even with the additive symmetric conditions, because the initial defects inside ruin the absolute symmetry of the RVE. One fact is found out : as long as the symmetry condition is not completely satisfied, the composite plate will have a shear deformation even if it is subjected to pure compressive loads. This fact coincides with the reports in Parnes and Chiskis [218] that the tension buckling mode is a spurious mode and that buckling of a composite always occurs in the shear buckling mode for a dilute composite.

In summary, all these possible modes lead to a common phenomenon that the compressive failure of the composite plate is more likely to evolve from the shearing of its components. Nevertheless, as it is depicted in the above figures, the microscopic displacement fields of the above modes are different to each other even though their critical buckling loads are almost the same. It implies that the post-buckling of fiber reinforced composites may be related to the fiber wavelength, which is therefore discussed in subsequent subsections.

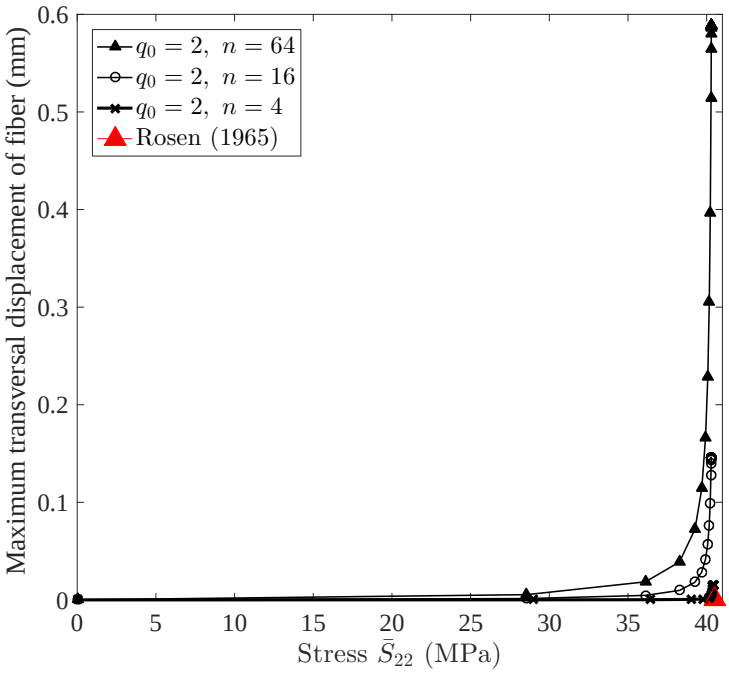

FIGURE 3.7 – The bifurcation curves of the fiber with three different RVE length n.

3.2.3 Computation efficiency

In previous subsections, a fully meshed model is used as a reference for validation. However, for a realistic fiber reinforced composite, there are so many fibers in the microscopic scale that the composite is impossible to be fully meshed directly for simulation. Thus, the computational efficiency of the multiscale Fourier model is discussed only by comparing with a FE^2 scheme with fine-meshed RVE. It is worth noting that the macroscopic stress fields are not uniform, which results in the various strain states of RVEs. Thus, only by adopting this multiscale model with the

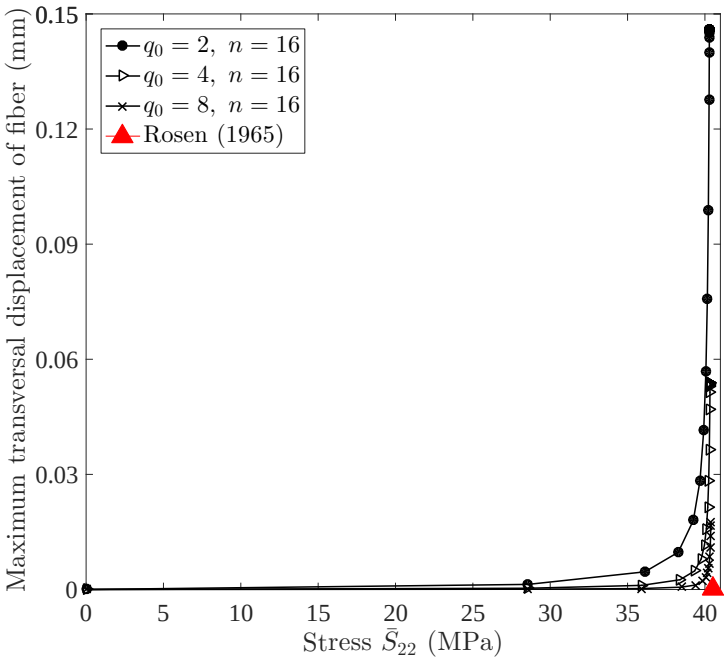

FIGURE 3.8 – The bifurcation curves of the fiber with three different half-wave number q_0.

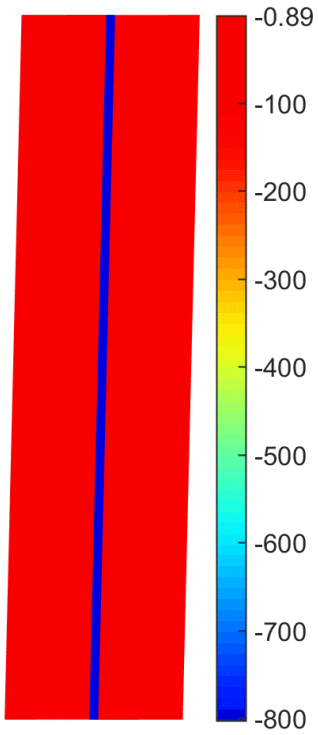

FIGURE 3.9 – The compressive stress (MPa), along the fiber's length direction, distribution in the RVE with a global shearing mode when the failure of composite begins.

real-time scale transition technique and fine-meshed microscopic RVE, the fiber instability can be described in detail. However, it makes the multiscale approach very time consuming. To avoid this shortcoming, a Fourier slowly varying coefficient based microscopic model meshed by only a few elements is adopted in our proposed approach, which saves many computing resources in comparison with a fine-meshed RVE. The computational efficiency of the proposed model shows obvious advantages especially in the case of RVEs with a large half-wave number. The differences of the computational efficiency between two multiscale models could be estimated by RVEs' total DOFs according to van Tuijl et al. [126]. For example, in the case of $m = 1$, $n = 16$, $q_0 = 8$, our proposed microscopic model uses about total 150 DOFs, while the fine-meshed RVE model needs about 4000 DOFs. Therefore, the computation cost could be reduced more than an order of magnitude. Considering the microscopic fiber buckling mode with more waves, the proposed model does not need more DOFs, while the fine-meshed RVEs will require much more DOFs. Moreover, the Fourier-related microscopic model can introduce a defect for a given wavelength without initial geometrical imperfections but a small perturbation force, which could reduce the work on geometrical modeling. The high efficiency of the Fourier model has also been discussed in instabilities of sandwich structures (Huang et al. [132], Liu et al. [134]).

3.2.4 Macro-micro coupled instabilities

In previous subsections, the compressive failure of microscopic fibers and its influence on a stable macroscopic structure are focused. While in this subsection, a more complicated case is examined considering both the macroscopic and microscopic instabilities simultaneously.

Let us consider a composite beam with fibers arranged along the beam's length direction, see Fig. 3.10. The left and right edges are fixed in the vertical direction and subjected to a compressive displacement load $\bar{\lambda}\hat{\boldsymbol{u}}$ in the horizontal direction. The beam is meshed with 4 elements along its width and 20 elements along its length direction based on 8-node quadrilateral elements and Gauss-Legendre quadrature with 9 integration points per element. The RVE is depicted with RVE_{mn} where a small transversal perturbation force $f = 1$ N is applied on the middle of the fiber. Here, three types of RVEs are used : 1) $m = 1$, $n = 4$, $q_0 = 2$, asymmetric boundary ; 2) $m = 1$, $n = 16$, $q_0 = 8$, asymmetric boundary ; 3) $m = 1$, $n = 4$, $q_0 = 2$, symmetric boundary.

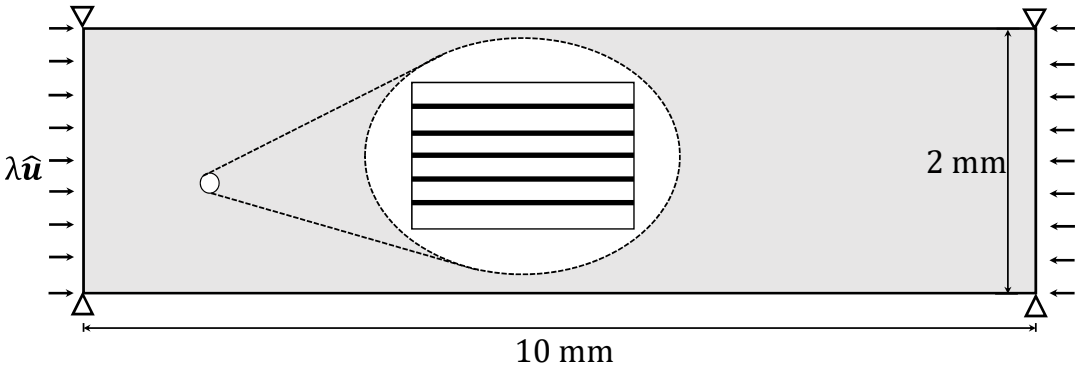

FIGURE 3.10 – The fiber reinforced beam subjected to compressive displacement load.

Fig. 3.11 gives the transversal displacement distribution of the macroscopic structure under two levels of loads. The beam subjected to compressive loads on its ends is buckled in its transversal direction. For a better knowledge of this failure, the transversal displacement of point A, as specified in Fig. 3.11, is depicted in Fig. 3.12. Thanks to the nonlinear solver ANM, a set

of points where instabilities occur are captured, as denoted in Fig. 3.12. These failure points could be separated into two groups : 1) Points A1, A2 and B corresponding to the first global failure shown in Fig. 3.11a ; 2) Points C and D corresponding to the second local failure shown in Fig. 3.11b. For a better understanding of these two failure steps, the compressive stress, along the fiber's length direction, distributions of RVEs around point A are illustrated in Fig. 3.13. For the first group, all the fibers remain straight and their maximum absolute compressive stresses are between 600–700 MPa. At these states, the stresses are not large enough to trigger the fiber buckling. However, the initial defects in RVEs are strong enough to trigger the macroscopic structural failure, since this macroscopic structure is not fully stable. Thus, the first global failure originates from the macroscopic instability and the initial microscopic defects. For the second group, point C and D, buckled fibers are observed with a relatively high compressive stress level. The fiber buckling in the area around point A causes the local instability in this area.

With a general knowledge of this failure response, these different RVEs are discussed in detail. For RVE types 1 and 2, as the red and blue curves depicted in Fig. 3.12, the first global structural failure is independent of the fiber wavelength and the RVE size. However, as we have mentioned in Section 3.2.2, the post-buckling may differ with wavelength or RVE size. The second microscopic instabilities corresponding to point C and D verify our assumption. For RVE type 3, its boundary is constrained with an additive symmetric condition, which has been introduced in previous subsections. Its global failure load is higher than that of the case with asymmetric conditions. Besides, since the first global instability brings the whole structure into a bending strain state, the microscopic symmetric failure is no longer possible. Thus, we cannot observe its fiber buckling mode in the post-buckling process.

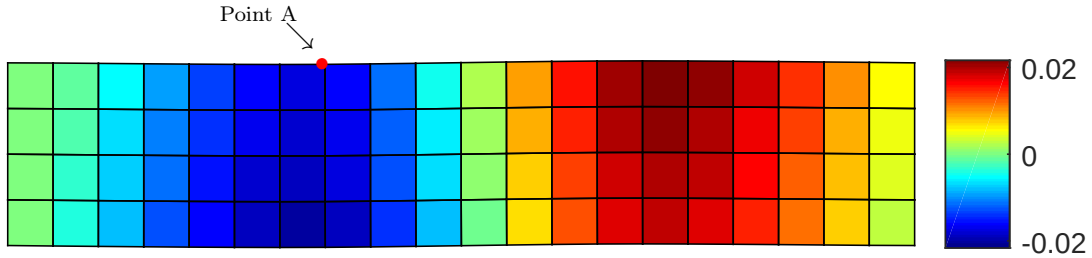

(a) The first global failure related to macroscopic structural instability.

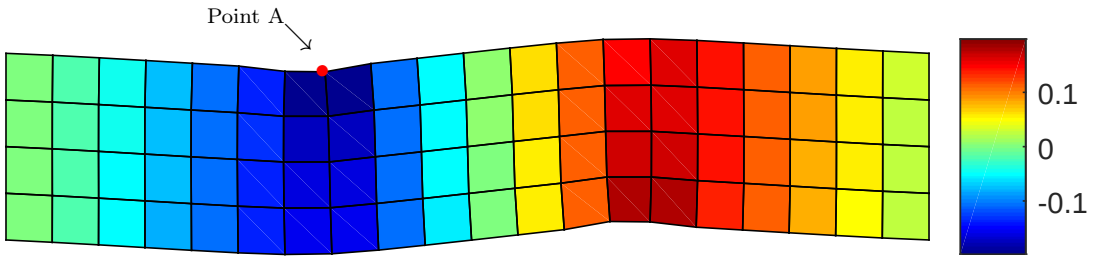

(b) The second local failure related to microscopic fiber buckling.

FIGURE 3.11 – The transversal displacement distribution of the macroscopic structure corresponding to two failure steps.

General speaking, this example shows how the real-time interaction between the microscopic fiber and macroscopic structure proceeds. Also, as what it implies in Section 3.2.2, different fiber buckling modes do affect the failure of the composite.

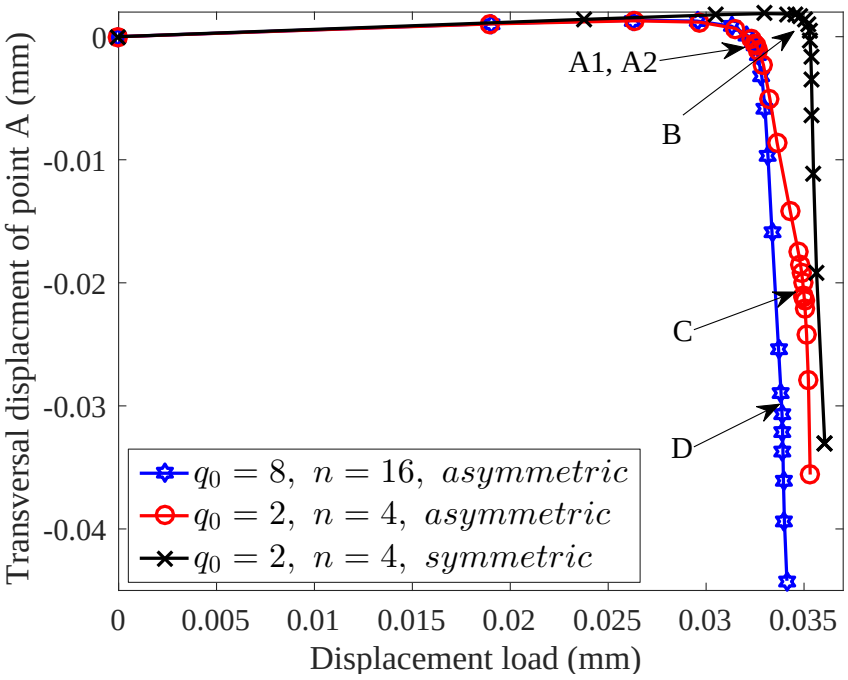

FIGURE 3.12 – The transversal displacement of point A versus the displacement load with three kinds of RVEs.

3.3 Conclusion

This chapter presents a multiscale approach with an efficient microscopic model for simulating fiber reinforced composites. This approach is developed in the framework of the FE^2 method which considers the composite as a homogenized material. The microscopic structures are simulated by the proposed reduced model where all unknowns are expanded with Fourier slowly varying coefficients. This microscopic model can identify the fibers' instability modes precisely and predict the compressive failure of composites accurately. Moreover, the ANM is adopted as the solver to efficiently and accurately predict the nonlinear path.

This multiscale approach is validated firstly by a fully meshed model simulated on ABAQUS. A fiber reinforced composite plate subjected to the pure compressive load is carried out respectively by these two models. The results show that the fibers' stress distributions simulated by these two models are very close when fiber buckling occurs. The critical fiber buckling load is consistent with the analytical solution by Rosen [217] and the numerical solution by Nezamabadi et al. [98]. It is worth to note that this critical stress is independent on the fiber buckling wavelengths for the studied fiber volume fraction, but on the shear strength of the composite. Moreover, taking advantage of the microscopic model, the DOFs in the RVE are reduced more than an order of magnitude compared with that of a fine mesh RVE. After, an unstable composite beam subjected to compressive load is studied by the proposed model. Here, the interaction of the microscopic fiber and macroscopic structure is observed. Specifically, a first global macroscopic failure arises from the unstable composite structure while a second local macroscopic failure originates from the microscopic fiber buckling. These failures are coupled together and could be affected by the microscopic fiber buckling conditions.

Although a reduced RVE model is developed to improve the overall computational efficiency of the multiscale modeling approach, the computational cost is still high in this concurrent fra-

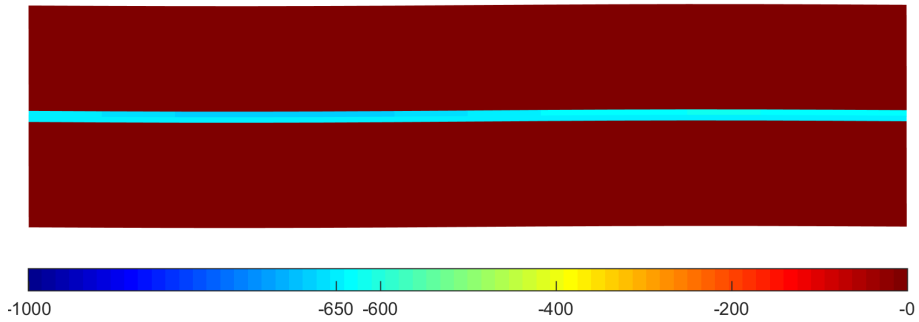

(a) State A1

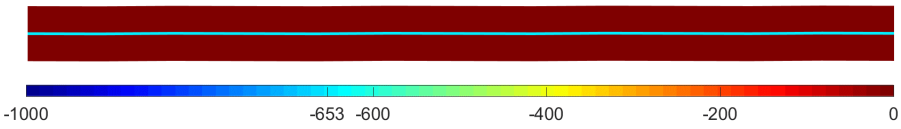

(b) State A2

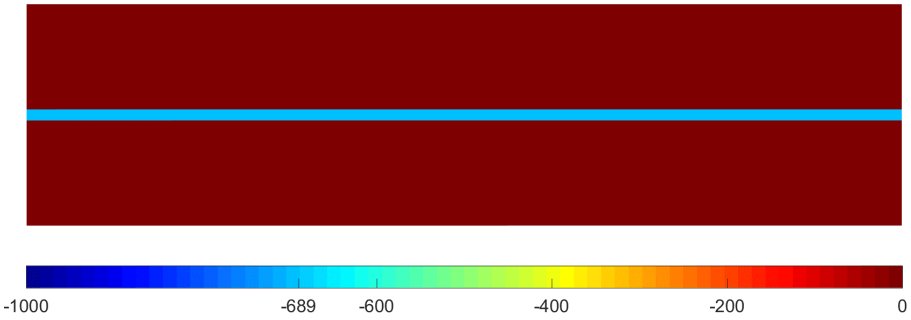

(c) State B

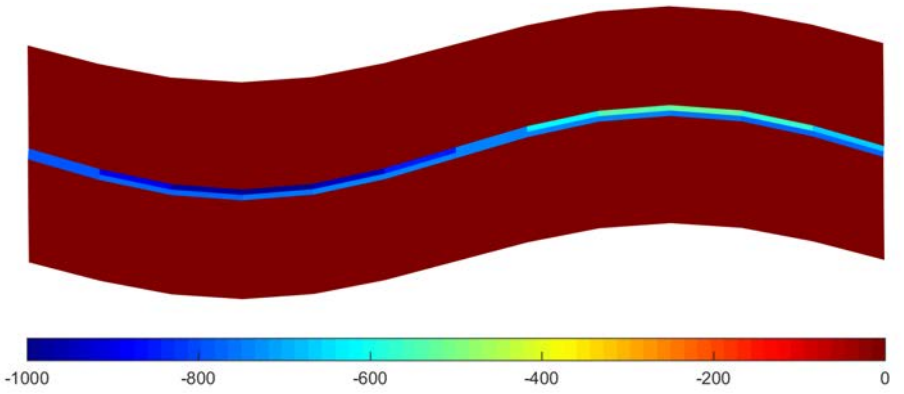

(d) State C

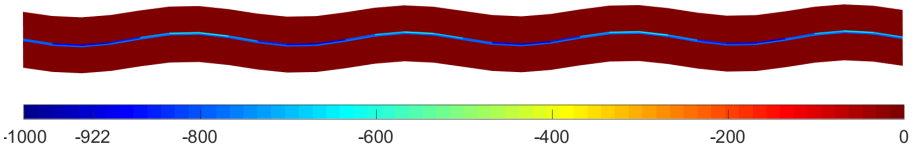

(e) State D

FIGURE 3.13 – The compressive stress (MPa), along the fiber's length direction, distributions in RVEs corresponding to different states.

mework, in which tremendous microscopic problems are solved online to update the macroscopic stress and constitutive information. In the next chapter, inspired by data-driven computing, novel approaches which decouple scales are proposed to improve the online computational efficiency significantly.

4

Data-driven multiscale modeling methods

Contents

This chapter aims to develop novel efficient data-driven multiscale computing approaches, named data-driven FE^2 and Structural-Genome-Driven (SGD) computing for composite structures. In the data-driven FE^2 method, the correlated scales in the classical FE^2 method are here split to be computed sequentially and separately : the microscopic problems are calculated in advance to construct an offline material genome database, which is later used in the macroscopic data-driven analysis. In this new framework, the difficulties in formulating and solving complicated multiscale system are avoided by dealing with single scale problems. Moreover, the online computation of microscopic problems in classical FE^2 method is replaced by searching data points over the offline database resulting in a data-driven FE^2 method. Thus, the online computing efficiency of structural analysis is significantly improved. After that, SGD computing is proposed for thin-walled composite structures, where the Structural-Genome database is collected through the FE^2. Compared to MGD analysis, proposed by Kirchdoerfer and Ortiz, 2016, the new SGD method benefits from not only the model reduction, but also the ability to easily deal with complex microscopic geometry and material properties. Several numerical tests are considered to demonstrate the efficiency and robustness of the proposed method.

The layout of this chapter is as follows. After recalling the basic principles of the classical FE^2 method, Section 4.1 presents the proposed data-driven FE^2 procedure. In Section 4.2, a matrix-round inclusion composite plate and a fiber reinforced plate with a hole are considered to validate the effectiveness and robustness of the proposed method. In Section 4.3.1, the procedure of SGD computing is presented via taking an example of Euler-Bernoulli beam. Section 4.3.2 details the process of extracting structural-genome database from numerical experiments, whilst the formulations of the multi-scale finite element method is briefly recalled for composite structures with complex heterogeneous materials. In Section 4.4, two cases are considered to validate the effectiveness and robustness of the proposed SGD method. Some conclusions are provided in Section 4.5.

4.1 Formulation of data-driven FE^2

4.1.1 Classical FE^2

The classical FE^2 method which has been introduced in Section 2.1 is recalled. In this method, composites are assumed to have infinite periodic microscopic configuration (RVE), as shown in Fig. 4.1. The unknown constitutive relation of the composite is represented by an homogenized stress-strain relation from the RVE. Specifically, the strain of a macroscopic point is used for piloting the microscopic finite element analysis on the related RVE, while the effective tangent matrix $\bar{\mathbb{C}}_t$ and stress of the macroscopic point are averaged over the RVE.

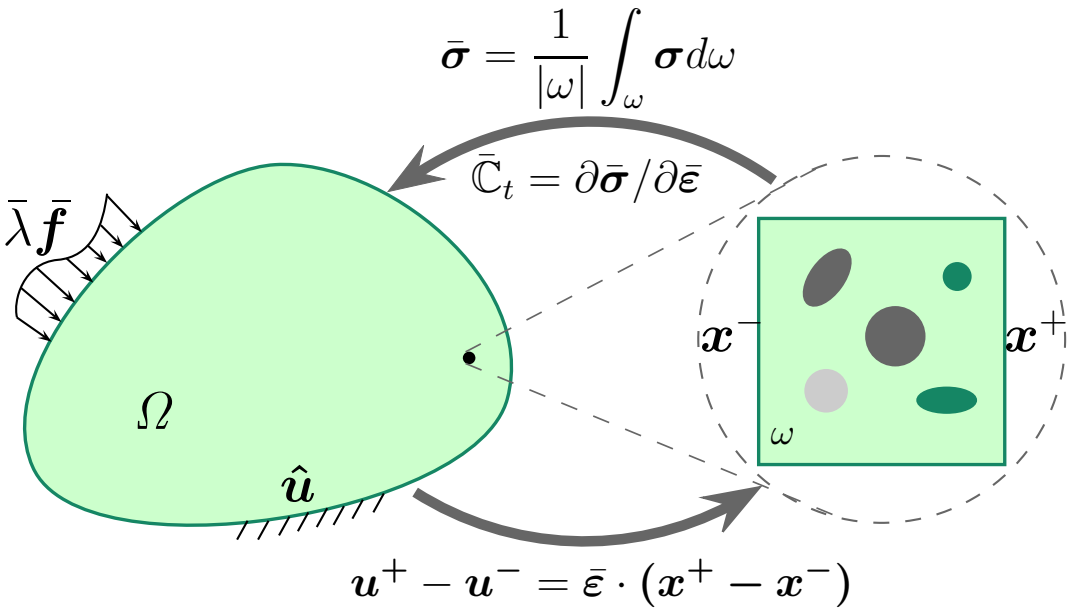

FIGURE 4.1 – Basic principle of the classical FE^2 method.

The control equations in a linear case are given as follows :

— The macroscopic problem :

$$\int_{\Omega} \bar{\boldsymbol{\sigma}} : \boldsymbol{\delta}\bar{\boldsymbol{\varepsilon}} d\Omega = \bar{\lambda} \int_{\partial\Omega_\sigma} \bar{\boldsymbol{f}} \cdot \boldsymbol{\delta}\bar{\boldsymbol{u}} d\Gamma \tag{4.1a}$$

$$\bar{\boldsymbol{\varepsilon}} = \frac{1}{2}\left(\boldsymbol{\nabla}\bar{\boldsymbol{u}} + {}^t\boldsymbol{\nabla}\bar{\boldsymbol{u}}\right) \tag{4.1b}$$

— Scale coupling :

$$\bar{\boldsymbol{\sigma}} = \frac{1}{|\omega|}\int_{\omega} \boldsymbol{\sigma} d\omega \tag{4.2a}$$

$$\bar{\mathbb{C}}_t = \partial\bar{\boldsymbol{\sigma}}/\partial\bar{\boldsymbol{\varepsilon}}. \tag{4.2b}$$

— The microscopic problem :

$$\int_{\omega} \boldsymbol{\sigma} : \boldsymbol{\delta\varepsilon} d\omega = 0 \tag{4.3a}$$

$$d\boldsymbol{\sigma} = \mathbb{C}_t^{(r)} : d\boldsymbol{\varepsilon} \tag{4.3b}$$

$$\boldsymbol{u}^+ - \boldsymbol{u}^- = \bar{\boldsymbol{\varepsilon}} \cdot (\boldsymbol{x}^+ - \boldsymbol{x}^-) \quad on \quad \partial\omega. \tag{4.3c}$$

Taking into account Eqs. (4.1) to (4.3), the problems in two scales are to be solved together in one multiscale system. Considering the coupled macroscopic and microscopic nonlinearities, iterating algorithms, such as Newton-Raphson method, are adopted in both two scales. To ensure the convergence, fine meshes and small increments are sometimes required, which could result in very expensive computational costs. Thus, to simplify this system, we are going to adopt a data-driven computing scheme to split the problem into two separated scales as discussed in the next subsection.

4.1.2 Data-driven computing and scale decoupling

To drive an elasticity simulation, normally, a constitutive relation, a balance equation and some compatibility constraints are required. However, in data-driven computing, the material behavior is not explicitly given as in Eq. (4.2b), but is characterized by a pair $(\bar{\boldsymbol{\varepsilon}}', \bar{\boldsymbol{\sigma}}')$ of strain and stress tensors in the material genome database. To search the most suitable strain-stress pairs from the database, a global penalty function is constructed :

$$\bar{\mathscr{F}}(\bar{\boldsymbol{\varepsilon}}, \bar{\boldsymbol{\sigma}}) = \min_{(\bar{\boldsymbol{\varepsilon}}', \bar{\boldsymbol{\sigma}}') \in \bar{\mathscr{D}}} \frac{1}{2}\int_{\Omega} \left((\bar{\boldsymbol{\varepsilon}} - \bar{\boldsymbol{\varepsilon}}') : \bar{\mathbb{C}} : (\bar{\boldsymbol{\varepsilon}} - \bar{\boldsymbol{\varepsilon}}') + (\bar{\boldsymbol{\sigma}} - \bar{\boldsymbol{\sigma}}') : \bar{\mathbb{C}}^{-1} : (\bar{\boldsymbol{\sigma}} - \bar{\boldsymbol{\sigma}}') \right) d\Omega \tag{4.4}$$

where $\bar{\mathscr{D}}$ is a phase space of material genome database, and $\bar{\mathbb{C}}$ a given tensor which is numerical in nature and does not represent a material property.

The balance equation and the compatibility constraints in Eq. (4.1) are reformulated as :

$$\int_{\Omega} \bar{\boldsymbol{\sigma}} : \bar{\boldsymbol{B}} d\Omega - \bar{\lambda}\int_{\partial\Omega_\sigma} \bar{\boldsymbol{f}} d\Gamma = 0 \tag{4.5a}$$

$$\bar{\boldsymbol{\varepsilon}} = \bar{\boldsymbol{B}} \cdot \bar{\boldsymbol{u}} \tag{4.5b}$$

where the third-order tensor $\bar{\boldsymbol{B}}$ can be derived from Eq. (4.1b). With Eq. (4.5a) being enforced by Lagrange multipliers $\bar{\boldsymbol{\eta}}$, the macroscopic problem is formulated as the minimization of the following functional :

$$\Pi = \bar{\mathscr{F}}(\bar{\boldsymbol{\varepsilon}}, \bar{\boldsymbol{\sigma}}) + \bar{\boldsymbol{\eta}} \left(\int_{\Omega} \bar{\boldsymbol{\sigma}} : \bar{\boldsymbol{B}} d\Omega - \bar{\lambda}\int_{\partial\Omega_\sigma} \bar{\boldsymbol{f}} d\Gamma \right) \tag{4.6}$$

Using Eq. (4.5b) in Eq. (4.6), all the variations of Eq. (4.6) read :

$$\delta\bar{\boldsymbol{u}}: \quad \int_{\Omega} \bar{\mathbb{C}} : (\bar{\boldsymbol{B}} \cdot \bar{\boldsymbol{u}} - \bar{\boldsymbol{\varepsilon}}^*) : \bar{\boldsymbol{B}} d\Omega = 0 \tag{4.7a}$$

$$\delta\bar{\boldsymbol{\sigma}}: \quad \bar{\boldsymbol{\sigma}} - \bar{\boldsymbol{\sigma}}^* = \bar{\mathbb{C}} : \bar{\boldsymbol{B}} \cdot \bar{\boldsymbol{\eta}} \tag{4.7b}$$

$$\delta\bar{\boldsymbol{\eta}}: \quad \int_{\Omega} \bar{\boldsymbol{\sigma}} : \bar{\boldsymbol{B}} d\Omega - \bar{\lambda} \int_{\partial\Omega_\sigma} \bar{\boldsymbol{f}} d\Gamma = 0 \tag{4.7c}$$

where $(\bar{\boldsymbol{\varepsilon}}^*, \bar{\boldsymbol{\sigma}}^*)$ denote optimal data points when $\bar{\mathscr{F}}$ reaches its minimum value :

$$\begin{aligned} &\int_{\Omega} \left((\bar{\boldsymbol{\varepsilon}} - \bar{\boldsymbol{\varepsilon}}^*) : \bar{\mathbb{C}} : (\bar{\boldsymbol{\varepsilon}} - \bar{\boldsymbol{\varepsilon}}^*) + (\bar{\boldsymbol{\sigma}} - \bar{\boldsymbol{\sigma}}^*) : \bar{\mathbb{C}}^{-1} : (\bar{\boldsymbol{\sigma}} - \bar{\boldsymbol{\sigma}}^*) \right) d\Omega \\ &\leq \int_{\Omega} \left((\bar{\boldsymbol{\varepsilon}} - \bar{\boldsymbol{\varepsilon}}') : \bar{\mathbb{C}} : (\bar{\boldsymbol{\varepsilon}} - \bar{\boldsymbol{\varepsilon}}') + (\bar{\boldsymbol{\sigma}} - \bar{\boldsymbol{\sigma}}') : \bar{\mathbb{C}}^{-1} : (\bar{\boldsymbol{\sigma}} - \bar{\boldsymbol{\sigma}}') \right) d\Omega \end{aligned} \tag{4.8}$$

By substituting Eq. (4.7b) into Eq. (4.7c), Eq. (4.7) yield the following linear system :

$$\begin{cases} \int_{\Omega} \bar{\boldsymbol{B}} : \bar{\mathbb{C}} : \bar{\boldsymbol{B}} \cdot \bar{\boldsymbol{u}} d\Omega = \int_{\Omega} \bar{\mathbb{C}} : \bar{\boldsymbol{\varepsilon}}^* : \bar{\boldsymbol{B}} d\Omega \\ \int_{\Omega} \bar{\boldsymbol{B}} : \bar{\mathbb{C}} : \bar{\boldsymbol{B}} \cdot \bar{\boldsymbol{\eta}} d\Omega = \bar{\lambda} \int_{\partial\Omega_\sigma} \bar{\boldsymbol{f}} d\Gamma - \int_{\Omega} \bar{\boldsymbol{\sigma}}^* : \bar{\boldsymbol{B}} d\Omega \end{cases} \tag{4.9}$$

Finally, the macroscopic problem turns into searching the optimal strain-stress pair $(\bar{\boldsymbol{\varepsilon}}^*, \bar{\boldsymbol{\sigma}}^*)$, the closest possible satisfaction of compatibility and equilibrium, from the database $\bar{\mathscr{D}}$ over the domain Ω. In data-driven computing, Eq. (4.9) are solved iteratively with trial strain-stress pairs $(\bar{\boldsymbol{\varepsilon}}^{*(k)}, \bar{\boldsymbol{\sigma}}^{*(k)})$ in the (k)th iteration until their solution remains constant, where $(\bar{\boldsymbol{\varepsilon}}^{*(k)}, \bar{\boldsymbol{\sigma}}^{*(k)})$ are the data points closest to the solution $(\bar{\boldsymbol{\varepsilon}}^{(k-1)}, \bar{\boldsymbol{\sigma}}^{(k-1)})$ in the $(k-1)$th iteration, see Kirchdoerfer and Ortiz [189], Yang et al. [199] for details. The first trial pairs to initiate the iteration could be randomly chosen from the database. However, a random value, which may be too far from the solution, could slow down the solution convergence. Thus, in the whole nonlinear loading process, the stress-strain solution of the previous loading step is assigned to the current initial pair herein to accelerate the computation. It should be noted that macroscopic problem in Eq. (4.9) is fully compatible with the finite element method. Using the data-driven computing framework, the macroscopic problem is to be solved with an offline material genome database without solving microscopic problems simultaneously, see Fig. 4.2. As for the database, it can be constructed by solving a series of offline microscopic problems independently. It should be noted that the database can be constructed before an online macroscopic structural analysis, and it could be used repeatedly for various different simulations.

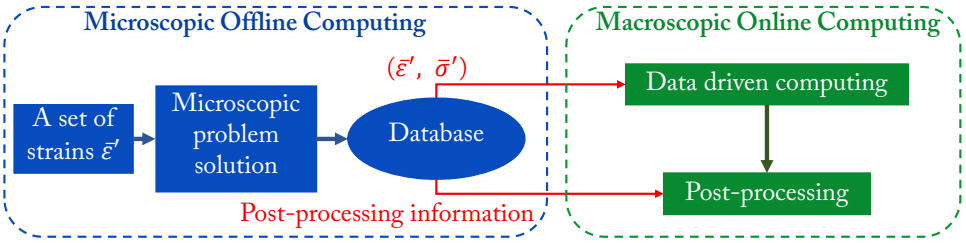

FIGURE 4.2 – The flowchart of the proposed data-driven FE^2 method.

As shown in Fig. 4.2, to construct database $\bar{\mathscr{D}}$, a set of strains $\bar{\boldsymbol{\varepsilon}}'$ is successively applied on the microscopic boundaries. The microscopic system in Eq. (4.3) can be solved in a finite element model on existing commercial platforms, such as ABAQUS, using homogenization theory. Then,

the stress $\bar{\boldsymbol{\sigma}}'$ associated to each applied strain $\bar{\boldsymbol{\varepsilon}}'$ can be calculated according to Eq. (4.2a). For the sake of simplicity, the examples in this chapter do not consider cases with path-dependent behaviors. However, the proposed multiscale computing scheme could be further extended for those problems according to Eggersmann et al. [200]. All useful microscopic post-processing information, such as the displacement, stress and strain fields, can also be saved in the database, which can be recalled when post-processing the results from the structural analysis.

4.2 Validation and application of data-driven FE^2

In this section, a matrix-round inclusion composite plate with round inclusions under uniaxial compression is considered to validate the proposed data-driven FE^2 method. Plane stress analysis is considered for all the examples in this chapter.

As shown in Fig. 4.3a, a composite square plate reinforced by round inclusions is subjected to a compressive load over the top and bottom edges. The length and width of the plate are $L = H = 20$ mm. Considering the symmetry of the geometrical configuration and the applied load, only 1/4 of the plate is modeled, see Fig. 4.3b. The microscopic material is represented by the RVE given in Fig. 4.3.

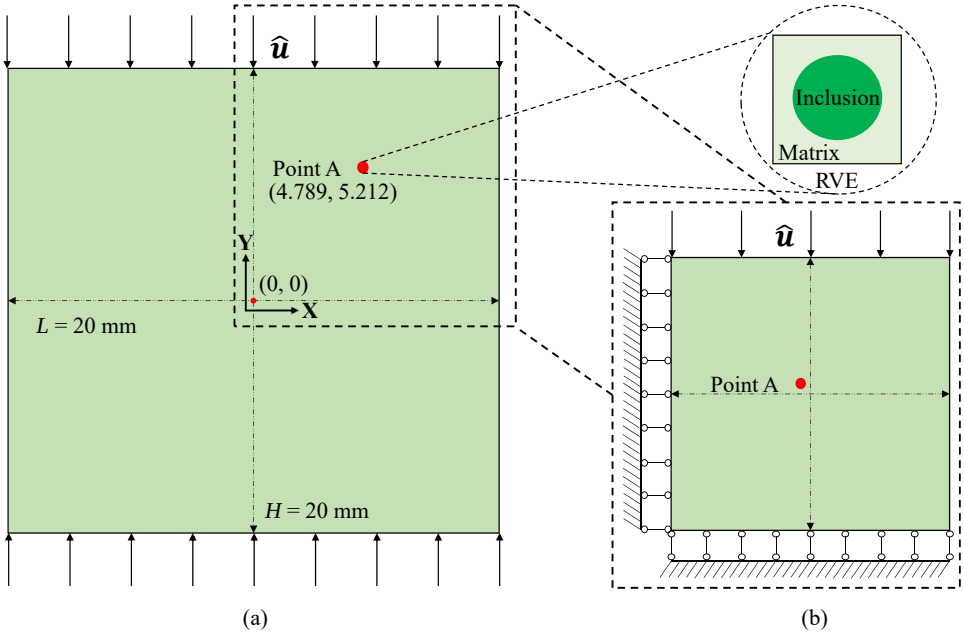

FIGURE 4.3 – Configuration of the composite plate subjected to compressive displacement.

As far as the macroscopic model is concerned, 100 plane stress 8-node elements (CPS8R in ABAQUS) with 4 integration points per element are used, see Fig. 4.4b. The size of the dimensionless RVE is 1x1. The mesh of the RVE using the plane stress 3-node element (CPS3 in ABAQUS) is shown in Fig. 4.4a. Note that the proposed meshes are fully refined to guarantee convergent solution.

4.2.1 Convergence analysis

A convergence analysis on the database density is conducted at first. We assume the inclusion and the matrix of composite plate have the same properties and are isotropic, with Young's

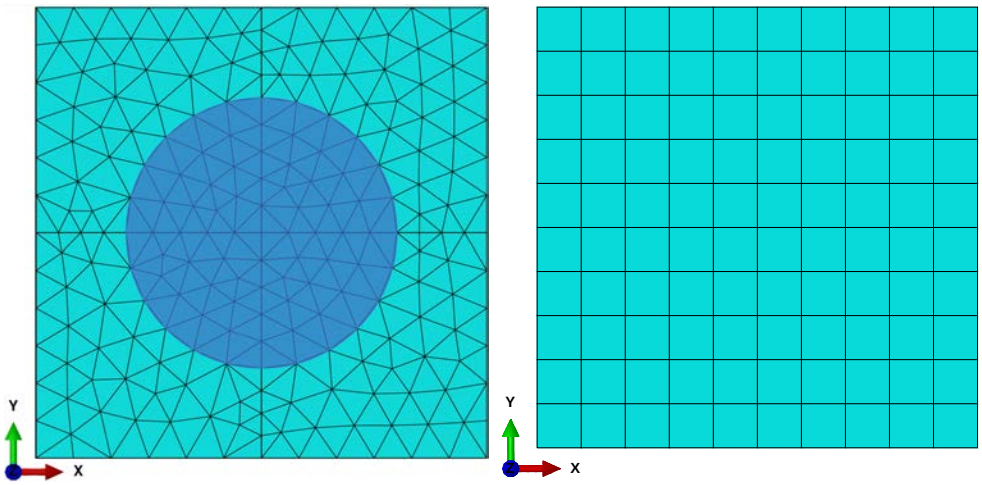

(a) Microscopic (b) Macroscopic

FIGURE 4.4 – Mesh of the RVE and the 1/4 composite plate.

modulus $E = 10000$ MPa and Poisson's ratio $\nu = 0.3$. Thus, the plate could be regarded as isotropic and provide analytical reference solution. The effective Young's modulus and Poisson's ratio are : $\bar{E} = E$ and $\bar{\nu} = \nu$. A pressure load whose intensity $P_y = 12$ MPa is applied on the top and bottom edges. According to analytical solution, the displacement of point A in Y-axial direction is $u_{Ay} = -P_y/\bar{E} \cdot Y_A$, where Y_A is the Y coordinate of point A. The material database is constructed by the analytical material properties $\bar{E}$ and $\bar{\nu}$, where the macroscopic strain $\bar{\boldsymbol{\varepsilon}}' = (\bar{\varepsilon}'_{11}, \bar{\varepsilon}'_{22}, \bar{\varepsilon}'_{12})$ is within the range $[0 \leq \bar{\varepsilon}'_{11} \leq 7{\cdot}10^{-4}, -2.4{\cdot}10^{-3} \leq \bar{\varepsilon}'_{22} \leq 0, -10^{-5} \leq \bar{\varepsilon}'_{12} \leq 0]$. As suggested in Yang et al. [199], $\bar{\mathbb{C}}$ was assigned a proper value, whose elements should be relative lower than those of analytical constitutive tensor, to ensure the convergence of the data matching progress. Fig. 4.5 shows that the relative errors in the displacement of plate decreases along with the increasing of the density of database, while the number of iterations is less than 4 times. To be noticed, the iteration number depends on many factors, such as the initial data points, the value of $\bar{\mathbb{C}}$, the database and the problem to be solved. For example, we need 2∼10 iterations per step in the next example.

4.2.2 Inelastic composite plate

The real composite plate is considered herein after the convergence analysis, where the stiff round inclusion and the soft matrix are both assumed elastoplastic. Compressive displacement $\hat{\boldsymbol{u}} = 0.1$ mm is applied on the top and bottom edges of the plate.

Ramberg-Osgood constitutive relation (Ramberg and Osgood [221]) is used to describe the nonlinear behavior of the materials :

$$E\boldsymbol{\varepsilon} = (1+\nu)\boldsymbol{S}_d - (1-2\nu)p\boldsymbol{I} + \frac{3}{2}\alpha\left(\frac{q_d}{\sigma_0}\right)^{n-1}\boldsymbol{S}_d \tag{4.10}$$

where α is the yield offset, σ_0 the yield stress, $\boldsymbol{S}_d = \boldsymbol{\sigma} + p\boldsymbol{I}$ the stress deviator, $p = -\frac{1}{3}\boldsymbol{\sigma} : \boldsymbol{I}$ the equivalent hydrostatic stress, $q_d = \sqrt{\frac{3}{2}\boldsymbol{S}_d : \boldsymbol{S}_d}$ the Mises equivalent stress, and n the hardening exponent for plasticity. Young's modulus and Poisson's ratios are denoted by E and ν. The material parameters are given in Table 4.1, where the subscripts i and m denote the inclusion

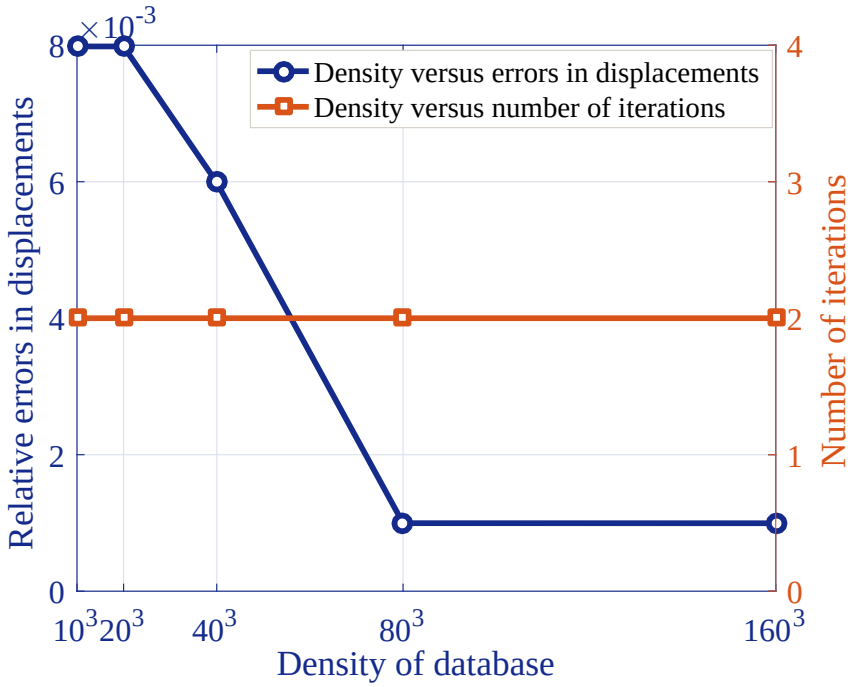

FIGURE 4.5 – The evolution of relative errors in displacements and iteration numbers along with the increasing of data density.

and the matrix, respectively. To be noticed, this model is adopted in the total deformation form, which does not consider path-dependent behaviors (loading/unloading) in the following examples.

TABLE 4.1 – Material parameters of the inclusion and the matrix.

E_i (MPa)	ν_i	α_i	σ_{0i} (MPa)	n_i
10^5	0.3	3	100	2
E_m (MPa)	ν_m	α_m	σ_{0m} (MPa)	n_m
10^4	0.3	3	10	2

As mentioned in Section 4.1, the microscopic problems are firstly solved by the finite element method to construct the material genome database. According to the maximum load $\hat{\boldsymbol{u}}$ applied on the plate, the macroscopic strain $\bar{\boldsymbol{\varepsilon}}' = (\bar{\varepsilon}'_{11}, \bar{\varepsilon}'_{22}, \bar{\varepsilon}'_{12})$ of each integration point is approximately within the range $[0 \leq \bar{\varepsilon}'_{11} \leq 5 \cdot 10^{-3}, -10^{-2} \leq \bar{\varepsilon}'_{22} \leq 0, -10^{-5} \leq \bar{\varepsilon}'_{12} \leq 0]$ via a preliminary analysis. Of course, this range could be extended. To collect material genome data, macroscopic strains within this range are sequentially applied on the RVE, and then the macroscopic stress $\bar{\boldsymbol{\sigma}}'$ related to each strain point is derived using Eq. (4.2a). Two databases with density of 50^3 and 100^3 points are created, respectively. All the information during the loading process are saved in the ABAQUS ".odb" files which can be recalled whenever post-processing is needed. Note that a database only represent the information of constitutive relationship and does not dependent on the macroscopic boundary conditions. Thus, it can be used for various loading cases. A classical FE^2 model with exactly the same properties and meshes as those of the data-driven model is considered as reference solution.

Fig. 4.6a illustrates the nonlinear evolution of the reaction force and the displacement of the

top edge of the plate along the Y-axial direction simulated by the data-driven multiscale model using two databases of different size and the classical multiscale model respectively. The three curves show a good agreement. Results of the data-driven model with data density equal to 50^3 match those using a data density equal to 100^3. Besides, the maximum difference between data-driven and classical FE^2 model is at worst 1%. In Fig. 4.6b, the stress-strain evolutions of integration point A (see Fig. 4.3) modeled by two models also show very good agreement. Since the macroscopic model does not consider geometrical nonlinearity and the data-driven solver is a fixed-point scheme, the strong nonlinear response is due to the nonlinearity of stress-strain data (the effective behavior of RVE). Although the data-driven multiscale model splits the multiscale system into two scales, the interaction between these scales still remains without any loss of accuracy.

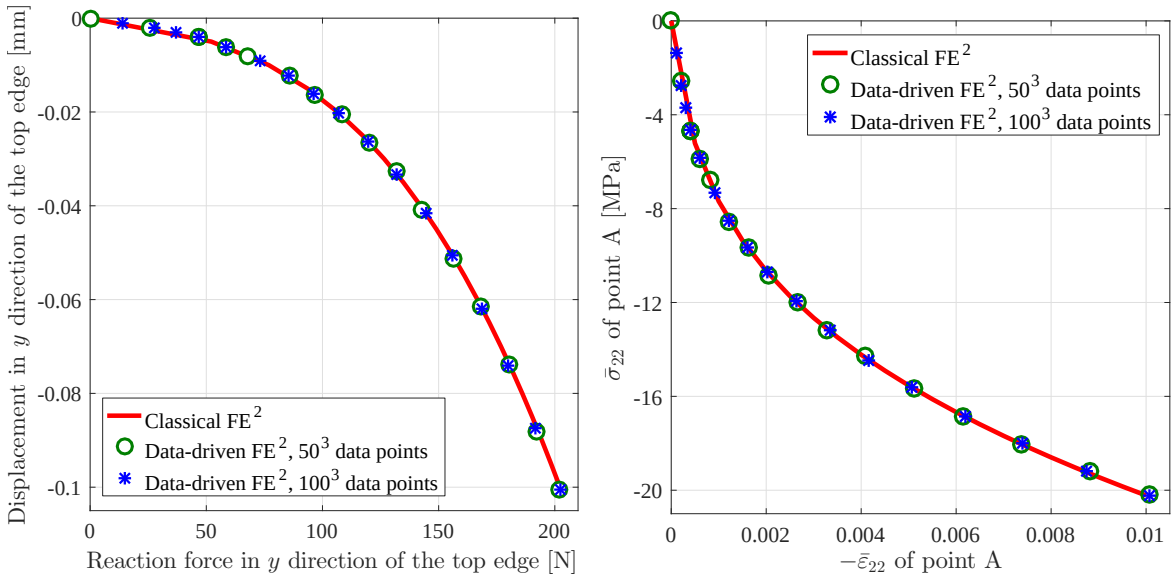

FIGURE 4.6 – (a) Force-displacement curves at the top edge of the composite plate ; (b) stress-strain curves of point A.

In the post-processing, the microscopic information can be accessed in the database. Fig. 4.7 shows the plastic strain distribution over the RVE corresponding to point A. The left one is retrieved from the ".odb" database by matching the calculated macroscopic strain-stress pairs $(\bar{\boldsymbol{\varepsilon}}^*, \bar{\boldsymbol{\sigma}}^*)$ and the offline pairs $(\bar{\boldsymbol{\varepsilon}}', \bar{\boldsymbol{\sigma}}')$, while the right one is obtained during the online computing of the classical FE^2 model. The two figures present a matching plastic deformation distribution over the RVE.

4.2.3 Computational cost

In the classical FE^2 framework, the stress of each macroscopic integration point has to be updated repeatedly by solving microscopic problems during the online structural analysis. However, in the data-driven FE^2 framework, this updating is done by searching stress-strain pairs in a genome database : the solution of complex mechanical problems is replaced by a fairly simple computer operation. In this example, the meshes of two methods are exactly the same.

Table 4.2 presents the time cost of the data-driven method in both the online and offline

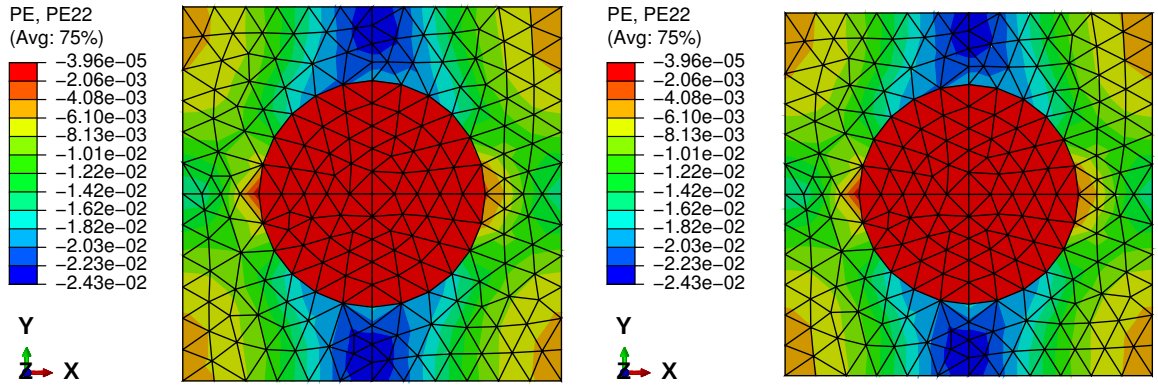

(a) Data-driven FE^2 (b) Classical FE^2

FIGURE 4.7 – The distribution of plastic strain along the Y-axial direction (PE22 in figures) in the RVE associated to point A, when the macroscopic strain reaches 1% : (a) simulated by the data-driven FE^2 method ; (b) simulated by the classical FE^2 method.

TABLE 4.2 – The computational time cost of the data-driven method using 50 steps and the classical FE^2 method using 50 steps, and the relative errors in displacements of the data-driven FE^2 method.

Classical method	Proposed method			
	Density	Online	Offline	Avg. Err. (%)
75453 (s)	50^3	2734 (s)	1981 (s)	0.067
	100^3	30975 (s)	17405 (s)	0.033

TABLE 4.3 – The total number of microscopic problems on all the integration points in the classical computing for 50 steps, the number of iterations in the online data-driven computing per step and the number of microscopic problems in the offline data-driven computing.

RVE problems in classical method	Proposed method		
	Density	Online Itrt.	Offline RVE problems
32800	50^3	$2 \sim 10$ times/step	125000
	100^3	$2 \sim 10$ times/step	1000000

stages. In the online computing stage, the data-driven FE^2 method took 2734 seconds with 50^3 data points and 30975 seconds with 100^3 data points, while the classical FE^2 method took 75453 seconds. Note that the step length has been optimized and parallel computation has been considered to improve the computational efficiency of the classical method. Compared with classical FE^2 method, 58.9% of online computing time per step is saved by the data-driven FE^2 method with 100^3 data points and 96.4% per step with 50^3 data points. There is no doubt that both the online and the offline time cost increases rapidly along with the increasing of data density, even could be more computationally expensive than the overall cost of classical FE^2 method if the size of data is huge. However, the averaged relative error in the force-displacement response using 50^3 is already lower than 0.1% for this example. In this case the online computational cost is significantly saved by the proposed method.

To show offline computational efforts more intuitively, Table 4.3 gives the number of microscopic problems solved respectively by two methods. Although the number of microscopic problems in the offline stage of the data-driven method is larger than the overall number of microscopic problems in the classical method, in practice, the offline time cost for database could be less than the overall cost in the classical method as it is shown in Table 4.2. One possible reason may be that there is no data exchange between parallel offline computations (16 processors were used). Besides, the numbers of online iterations of the proposed method in one step are no more than 10 times in this example as presented in Table 4.3.

Considering cases with more time consuming microscopic problems, such as fiber buckling or cracks, the advantages of the data-driven FE^2 method will be more obvious. Remark such comparisons are never perfectly fair because they can be implementation-dependent, computer-dependent, and even author-dependent. The searching algorithm in the implemented data-driven model could be further improved by dichotomy and parallel computing. Comparing to the concurrent FE^2 method, the proposed data-driven approach presents two merits : (1) The online computational efficiency is significantly improved ; (2) A enriched database could be repeatedly used for various simulations. However the offline computational cost of the proposed method could be expansive and this point deserves further discussion.

4.2.4 Fiber reinforced plate

In this section, a fiber reinforced composite plate with stress concentration is studied by the proposed method. The microscopic fiber buckling is observed in the stress concentration area of the plate, which results in local stiffness reduction.

The studied square plate with a hole in the center is presented in Fig. 4.8a. The radius of the hole is $r = 3$ mm, while the length and the width of the plate are 48 mm. A pressure load $\boldsymbol{p} = 2.6$ MPa is applied on the right and left sides of the plate. The fibers are oriented along the load direction to reinforce the plate. Due to the symmetry of the geometrical configuration, material properties and applied load, only 1/4 of the plate is modeled, see Fig. 4.8b. For a classical hole stress concentration problem considering isotropic properties, the stress along the load direction around point B is the highest stress (3 times of the given load $\boldsymbol{p}$ according to classical analytical and numerical solutions). For this composite plate, point B also presents the stress concentration effect due to the hole. However, the accurate stress distribution of the plate is difficult to be predicted via analytical solution or direct finite element methods.

The fiber is elastic and occupies 2% of the volume, while the matrix is plastic and described by Ramberg-Osgood constitutive relation. The detailed material properties of the fiber and the matrix are given in Table 4.4, where subscripts f and m represent the fiber and the matrix, respectively.

The dimensionless RVE with size of 1x1 is meshed with plane stress 6-node element (CPS6

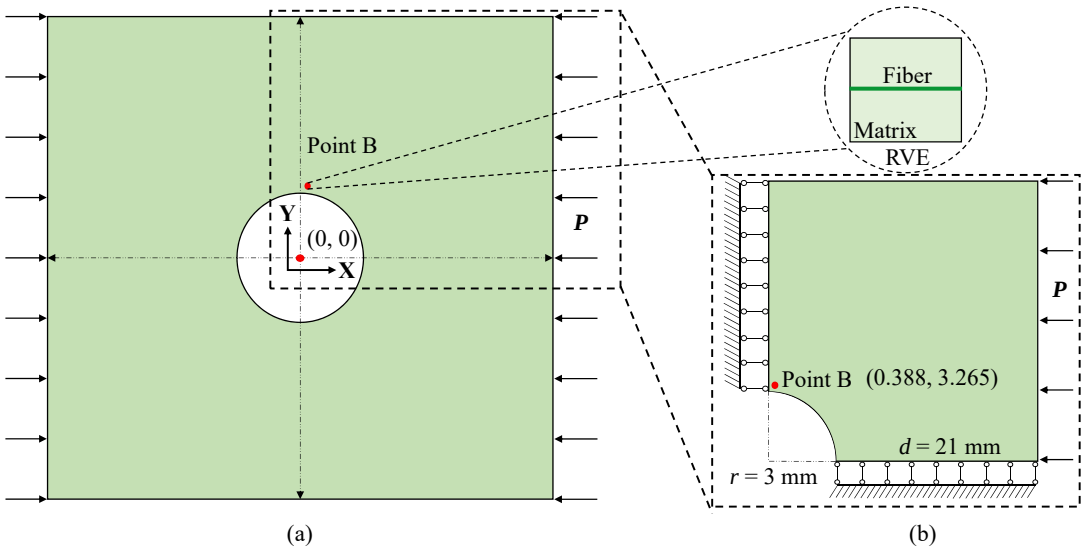

FIGURE 4.8 – Configuration of the composite plate with an hole in the center.

TABLE 4.4 – Material parameters of the fiber and the matrix.

E_f (MPa)	ν_f	E_m (MPa)	ν_m	α_m	σ_{0m} (MPa)	n_m
10^5	0.3	10^2	0.3	3	10	2

in ABAQUS), while the plate is meshed with plane stress 3-node element (CPS3), as shown in Fig. 4.9.

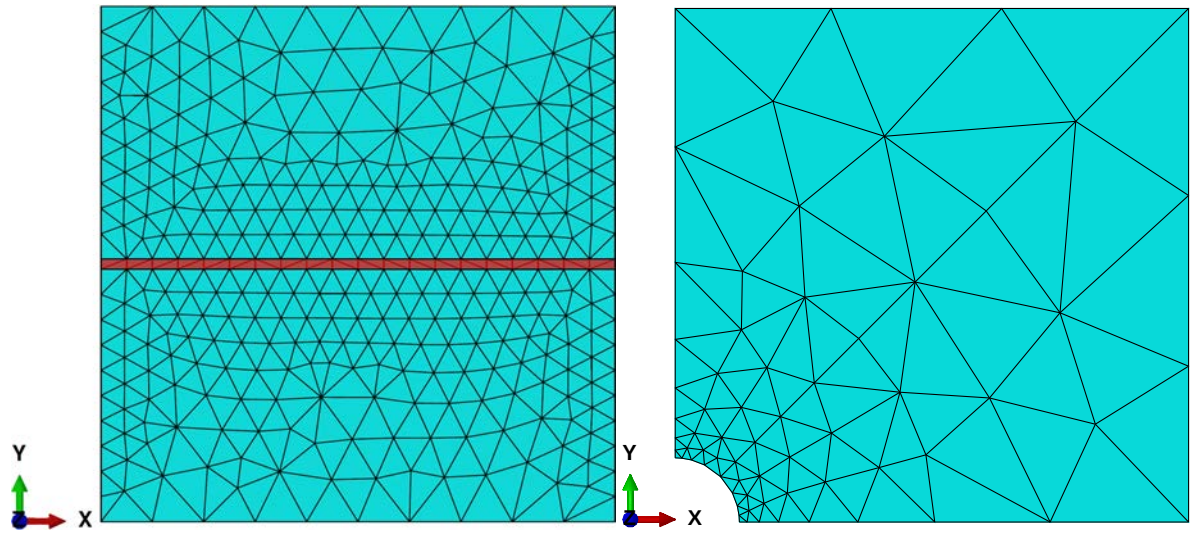

(a) Microscopic (b) Macroscopic

FIGURE 4.9 – The meshes for the RVE and 1/4 composite plate.

Fig. 4.10 illustrates the distribution of stress component $\bar{\sigma}_{11}$ over the global plate and around the local hole, when the fiber buckling at point B is triggered. The stress fields simulated respectively by data-driven and classical FE^2 models present good agreement. The stress component

$\bar{\sigma}_{11}$ at point B is -19.3 MPa, which is 7.4 times the applied load $\boldsymbol{p}$. Due to the reinforcing fibers, the stress concentration effect around the hole is more pronounced than that of an isotropic plate.

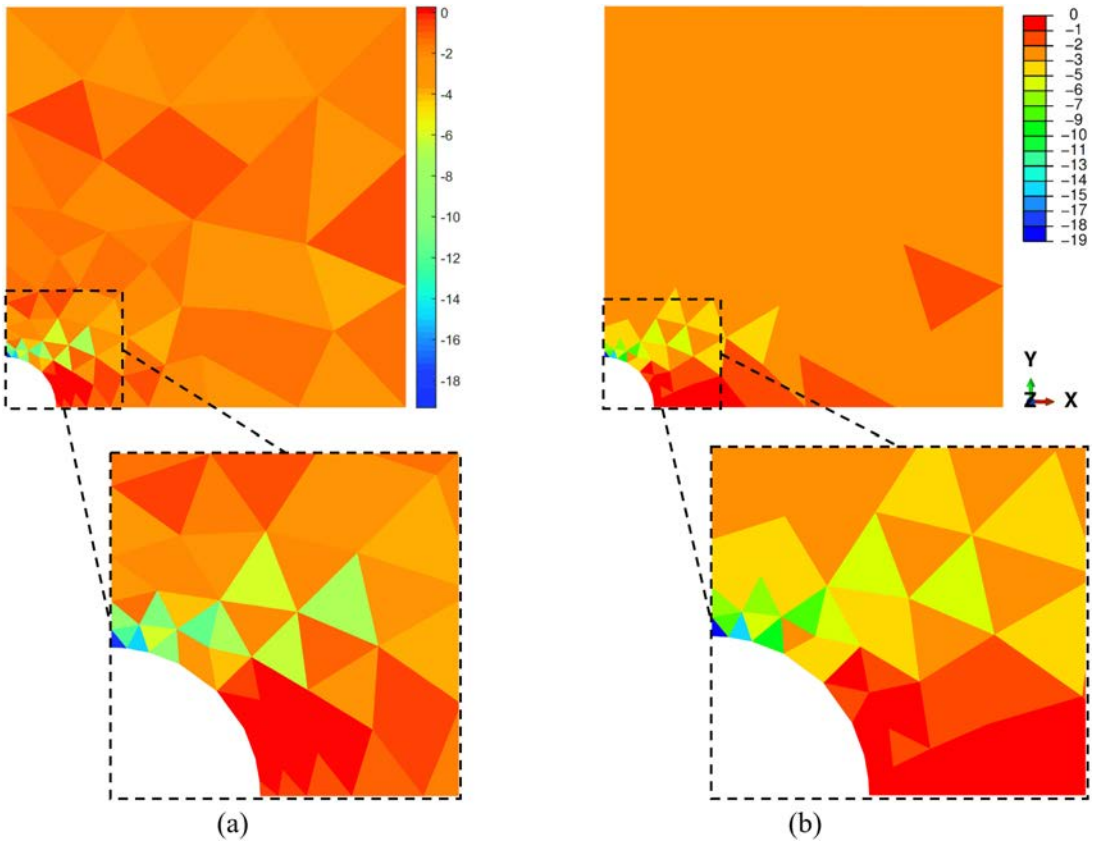

FIGURE 4.10 – The distribution of stress component $\bar{\sigma}_{11}$ (MPa) over the local hole and the global plate when the fiber buckling at point B is triggered : (a) data-driven FE^2 method ; (b) classical FE^2 method.

The evolution of the stress-strain relation at point B is given in Fig. 4.11. As expected the material nonlinearity is governed by the buckling of the fiber and the plasticity of the matrix. The deformation and the strain over the RVE related to point B at state fiber buckling is given in Fig. 4.12, where the microscopic fiber instability is observed.

Considering the separation between online and offline computations, the online computational time for this problem can be considerably reduced. Furthermore, the complex multiscale system is simplified by splitting it into two single scale problems. It should be noted that microscopic fiber instability depends on the amplitude of the imperfections of the fiber (Nezamabadi et al. [98]), the wavelength of the fiber (Yang et al. [145], Yu et al. [207]), and even the accuracy and step length of the nonlinear solver (Huang et al. [130], Choe et al. [146]). Considering all these parameters in a multiscale system will result in a much heavier simulation burden than that of the round inclusion example. For example, the step length of the RVE is required to be very small (about 1/10 of that of the round inclusion example) when the applied load is close to the critical buckling load. It is also difficult to prescribe a wavelength of buckled fiber in a multiscale system. However, in the single scale problem of the RVE, the buckling mode could be efficiently obtained by a linearized buckling analysis. In summary, using the proposed method in multiscale

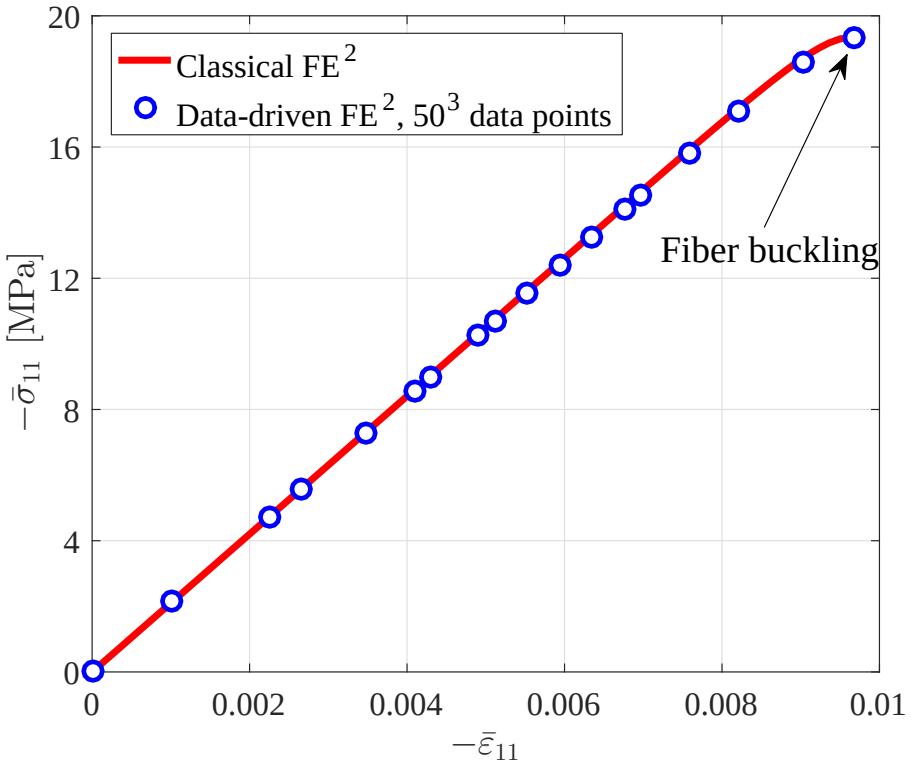

FIGURE 4.11 – Evolution of stress-strain relation at point B until the fiber buckles.

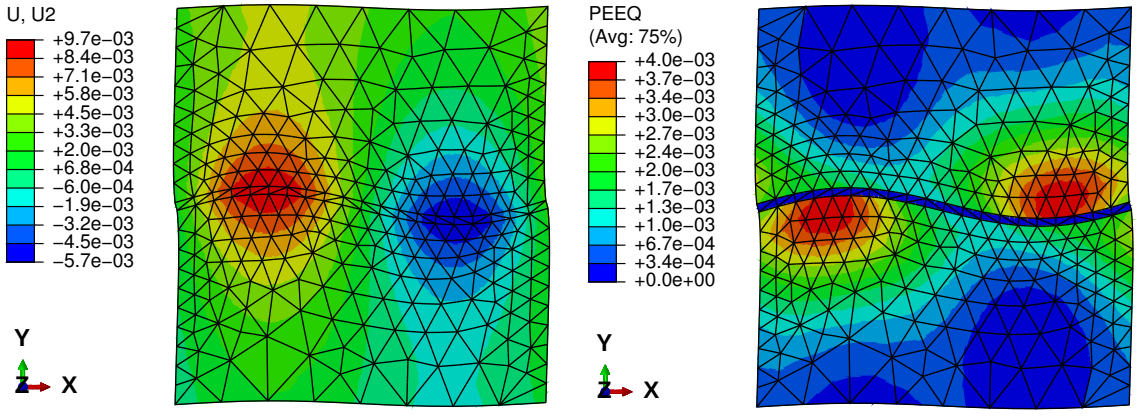

(a) Transverse displacement

(b) Equivalent plastic strain

FIGURE 4.12 – Deformation and strain distribution over the RVE related to point B at state fiber buckling.

problems like this one will save online computational time and ensure high efficiency in solving the system thanks to the scale separation.

4.3 Formulation of SGD computing

This section consists of two parts : the first one in Section 4.3.1 relates to the formulation of SGD computing for an example of Euler-Bernoulli beam, whilst the second part in Section 4.3.2 concerns the construction of structural-genome database of thin-walled composite structures by the FE^2 method.

4.3.1 SGD method

The Principle of Virtual Work of the Euler-Bernoulli beam reads :

$$\int_0^L \left[N\delta\varepsilon + M\delta\kappa\right] dx = \int_0^L \boldsymbol{f}(x)\delta\boldsymbol{v}dx \tag{4.11}$$

where N and M represent the normal force and bending moment, ε and κ are the corresponding normal strain and curvature of the neutral-plane, $\boldsymbol{f}$ and $\boldsymbol{v}$ denote the external force and the displacements fields respectively. The definitions of ε and κ are given by $\varepsilon = u_{,x}$ and $\kappa = -w_{,xx}$, where u and w are the axial and transverse displacements of the neutral-plane, the subscript x preceded by comma represents the derivative of the function with respect to the axial coordinate.

In case that the constitutive relationship of the material is not available, one can not solve Eq. (4.11) by the standard finite element process. Motivated by Material-Genome-Database (MGD) (Kirchdoerfer and Ortiz [189]), the structural-genome (i.e., the normal force N and normal strain ε, the bending moment M and curvature κ) is employed to drive the computing instead of the material-genome (strain and stress). Based on MGD framework, here one constructs a new penalty function containing two sets of global states, namely $\mathfrak{S} = \langle N, M, \varepsilon, \kappa\rangle$ and $\mathfrak{S}' = \langle N', M', \varepsilon', \kappa'\rangle$, in the following :

$$\mathscr{F}(\mathfrak{S}) = \min_{\mathfrak{S}\in\mathscr{Z},\mathfrak{S}'\in\mathscr{D}} \int_0^L \frac{1}{2}\left[\frac{(N-N')^2}{AC} + \frac{(M-M')^2}{CI} + AC(\varepsilon-\varepsilon')^2 + CI(\kappa-\kappa')^2\right] dx \tag{4.12}$$

where $\mathscr{Z}$ denotes a phase space containing the generic structural-genome, $\mathscr{D}$ a subset of the phase space $\mathscr{Z}$, A and I represent the area and the moment of inertia of the cross-section, C is a given constant and not a material property. One should note that the global state $\mathfrak{S}'$ in a collected structural-genome database $\mathscr{D}$ has satisfied the constitutive relation of the considered materials. If the global state $\mathfrak{S}$ satisfies the compatibility constraints and conservation laws, the considered problems can be solved by minimizing the distance between the two sets of global states.

Since the structural-genome data set $\mathfrak{S}' \in \mathscr{D}$ is rendered as scattered data points, the integral form of Eq. (4.12) is discretized with a finite element method :

$$\mathscr{F} = \sum_{g=1}^{m} \omega_g \mathscr{F}_g(\mathfrak{S}_g) \tag{4.13}$$

where m is the total number of Gauss points, ω_g the integration weight, and the local penalty function for each integration point can be expressed as :

$$\mathscr{F}_g(\mathfrak{S}_g) = \min_{\mathfrak{S}\in\mathscr{Z},\mathfrak{S}'\in\mathscr{D}} \frac{1}{2}\left[\frac{(N_g-N'_g)^2}{AC} + \frac{(M_g-M'_g)^2}{CI} + AC(\varepsilon_g-\varepsilon'_g)^2 + CI(\kappa_g-\kappa'_g)^2\right] \tag{4.14}$$

where the two sets of local states for each integration point are denoted by $\mathfrak{S}_g = \langle N_g, M_g, \varepsilon_g, \kappa_g \rangle$ and $\mathfrak{S}'_g = \langle N'_g, M'_g, \varepsilon'_g, \kappa'_g \rangle$.

As mentioned above, the local state $\mathfrak{S}_g$ should satisfy the conservation law in Eq. (4.11) and the compatibility conditions, namely $\varepsilon = u_{,x}$ and $\kappa = -w_{,xx}$. The Lagrange linear shape functions and the Hermite cubic polynomials are used for interpolations of axial displacement u and transverse displacement w of neutral-plane respectively, which could be easily found in Bathe [222] and thus are not presented here for the sake of brevity. Then ε_g and κ_g can be expressed by :

$$\begin{cases} \varepsilon_g = \sum_{i=1}^{n} B^1_{gi} v_i = \boldsymbol{B}^1 \boldsymbol{v} \\ \kappa_g = \sum_{i=1}^{n} B^2_{gi} v_i = \boldsymbol{B}^2 \boldsymbol{v} \end{cases} \tag{4.15}$$

where n represents the total number of DOFs and $\boldsymbol{v}$ consists of $u, w, w_{,x}$ of all nodes, the vectors $\boldsymbol{B}^1$ and $\boldsymbol{B}^2$ are the global interpolation functions. Assuming that $\boldsymbol{f}$ in Eq. (4.11) is a vector of applied nodal concentrated forces and considering the interpolations shown in Eq. (4.15), the discrete form of Eq. (4.11) can be easily deduced as :

$$\delta v_i \left[\sum_{g=1}^{m} \omega_g \left(N_g B^1_{gi} + M_g B^2_{gi} \right) - f_i \right] = 0 \tag{4.16}$$

The discrete form conservation law shown in Eq. (4.16) can be enforced by Lagrange multipliers, whilst the compatibility conditions can be easily enforced by substitution of Eq. (4.15) in Eq. (4.14). Then whole problem is equivalent to minimizing the following function :

$$\Pi = \sum_{g=1}^{m} \omega_g \mathscr{F}_g (N_g, M_g, \sum_{i=1}^{n} B^1_{gi} v_i, \sum_{i=1}^{n} B^2_{gi} v_i) + \sum_{i=1}^{n} \left(\sum_{g=1}^{m} \omega_g \left(N_g B^1_{gi} + M_g B^2_{gi} \right) - f_i \right) \eta_i \tag{4.17}$$

The variations of Eq. (4.17) read

$$\delta v_i : \quad \sum_{j=1}^{n} \sum_{g=1}^{m} \omega_g \left(AC B^1_{gj} B^1_{gi} + CI B^2_{gj} B^2_{gi} \right) v_j = \sum_{g=1}^{m} \omega_g \left(\varepsilon^*_g B^1_{gi} + \kappa^*_g B^2_{gi} \right) \tag{4.18}$$

$$\delta N_g : \quad N_g = N^*_g - AC \sum_{i=1}^{n} B^1_{gi} \eta_i \tag{4.19}$$

$$\delta M_g : \quad M_g = M^*_g - CI \sum_{i=1}^{n} B^2_{gi} \eta_i \tag{4.20}$$

$$\delta \eta_i : \quad \sum_{g=1}^{m} \omega_g \left(N_g B^1_{gi} + M_e B^2_{gi} \right) = f_i \tag{4.21}$$

where $\mathfrak{S}^*_g = \langle N^*_g, M^*_g, \varepsilon^*_g, \kappa^*_g \rangle \in \mathscr{D}$ denotes the optimal structural data points for each cross-section at these integration points such that

$$\mathscr{F}_g(\mathfrak{S}_g, \mathfrak{S}^*_g) \leq \mathscr{F}_g(\mathfrak{S}_g, \mathfrak{S}'_g) \tag{4.22}$$

Eliminating N_g and M_g in Eq. (4.21) by using Eqs. (4.19) and (4.20), then the linear system shown in Eqs. (4.18) to (4.21) can be reduced as the following simple form :

$$\begin{cases} \boldsymbol{K} \boldsymbol{v} = \boldsymbol{b}^1 \\ \boldsymbol{K} \boldsymbol{\eta} = \boldsymbol{b}^2 \end{cases} \tag{4.23}$$

where the components of the matrix $\boldsymbol{K}$ and the vectors $\boldsymbol{b}^1$ and $\boldsymbol{b}^2$ write :

$$K_{ij} = \sum_{g=1}^{m} \omega_g \left(AC B^1_{gj} B^1_{gi} + CI B^2_{gj} B^2_{gi} \right) \tag{4.24}$$

$$b^1_i = \sum_{g=1}^{m} \omega_g \left(AC \varepsilon^*_g B^1_{gi} + CI \kappa^*_g B^2_{gi} \right) \tag{4.25}$$

$$b^2_i = \sum_{g=1}^{m} \omega_g \left(N^*_g B^1_{gi} + M^*_g B^2_{gi} \right) - f_i \tag{4.26}$$

Finally the whole problem remains to search iteratively the optimal structural-genome data for each integration point from the database $\mathscr{D}$ that satisfying Eq. (4.23). The flowchart of the proposed SGD method is sketched in Fig. 4.13 and detailed as follows :

Step 1 : The structural-genome data $\mathfrak{S}^{*(k)}_g$ $(k = 0)$ chosen randomly from the prepared database $\mathscr{D}$ is assigned to each integration point of the beam structure.

Step 2 : Driven by the structural-genome data $\mathfrak{S}^{*(k)}_g$, the vectors of displacements $\boldsymbol{v}^{(k)}$ and the Lagrange multipliers $\boldsymbol{\eta}^{(k)}$ can be easily obtained by Eq. (4.23). Then the global structural-genome of each integration point $\mathfrak{S}_g{}^{(k)} = \langle N^{(k)}_g, M^{(k)}_g, \varepsilon^{(k)}_g, \kappa^{(k)}_g \rangle$ corresponding to $\boldsymbol{v}^{(k)}$ and $\boldsymbol{\eta}^{(k)}$ can be computed by Eqs. (4.15), (4.19) and (4.20).

Step 3 : From the database $\mathscr{D}$, find the best structural-genome data $\mathfrak{S}_g{}^{*(k+1)}$ that is closest to the global structural-genome $\mathfrak{S}_g{}^{(k)}$ computed in Step 2 such that $\mathscr{F}_g(\mathfrak{S}_g{}^{(k)}, \mathfrak{S}^{*(k+1)}_g) \leq \mathscr{F}_g(\mathfrak{S}_g{}^{(k)}, \mathfrak{S}'_g)$, where $\mathfrak{S}'_g$ can be considered as any data point in the database $\mathscr{D}$.

Step 4 : Stop the iteration in case of $\mathfrak{S}^{*(k+1)}_g = \mathfrak{S}^{*(k)}_g$ for each integration point, otherwise update the structural-genome data by considering $\mathfrak{S}^{*(k)}_g \leftarrow \mathfrak{S}^{*(k+1)}_g$ and repeat Step 2 to Step 4 until it converges.

4.3.2 Structure-genome database prepared via FE^2 technique

To conduct SGD computing for thin-walled composite structures, the key issue is to collect structural-genome databases by either experiments or numerical simulations. Therefore, the construction of these databases is explained herein via taking an example of the Euler-Bernoulli beam. Specifically, two sets of numerical experiments are carried out for beam genomes : 1) a tension experiment along the axial direction for the normal force N and related normal strain ε of neutral-plane at $x = L/2$, see Fig. 4.14a; 2) a three-point bending experiment for the bending moment M and related curvature k of the neutral-plane at $x = 3L/4$, see Fig. 4.14b. Through continuous loading in the two sets of numerical experiments, a sequence of sampling structural-genome data points can be collected. The sampling location is chosen far away from the boundaries to avoid the boundary effect.

With the classical FE^2 method introduced in 4.1.1, the composite beam could be successfully simulated, and its structural-genome database could be constructed via the numerical experiments shown in Fig. 4.14. The methodology could be further extended to construct structural-genome databases for other thin-walled composites.

4.4 Validation and application of SGD computing

In this section, two cases are considered to validate the effectiveness and robustness of the proposed SGD method. The first one is a linear elastic beam under axial stretch and transverse

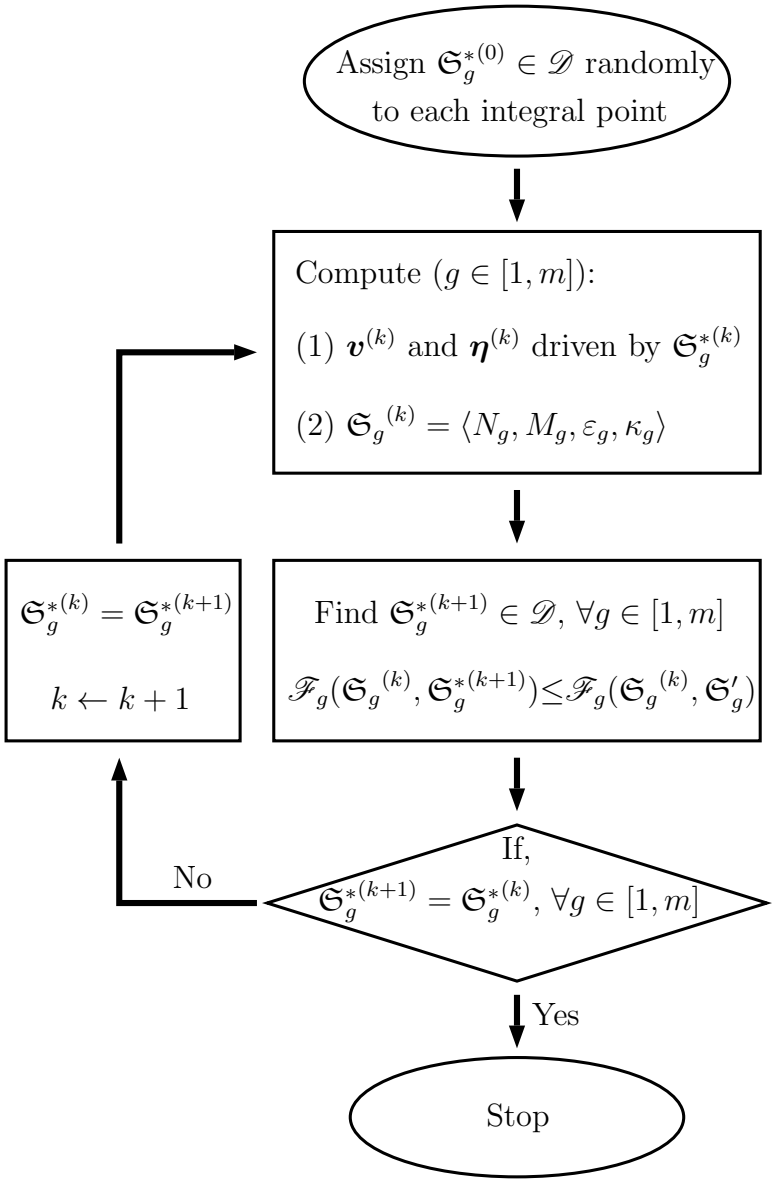

FIGURE 4.13 – The flowchart of the proposed SGD computing.

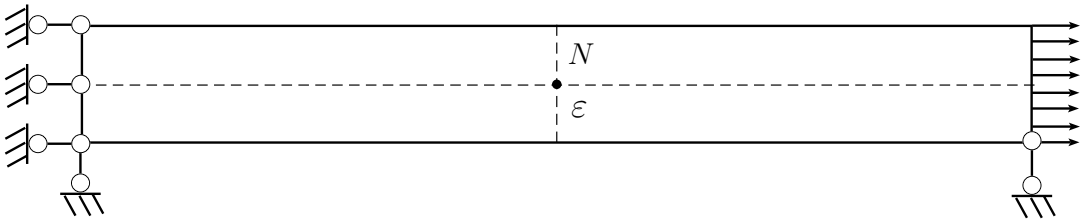

(a) Uniaxial tension

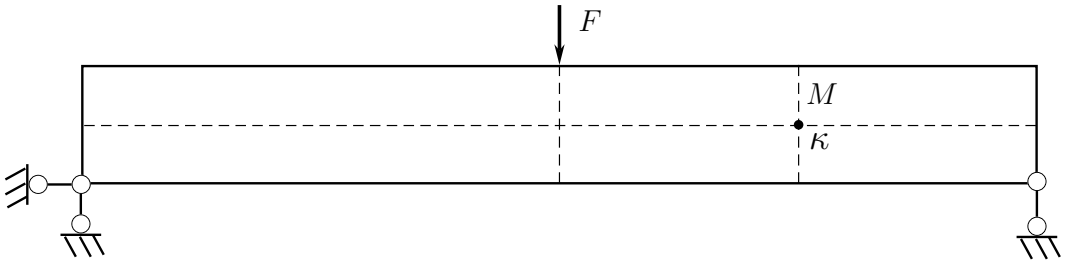

(b) Three-point bending

FIGURE 4.14 – Numerical experiments for computing the structural-genome of thin beam structures.

load, in which one thing is discussed carefully, that is the influences of structure and data informations (i.e. the amount of structural-genome data, the constant C in the penalty function $\mathscr{F}$, data noise) on the accuracy of solution and the number of iterations required for the convergence. The second one is a thin composite beam under axial compression and transverse load, which consists of two steps : the preparation of structural-genome database through the FE^2 method (see details in Section 4.3.2) and SGD computing. The latter numerical test aims to verify the proposed method is able to analyze thin-walled composite structures with complex microscopic geometry and variable material properties by an extremely efficient and simple manner.

4.4.1 Validation

Here we consider a linear elastic homogeneous cantilever beam subjected to a point load at its free end, where the components of the concentrated force along x-axis and z-axis directions are denoted by $F_1 = 100$ N and $F_2 = 0.1$ N respectively, see Fig. 4.15. The geometric and material parameters of the thin elastic beam are as follows : the Young's modulus $E = 1000$ MPa, the length and thickness of the beam are $L = 20$ mm and $h = 1$ mm respectively.

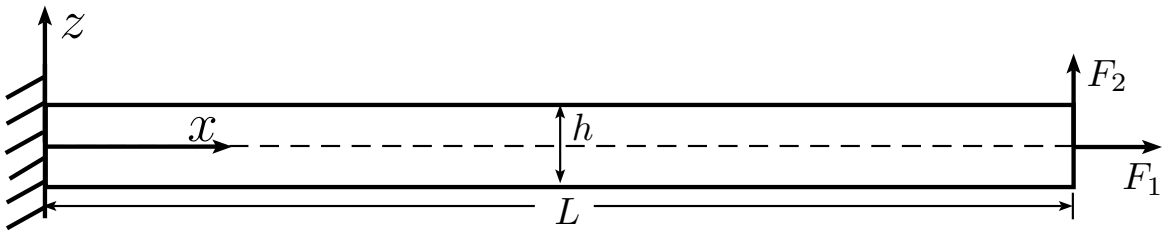

FIGURE 4.15 – A linear elastic homogeneous cantilever beam subjected to a point load at its free end.

The numerical results via the proposed SGD method are compared with 1D finite element (FE) solutions. Unless additional statement, the beam is meshed by using 40 two-node one-dimensional elements and 3 Gauss points per element, which is confirmed to be sufficient for the convergence, for both SGD computing and finite element computing throughout this subsection. The structural-genome database is constructed by the analytical relations $N = EA\varepsilon$ and $M = -EI\kappa$, with the ranges of normal force and bending moment given by $N \in [-200, 200]$ (N) and $M \in [-4, 4]$ (N·mm) for all numerical tests in the current subsection.

The first numerical test is carried out to demonstrate the effectiveness of the proposed SGD method. SGD computing is driven by 400^2 data points with the constant $C = 1000$ in Eq. (4.12). The deformed shapes of the considered cantilever beam via the proposed SGD method with 9 iterations and 1D FE method are shown in Fig. 4.16. The result illustrates a very good agreement.

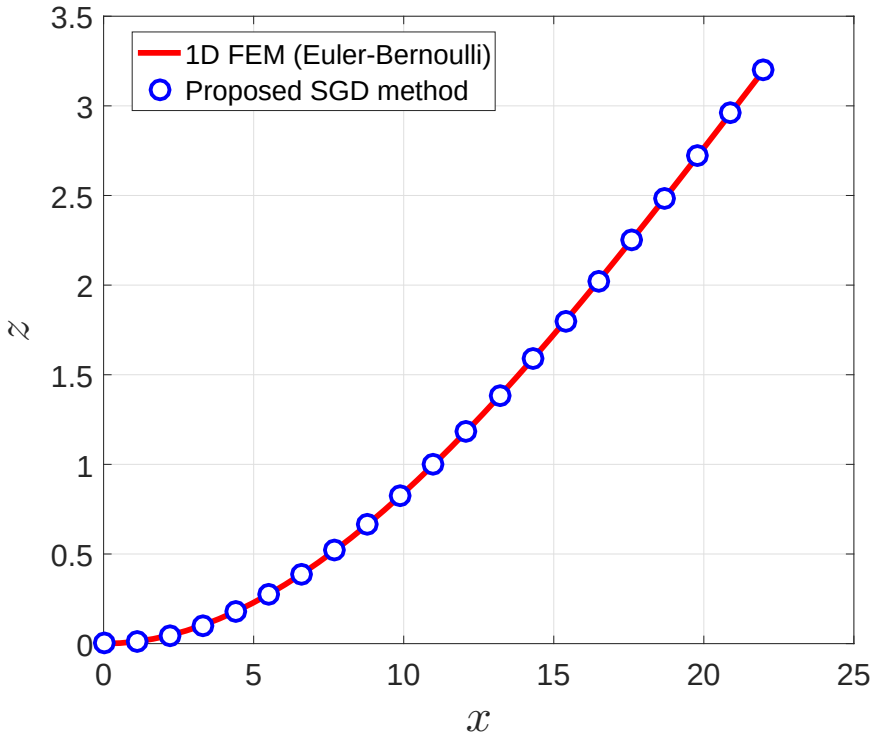

FIGURE 4.16 – Deformed shapes of the cantilever beam under tension and bending simulated by two methods.

Then, the influences of the amount of data points on the accuracy and the number of iterations of the proposed SGD method are studied. To this end, four numerical tests are considered with the numbers of data points being 100^2, 200^2, 400^2 and 800^2 respectively and with the same parameter $C = 1000$. To avoid the influence of the initial assignments of the structural-genome data for each integration point on the accuracy, the same random seed is used in this numerical test. The convergence of the residual of the penalty function $\mathscr{F}$ (see Eq. (4.13)) with various numbers of data points and with the number of iterations is illustrated in Fig. 4.17. The residual of $\mathscr{F}$ decreases rapidly with the number of data points, whilst the number of iterations required for the convergence of SGD method increases slightly. With a larger amount of data points, such

phenomenon could be anticipated.

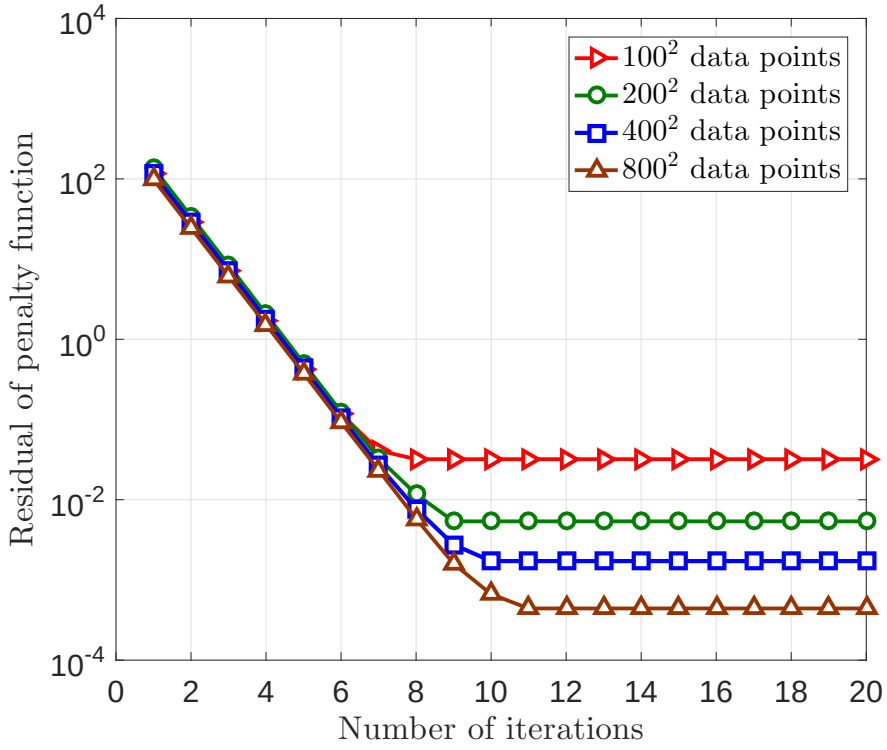

FIGURE 4.17 – Convergence of the penalty function $\mathscr{F}$ with the number of iterations and with the number of structural-genome data points.

To investigate the influence of the parameter C in Eq. (4.12) on the accuracy and the required number of iterations of the proposed SGD method, here we consider numerical tests with various values of constant C in the range $[10^{-10}, 10^6]$ and with the number of data points being 200^2. As conducted previously, a fixed assignments of the initial structural-genome data is applied. The convergence with the value of the constant C is presented in Fig. 4.18. The maximum relative error of displacements decreases with the decrease of C until $C = 10$ and from then on it remains constant. The similar behavior has been observed for the number of iterations required for the convergence. Based on these results, one may obtain a reasonable accuracy, 1% for instance, if $C \leq E$. To ensure the convergence of the proposed method, a relatively small value of C is recommended.

The preparation of structural-genome database by numerical or experimental tests may yield data noise. To explore the influence of data noise on the accuracy of the proposed method, the Gaussian random noises containing 200 data points for both of the relations (N, ε) and (M, κ) are considered and presented in Fig. 4.19. Note that the structural-genome database with data noise consists of two parts : the data noise illustrated in Fig. 4.19 and the exact data points constructed by using the analytical relations $N = EA\varepsilon$ and $M = -EI\kappa$. As recommended previously, the constant C is chosen to be 10 for the present test.

Note that the accuracy of SGD method relates to the initial assignments of the structural-genome data points. Here the computing is conducted repeatedly for 100 times for each numerical test and takes the average value of the relative errors. The convergence of the proposed SGD

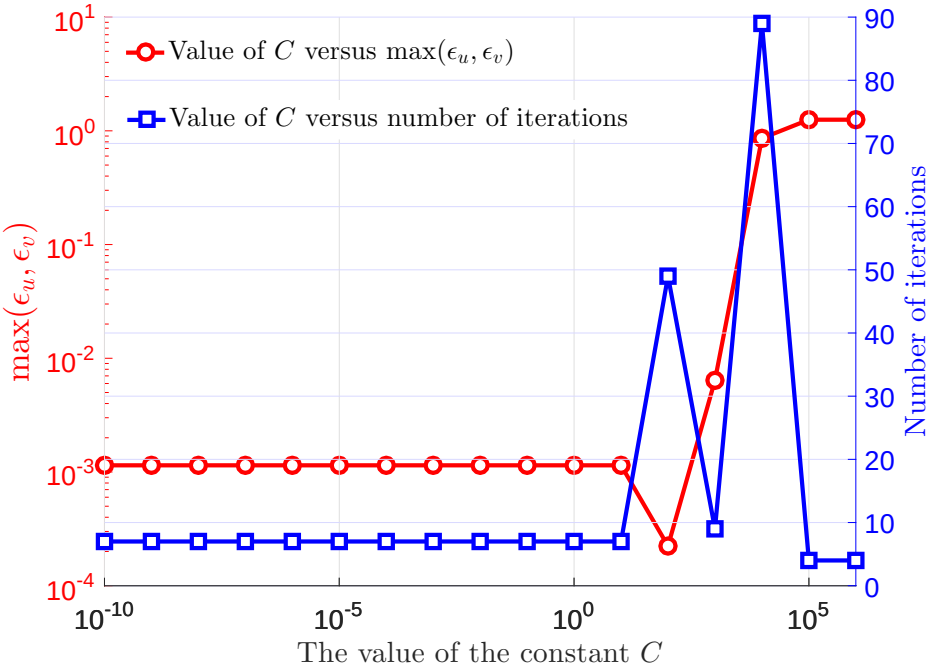

FIGURE 4.18 – Influence of the constant C in the penalty function $\mathscr{F}$ on the accuracy of solution and the number of iterations required for the convergence, where the $\max(\epsilon_u, \epsilon_v)$ represents the maximum relative error of displacements u and w.

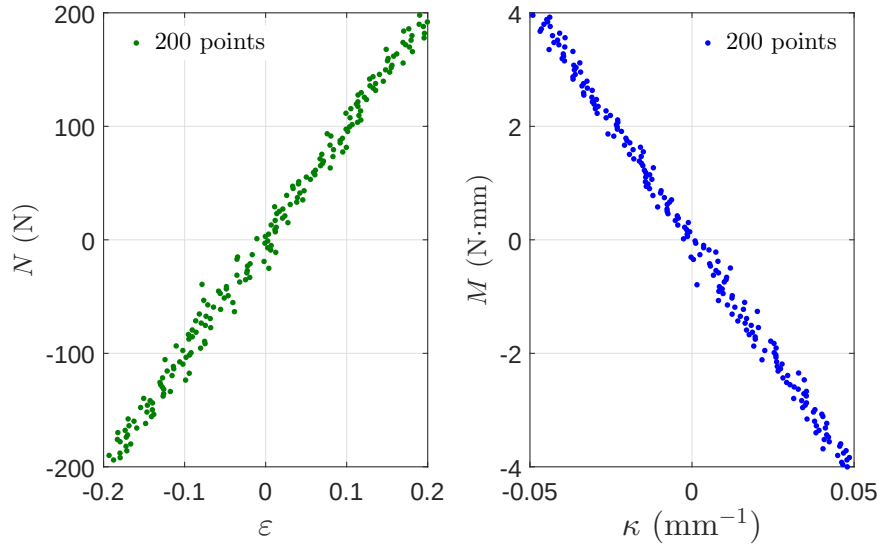

FIGURE 4.19 – Gaussian random noise in the structural-genome database.

method with the number of data points is presented in Fig. 4.20. The accuracy of solutions driven by the database with Gaussian random noise is compared with the one without data noise. The results show that the accuracy is reduced by the intrusion of noisy data points. However one can still obtain a reasonable accurate result by increasing the size of structural-genome database.

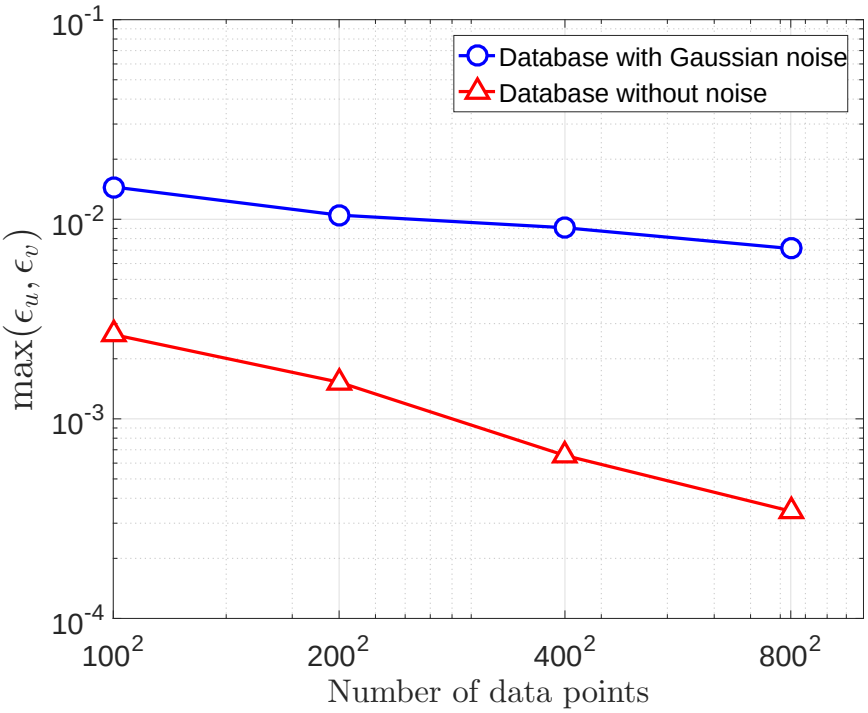

FIGURE 4.20 – Convergence with the number of data points in cases of structural-genome database with Gaussian random noise.

4.4.2 Thin composite beam

A thin composite beam made of a three-phase micro-structure is considered in this subsection, see Fig. 4.21. The left end of the beam is clamped, whilst the right end is subjected to a concentrated force, the components of which along x-axis and z-axis directions are denoted by F_1 and F_2 respectively. The beam length and width are $L = 200$ mm and $h = 10$ mm.

The three-phase RVE given in Fig. 4.21 consists of a stiff external frame and a soft fiber embedded in a plastic matrix. The external frame and the fiber are made of elastic materials, while the plastic matrix is modeled by Ramberg-Osgood relationship (Ramberg and Osgood [221]) as the following

$$\varepsilon = \frac{\sigma}{E} + \alpha \frac{\sigma}{E} \left(\frac{\sigma}{\sigma_0} \right)^{p-1} \tag{4.27}$$

where α is the yield offset, σ_0 the yield stress, and p the hardening exponent for plasticity. The Young's modulus and the Poisson's ratios are denoted by E and ν. The material parameters of the three-phase RVE are given in Table 4.5, where the subscripts f, m and e represent the fiber, matrix and external frame respectively.

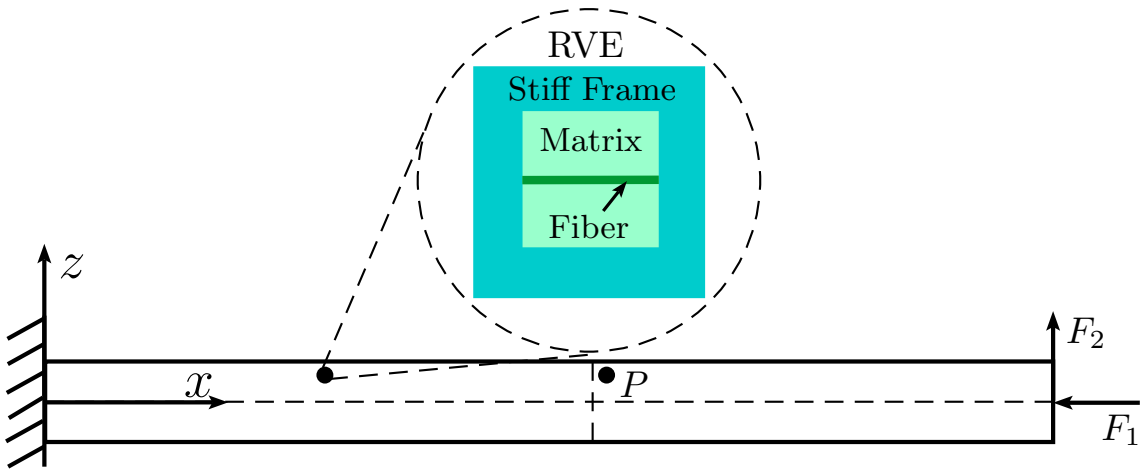

FIGURE 4.21 – A composite cantilever beam subjected to a point load at its free end.

TABLE 4.5 – Material parameters for the external frame, the fiber and the matrix.

E_e (MPa)	ν_e	E_f (MPa)	ν_f	E_m (MPa)	ν_m	α	σ_0 (MPa)	p
10^5	0.3	1000	0.3	100	0.3	2	0.1	3

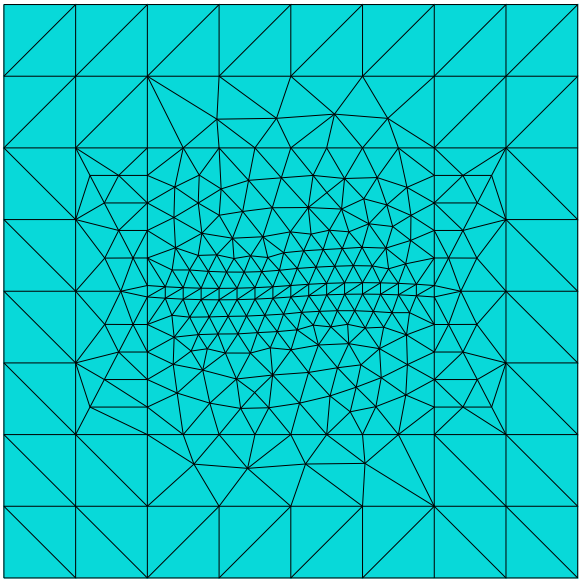

FIGURE 4.22 – Mesh of the RVE.

Numerical tests using the FE^2 method are carried out to construct the structural-genome database and to provide the reference solutions of the considered thin composite beam, see details in Section 4.3.2. The macroscopic model of the thin beam is meshed with 4 elements along the z-axis direction and 40 elements along the x-axis direction, based on 8-node quadrilateral elements with 4 reduced integration points per element. The RVE is fully meshed with plane stress 3-node element shown in Fig. 4.22. The mesh density mentioned above for both of the macroscopic model and the RVE has been confirmed to be sufficient to ensure the convergence. Note that a very small imperfection in the fiber is introduced to trigger the fiber buckling.

To construct the structural-genome database for this beam structure, two sets of numerical experiments are carried out, as described in Section 4.3.2. The data pairs (N, ε) are collected from the cross-section at $x = L/2$ in the tension experiments, whilst the pairs (M, κ) are collected from the cross-section at $x = 3L/4$ in the three-point bending experiments. The database containing 400 data points for both pairs, namely (N, ε) and (M, κ), is presented respectively in Fig. 4.23. The combinations of these data pairs yield the structural-genome data set $(N, M, \varepsilon, \kappa)$, the number of which is 400^2.

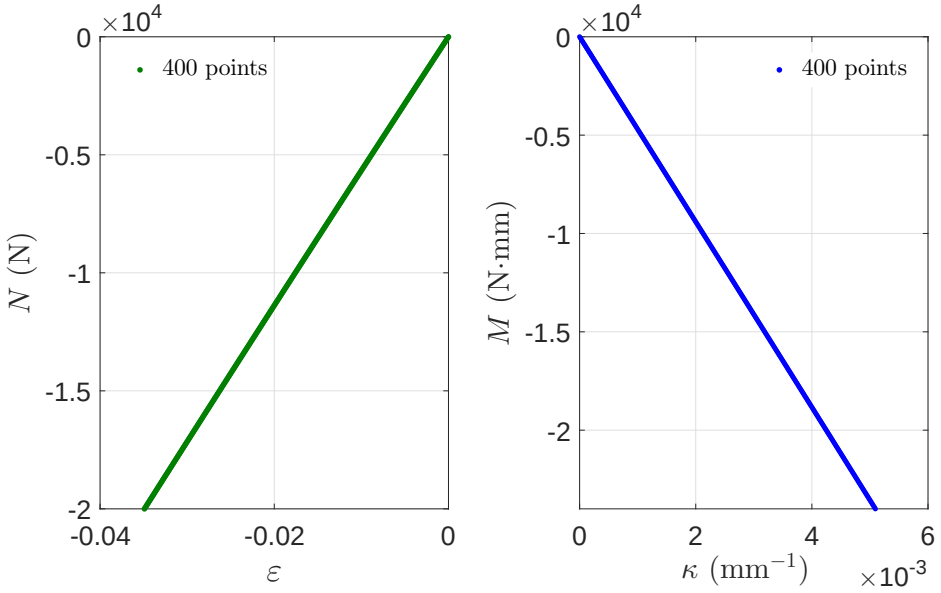

FIGURE 4.23 – Structural-genome database for the thin composite beam.

To monitor the instability of micro-structures, the deformation of the RVE at point P (see Fig. 4.21) during the processes of uniaxial compression and three-point bending are presented in Fig. 4.24 and Fig. 4.25. Although the constitutive relation at the macroscopic level of the composite beam is approximately linear, the plastic deformation of the micro-structure occurs and the fiber buckling is observed during the loading process.

The proposed SGD method with the yielded structural-genome database is used to compute the case shown in Fig. 4.21. Two finite element discretizations, namely 20 and 40 two-node 1D elements respectively with 3 Gauss points per element, are considered for SGD computing to reveal the influence of mesh density. The constant C is set to be 1 as suggested in the previous subsection. The numerical solution via SGD method is compared with that obtained by the FE^2 method. To avoid the influence of the initial assignments of structural-genome data points on the accuracy, the computing is conducted repeatedly for 100 times for each numerical

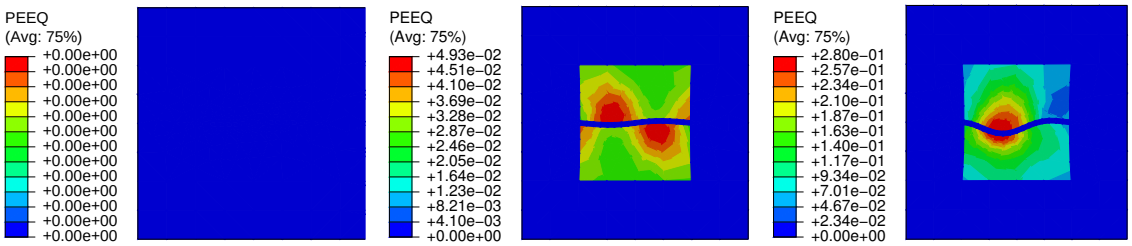

(a) $N = 0$ N (b) $N = -13682.5$ N (c) $N = -27669.8$ N

FIGURE 4.24 – The plastic deformation and the fiber instability in the RVE of point P during uniaxial compression.

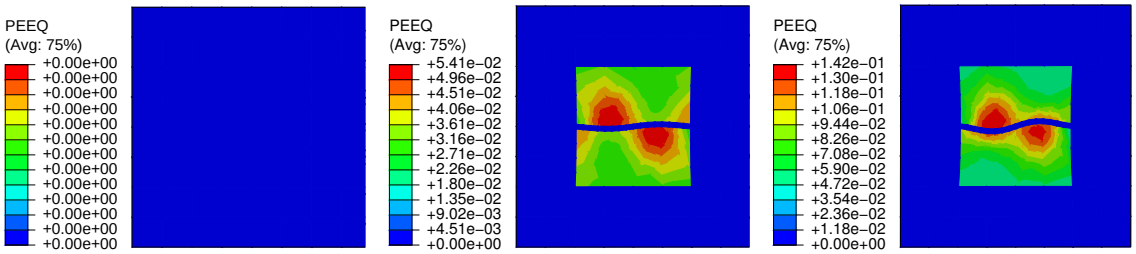

(a) $M = 0$ N·mm (b) $M = -12508.3$ N·mm (c) $M = -20845.8$ N·mm

FIGURE 4.25 – The plastic deformation and the fiber instability in the RVE of point P during three-point bending.

TABLE 4.6 – Relative errors of displacements $\tilde{u} = u(3L/4, 0)$ and $\tilde{w} = w(3L/4, 0)$.

		20 SGD elements		40 SGD elements	
F_1 (N)	F_2 (N)	Avg. $\epsilon_{\tilde{u}}$ (%)	Avg. $\epsilon_{\tilde{w}}$ (%)	Avg. $\epsilon_{\tilde{u}}$ (%)	Avg. $\epsilon_{\tilde{w}}$ (%)
−5244.04	7.03	0.76	0.84	0.78	0.59
−7876.12	10.58	0.07	0.59	0.06	0.59
−10512.90	14.16	0.36	0.80	0.36	0.85
−13151.90	17.76	0.47	1.03	0.48	1.03
−15790.90	21.44	0.47	1.63	0.47	1.57

test and the average value of the relative errors is taken into account. The average relative errors of displacements u and w of the neutral-plane at $x = 3L/4$ and the average number of iterations required for the convergence within various loading cases are illustrated in Table 4.6. The maximum error of displacements is less than 2%, and the number of iterations required for the convergence is less than 11 for the considered cases. Therefore, the accuracy and efficiency of SGD method is verified.

The results presented here exhibits the ability of the proposed SGD method for dealing with thin-walled composite structures with complex microscopic geometry and material properties. Once the structural-genome database is constructed, SGD method is able to solve various macroscopic loading cases efficiently without computing microscopic problems online simultaneously. Besides, for composite structures with unclear microscopic geometry and material properties, practical experiments could be employed to construct the required structural-genome database. Moreover, compared to MGD proposed by Kirchdoerfer and Ortiz [189], SGD method benefits from dimensional reduction of macroscopic model and the required database. For instance, to solve the same thin composite beam, MGD method requires a two-dimensional mesh and three-dimensional phase space of material database, that leads to a more expensive computational cost than the proposed one-dimension SGD method.

4.5 Conclusion

In the first part of this chapter, a novel multiscale finite element method (data-driven FE^2) based on a data-driven computing scheme is proposed for the structural analysis of composite structures. This method splits the multiscale system into two single scale problems, which can be solved sequentially and separately. In detail, the macroscopic computation is conducted by searching a stress-strain data point in a database constructed by solving microscopic problems in advance. This method inherits the features of data-driven computing scheme and computational homogenization. The results show that the proposed data-driven FE^2 method ensures high accuracy and the whole information in comparison with the classical FE^2 method. At the mean time, the highly demanding microscopic computation for real-time macroscopic constitutive relations in a classical FE^2 computing is replaced by searching stress-strain points in the material genome database. In this way, the online computing time is significantly saved because the latter is a fairly simple matching process, which can still be optimized by introducing algorithms such as dichotomy in the future. In comparison with the original multiscale problem, single scale problems are better addressed in literature and can be relatively more efficiently analyzed. As future work, we can expect that some high performance finite element models such as beams (De Pietro et al. [204], Hui et al. [205]), plates (Huang et al. [132]) and shells (Cong et al. [99]), can be adopted in both the macroscopic and the microscopic scales.

Adopting structural elements in the macroscopic scale, a novel SGD computing paradigm is proposed in the second part of this chapter for the analysis of thin-walled composite structures. The basic idea of SGD method is to search the best local state from the structural-genome database for the assignment of each integration point. The database is collected via FE^2 method which can conduct structural analysis for thin-walled composites with irregular microscopic heterogeneities. To evaluate the effectiveness of the proposed SGD method, a thin elastic beam was considered first. According to the results, the following conclusions can be drawn. Firstly, the numerical solution via SGD method matches well with the standard finite element solution. Secondly, the residual of penalty function and the maximum relative error of displacements converge with the number of sampling points in the structural-genome database. Thirdly, a re-

latively small value of the constant C in the penalty function is recommended to ensure the convergence. Finally, the accuracy of SGD solution is reduced by the intrusion of noisy data, but it remains acceptable. Thereafter, an example of composite beam with complex heterogeneities shows that the proposed SGD method is able to conduct numerical simulation precisely for thin-walled composite structures along with complex microscopic mechanisms. In summary, the proposed SGD scheme permits to efficiently conduct the numerical analysis of thin-walled composites especially with complex microscopic heterogeneities where the constitutive equations are quite difficult to be obtained. Apart from the beam modeling in this chapter, almost all the plate and shell models in the literature could be further employed in SGD framework for structural analysis of thin-walled composites. At the current data age, this combination of traditional structural analysis and data-driven technique has great potential in engineering design and optimization of composite structures.

5

Conclusion and perspectives

This thesis seeks to propose efficient numerical methods for the multiscale simulation of SMA based composites and cellular materials. To this end, multiscale finite element method is adopted to formulate the basic multiscale framework. Furthermore, typical problems such as instability and computational efficiency are studied to optimize the basic multiscale framework. The main contributions can be summarized as the following 3 points :

— Firstly, a multiscale numerical tool implemented on ABAQUS is developed for the modeling of SMAs based composites and architected materials. Results show that this proposed model could be applied for predicting the response of fiber reinforced composite taking advantage of SMAs' PE and SME. In addition to the SMA fiber reinforced composite, the superelasticity behavior of an architected SMA structure is also studied with the multiscale finite element model. The effect of changing the void fraction on cellular stiffness, maximum martensitic volume fraction, hysteresis effect and the structural responses are discussed in detail. Results show that the multiscale tool is necessary and successful for simulating the nonlinear behavior of the architected SMA structure.

— Secondly, model reduction method (TSVFC), efficient nonlinear solver (ANM) are further adopted to improve the computational efficiency in multiscale modeling for instability phenomenon of composite structures. The multiscale model implemented with TSVFC and ANM can accurately and efficiently simulate the instability phenomenon of long fiber reinforced composites, in which a first global macroscopic failure arises from the unstable composite structure while a second local macroscopic failure originates from the microscopic fiber buckling.

— Thirdly, the online computational efficiency of the macroscopic analysis is significantly improved by decoupling scales in the data-driven computing framework. The results show that the proposed data-driven FE^2 method ensures high accuracy and the whole information in comparison with the classical FE^2 method. Furthermore, a novel SGD computing paradigm is proposed for the analysis of thin-walled composite structures by introducing generalized stress and strain with structural elements in the macroscopic scale. Results show that the proposed SGD scheme permits to efficiently conduct the numerical analysis of thin-walled composites especially with complex microscopic heterogeneities where the constitutive equations are quite difficult to be obtained.

The present thesis leaves some topics that would be the possible research directions to address in the future :

— The proposed numerical tool for SMA based materials and structures can be used for designing other SMA composite structures thanks to the versatility and reliability of its

computing platform ABAQUS. For a further application of the multiscale procedure with ANM nonlinear solver, the instability of thin architected or composite SMA structures in 3D cases may be considered.

— In data-driven computing scheme, the data matching process can still be optimized by introducing algorithms such as dichotomy in the future. In comparison with the original multiscale problem in concurrent framework, single scale problems are better addressed in literature and can be relatively more efficiently analyzed. As future work, we can expect that some high performance finite element models such as beams De Pietro et al. [204], Hui et al. [205], plates Huang et al. [132] and shells Cong et al. [99], can be adopted in both the macroscopic and the microscopic scales to reduce the computational cost in both the online and offline stages. For example, the SGD computing significantly alleviates the burden of data dimensionality by adopting structural elements in the macroscopic scale. At the current data age, this combination of traditional structural analysis and data-driven technique has great potential in engineering design and optimization of composite structures.

— To apply the data-driven procedures on SMA based materials and structures, existing data-driven computing procedures still remain to be developed for path-dependent mechanisms. Meanwhile, considering the complicated thermomechanical behavior of SMAs with lots of parameters, the reduction of dimensionality of database will be another worthy investigating topic.

Appendix A. Asymptotic numerical method

The solution to many physics problems can be achieved through resolution of nonlinear problems depending on real parameter $\mathbf{\Theta}$. The corresponding nonlinear system of equations can be written as follow :

$$\mathbf{R}\left(\mathbf{\Theta};\vartheta\right)=0 \tag{1}$$

Assuming that a solution of Eq. (1) at point j is known, the solution $(\mathbf{\Theta};\vartheta)^{j+1}$ at point $j+1$ is obtained from this latter following a perturbation technique. An approached solution path at step $j+1$ is represented by a n-order Taylor series expansion of $\mathbf{\Theta}$ and ϑ :

$$\begin{aligned}\mathbf{\Theta}&=\mathbf{\Theta}^{j}+a\mathbf{\Theta}_1+a^2\mathbf{\Theta}_2+\ldots+a^n\mathbf{\Theta}_n=\mathbf{\Theta}^{j}+a^p\mathbf{\Theta}_p\\ \vartheta&=\vartheta^{j}+a\vartheta_1+a^2\vartheta_2+\ldots+a^n\vartheta_n=\vartheta^{j}+a^p\vartheta_p\end{aligned} \tag{2}$$

where $a\in\mathbb{R}$ is a solution path parameter for the non-linear problem. According to Einstein's notation, p is a dummy index that implicitly stands for summation over the range $[1,n]$. By replacing Eq. (2) within the non-linear problem, Eq. (1) reads :

$$\mathbf{R}\left(\mathbf{\Theta}^{j}+a^p\mathbf{\Theta}_p;\vartheta^{j}+a^p\vartheta_p\right)=0 \tag{3}$$

Its n-order Taylor series expansion about the point $(\mathbf{\Theta};\vartheta)^{j}$ is, then :

$$\begin{aligned}&\mathbf{R}\left(\mathbf{\Theta}^{j};\vartheta^{j}\right)+\left.\frac{\partial\mathbf{R}}{\partial\mathbf{\Theta}}\right|_j a^p\mathbf{\Theta}_p+\left.\frac{\partial\mathbf{R}}{\partial\vartheta}\right|_j a^p\vartheta_p+\\ &+\frac{1}{2}\left[\left.\frac{\partial^2\mathbf{R}}{\partial\mathbf{\Theta}^2}\right|_j a^p\mathbf{\Theta}_p a^s\mathbf{\Theta}_s+\left.\frac{\partial^2\mathbf{R}}{\partial\vartheta^2}\right|_j a^p\vartheta_p a^s\vartheta_s+\left.\frac{\partial^2\mathbf{R}}{\partial\mathbf{\Theta}\partial\vartheta}\right|_j a^p\mathbf{\Theta}_p a^s\vartheta_s\right]+\\ &+\frac{1}{3!}\left[\left.\frac{\partial^3\mathbf{R}}{\partial\mathbf{\Theta}^3}\right|_j a^p\mathbf{\Theta}_p a^s\mathbf{\Theta}_s a^q\mathbf{\Theta}_q+\left.\frac{\partial^3\mathbf{R}}{\partial\vartheta^3}\right|_j a^p\vartheta_p a^s\vartheta_s a^q\vartheta_q+\right.\\ &\left.+\left.\frac{\partial^3\mathbf{R}}{\partial\mathbf{\Theta}^2\partial\vartheta}\right|_j a^p\mathbf{\Theta}_p a^s\mathbf{\Theta}_s a^q\vartheta_q+\left.\frac{\partial^3\mathbf{R}}{\partial\mathbf{\Theta}\partial\vartheta^2}\right|_j a^p\mathbf{\Theta}_p a^s\vartheta_s a^q\vartheta_q\right]+\ldots=0\end{aligned} \tag{4}$$

where $\mathbf{R}\left(\mathbf{\Theta}^{j};\vartheta^{j}\right)=0$ since $(\mathbf{\Theta};\vartheta)^{j}$ belongs to the solution domain. Eq. (4) can be re-arranged in the following manner :

$$\begin{gathered}
\mathbf{R}\left(\boldsymbol{\Theta};\vartheta\right)=a\left[\left.\frac{\partial\mathbf{R}}{\partial\boldsymbol{\Theta}}\right|_j\boldsymbol{\Theta}_1+\left.\frac{\partial\mathbf{R}}{\partial\vartheta}\right|_j\vartheta_1\right]+\\
a^2\left\{\left.\frac{\partial\mathbf{R}}{\partial\boldsymbol{\Theta}}\right|_j\boldsymbol{\Theta}_2+\left.\frac{\partial\mathbf{R}}{\partial\vartheta}\right|_j\vartheta_2+\frac{1}{2}\left[\left.\frac{\partial^2\mathbf{R}}{\partial\boldsymbol{\Theta}^2}\right|_j\boldsymbol{\Theta}_1^2+\left.\frac{\partial^2\mathbf{R}}{\partial\vartheta^2}\right|_j\vartheta_1^2+\left.\frac{\partial^2\mathbf{R}}{\partial\boldsymbol{\Theta}\partial\vartheta}\right|_j\boldsymbol{\Theta}_1\vartheta_1\right]\right\}+\\
a^3\left[\left.\frac{\partial\mathbf{R}}{\partial\boldsymbol{\Theta}}\right|_j\boldsymbol{\Theta}_3+\left.\frac{\partial\mathbf{R}}{\partial\vartheta}\right|_j\vartheta_3-\mathscr{F}_3\left(\boldsymbol{\Theta}_1,\boldsymbol{\Theta}_2;\vartheta_1,\vartheta_2\right)\right]+\ldots+\\
+a^n\left[\left.\frac{\partial\mathbf{R}}{\partial\boldsymbol{\Theta}}\right|_j\boldsymbol{\Theta}_n+\left.\frac{\partial\mathbf{R}}{\partial\vartheta}\right|_j\vartheta_n-\mathscr{F}_n\left(\boldsymbol{\Theta}_1,\boldsymbol{\Theta}_2,\ldots,\boldsymbol{\Theta}_{n-1};\vartheta_1,\vartheta_2,\ldots,\vartheta_{n-1}\right)\right]=0
\end{gathered}\tag{5}$$

where, for a give order p of a, $\mathscr{F}_p$ is a function of the unknowns $\boldsymbol{\Theta}_k$ and ϑ_k up to the order $p-1$. Eq. (5) must be valid for a generic value of a, therefore, the following linear system of N equations in $N+1$ unknowns :

$$\left.\frac{\partial\mathbf{R}}{\partial\boldsymbol{\Theta}}\right|_j\boldsymbol{\Theta}_p+\left.\frac{\partial\mathbf{R}}{\partial\vartheta}\right|_j\vartheta_p=\mathscr{F}_p\left(\boldsymbol{\Theta}_1,\boldsymbol{\Theta}_2,\ldots,\boldsymbol{\Theta}_{p-1};\vartheta_1,\vartheta_2,\ldots,\vartheta_{p-1}\right)\tag{6}$$

is obtained from each term a^p. $\mathscr{F}_p$ is known once the linear system derived form the orders lower than the p-th one have been solved. The problem in Eq. (6) is not well posed and a complementary condition for each expansion term p should be provided. This complementary condition is obtained from the definition of the path parameter a as a pseudo-arc-length by projecting the solution increment $\left(\boldsymbol{\Theta};\vartheta\right)^{j+1}=\left(\boldsymbol{\Theta}-\boldsymbol{\Theta}^j;\vartheta-\vartheta^j\right)$ over the tangent direction $\left(\boldsymbol{\Theta}_1;\vartheta_1\right)$:

$$a=\left(\boldsymbol{\Theta}-\boldsymbol{\Theta}^j\right)^T\boldsymbol{\Theta}_1+\left(\vartheta-\vartheta^j\right)\vartheta_1\tag{7}$$

The following equations are, then, obtained by replacing Eq. (2) within Eq. (7) :

$$\begin{gathered}
\left\|\boldsymbol{\Theta}_1\right\|^2+\vartheta_1^2=1\\
\boldsymbol{\Theta}_p^T\boldsymbol{\Theta}_1+\vartheta_p\vartheta_1=0\quad p\geq 2
\end{gathered}\tag{8}$$

being $\|\cdot\|$ the Euclidean norm. As a concluding remark, it should be noted that at each step j, the matrix $\left.\dfrac{\partial\mathbf{R}}{\partial\boldsymbol{\Theta}}\right|_j$ is the same for each expansion term p which allows to save a relevant amount of calculation time. Once the values $\boldsymbol{\Theta}_p$ and ϑ_p have been all computed, the path solution at step $j+1$ is obtained by Eq. (2). Finally, the maximum value of path parameter a is adopted with the same principle as in Cochelin [138], :

$$a=\left(\epsilon\frac{\left\|\boldsymbol{\Theta}_1\right\|}{\left\|\boldsymbol{\Theta}_p\right\|}\right)^{\frac{1}{p-1}},\tag{9}$$

where ϵ is a precision parameter, which is determined by the user.

Publications

• **Papers in ISI Web of Sciences :**

— **Xu R.**†, Yang J.†, Yan W., Huang Q., Giunta G., Belouettar S., Zahrouni H., Ben Zineb T., Hu H.*, 2020. Data-driven multiscale finite element method : from concurrence to separation. Computer Methods in Applied Mechanics and Engineering, 363 : 112893.

— Hui Y.†, **Xu R.**†, Giunta G., De Pietro G., Hu H.*, Belouettar S., Carrera E., 2019. Multiscale CUF-FE^2 nonlinear analysis of composite beam structures. Computers & Structures, 221 : 28-43.

— **Xu R.**†, Hui Y.†, Hu H.*, Huang Q., Zahrouni H., Ben Zineb T., Potier-Ferry M., 2019. A Fourier-related FE^2 multiscale model for instability phenomena of long fiber reinforced materials. Composite Structures, 211 : 530-539.

— **Xu R.**, Bouby C., Zahrouni H.*, Ben Zineb T., Hu H., Potier-Ferry M., 2018. A multiscale analysis on the superelasticity behavior of architected shape memory alloy materials. Materials, 11(9), 1746.

— **Xu R.**, Bouby C., Zahrouni H., Ben Zineb T., Hu H.*, Potier-Ferry M., 2018. 3D modeling of shape memory alloy fiber reinforced composites by multiscale finite element method. Composite Structures, 200 : 408-419.

— Huang Q., Choe J., Yang J., **Xu R.**, Hui Y., Hu H.*, 2019. The effects of kinematics on post-buckling analysis of sandwich structures. Thin-Walled Structures, 143 : 106204.

— Huang Q., Choe J., Yang J., Hui Y., **Xu R.**, Hu H.*, 2019. An efficient approach for post-buckling analysis of sandwich structures with elastic-plastic material behavior. International Journal of Engineering Science, 142 : 20-35.

— Yang J., **Xu R.**, Hu H.*, Huang Q., Huang W., 2019. Structural-Genome-Driven computing for composite structures. Composite Structures, 215 : 446-453.

— Huang Q., **Xu R.**, Liu Y., Hu H.*, Giunta G., Belouettar S., Potier-Ferry M., 2017. A two-dimensional Fourier-series finite element for wrinkling analysis of thin films on compliant substrates. Thin-Walled Structures, 114 : 144-153.

• **International conferences :**

— **Rui Xu**, Wei Yan, Heng Hu, Qun Huang, Jie Yang. A data-driven multiscale finite element method for composite materials. Accepted to oral presentation in 4th China International Congress on Composite Materials (CCCM-4), Zhuhai, China, 2019.

— **Rui Xu**, Wei Yan, Heng Hu, Qun Huang, Jie Yang, Tarak Ben Zineb, Hamid Zahrouni. A data-driven multiscale finite element method for composite structures. Accepted to oral presentation in 22th International Conference on Composite Structures (ICCS22), Wuhan, China, 2019.

— **Rui Xu**, Céline Bouby, Hamid Zahrouni, Tarak Ben Zineb, Heng Hu, Michel Potier-Ferry. Multiscale finite element modeling for shape memory alloy fiber reinforced composite. Accepted to oral presentation in 7th International Conference on Smart Materials and Nanotechnology in Engineering (SMN2019), Harbin, China, 2019.

— **Rui Xu**, Wei Yan, Heng Hu, Qun Huang, Jie Yang. A novel multiscale computational homogenization framework based on data-driven computing. Accepted to oral presentation in 5th International Conference on Mechanics of Composites (MECHCOMP 2019), Lisbon, Portugal, 2019.

— **Rui Xu**, Céline Bouby, Hamid Zahrouni, Tarak Ben Zineb, Heng Hu, Michel Potier-Ferry. A multiscale modeling on alloy based cellular materials shape memory. Accepted to oral presentation in 14th Colloque National en Calcul des Structures (CSMA 2019), Giens, France, 2019.

— **Rui Xu**, Yanchuan Hui, Heng Hu, Qun Huang, Hamid Zahrouni, Tarak Ben Zineb, Michel Potier-Ferry. A double scale analysis on the phenomena of long fiber reinforced materials. Accepted to oral presentation in 14th Colloque National en Calcul des Structures (CSMA 2019), Giens, France, 2019.

— **Rui Xu**, Céline Bouby, Hamid Zahrouni, Tarak Ben Zineb, Heng Hu, Michel Potier-Ferry. A multiscale approach for the thermomechanical modeling of shape memory alloy fiber reinforced composites. Accepted to poster in 11th European Symposium on Martensitic Transformations (ESOMAT 2018), Metz, France, 2018.

— **Rui Xu**, Wei Yan, Yanchuan Hui, Qun Huang, Heng Hu. Multiscale modeling for instability phenomena of long fiber reinforced composite with a reduced microscopic model. Accepted to oral presentation in Chinese Conference on Computational Mechanics in conjunction with International Symposium on Computational Mechanics' 2018 (CCCM-ISCM 2018), Nanjing, China, 2018.

— **Rui Xu**, Yanchuan Hui, Qun Huang, Heng Hu, Hamid Zahrouni, Tarak Ben-zineb, Shaobo Zhu. Multiscale modeling for instability phenomena of long fiber reinforced composite with a double scale microscopic model. Accepted to oral presentation in World Congress on Computational Mechanics (WCCM XIII), New York City, USA, 2018.

— **Rui Xu**, Yanchuan Hui, Qun Huang, Heng Hu, Hamid Zahrouni, Tarak Ben-zineb, Shaobo Zhu. A reduced model for handling the instabilities of long fiber reinforced composite with multilevel finite element method. Accepted to oral presentation in 1st International Conference on Mechanics of Advanced Materials and Structures (ICMAMS 2018), Torino, Italy, 2018.

— **Rui Xu**, Céline Bouby, Hamid Zahrouni, Tarak Ben Zineb, Heng Hu, Michel Potier-Ferry. Multi-scale modeling of the thermomechanical behavior of shape memory alloy/polymer composites by multilevel finite element method. Accepted to oral presentation in 1st International Conference on Theoretical, Analytical and Computational Methods for Composite Materials and Composite Structures (ICOMP 2018), Wuhan, China, 2018.

— Jongchol Choe, Jian Liu, **Rui Xu**, Qun Huang, Heng Hu. A Fourier-reduced model for global-local-coupling wrinkling analysis of sandwich plates. Accepted to oral presentation in 20th International Conference on Composite Structures, Paris, France, 2017.

— **Rui Xu**, Céline Bouby, Hamid Zahrouni, Tarak Ben Zineb, Heng Hu, Michel Potier-Ferry. Modélisation multiéchelle du comportement thermomécanique des composites en alliage à mémoire de forme/polymère par la méthode des éléments finis au carré. Accepted to oral presentation in Congrès Français de Mécanique 2017, Lille, France, 2017.

— **Rui Xu**, Céline Bouby, Hamid Zahrouni, Tarak Ben Zineb, Heng Hu, Michel Potier-Ferry. Multiscale modeling of the thermomechanical behavior of shape memory alloy/ polymer composites by finite element square method. Accepted to oral presentation in 3rd International Conference on Mechanics of Composites, Bologna, Italy, 2017.

— Yanchuan Hui, **Rui Xu**, Heng Hu, Gaetano Giunta, Salim Belouettar. A novel FE^2 method based Fourier macroscopic model for instability phenomena of long fiber reinforced composites. Accepted by 19th International Conference on Composite Structures, Porto, Portugal, 2016.

— Yanchuan Hui, **Rui Xu**, Qun Huang, Heng Hu. A Fourier-related FE^2 multi-scale model for instability phenomena of long fiber reinforced materials. Accepted to oral presentation in World Congress on Computational Mechanics (WCCM XII), Seoul, Korea, 2016.

Bibliographie

[1] Y. Chemisky, A. Duval, E. Patoor, T. Ben Zineb, Constitutive model for shape memory alloys including phase transformation, martensitic reorientation and twins accommodation, Mechanics of Materials 43 (7) (2011) 361–376.

[2] D. C. Lagoudas, Shape memory alloys : modeling and engineering applications, Springer, 2008.

[3] J. M. Jani, M. Leary, A. Subic, M. A. Gibson, A review of shape memory alloy research, applications and opportunities, Materials & Design 56 (2014) 1078–1113.

[4] D. J. Hartl, D. C. Lagoudas, Aerospace applications of shape memory alloys, Proceedings of the Institution of Mechanical Engineers, Part G : Journal of Aerospace Engineering 221 (4) (2007) 535–552.

[5] A. Y. N. Sofla, S. Meguid, K. Tan, W. Yeo, Shape morphing of aircraft wing : status and challenges, Materials & Design 31 (3) (2010) 1284–1292.

[6] L. Sun, W. M. Huang, Nature of the multistage transformation in shape memory alloys upon heating, Metal Science & Heat Treatment 51 (11-12) (2009) 573–578.

[7] T. Uehara, T. Tamai, N. Ohno, Molecular dynamics simulations of shape-memory behavior based on martensite transformation and shear deformation, JSME International Journal Series A Solid Mechanics and Material Engineering 49 (3) (2006) 300–306.

[8] K. Saitoh, W. K. Liu, Molecular dynamics study of surface effect on martensitic cubic-to-tetragonal transformation in Ni–Al alloy, Computational Materials Science 46 (2) (2009) 531–544.

[9] X. Wang, B. Xu, Z. Yue, Micromechanical modelling of the effect of plastic deformation on the mechanical behaviour in pseudoelastic shape memory alloys, International Journal of Plasticity 24 (8) (2008) 1307–1332.

[10] C. Niclaeys, T. Ben Zineb, S. Arbab-Chirani, E. Patoor, Determination of the interaction energy in the martensitic state, International Journal of Plasticity 18 (11) (2002) 1619–1647.

[11] C. Cisse, W. Zaki, T. Ben Zineb, A review of constitutive models and modeling techniques for shape memory alloys, International Journal of Plasticity 76 (2016) 244–284.

[12] J. G. Boyd, D. C. Lagoudas, A thermodynamical constitutive model for shape memory materials. Part I. The monolithic shape memory alloy, International Journal of Plasticity 12 (6) (1996) 805–842.

[13] E. Patoor, A. Eberhardt, M. Berveiller, On Micromechanics of Thermoelastic Phase Transition, in : proceedings of Plasticity, vol. 93, 1993.

[14] B. Raniecki, C. Lexcellent, RL-models of pseudoelasticity and their specification for some shape memory solids, European Journal of Mechanics. A. Solids 13 (1) (1994) 21–50.

[15] Q. P. Sun, K. C. Hwang, Micromechanics modelling for the constitutive behavior of polycrystalline shape memory alloys—I. Derivation of general relations, Journal of the Mechanics and Physics of Solids 41 (1) (1993) 1–17.

[16] Q. P. Sun, K. C. Hwang, Micromechanics modelling for the constitutive behavior of polycrystalline shape memory alloys—II. Study of the individual phenomena, Journal of the Mechanics and Physics of Solids 41 (1) (1993) 19–33.

[17] D. C. Lagoudas, Z. Bo, M. A. Qidwai, A unified thermodynamic constitutive model for SMA and finite element analysis of active metal matrix composites, Mechanics of Composite Materials and Structures 3 (2) (1996) 153–179.

[18] S. Leclercq, C. Lexcellent, A general macroscopic description of the thermomechanical behavior of shape memory alloys, Journal of the Mechanics and Physics of Solids 44 (6) (1996) 953–980.

[19] A. C. Souza, E. N. Mamiya, N. Zouain, Three-dimensional model for solids undergoing stress-induced phase transformations, European Journal of Mechanics-A/Solids 17 (5) (1998) 789–806.

[20] P. Sittner, Y. Hara, M. Tokuda, Experimental study on the thermoelastic martensitic transformation in shape memory alloy polycrystal induced by combined external forces, Metallurgical and Materials Transactions A 26 (11) (1995) 2923–2935.

[21] F. Auricchio, L. Petrini, Improvements and algorithmical considerations on a recent three-dimensional model describing stress-induced solid phase transformations, International Journal for Numerical Methods in Engineering 55 (11) (2002) 1255–1284.

[22] B. Peultier, T. Ben Zineb, E. Patoor, Macroscopic constitutive law of shape memory alloy thermomechanical behaviour. Application to structure computation by FEM, Mechanics of Materials 38 (5-6) (2006) 510–524.

[23] B. Peultier, T. Ben Zineb, E. Patoor, A simplified micromechanical constitutive law adapted to the design of shape memory applications by finite element methods, Materials Science and Engineering : A 481 (2008) 384–388.

[24] W. Zaki, Z. Moumni, A three-dimensional model of the thermomechanical behavior of shape memory alloys, Journal of The Mechanics and Physics of Solids 55 (11) (2007) 2455–2490.

[25] B. Halphen, N. Q. Son, Plastic and visco-plastic materials with generalized potential, Mechanics Research Communications 1 (1) (1974) 43–47.

[26] L. Saintsulpice, S. A. Chirani, S. Calloch, A 3D super-elastic model for shape memory alloys taking into account progressive strain under cyclic loadings, Mechanics of Materials 41 (1) (2009) 12–26.

[27] W. Khalil, A. Mikolajczak, C. Bouby, T. Ben Zineb, A constitutive model for Fe-based shape memory alloy considering martensitic transformation and plastic sliding coupling : application to a finite element structural analysis, Journal of Intelligent Material Systems and Structures 23 (10) (2012) 1143–1160.

[28] A. Sallami, W. Khalil, T. Bouraoui, T. Ben Zineb, A finite-strain thermomechanical behavior model for iron-based shape memory alloys accounting for coupling between phase transformation and plastic slip, International Journal of Plasticity 124 (2020) 96–116.

[29] J. Wang, Z. Moumni, W. Zhang, Y. Xu, W. Zaki, A 3D finite-strain-based constitutive model for shape memory alloys accounting for thermomechanical coupling and martensite reorientation, Smart Materials and Structures 26 (6) (2017) 065006.

[30] H. Xiao, An explicit, straightforward approach to modeling SMA pseudoelastic hysteresis, International Journal of Plasticity 53 (2014) 228–240.

[31] A. Ojha, H. Sehitoglu, Transformation stress modeling in new FeMnAlNi shape memory alloy, International Journal of Plasticity 86 (2016) 93–111.

[32] R. Mahnken, M. Wolff, C. Cheng, A multi-mechanism model for cutting simulations combining visco-plastic asymmetry and phase transformation, International Journal of Solids and Structures 50 (20-21) (2013) 3045–3066.

[33] X. Gu, W. Zaki, C. Morin, Z. Moumni, W. Zhang, Time integration and assessment of a model for shape memory alloys considering multiaxial nonproportional loading cases, International Journal of Solids and Structures 54 (2015) 82–99.

[34] S. Hazar, W. Zaki, Z. Moumni, G. Anlas, Modeling of steady-state crack growth in shape memory alloys using a stationary method, International Journal of Plasticity 67 (2015) 26–38.

[35] B. T. Węcławski, M. Fan, D. Hui, Compressive behaviour of natural fibre composite, Composites Part B : Engineering 67 (2014) 183–191.

[36] I. Vesely, D. Boughner, T. Song, Tissue buckling as a mechanism of bioprosthetic valve failure, The Annals of Thoracic Surgery 46 (3) (1988) 302–308.

[37] L. Liu, D. Hu, X. Han, A three-dimensional unit cell model with controllable crimped structure for investigating finite strain response of collagen fiber reinforced biological composites, Composites Science and Technology 164 (2018) 178–186.

[38] C. Jochum, J.-C. Grandidier, M. A. Smaali, Experimental study of long T300 carbon fibre undulations during the curing of LY556 epoxy resin, Composites Science and Technology 67 (11-12) (2007) 2633–2642.

[39] A. Murdani, S. Hadi, U. S. Amrullah, Flexural properties and vibration behavior of jute/glass/carbon fiber reinforced unsaturated polyester hybrid composites for wind turbine blade, Key Engineering Materials 748 (2017) 62–68.

[40] A. Fasana, A. Ferraris, A. G. Airale, D. B. Polato, M. Carello, Experimental characterization of damped CFRP materials with an application to a lightweight car door, Shock and Vibration 2017 (2017) 1–9.

[41] Q. Ge, C. K. Dunn, H. J. Qi, M. L. Dunn, Active origami by 4D printing, Smart Materials and Structures 23 (9) (2014) 094007.

[42] F. Momeni, S. M.Mehdi Hassani.N, X. Liu, J. Ni, A review of 4D printing, Materials & Design 122 (Complete) (2017) 42–79.

[43] Tibbits, Skylar, 4D printing : multi-material shape change, Architectural Design 84 (1) (2014) 116–121.

[44] Z. Ding, C. Yuan, X. Peng, T. Wang, H. J. Qi, M. L. Dunn, Direct 4D printing via active composite materials, Science Advances 3 (4) (2017) e1602890.

[45] B. T. Lester, T. Baxevanis, Y. Chemisky, D. C. Lagoudas, Review and perspectives : shape memory alloy composite systems, Acta Mechanica 226 (12) (2015) 3907–3960.

[46] M. Meo, F. Marulo, M. Guida, S. Russo, Shape memory alloy hybrid composites for improved impact properties for aeronautical applications, Composite Structures 95 (2013) 756–766.

[47] A. M. Halahla, Y. B. A. Tahnat, A. H. Almasri, G. Z. Voyiadjis, The effect of shape memory alloys on the ductility of exterior reinforced concrete beam-column joints using the damage plasticity model, Engineering Structures 200 (2019) 109676.

[48] N. Feng, L. Liu, Y. Liu, J. Leng, Characteristics of multi-functional composites using elastomer embedded with Shape Memory Alloy wires, Materials & Design 88 (2015) 75–81.

[49] Z. Li, R. Huang, Z. Liu, A periodic deformation mechanism of a soft actuator for crawling and grasping, Advanced Materials and Technologies 4 (12) (2019) 1900653.

[50] D. Lagoudas, J. Boyd, Z. Bo, Micromechanics of active composites with SMA fibers .

[51] N. Siredey, E. Patoor, M. Berveiller, A. Eberhardt, Constitutive equations for polycrystalline thermoelastic shape memory alloys : Part I. Intragranular interactions and behavior of the grain, International Journal of Solids and Structures 36 (28) (1999) 4289–4315.

[52] E. Patoor, D. Entemeyer, A. Eberhardt, M. Berveiller, Stress-induced martensitic transformation in polycrystalline alloys, Zamm-zeitschrift Fur Angewandte Mathematik Und Mechanik 80 (2000) 443–444.

[53] D. Helm, P. Haupt, Thermomechanical behavior of shape memory alloys, in : Smart Structures and Materials 2001 : Active Materials : Behavior and Mechanics, vol. 4333, International Society for Optics and Photonics, 302–313, 2001.

[54] S. Marfia, Micro–macro analysis of shape memory alloy composites, International Journal of Solids and Structures 42 (13) (2005) 3677–3699.

[55] A. Damanpack, M. Aghdam, M. Shakeri, Micro-mechanics of composite with SMA fibers embedded in metallic/polymeric matrix under off-axial loadings, European Journal of Mechanics-A/Solids 49 (2015) 467–480.

[56] M. Kawai, H. Ogawa, V. Baburaj, T. Koga, Micromechamical analysis for hysteretic behavior of unidirectional TiNi SMA fiber composites, Journal of Intelligent Material Systems and Structures 10 (1) (1999) 14–28.

[57] G. Chatzigeorgiou, N. Charalambakis, Y. Chemisky, F. Meraghni, Periodic homogenization for fully coupled thermomechanical modeling of dissipative generalized standard materials, International Journal of Plasticity 81 (2016) 18–39.

[58] P. F. Dehaghani, S. H. Ardakani, H. Bayesteh, S. Mohammadi, 3D hierarchical multiscale analysis of heterogeneous SMA based materials, International Journal of Solids and Structures 118 (2017) 24–40.

[59] B. Kohlhaas, S. Klinkel, An FE^2 model for the analysis of shape memory alloy fibercomposites, Computational Mechanics 55 (2) (2015) 421–437.

[60] G. Chatzigeorgiou, Y. Chemisky, F. Meraghni, Computational micro to macro transitions for shape memory alloy composites using periodic homogenization, Smart Materials and Structures 24 (3) (2015) 035009.

[61] M. A. Qidwai, D. C. Lagoudas, On thermomechanics and transformation surfaces of polycrystalline NiTi shape memory alloy material, International Journal of Plasticity 16 (10) (2000) 1309–1343.

[62] M. Ashby, L. Gibson, Cellular solids : structure and properties, Press Syndicate of the University of Cambridge, Cambridge, UK (1997) 175–231.

[63] M. F. Ashby, T. Evans, N. A. Fleck, J. Hutchinson, H. Wadley, L. Gibson, Metal foams : a design guide, Elsevier, 2000.

[64] H. Y. Sarvestani, A. Akbarzadeh, H. Niknam, K. Hermenean, 3D printed architected polymeric sandwich panels : energy absorption and structural performance, Composite Structures 200 (2018) 886–909.

[65] F. García-Moreno, Commercial applications of metal foams : their properties and production, Materials 9 (2) (2016) 85.

[66] Y. Hangai, Y. Nakano, S. Koyama, O. Kuwazuru, S. Kitahara, N. Yoshikawa, Fabrication of aluminum tubes filled with aluminum alloy foam by friction welding, Materials 8 (10) (2015) 7180–7190.

[67] M. Strano, A. Marra, V. Mussi, M. Goletti, P. Bocher, Endurance of damping properties of foam-filled tubes, Materials 8 (7) (2015) 4061–4079.

[68] M. Rashed, M. Ashraf, R. Mines, P. J. Hazell, Metallic microlattice materials : a current state of the art on manufacturing, mechanical properties and applications, Materials & Design 95 (2016) 518–533.

[69] M. Taherishargh, I. Belova, G. Murch, T. Fiedler, Pumice/aluminium syntactic foam, Materials Science and Engineering : A 635 (2015) 102–108.

[70] M. Taherishargh, M. Sulong, I. Belova, G. Murch, T. Fiedler, On the particle size effect in expanded perlite aluminium syntactic foam, Materials & Design 66 (2015) 294–303.

[71] M. Taherishargh, I. Belova, G. Murch, T. Fiedler, The effect of particle shape on mechanical properties of perlite/metal syntactic foam, Journal of Alloys and Compounds 693 (2017) 55–60.

[72] S. Broxtermann, M. Taherishargh, I. Belova, G. Murch, T. Fiedler, On the compressive behaviour of high porosity expanded Perlite-Metal Syntactic Foam (P-MSF), Journal of Alloys and Compounds 691 (2017) 690–697.

[73] E. Linul, N. Movahedi, L. Marsavina, On the lateral compressive behavior of empty and ex-situ aluminum foam-filled tubes at high temperature, Materials 11 (4) (2018) 554.

[74] D. Luong, D. Lehmhus, N. Gupta, J. Weise, M. Bayoumi, Structure and compressive properties of invar-cenosphere syntactic foams, Materials 9 (2) (2016) 115.

[75] S. Pingle, N. Fleck, V. Deshpande, H. Wadley, Collapse mechanism maps for the hollow pyramidal core of a sandwich panel under transverse shear, International Journal of Solids and Structures 48 (25-26) (2011) 3417–3430.

[76] T. A. Schaedler, C. J. Ro, A. E. Sorensen, Z. Eckel, S. S. Yang, W. B. Carter, A. J. Jacobsen, Designing metallic microlattices for energy absorber applications, Advanced Engineering Materials 16 (3) (2014) 276–283.

[77] T. A. Schaedler, W. B. Carter, Architected cellular materials, Annual Review of Materials Research 46 (2016) 187–210.

[78] D. Lehmhus, M. Vesenjak, S. Schampheleire, T. Fiedler, From stochastic foam to designed structure : balancing cost and performance of cellular metals, 2017.

[79] T. D. Ngo, A. Kashani, G. Imbalzano, K. T. Nguyen, D. Hui, Additive manufacturing (3D printing) : a review of materials, methods, applications and challenges, Composites Part B : Engineering 143 (2018) 172–196.

[80] A. Mostafaei, P. R. De Vecchis, E. L. Stevens, M. Chmielus, Sintering regimes and resulting microstructure and properties of binder jet 3D printed Ni-Mn-Ga magnetic shape memory alloys, Acta Materialia 154 (2018) 355–364.

[81] M. Mehrpouya, A. Gisario, M. Elahinia, Laser welding of NiTi shape memory alloy : a review, Journal of Manufacturing Processes 31 (2018) 162–186.

[82] T. A. Schaedler, A. J. Jacobsen, A. Torrents, A. E. Sorensen, J. Lian, J. R. Greer, L. Valdevit, W. B. Carter, Ultralight metallic microlattices, Science 334 (6058) (2011) 962–965.

[83] R. Mines, On the characterisation of foam and micro-lattice materials used in sandwich construction, Strain 44 (1) (2008) 71–83.

[84] E. Patoor, D. C. Lagoudas, P. B. Entchev, L. C. Brinson, X. Gao, Shape memory alloys, Part I : general properties and modeling of single crystals, Mechanics of Materials 38 (5-6) (2006) 391–429.

[85] D. C. Lagoudas, P. B. Entchev, P. Popov, E. Patoor, L. C. Brinson, X. Gao, Shape memory alloys, Part II : modeling of polycrystals, Mechanics of Materials 38 (5-6) (2006) 430–462.

[86] H. Tobushi, S. Hayashi, Y. Sugimoto, et al., Two-way bending properties of shape memory composite with SMA and SMP, Materials 2 (3) (2009) 1180–1192.

[87] C. Cisse, W. Zaki, T. Ben Zineb, A review of modeling techniques for advanced effects in shape memory alloy behavior, Smart Materials and Structures 25 (10) (2016) 103001.

[88] G. Machado, H. Louche, T. Alonso, D. Favier, Superelastic cellular NiTi tube-based materials : fabrication, experiments and modeling, Materials & Design 65 (2015) 212–220.

[89] M. K. Ravari, S. N. Esfahani, M. T. Andani, M. Kadkhodaei, A. Ghaei, H. Karaca, M. Elahinia, On the effects of geometry, defects, and material asymmetry on the mechanical response of shape memory alloy cellular lattice structures, Smart Materials and Structures 25 (2) (2016) 025008.

[90] M. J. Ashrafi, A. Amerinatanzi, Z. Saebi, N. S. Moghaddam, R. Mehrabi, H. Karaca, M. Elahinia, Shape memory response of cellular lattice structures : unit cell finite element prediction, Mechanics of Materials 125 (2018) 26–34.

[91] C. Cissé, W. Zaki, T. Ben Zineb, Development and implementation of an effective constitutive model for architected cellular iron-based shape memory alloys : pressure dependency and transformation-plasticity interaction, Journal of Intelligent Material Systems and Structures 30 (12) (2019) 1789–1822.

[92] S. Zhu, C. Bouby, A. Cherouat, T. Ben Zineb, 3D reconstitution and numerical analysis of superelastic behavior of porous shape memory alloy, International Journal of Solids and Structures 168 (2019) 109–122.

[93] P. Kanouté, D. Boso, J. Chaboche, B. Schrefler, Multiscale methods for composites : a review, Archives of Computational Methods in Engineering 16 (1) (2009) 31–75.

[94] M. G. Geers, V. G. Kouznetsova, W. Brekelmans, Multi-scale computational homogenization : trends and challenges, Journal of Computational and Applied Mathematics 234 (7) (2010) 2175–2182.

[95] M. El Hachemi, Y. Koutsawa, H. Nasser, G. Giunta, A. Daouadji, E. Daya, S. Belouettar, An intuitive computational multi-scale methodology and tool for the dynamic modelling of viscoelastic composites and structures, Composite Structures 144 (2016) 131–137.

[96] G. Kinvi-Dossou, R. M. Boumbimba, N. Bonfoh, Y. Koutsawa, D. Eccli, P. Gerard, A numerical homogenization of E-glass/acrylic woven composite laminates : application to low velocity impact, Composite Structures 200 (2018) 540–554.

[97] F. Feyel, A multilevel finite element method (FE^2) to describe the response of highly nonlinear structures using generalized continua, Computer Methods in Applied Mechanics and Engineering 192 (28-30) (2003) 3233–3244.

[98] S. Nezamabadi, M. Potier-Ferry, H. Zahrouni, J. Yvonnet, Compressive failure of composites : a computational homogenization approach, Composite Structures 127 (2015) 60–68.

[99] Y. Cong, S. Nezamabadi, H. Zahrouni, J. Yvonnet, Multiscale computational homogenization of heterogeneous shells at small strains with extensions to finite displacements and buckling, International Journal for Numerical Methods in Engineering 104 (4) (2015) 235–259.

[100] E. Tikarrouchine, G. Chatzigeorgiou, F. Praud, B. Piotrowski, Y. Chemisky, F. Meraghni, Three-dimensional FE^2 method for the simulation of non-linear, rate-dependent response of composite structures, Composite Structures 193 (2018) 165–179.

[101] Z. Yuan, J. Fish, Toward realization of computational homogenization in practice, International Journal for Numerical Methods in Engineering 73 (3) (2008) 361–380.

[102] A. Tchalla, S. Belouettar, A. Makradi, H. Zahrouni, An ABAQUS toolbox for multiscale finite element computation, Composites Part B : Engineering 52 (2013) 323–333.

[103] Y. Su, B. Ji, K.-C. Hwang, Y. Huang, Micro-buckling in the nanocomposite structure of biological materials, Journal of the Mechanics and Physics of Solids 60 (10) (2012) 1771–1790.

[104] U. Farooq, P. Myler, Finite element simulation of buckling-induced failure of carbon fibre-reinforced laminated composite panels embedded with damage zones, Acta Astronautica 115 (2015) 314–329.

[105] K. Poulios, C. F. Niordson, Homogenization of long fiber reinforced composites including fiber bending effects, Journal of the Mechanics and Physics of Solids 94 (2016) 433–452.

[106] B. Budiansky, N. A. Fleck, Compressive failure of fibre composites, Journal of the Mechanics and Physics of Solids 41 (1) (1993) 183–211.

[107] F. Chiti, C. M. Dobson, Protein misfolding, functional amyloid, and human disease, Annual Review of Biochemistry 75 (2006) 333–366.

[108] T. Vogler, S. Kyriakides, On the axial propagation of kink bands in fiber composites : part I experiments, International Journal of Solids and Structures 36 (4) (1999) 557–574.

[109] E. G. Guynn, O. O. Ochoa, W. L. Bradley, A parametric study of variables that affect fiber microbuckling initiation in composite laminates : part 1-analyses, Journal of Composite Materials 26 (11) (1992) 1594–1616.

[110] R. Gutkin, S. Pinho, P. Robinson, P. Curtis, Micro-mechanical modelling of shear-driven fibre compressive failure and of fibre kinking for failure envelope generation in CFRP laminates, Composites Science and Technology 70 (8) (2010) 1214–1222.

[111] S. Kyriakides, R. Arseculeratne, E. Perry, K. Liechti, On the compressive failure of fiber reinforced composites, International Journal of Solids and Structures 32 (6-7) (1995) 689–738.

[112] T. Vogler, S.-Y. Hsu, S. Kyriakides, On the initiation and growth of kink bands in fiber composites. Part II : analysis, International Journal of Solids and Structures 38 (15) (2001) 2653–2682.

[113] J.-M. Guimard, O. Allix, N. Pechnik, P. Thevenet, Energetic analysis of fragmentation mechanisms and dynamic delamination modelling in CFRP composites, Computers & Structures 87 (15-16) (2009) 1022–1032.

[114] N. Feld, O. Allix, E. Baranger, J.-M. Guimard, A micromechanics-based mesomodel for unidirectional laminates in compression up to failure, Journal of Composite Materials 46 (23) (2012) 2893–2909.

[115] M. Romanowicz, Initiation of kink bands from regions of higher misalignment in carbon fiber-reinforced polymers, Journal of Composite Materials 48 (19) (2014) 2387–2399.

[116] J. L. Wind, S. Steffensen, H. M. Jensen, Comparison of a composite model and an individually fiber and matrix discretized model for kink band formation, International Journal of Non-Linear Mechanics 67 (2014) 319–325.

[117] V. Kouznetsova, M. G. Geers, W. Brekelmans, Multi-scale second-order computational homogenization of multi-phase materials : a nested finite element solution strategy, Computer Methods in Applied Mechanics and Engineering 193 (48-51) (2004) 5525–5550.

[118] Y. Koutsawa, Overall properties of piezoelectric composites with spring-type imperfect interfaces using the mechanics of structure genome, Composites Part B : Engineering 153 (2018) 337–345.

[119] Y. Koutsawa, A. Karatrantos, W. Yu, D. Ruch, A micromechanics approach for the effective thermal conductivity of composite materials with general linear imperfect interfaces, Composite Structures 200 (2018) 747–756.

[120] N. A. Fleck, J. Y. Shu, Microbuckle initiation in fibre composites : a finite element study, Journal of the Mechanics and Physics of Solids 43 (12) (1995) 1887–1918.

[121] H. M. Jensen, J. Christoffersen, Kink band formation in fiber reinforced materials, Journal of the Mechanics and Physics of Solids 45 (7) (1997) 1121–1136.

[122] S. Drapier, J.-C. Grandidier, M. Potier-Ferry, A structural approach of plastic microbuckling in long fibre composites : comparison with theoretical and experimental results, International Journal of Solids and Structures 38 (22-23) (2001) 3877–3904.

[123] K. Poulios, C. F. Niordson, Micro-buckling of periodically layered composites in regions of stress concentration, Composite Structures 157 (2016) 424–435.

[124] S. Nezamabadi, J. Yvonnet, H. Zahrouni, M. Potier-Ferry, A multilevel computational strategy for handling microscopic and macroscopic instabilities, Computer Methods in Applied Mechanics and Engineering 198 (27-29) (2009) 2099–2110.

[125] J. Yvonnet, H. Zahrouni, M. Potier-Ferry, A model reduction method for the post-buckling analysis of cellular microstructures, Computer Methods in Applied Mechanics and Engineering 197 (1-4) (2007) 265–280.

[126] R. A. van Tuijl, J. J. Remmers, M. G. Geers, Integration efficiency for model reduction in micro-mechanical analyses, Computational Mechanics 62 (2) (2018) 151–169.

[127] J. Hernández, J. Oliver, A. E. Huespe, M. Caicedo, J. Cante, High-performance model reduction techniques in computational multiscale homogenization, Computer Methods in Applied Mechanics and Engineering 276 (2014) 149–189.

[128] N. Damil, M. Potier-Ferry, A generalized continuum approach to predict local buckling patterns of thin structures, European Journal of Computational Mechanics/revue Européenne de Mécanique Numérique 17 (5-7) (2008) 945–956.

[129] N. Damil, M. Potier-Ferry, Influence of local wrinkling on membrane behaviour : a new approach by the technique of slowly variable Fourier coefficients, Journal of the Mechanics and Physics of Solids 58 (8) (2010) 1139–1153.

[130] Q. Huang, J. Yang, W. Huang, Y. Liu, H. Hu, G. Giunta, S. Belouettar, A new Fourier-related double scale analysis for wrinkling analysis of thin films on compliant substrates, Composite Structures 160 (2017) 613–624.

[131] Q. Huang, H. Hu, K. Yu, M. Potier-Ferry, S. Belouettar, N. Damil, Macroscopic simulation of membrane wrinkling for various loading cases, International Journal of Solids and Structures 64 (2015) 246–258.

[132] Q. Huang, Y. Liu, H. Hu, Q. Shao, K. Yu, G. Giunta, S. Belouettar, M. Potier-Ferry, A Fourier-related double scale analysis on the instability phenomena of sandwich plates, Computer Methods in Applied Mechanics and Engineering 318 (2017) 270–295.

[133] N. Damil, M. Potier-Ferry, H. Hu, New nonlinear multi-scale models for wrinkled membranes, Comptes Rendus Mécanique 341 (8) (2013) 616–624.

[134] Y. Liu, K. Yu, H. Hu, S. Belouettar, M. Potier-Ferry, N. Damil, A new Fourier-related double scale analysis for instability phenomena in sandwich structures, International Journal of Solids and Structures 49 (22) (2012) 3077–3088.

[135] K. Mhada, B. Braikat, N. Damil, A 2D Fourier double scale analysis of global-local instability interaction in sandwich structures, in : Congrès français de mécanique, AFM, Maison de la Mécanique, 39/41 rue Louis Blanc, 92400 Courbevoie, France, 2013.

[136] K. Attipou, H. Hu, F. Mohri, M. Potier-Ferry, S. Belouettar, Thermal wrinkling of thin membranes using a Fourier-related double scale approach, Thin-Walled Structures 94 (2015) 532–544.

[137] W. Huang, Q. Huang, Y. Liu, J. Yang, H. Hu, F. Trochu, P. Causse, A Fourier based reduced model for wrinkling analysis of circular membranes, Computer Methods in Applied Mechanics and Engineering 345 (2019) 1114–1137.

[138] B. Cochelin, A path-following technique via an asymptotic-numerical method, Computers & Structures 53 (5) (1994) 1181–1192.

[139] E. Boutyour, H. Zahrouni, M. Potier-Ferry, M. Boudi, Bifurcation points and bifurcated branches by an asymptotic numerical method and Padé approximants, International Journal for Numerical Methods in Engineering 60 (12) (2004) 1987–2012.

[140] H. Zahrouni, B. Cochelin, M. Potier-Ferry, Computing finite rotations of shells by an asymptotic-numerical method, Computer Methods in Applied Mechanics and Engineering 175 (1-2) (1999) 71–85.

[141] J. Cadou, M. Potier-Ferry, B. Cochelin, N. Damil, ANM for stationary Navier–Stokes equations and with Petrov–Galerkin formulation, International Journal for Numerical Methods in Engineering 50 (4) (2001) 825–845.

[142] H. Abichou, H. Zahrouni, M. Potier-Ferry, Asymptotic numerical method for problems coupling several nonlinearities, Computer Methods in Applied Mechanics and Engineering 191 (51-52) (2002) 5795–5810.

[143] M. Assidi, H. Zahrouni, N. Damil, M. Potier-Ferry, Regularization and perturbation technique to solve plasticity problems, International Journal of Material Forming 2 (1) (2009) 1–14.

[144] A. Tri, H. Zahrouni, M. Potier-Ferry, High order continuation algorithm and meshless procedures to solve nonlinear Poisson problems, Engineering Analysis with Boundary Elements 36 (11) (2012) 1705–1714.

[145] J. Yang, Q. Huang, H. Hu, G. Giunta, S. Belouettar, M. Potier-Ferry, A new family of finite elements for wrinkling analysis of thin films on compliant substrates, Composite Structures 119 (2015) 568–577.

[146] J. Choe, Q. Huang, J. Yang, H. Hu, An efficient approach to investigate the post-buckling behaviors of sandwich structures, Composite Structures 201 (2018) 377–388.

[147] Q. Huang, R. Xu, Y. Liu, H. Hu, G. Giunta, S. Belouettar, M. Potier-Ferry, A two-dimensional Fourier-series finite element for wrinkling analysis of thin films on compliant substrates, Thin-Walled Structures 114 (2017) 144–153.

[148] P. Vannucci, B. Cochelin, N. Damil, M. Potier-Ferry, An asymptotic-numerical method to compute bifurcating branches, International Journal for Numerical Methods in Engineering 41 (8) (1998) 1365–1389.

[149] F. Xu, M. Potier-Ferry, S. Belouettar, H. Hu, Multiple bifurcations in wrinkling analysis of thin films on compliant substrates, International Journal of Non-Linear Mechanics 76 (2015) 203–222.

[150] S. Nemat-Nasser, M. Hori, Micromechanics : overall properties of heterogeneous materials, vol. 37, Elsevier, 2013.

[151] E. S. Perdahcıoğlu, H. J. Geijselaers, Constitutive modeling of two phase materials using the mean field method for homogenization, International Journal of Material Forming 4 (2) (2011) 93–102.

[152] L. Wu, F. Sket, J. M. Molina-Aldareguia, A. Makradi, L. Adam, I. Doghri, L. Noels, A study of composite laminates failure using an anisotropic gradient-enhanced damage mean-field homogenization model, Composite Structures 126 (2015) 246–264.

[153] H. Li, B. Zhang, G. Bai, Effects of constructing different unit cells on predicting composite viscoelastic properties, Composite Structures 125 (2015) 459–466.

[154] S. Green, M. Matveev, A. Long, D. Ivanov, S. Hallett, Mechanical modelling of 3D woven composites considering realistic unit cell geometry, Composite Structures 118 (2014) 284–293.

[155] F. Feyel, J.-L. Chaboche, FE^2 multiscale approach for modelling the elastoviscoplastic behaviour of long fibre SiC/Ti composite materials, Computer Methods in Applied Mechanics and Engineering 183 (3-4) (2000) 309–330.

[156] C. Miehe, J. Schröder, J. Schotte, Computational homogenization analysis in finite plasticity simulation of texture development in polycrystalline materials, Computer Methods in Applied Mechanics and Engineering 171 (3-4) (1999) 387–418.

[157] F. Feyel, Multiscale FE^2 elastoviscoplastic analysis of composite structures, Computational Materials Science 16 (1-4) (1999) 344–354.

[158] D. Boso, M. Lefik, B. Schrefler, A multilevel homogenised model for superconducting strand thermomechanics, Cryogenics 45 (4) (2005) 259–271.

[159] J. Fish, K. Shek, M. Pandheeradi, M. S. Shephard, Computational plasticity for composite structures based on mathematical homogenization : theory and practice, Computer Methods in Applied Mechanics and Engineering 148 (1-2) (1997) 53–73.

[160] K. Attipou, S. Nezamabadi, H. Zahrouni, et al., A multiscale approach for the vibration analysis of heterogeneous materials : application to passive damping, Journal of Sound and Vibration 332 (4) (2013) 725–739.

[161] T. J. Hughes, G. R. Feijóo, L. Mazzei, J.-B. Quincy, The variational multiscale method–a paradigm for computational mechanics, Computer Methods in Applied Mechanics and Engineering 166 (1-2) (1998) 3–24.

[162] K.-M. Kodjo, J. Yvonnet, M. Karkri, K. Sab, Multiscale modeling of the thermomechanical behavior in heterogeneous media embedding phase change materials particles, Journal of Computational Physics 378 (2019) 303–323.

[163] X. Liu, W. Yu, A novel approach to analyze beam-like composite structures using mechanics of structure genome, Advances in Engineering Software 100 (2016) 238–251.

[164] X. Liu, K. Rouf, B. Peng, W. Yu, Two-step homogenization of textile composites using mechanics of structure genome, Composite Structures 171 (2017) 252–262.

[165] K. Rouf, X. Liu, W. Yu, Multiscale structural analysis of textile composites using mechanics of structure genome, International Journal of Solids and Structures 136 (2018) 89–102.

[166] P. R. Budarapu, R. Gracie, S.-W. Yang, X. Zhuang, T. Rabczuk, Efficient coarse graining in multiscale modeling of fracture, Theoretical and Applied Fracture Mechanics 69 (2014) 126–143.

[167] H. Talebi, M. Silani, S. P. A. Bordas, P. Kerfriden, T. Rabczuk, A computational library for multiscale modeling of material failure, Computational Mechanics 53 (5) (2014) 1047–1071.

[168] J. A. Hernandez, M. A. Caicedo, A. Ferrer, Dimensional hyper-reduction of nonlinear finite element models via empirical cubature, Computer Methods in Applied Mechanics and Engineering 313 (2017) 687–722.

[169] J. Yvonnet, Q.-C. He, The reduced model multiscale method (R3M) for the non-linear homogenization of hyperelastic media at finite strains, Journal of Computational Physics 223 (1) (2007) 341–368.

[170] H. Moulinec, P. Suquet, A numerical method for computing the overall response of nonlinear composites with complex microstructure, Computer Methods in Applied Mechanics and Engineering 157 (1-2) (1998) 69–94.

[171] F. S. Göküzüm, L. T. K. Nguyen, M.-A. Keip, A multiscale FE-FFT framework for electroactive materials at finite strains, Computational Mechanics 64 (1) (2019) 63–84.

[172] M. Rambausek, F. S. Göküzüm, L. T. K. Nguyen, M.-A. Keip, A two-scale FE-FFT approach to nonlinear magneto-elasticity, International Journal for Numerical Methods in Engineering 117 (11) (2019) 1117–1142.

[173] S. Klarmann, F. Gruttmann, S. Klinkel, Homogenization assumptions for coupled multiscale analysis of structural elements : beam kinematics, Computational Mechanics (2019) 1–27.

[174] Y. Hui, R. Xu, G. Giunta, G. De Pietro, H. Hu, S. Belouettar, E. Carrera, Multiscale CUF-FE^2 nonlinear analysis of composite beam structures, Computers & Structures 221 (2019) 28–43.

[175] M. Praster, M. Klassen, S. Klinkel, An adaptive FE^2 approach for fiber–matrix composites, Computational Mechanics 63 (6) (2019) 1333–1350.

[176] B. Le, J. Yvonnet, Q.-C. He, Computational homogenization of nonlinear elastic materials using neural networks, International Journal for Numerical Methods in Engineering 104 (12) (2015) 1061–1084.

[177] X. Lu, D. G. Giovanis, J. Yvonnet, V. Papadopoulos, F. Detrez, J. Bai, A data-driven computational homogenization method based on neural networks for the nonlinear anisotropic electrical response of graphene/polymer nanocomposites, Computational Mechanics 64 (2) (2019) 307–321.

[178] V. M. Nguyen-Thanh, L. T. K. Nguyen, T. Rabczuk, X. Zhuang, A surrogate model for computational homogenization of elastostatics at finite strain using the HDMR-based neural network approximator, arXiv preprint arXiv :1906.02005 .

[179] H. Yang, X. Guo, S. Tang, W. K. Liu, Derivation of heterogeneous material laws via data-driven principal component expansions, Computational Mechanics (2019) 1–15.

[180] J. Yvonnet, D. Gonzalez, Q.-C. He, Numerically explicit potentials for the homogenization of nonlinear elastic heterogeneous materials, Computer Methods in Applied Mechanics and Engineering 198 (33-36) (2009) 2723–2737.

[181] A. Clément, C. Soize, J. Yvonnet, Computational nonlinear stochastic homogenization using a nonconcurrent multiscale approach for hyperelastic heterogeneous microstructures analysis, International Journal for Numerical Methods in Engineering 91 (8) (2012) 799–824.

[182] Z. Liu, M. Bessa, W. K. Liu, Self-consistent clustering analysis : an efficient multi-scale scheme for inelastic heterogeneous materials, Computer Methods in Applied Mechanics and Engineering 306 (2016) 319–341.

[183] Z. Liu, M. Fleming, W. K. Liu, Microstructural material database for self-consistent clustering analysis of elastoplastic strain softening materials, Computer Methods in Applied Mechanics and Engineering 330 (2018) 547–577.

[184] S. Tang, L. Zhang, W. K. Liu, From virtual clustering analysis to self-consistent clustering analysis : a mathematical study, Computational Mechanics 62 (6) (2018) 1443–1460.

[185] O. L. Kafka, C. Yu, M. Shakoor, Z. Liu, G. J. Wagner, W. K. Liu, Data-driven mechanistic modeling of influence of microstructure on high-cycle fatigue life of nickel titanium, JOM 70 (7) (2018) 1154–1158.

[186] M. Shakoor, O. L. Kafka, C. Yu, W. K. Liu, Data science for finite strain mechanical science of ductile materials, Computational Mechanics 64 (1) (2019) 33–45.

[187] X. Han, C. Xu, W. Xie, S. Meng, Multiscale computational homogenization of woven composites from microscale to mesoscale using data-driven self-consistent clustering analysis, Composite Structures 220 (2019) 760–768.

[188] M. Bessa, R. Bostanabad, Z. Liu, A. Hu, D. W. Apley, C. Brinson, W. Chen, W. K. Liu, A framework for data-driven analysis of materials under uncertainty : countering the curse of dimensionality, Computer Methods in Applied Mechanics and Engineering 320 (2017) 633–667.

[189] T. Kirchdoerfer, M. Ortiz, Data-driven computational mechanics, Computer Methods in Applied Mechanics and Engineering 304 (2016) 81–101.

[190] T. Kirchdoerfer, M. Ortiz, Data driven computing with noisy material data sets, Computer Methods in Applied Mechanics and Engineering 326 (2017) 622–641.

[191] L. T. K. Nguyen, M.-A. Keip, A data-driven approach to nonlinear elasticity, Computers & Structures 194 (2018) 97–115.

[192] F. Chinesta, P. Ladevèze, R. Ibáñez, J. V. Aguado, E. Abisset-Chavanne, E. Cueto, Data-Driven Computational Plasticity, Procedia Engineering 207 (2017) 209–214.

[193] T. Kirchdoerfer, M. Ortiz, Data-driven computing in dynamics, International Journal for Numerical Methods in Engineering 113 (11) (2018) 1697–1710.

[194] A. Oishi, G. Yagawa, Computational mechanics enhanced by deep learning, Computer Methods in Applied Mechanics and Engineering 327 (2017) 327–351.

[195] R. Ibáñez, D. Borzacchiello, J. V. Aguado, E. Abisset-Chavanne, E. Cueto, P. Ladevèze, F. Chinesta, Data-driven non-linear elasticity : constitutive manifold construction and problem discretization, Computational Mechanics 60 (5) (2017) 813–826.

[196] R. Ibáñez, E. Abisset-Chavanne, D. González, J.-L. Duval, E. Cueto, F. Chinesta, Hybrid constitutive modeling : data-driven learning of corrections to plasticity models, International Journal of Material Forming (2018) 1–9.

[197] M. Latorre, F. J. Montáns, Experimental data reduction for hyperelasticity, Computers & Structures (2018) in press, .

[198] A. J. Hey, S. Tansley, K. M. Tolle, et al., The fourth paradigm : data-intensive scientific discovery, vol. 1, Microsoft research Redmond, WA, 2009.

[199] J. Yang, R. Xu, H. Hu, Q. Huang, W. Huang, Structural-Genome-Driven computing for composite structures, Composite Structures 215 (2019) 446–453.

[200] R. Eggersmann, T. Kirchdoerfer, S. Reese, L. Stainier, M. Ortiz, Model-free data-driven inelasticity, Computer Methods in Applied Mechanics and Engineering 350 (2019) 81–99.

[201] J. Neggers, O. Allix, F. Hild, S. Roux, Big data in experimental mechanics and model order reduction : today's challenges and tomorrow's opportunities, Archives of Computational Methods in Engineering 25 (1) (2018) 143–164.

[202] N. Liu, W. Yu, Evaluation of smeared properties approaches and mechanics of structure genome for analyzing composite beams, Mechanics of Advanced Materials and Structures 25 (14) (2018) 1171–1185.

[203] Q. Z. He, H. Hu, S. Belouettar, G. Guinta, K. Yu, Y. Liu, F. Biscani, E. Carrera, M. Potier-Ferry, Multi-scale modelling of sandwich structures using hierarchical kinematics, Composite Structures 93 (9) (2011) 2375–2383.

[204] G. De Pietro, Y. Hui, G. Giunta, S. Belouettar, E. Carrera, H. Hu, Hierarchical one-dimensional finite elements for the thermal stress analysis of three-dimensional functionally graded beams, Composite Structures 153 (2016) 514–528.

[205] Y. Hui, G. Giunta, S. Belouettar, Q. Huang, H. Hu, E. Carrera, A free vibration analysis of three-dimensional sandwich beams using hierarchical one-dimensional finite elements, Composites Part B : Engineering 110 (2017) 7–19.

[206] J. N. Reddy, A simple higher-order theory for laminated composite plates, Journal of Applied Mechanics 51 (4) (1984) 745–752.

[207] K. Yu, H. Hu, H. Tang, G. Giunta, M. Potier-Ferry, S. Belouettar, A novel two-dimensional finite element to study the instability phenomena of sandwich plates, Computer Methods in Applied Mechanics and Engineering 283 (2015) 1117–1137.

[208] J. N. Reddy, Mechanics of laminated composite plates and shells : theory and analysis, CRC press, Boca Raton, 2004.

[209] R. Hill, On constitutive macro-variables for heterogeneous solids at finite strain, Proceedings of the Royal Society of London. A. Mathematical and Physical Sciences 326 (1565) (1972) 131–147.

[210] A. Duval, M. Haboussi, T. Ben Zineb, Modelling of localization and propagation of phase transformation in superelastic SMA by a gradient nonlocal approach, International Journal of Solids and Structures 48 (13) (2011) 1879–1893.

[211] P. Sittner, L. Heller, J. Pilch, P. Sedlak, M. Frost, Y. Chemisky, A. Duval, B. Piotrowski, T. Ben Zineb, E. Patoor, et al., Roundrobin SMA modeling, in : ESOMAT 2009-8th European Symposium on Martensitic Transformations, EDP Sciences, 08001, 2009.

[212] H. Hu, N. Damil, M. Potier-Ferry, A bridging technique to analyze the influence of boundary conditions on instability patterns, Journal of Computational Physics 230 (10) (2011) 3753–3764.

[213] K. Yu, H. Hu, S. Chen, S. Belouettar, M. Potier-Ferry, Multi-scale techniques to analyze instabilities in sandwich structures, Composite Structures 96 (2013) 751–762.

[214] A. Ammar, F. Chinesta, E. Cueto, M. Doblaré, Proper generalized decomposition of time-multiscale models, International Journal for Numerical Methods in Engineering 90 (5) (2012) 569–596.

[215] K. Kpogan, A. Tri, A. Sogah, N. Mathieu, H. Zahrouni, M. Potier-Ferry, Combining MFS and PGD methods to solve transient heat equation, Numerical Methods for Partial Differential Equations 34 (1) (2018) 257–273.

[216] W. Aggoune, H. Zahrouni, M. Potier-Ferry, Asymptotic numerical methods for unilateral contact, International Journal for Numerical Methods in Engineering 68 (6) (2006) 605–631.

[217] B. W. Rosen, Mechanics of composite strengthening, Fiber Comopsite Materials 72 (1965) 75.

[218] R. Parnes, A. Chiskis, Buckling of nano-fibre reinforced composites : a re-examination of elastic buckling, Journal of the Mechanics and Physics of Solids 50 (4) (2002) 855–879.

[219] H. Schuerch, Prediction of compressive strength in uniaxial boron fiber-metal matrix composite materials., AIAA Journal 4 (1) (1966) 102–106.

[220] N. Damil, M. Potier-Ferry, H. Hu, Membrane wrinkling revisited from a multi-scale point of view, Advanced Modeling and Simulation in Engineering Sciences 1 (1) (2014) 6.

[221] W. Ramberg, W. R. Osgood, Description of stress-strain curves by three parameters, Tech. Rep. NACA-TN-902, National Advisory Committee on Aeronautics (NACA), Washington, D.C., United States, 1943.

[222] K.-J. Bathe, Finite element procedures, Prentice Hall, New Jersey, USA, 2006.

Résumé

L'objectif principal de cette thèse est de développer des techniques de modélisation et de simulation multi-échelles avancées et efficaces pour les matériaux architecturés et composites à base d'Alliages à Mémoire de Forme (AMF). À cette fin, un modèle générique 3D multi-échelles pour les AMF architecturés est implémenté dans ABAQUS, où un modèle thermodynamique, proposé par Chemisky et al. [1], est adopté pour décrire le comportement constitutif local de l'AMF, et la méthode des éléments finis multi-échelles (EF^2) pour réaliser l'interaction en temps réel entre le niveau microscopique et le niveau macroscopique. L'instabilité élastique des fibres au niveau microscopique est également étudiée efficacement dans ce cadre en introduisant la Méthode Asymptotique Numérique (MAN) et la Technique des Coefficients de Fourier à Variation Lente (TCFVL). Pour améliorer l'efficacité du calcul de l'approche simultanée à plusieurs échelles, dans laquelle d'énormes problèmes microscopiques sont résolus en ligne pour mettre à jour les contraintes macroscopiques, des méthodes de calcul multi-échelles basées sur les données sont proposées pour les structures composites. En découplant les échelles corrélées dans le cadre FE^2, les problèmes microscopiques sont résolus hors ligne, tandis que le coût du calcul macroscopique en ligne est considérablement réduit. De plus, en formulant le schéma data-driven en contrainte et déformation généralisées, le calcul par la technique Structural-Genome-Driven est développé pour les structures composites à parois minces.

Mots-clés: Alliage à mémoire de forme, Matériau architecturé, Homogénéisation numérique, Méthode des éléments finis multi-échelles, Méthode asymptotique numérique, Data-driven.

Abstract

The main aim of this thesis is to develop advanced and efficient multiscale modeling and simulation techniques for Shape Memory Alloys (SMAs) composite and architected materials. Towards this end, a 3D generic multiscale model for architected SMAs is implemented in ABAQUS, where a thermodynamic model, proposed by Chemisky et al. [1], is adopted to describe the local constitutive behavior of the SMA, and the multiscale finite element method (FE^2) to realize the real-time interaction between the microscopic and macroscopic levels. Microscopic fiber instability is also efficiently investigated in this framework by introducing the Asymptotic Numerical Method (ANM) and the Technique of Slowly Variable Fourier Coefficients (TSVFC). To improve the computational efficiency of the concurrent mulitscale approach, in which tremendous microscopic problems are solved online to update macroscopic stress, data-driven multiscale computing methods are proposed for composite structures. Decoupling the correlated scales in concurrent FE^2 framework, microscopic problems are solved offline, while the online macroscopic computational cost is significantly reduced. Further, by formulating the data-driven scheme in generalized stress and strain, Structural-Genome-Driven computing is developed for thin-walled composite structures.

Keywords: Shape memory alloy, Architected material, Numerical homogenization, Multiscale finite element method, Asymptotic numerical method, Data-driven.